

DYNAMIC DEFORMATION PROPERTIES OF ENERGETIC COMPOSITE MATERIALS

Final Report

J.E. Field, W.G. Proud, C.R. Siviour, S.M. Walley,
S.G. Grantham, D.M. Williamson, H. Czerski

April 2005

United States Air Force
European Office of Aerospace Research (EOARD)
London, England
Contract Number FA8655-03-1-3063

PCS Fracture and Shock Physics Group
Cavendish Laboratory
Madingley Road
Cambridge
CB3 0HE
United Kingdom

REPORT No.: SP 1154

RG 34942

Report Documentation Page

*Form Approved
OMB No. 0704-0188*

Public reporting burden for the collection of information is estimated to average 1 hour per response, including the time for reviewing instructions, searching existing data sources, gathering and maintaining the data needed, and completing and reviewing the collection of information. Send comments regarding this burden estimate or any other aspect of this collection of information, including suggestions for reducing this burden, to Washington Headquarters Services, Directorate for Information Operations and Reports, 1215 Jefferson Davis Highway, Suite 1204, Arlington VA 22202-4302. Respondents should be aware that notwithstanding any other provision of law, no person shall be subject to a penalty for failing to comply with a collection of information if it does not display a currently valid OMB control number.

1. REPORT DATE 18 MAY 2005	2. REPORT TYPE N/A	3. DATES COVERED -
4. TITLE AND SUBTITLE Dynamic Deformation Properties of Energetic Composite Materials		
5a. CONTRACT NUMBER		
5b. GRANT NUMBER		
5c. PROGRAM ELEMENT NUMBER		
6. AUTHOR(S)		
5d. PROJECT NUMBER		
5e. TASK NUMBER		
5f. WORK UNIT NUMBER		
7. PERFORMING ORGANIZATION NAME(S) AND ADDRESS(ES) University of Cambridge Madingly Road Cambridge CB3 OHE United Kingdom		
8. PERFORMING ORGANIZATION REPORT NUMBER		
9. SPONSORING/MONITORING AGENCY NAME(S) AND ADDRESS(ES)		
10. SPONSOR/MONITOR'S ACRONYM(S)		
11. SPONSOR/MONITOR'S REPORT NUMBER(S)		
12. DISTRIBUTION/AVAILABILITY STATEMENT Approved for public release, distribution unlimited		
13. SUPPLEMENTARY NOTES The original document contains color images.		
14. ABSTRACT		
15. SUBJECT TERMS		
16. SECURITY CLASSIFICATION OF:		
a. REPORT unclassified	b. ABSTRACT unclassified	c. THIS PAGE unclassified
17. LIMITATION OF ABSTRACT UU		
18. NUMBER OF PAGES 163		
19a. NAME OF RESPONSIBLE PERSON		

EXECUTIVE SUMMARY

This final report consists of six chapters: (1) An introduction to the PCS Fracture and Shock Physics Group (PCS FSP) and some preliminary experiments on PBXs (pp. 3-46); (2) The effect of particle size and temperature on the high strain rate properties of an AP/HTPB PBX (pp. 47-55); (3) Developments in Hopkinson bar instrumentation (pp. 56-74); (4) Visits of Clive R. Siviour to Eglin Airforce Base and studies of impact-induced solid-state phase change in HMX (pp. 75-77); (5) High rate mechanical properties of PBXs (pp. 78-102); (6) Optical techniques (pp. 103-160). Also in Appendix 2 there is a list of the papers published by the PCS FSP Group (and one report from Eglin AFB) during the duration of this contract (2003-2005). Most of these documents are available in pdf format. Please contact Dr S.M. Walley (smw14@phy.cam.ac.uk) if you are interested.

(1) In accordance with Defense Federal Acquisition Regulation 252.227-7036, Declaration of Technical Data Conformity (Jan 1997), All technical data delivered under this contract shall be accompanied by the following written declaration:

The Contractor, University of Cambridge, hereby declares that, to the best of its knowledge and belief, the technical data delivered herewith under Contract No.FA8655-03-1-3063 (RG 34942, Univ. No.) is complete, accurate, and complies with all requirements of the contract.

(2) In accordance with the requirements in Federal Acquisition Regulation 52.227-13, Patent Rights-Acquisition by the U.S. Government (Jun 1989), CONTRACTOR WILL INCLUDE IN THE FINAL REPORT ONE OF THE FOLLOWING STATEMENTS:

(B) "I certify that there were no subject inventions to declare as defined in FAR 52.227-13, during the performance of this contract."

DATE: April 27th 2005

Name and Title of Authorized Official:
Prof. John E. Field, Principal Investigator

1. INTRODUCTION TO THE PCS FRACTURE & SHOCK PHYSICS GROUP AND SOME PRELIMINARY EXPERIMENTS ON PBXs

1.1. INTRODUCTION

The Physics and Chemistry of Solids (PCS) Fracture and Shock Physics Group at the Cavendish Laboratory, Cambridge has built up and continues to develop a wide range of techniques available for the study of energetic and inert materials at impact rates of strain. Table 1.1 lists the mechanical equipment available for measuring the strength properties of materials. Table 1.2 gives the wide range of high-speed cameras the group possesses. We have found over many years that the technique of high-speed photography gives invaluable information about the initiation and ignition mechanisms of energetic materials, particularly when applied to small-scale, well-characterized specimens. A drop-weight machine modified to allow photography of the deforming specimen has played a key role in this work. Much of the mechanistic information about hot spot mechanisms could not have been obtained from large explosive charges nor predicted in advance of performing the experiments.

In recent years, we have also built up an expertise in optical and microscopical techniques for the measurement of deformation in both quasistatic and dynamic tests (see Table 1.3). This is providing detailed and accurate information about the response of both energetic (Goldrein *et al.* 1995*a,b*; 2002) and inert (Synnergren and Goldrein 1999; Synnergren *et al.* 1999; Goldrein *et al.* 2000; Grantham *et al.* 2000) materials to various stimuli.

Hopkinson bars play a major role in our group for obtaining the mechanical properties of a wide range of materials at high rates of strain ($10^{+3} - 10^{+5} \text{ s}^{-1}$). The first Hopkinson bar to be built in our group was designed for obtaining stress-strain curves of very hard metals at strain rates in the range $10^{+4} - 10^{+5} \text{ s}^{-1}$ (Gorham 1980, 1991; Gorham *et al.* 1984, 1992), the limit at which it is feasible to perform experiments under conditions of 1D stress.

Since then, we have extended our capabilities by constructing compressive Hopkinson bars with a wide range of impedances, from magnesium at the lowest to tungsten at the highest (see Table 1.4). This allows us to obtain compressive stress-strain curves of materials with yield stresses of a few MPa (soft rubber binders, for example) to a few GPa (armour steels, for example). We have chosen to use a low impedance metal rather than a polymer for the bar material because the mathematics of elastic wave propagation is simpler for an elastic as compared to a viscoelastic bar (Bacon and Brun 2000; Gray III and Blumenthal 2000; Bacon *et al.* 2001; Bussac *et al.* 2002).

Data for constitutive modelling of materials should be obtained over a range of temperatures. We have therefore developed the capability of performing Hopkinson bar tests over a wide range of temperature (-196 to +600 °C). For high-conductivity metals, we use an induction heater. This has the advantage that it can

be computer-controlled so that the heating cycle can be as short as a few seconds. This is important in order to minimise changes in the microstructure before the test is carried out. For low conductivity materials such as polymers and PBXs, we enclose the bar ends and specimen within a chamber and pass in helium gas heated to the appropriate temperature. Helium has the twin advantages of being chemically inert and also having a large heat transfer coefficient.

Data should also be obtained for the three major states of stress (compression, tension and shear). We have therefore recently commissioned a fully momentum-trapped torsional bar and are in the process of constructing a tension bar similar in design to that of Nemat-Nasser *et al.* (1991).

Taylor impact is playing an increasingly key role in the validation of constitutive models for both ductile and brittle materials (Zerilli and Armstrong 1990; Armstrong *et al.* 1994; Murray *et al.* 1998; Walley *et al.* 2000; Armstrong and Zerilli 2001; Radford *et al.* 2001). It has also occasionally been used for energetic materials (Napadensky *et al.* 1970; Fugelso *et al.* 1982; Vorthman 1982; Quidot 1988; Chou *et al.* 1995; Huang *et al.* 1997; Bardenhagen *et al.* 1998; Christopher *et al.* 2000; Matheson *et al.* 2000a,b; Olsen *et al.* 2000; Quidot *et al.* 2000). High-speed photography is essential to obtain deformation profiles as a function of time for viscoelastic materials such as polymers or PBXs as they can recover substantially on unloading (Bernatskii and Rabinovich 1964; Briscoe and Hutchings 1976; 1978; Hutchings 1978; Kukureka and Hutchings 1981).

For rates of strain in the range 10^5 to 10^8 s $^{-1}$ and for obtaining Hugoniot data, we have a plate impact facility equipped with diagnostics such as stress and strain gauges, VISAR, high-speed photography, spectroscopy and flash X-rays.

TABLE 1.1
QUASISTATIC AND DYNAMIC MECHANICAL TESTING EQUIPMENT AVAILABLE
IN THE PCS GROUP

Machine	Strain rate range/s⁻¹
Instron	$10^{-6} - 10^{-2}$
Dropweight	$10^{+2} - 10^{+3}$
Hopkinson bars (compression, tension, torsion)	$10^{+3} - 10^{+4}$
Miniature Hopkinson bar	$10^{+4} - 10^{+5}$
Taylor impact	$10^{+3} - 10^{+6}$
Plate impact	$10^{+5} - 10^{+8}$

TABLE 1.2
HIGH-SPEED CAMERAS AVAILABLE IN THE PCS GROUP

Make	Framing speed
Kodak Fast video	up to 2×10^3 s ⁻¹
Hadland hyspeed (16 mm film)	up to 10^4 s ⁻¹
AWRE C4 rotating mirror (140 frames)	up to 2×10^5 s ⁻¹
Beckman & Whitley 189 (rotating mirror, 25 frames)	up to 4×10^6 s ⁻¹
Hadland Imacon 792 (8 full or up to 24 half frames)	up to 10^7 s ⁻¹ or streak
IMCO Ultranac (8 full or up to 24 half frames) (fully programmable)	up to 10^7 s ⁻¹ or streak
IMCO Ultra 8	up to 10^8 s ⁻¹

TABLE 1.3
OPTICAL, MICROSCOPY AND X-RAY TECHNIQUES
AVAILABLE IN PCS GROUP

Moiré Interferometry
Speckle Interferometry
Digital Speckle Photography (DSP)
Digital Speckle Radiography
Flash X-ray Image Analysis
Double Exposure Speckle Photography (DESP)
Digital Image Cross-Correlation
Automated Fine-Grid Technique
X-ray Microtomography
Environmental & Conventional Scanning Electron Microscopy (ESEM)
Atomic Force Microscopy (AFM)

TABLE 1.4
MECHANICAL PROPERTIES OF HOPKINSON BARS
AT THE CAVENDISH LABORATORY

Material	Density/kg m⁻³	Wave Speed/m s⁻¹	Impedance/kgm⁻² s⁻¹
Magnesium	1798	4920	8.85×10^6
AZM			
Dural	2711	5040	13.7×10^6
Ti6Al4V	4418	4840	21.4×10^6
Stainless steel	7835	4842	37.9×10^6
Maraging steel	8080	4830	39.1×10^6
Inconel 718	8269	4980	41.3×10^6
Tungsten	16900	4406	75.3×10^6

1.2. PRELIMINARY EXPERIMENTS ON TESTING POLYMER-BONDED EXPLOSIVES (PBXs) IN COMPRESSION USING A SPLIT HOPKINSON PRESSURE BAR (SHPB)

Introduction

PBXs were obtained with different grain sizes, but the same composition, and their stress-strain curves were measured in an SHPB to see if there are any effects of the grain sizes on the curves obtained.

Materials

For these preliminary tests, an AP/HTPB PBX was used (66% ammonium perchlorate and 33% HTPB). This was available in four different grain sizes: 3 μ m, 8 μ m, 30 μ m and 200-300 μ m. Previous work had shown there was indeed a difference in the stress-strain curves obtained between the material with the largest grain size (200-300 μ m) and material containing the three smaller particle sizes (Balzer 2001). However, in that work, single specimens were used for each condition. By using a larger number of samples, we hoped to see more clearly whether the materials with the smaller particle sizes could be distinguished in terms of their stress-strain curves. A statistical approach was required because of the probable spread in properties between samples of the same grain size.

Magnesium bars were used in this work (impedance 8,855,000 $\text{kgm}^{-2}\text{s}^{-1}$) as the PBX materials studied are known to have flow stresses of only a few MPa (Balzer 2001). Since the magnesium bars are of low impedance and are instrumented with silicon strain gauges, the transmitted signal from a 5-6 mm diameter sample was approximately 25mV, large enough for oscilloscope digitisation to be the primary source of noise (see later diagram). The change in resistance of the strain gauges was converted to a voltage by a potential divider. Stress-strain curves were calculated using the normal Hopkinson bar equations (Gray III 2000).

The PBXs were available in blocks of typical size 10cm by 5cm by 2cm. A way had to be found of making specimens of suitable size for a 1/2 inch diameter SHPB. In order to prepare the samples, strips of PBX approximately 2mm thick, were cut from the block using razor blades mounted 2mm apart. It was difficult to cut flat strips using this method, and although some approximately flat areas were available, many of the samples did not have parallel ends. The samples were taken from these strips using a vertical punch of 6mm diameter. Again this was not an ideal preparation method, because the punch creates slightly concave sides on the cylindrical samples. The larger grain size materials were easier to prepare than the smaller grain ones: the cutting instrument moved through the samples much more readily, and the quality of the ends, and in particular the sides, was higher.

Results

A number of samples of each grain size were studied. In general, the results from four samples would be consistent, but occasionally there would be an 'outlier'.

Figure 1.1 shows the stress-strain curves for the four different grain sizes obtained at room temperature. Comparisons of a few representative samples from each grain size are shown in figure 1.2. Figure 1.3 shows a comparison of these results with those obtained in previous work at room temperature (Balzer 2001). The agreement can be seen to be good.

Discussion

The graphs presented in figure 1.1 show there is no rate dependence of the samples over the strain rate range examined: *ca.* 1000-7000 s⁻¹.

It can be seen from the curves presented in figure 1.2 that there is no obvious difference in the stress-strain curves obtained for material with grain sizes ranging between 30 μm and 300 μm. However material with a grain size of 200-300 μm **does** exhibit a lower stress-strain curve. This suggests that there might be a grain size effect between 3 and 300 μm, but the spread in the data obtained has hidden it. Further studies with more accurately prepared samples, for example cast to size, might allow data to be obtained with a much lower variation. Cast specimens might also allow strain rate effects to be distinguished.

A further problem is the oscillation of the stress-strain curve, especially for the smaller grain size samples. This is quite a common phenomenon when testing very soft materials, such as rubbers e.g. Gray III *et al.* (1997, 1998, 2000), Gray III and Blumenthal (2000). These oscillations can be removed by Fourier analysis (see figure 1.4). The initial parts of the stress-strain curves show ramping, which is almost certainly the effect of the sample stress 'stepping up' as the stress wave passes backwards and forwards through it (Briscoe and Nosker 1984). The oscillations on the curve have the same wavelength as this ramping, and are therefore probably due to the movement of the wave within the sample, although a mechanism for this has not yet been determined. Measurement of the wavespeed in the sample will determine whether the time period of the oscillations is comparable to the travel time in the sample. Use of high-speed photography would possibly also allow the cause of these oscillations to be determined. Speckle photography gives detail on the deformation fields over the whole sample surface (Huntley and Field 1986; Goldrein *et al.* 1995a; Goldrein 1996).

Knowledge of the transverse and longitudinal sound wavespeeds allows the Poisson's ratio of these materials to be found. Such a measurement is a check on the assumption that volume is conserved during the deformation. Volume conservation has been assumed on the grounds that the polymer is a minority component of the sample, and this is the only part of the sample which behaves in a non-conservative manner, and that only during the 'elastic' part of the deformation (G'Sell and Jonas 1979, 1981). Since rubber generally conserves volume to better than 5%, the total volume change in the PBX may only be around 0.5%, which is negligible compared to the strains applied by the SHPB.

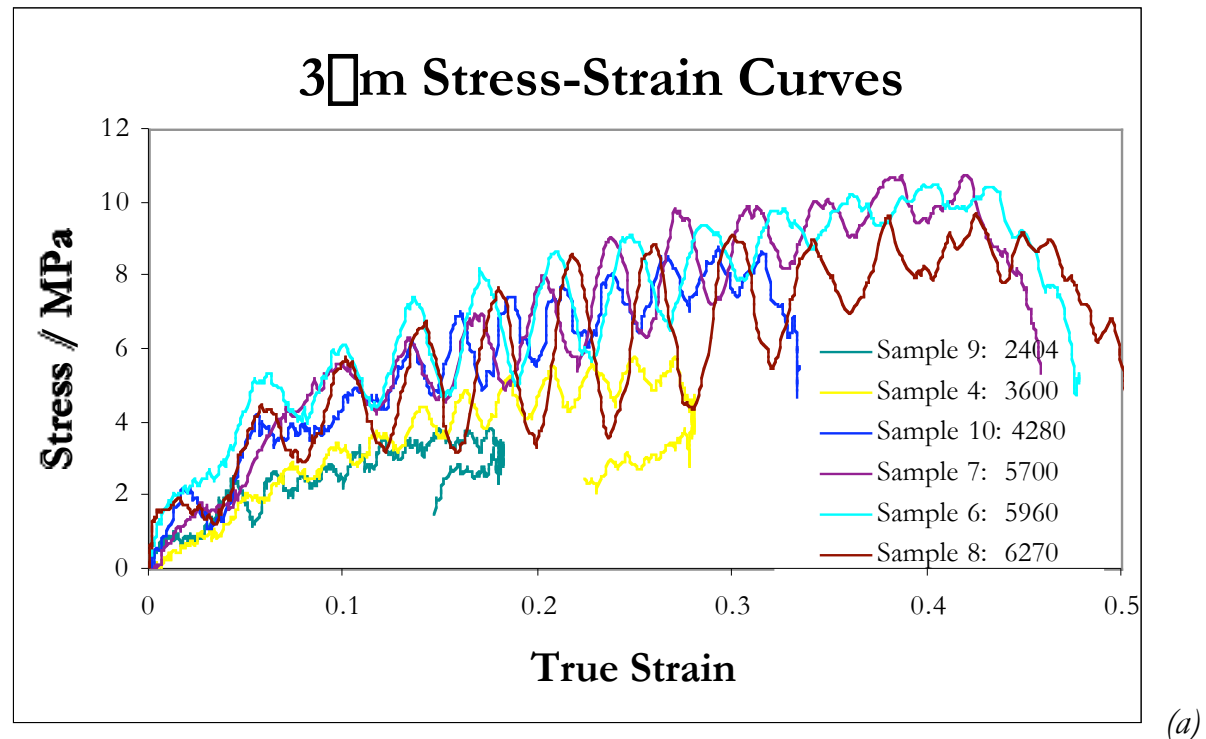
The samples used were $\sim 2.5\text{mm}$ long, and 5.5mm diameter. Therefore their volume was $\sim 240\text{mm}^3$. The volume of the largest ($300\text{ }\mu\text{m}$) grains was 0.11mm^3 . Therefore there were at least 2000 grains in each sample, and hence the samples can be taken as representative of the bulk material. (Armstrong *et al.* 1962).

Recovered samples of materials with small particle sizes showed very little difference to untested specimens. However the larger grain size samples did show some changes: they were much whiter after testing, probably due to fracture of the AP crystals. All the samples studied recovered to almost their original dimensions, as expected for a rubber. It would be a very useful to examine the effect of different particle loadings, especially to compare PBX specimens to samples of the pure polymer binder.

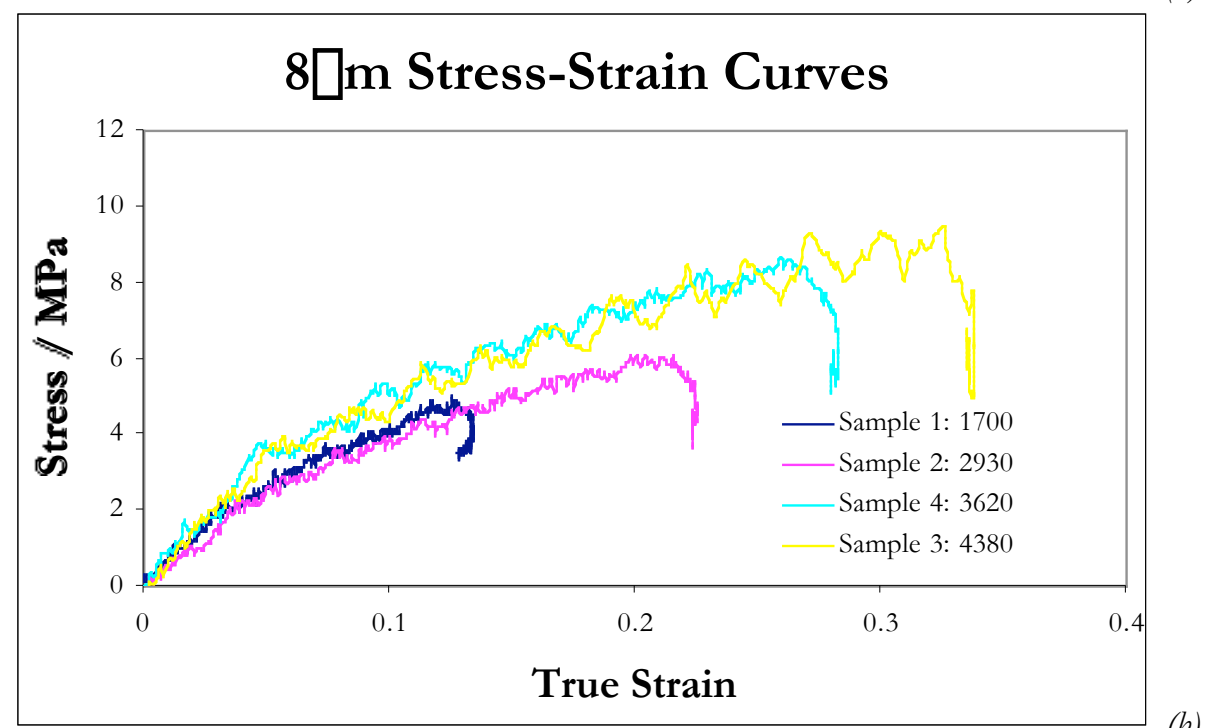
Some preliminary work has been performed on the effect of temperature on the SJPB stress-strain curves (figure 1.5). There can be seen to be a strong effect of temperature on the impact strength of these materials, particularly as the temperature is taken down below room temperature.

Conclusions:

Preliminary Hopkinson bar testing has shown some evidence of grain size effects in the stress-strain curves of a PBX. This was only noticeable when the grain size was increased from $30\text{ }\mu\text{m}$ to $300\text{ }\mu\text{m}$: not much change was observed between $3\text{ }\mu\text{m}$ and $30\text{ }\mu\text{m}$.



(a)



(b)

Figure 1.1 (caption on next page)

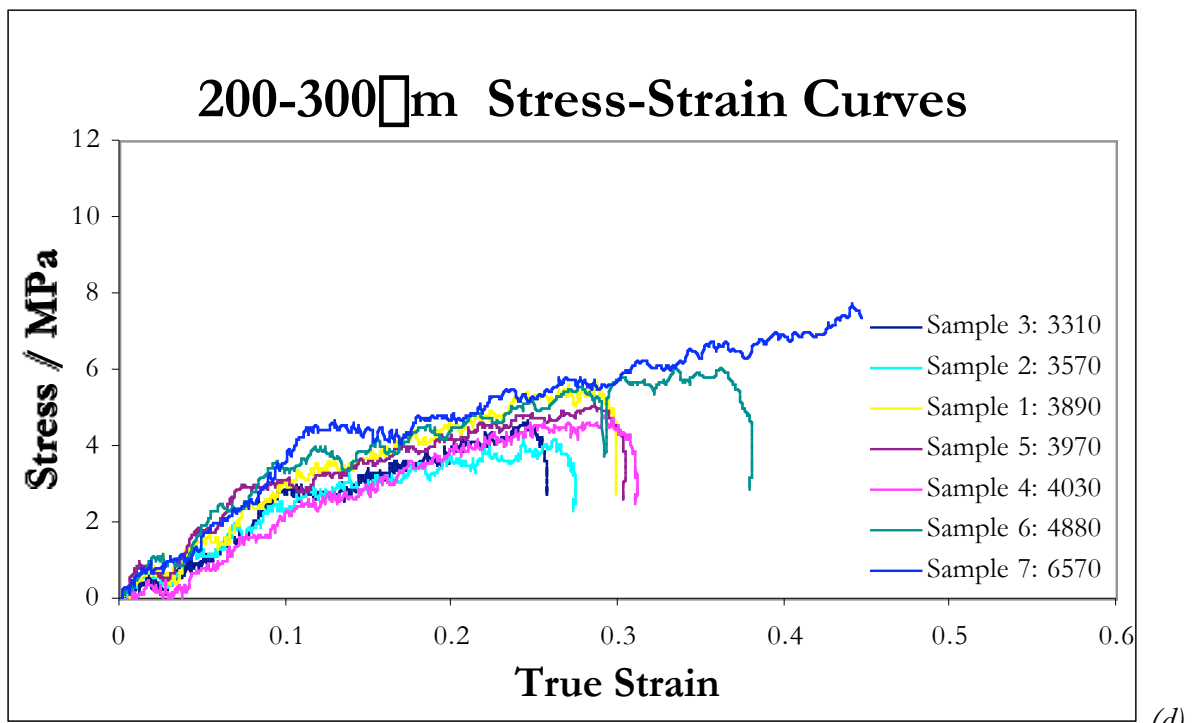
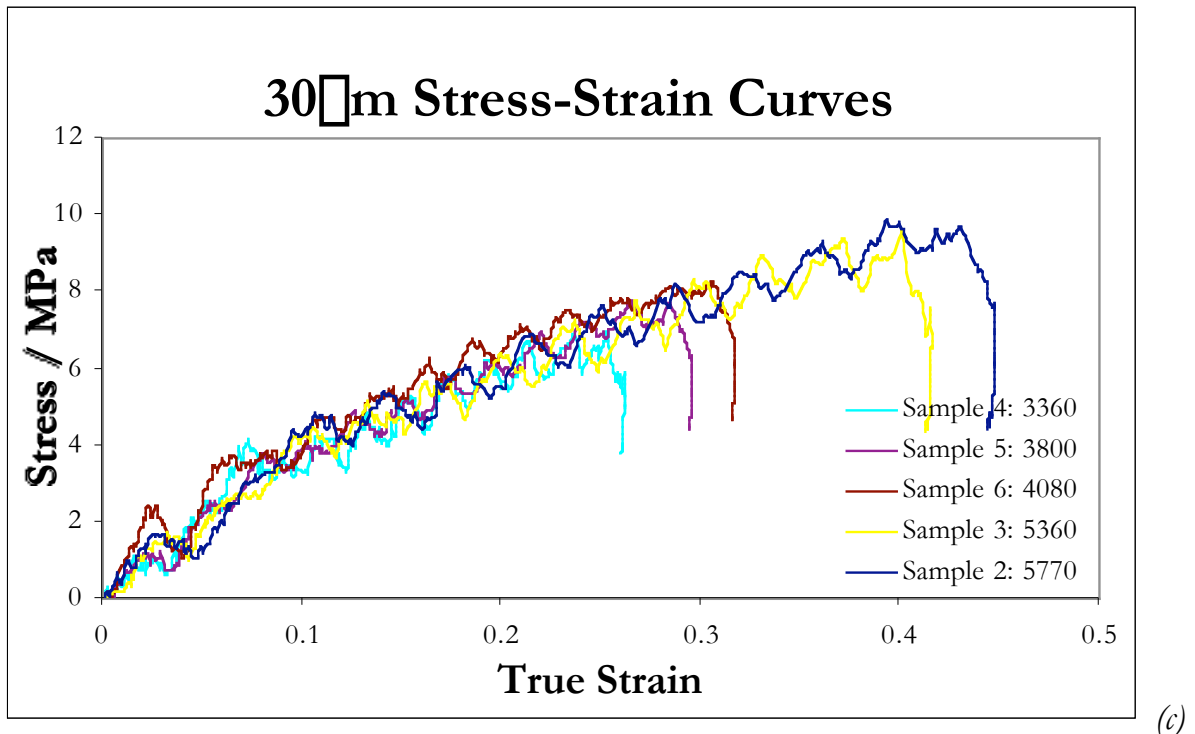


Figure 1.1. Stress-strain curves obtained in a compression SHPB for AP+HTPB PBXs of various AP grain sizes: (a) 3 μm , (b) 8 μm , (c) 30 μm , (d) 200-300 μm

The figures in the lists on the RHS of the graphs are the strain rates in reciprocal seconds.

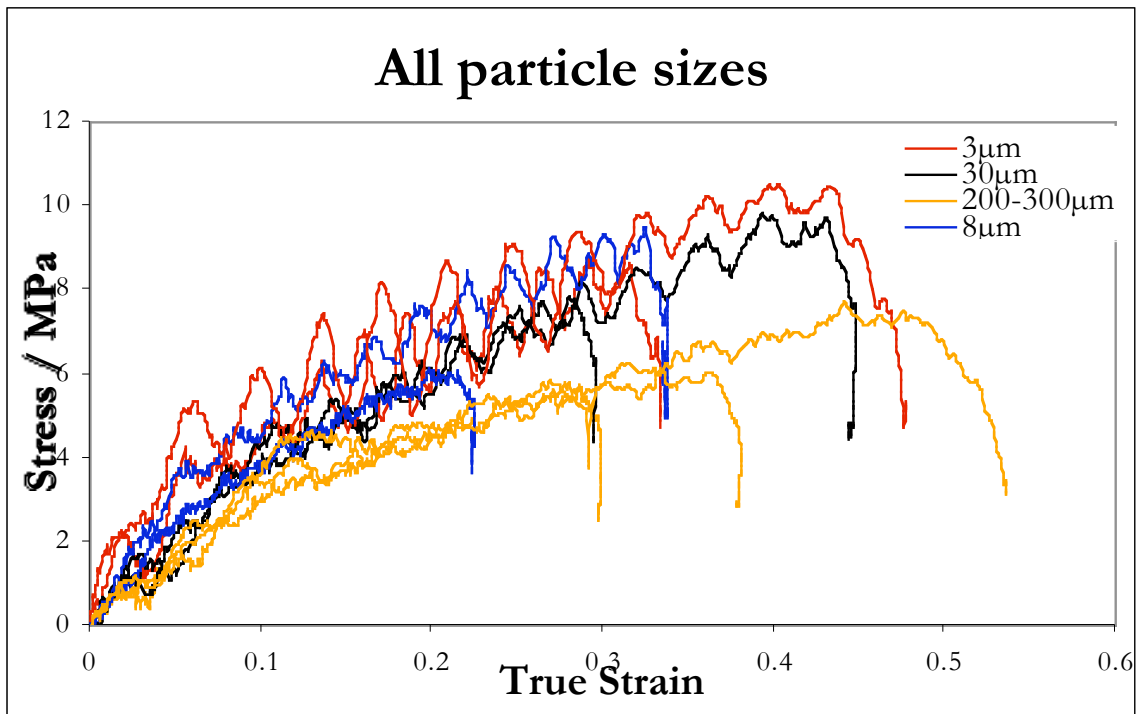


Figure 1.2. Comparison of SHPB stress-strain data for all grain sizes tested.

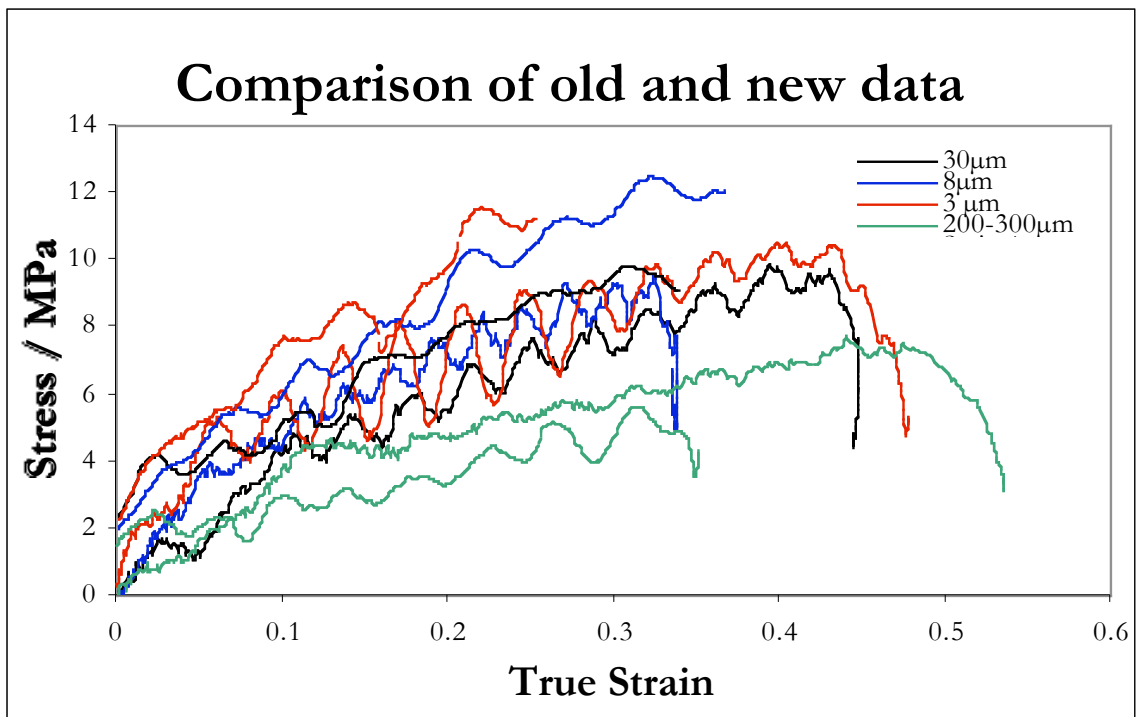


Figure 1.3. Comparison of old and new stress-strain data at room temperature.

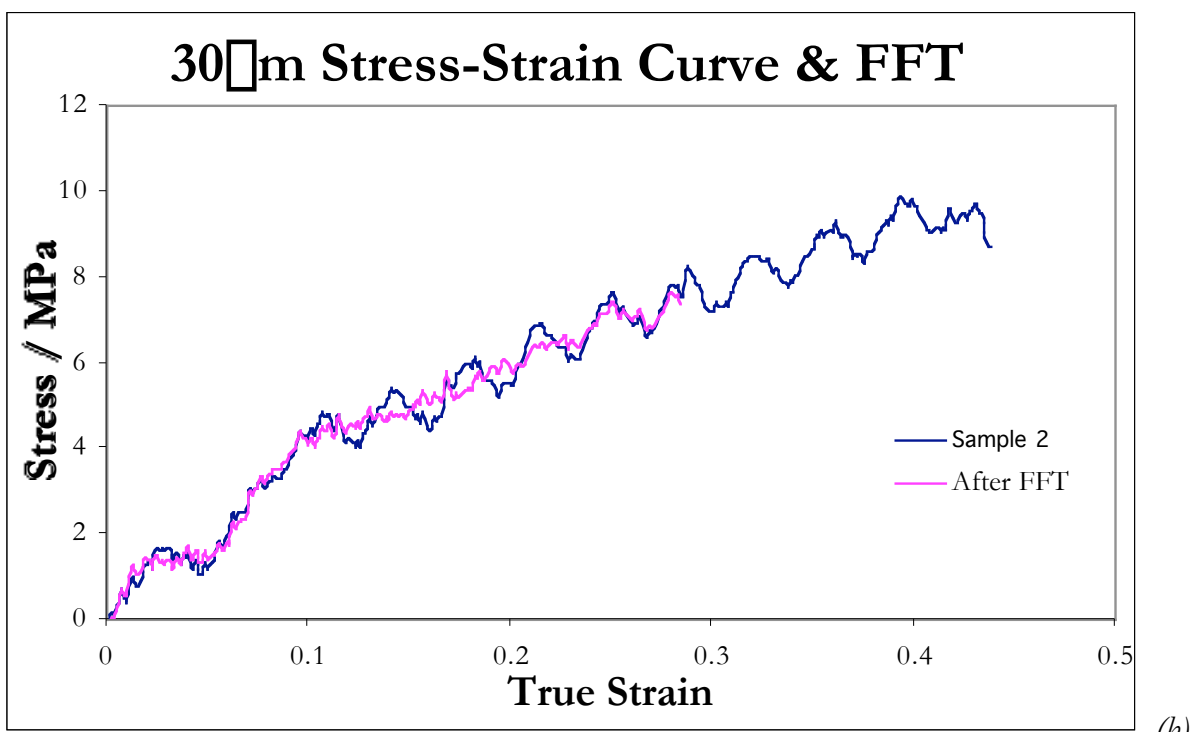
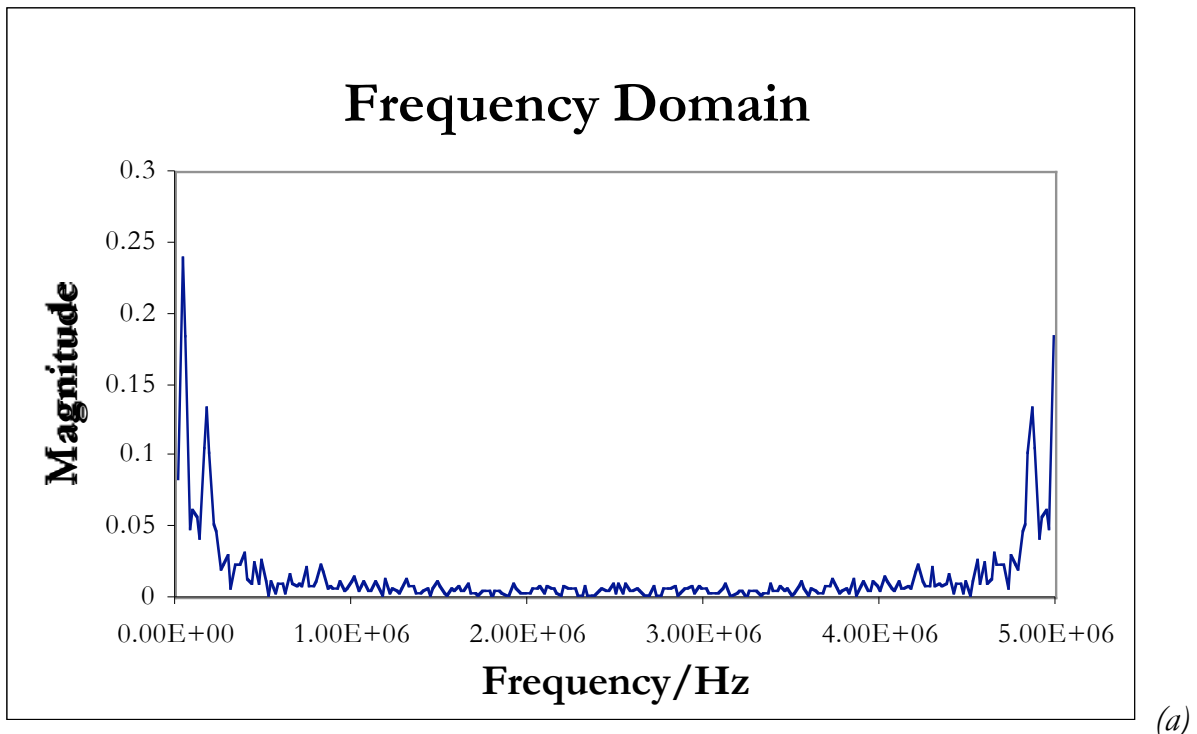


Figure 1.4. (a) Frequency spectrum obtained by Fast Fourier Transform (FFT) analysis of one of the 30 μ m AP particle size stress-strain curves. The frequency of the oscillation can be clearly seen to be around 5 MHz. (b) Comparison of stress-strain curves with and without removal of the main oscillatory frequency component.

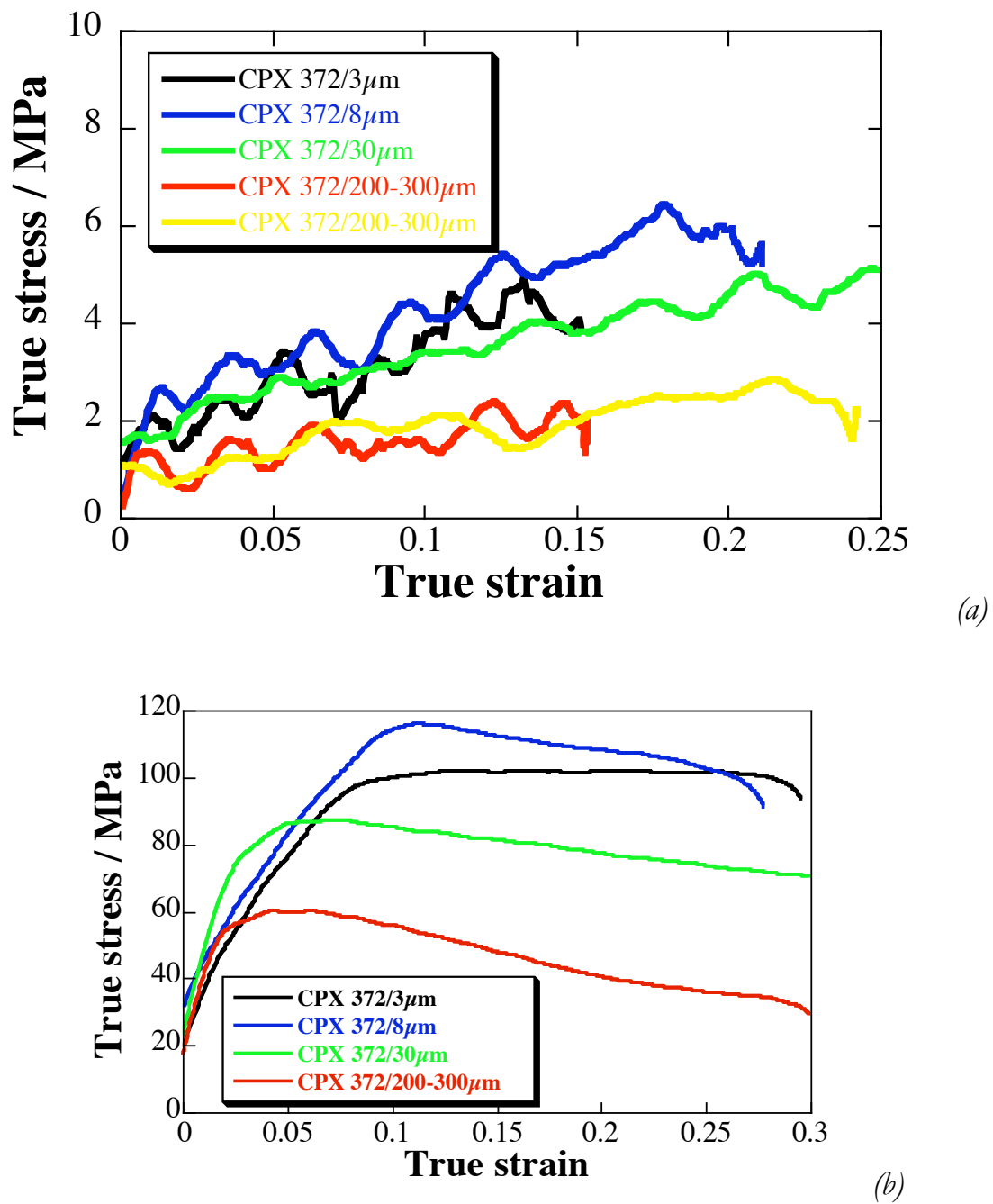


Figure 1.5. SHPB stress-strain curves obtained for the AP+HTPB PBXs of various AP particle sizes for two different temperatures: (a) +60 °C, (b) -60 °C.
From Balzer (2001).

1.3. RECOMMISSIONING OF MINIATURISED DIRECT IMPACT HOPKINSON PRESSURE BAR AND COMPARISON WITH A CONVENTIONAL SPLIT HOPKINSON PRESSURE BAR SYSTEM

In order to be able to carry out uniaxial compression tests at strain rates up to the limit of Hopkinson bar techniques (10^5 s^{-1}), Gorham and Field developed in this laboratory a miniaturised direct impact Hopkinson pressure bar system (Gorham *et al.* 1984; Gorham *et al.* 1992). It has also been used to obtain very high strain rate data of soft materials such as polymers and PBXs (Walley *et al.* 1989, 1991, 1992; Walley and Field 1994).

The advantage of not having an input bar is that the strain rate that can be applied is not limited by dispersion of the signal within the pressure bar (Dharan and Hauser 1970). The advantages of miniaturisation are that (i) radial inertia within the specimen is kept small (see below), (ii) the range of frequencies can be transmitted down the output bar is increased, and (iii) the bar can be made from a hard, relatively brittle material such as tungsten carbide. Our system consists of a tungsten carbide (WC) pressure bar 3mm in diameter instrumented with high gain semiconductor strain gauges (BLH Electronics type SPB1-03-12U1) which need no amplification, so there are no complications introduced by bandwidth limitations of amplifiers. Specimens are typically 1mm diameter and 0.5mm thick (pinhead size).

Tungsten carbide was chosen as a bar material because of its strength (which allows very strong metals to be tested) and its low Poisson ratio (0.22, compared to typically 0.33 for most metals), which reduces elastic wave dispersion effects (Bancroft 1941; Davies 1948; Safford 1988, 1992; Mason 1999). It also has a high acoustic impedance which helps to ensure a nearly constant strain rate during an experiment. It has not been used widely in Hopkinson bar applications because of its brittleness. Indeed we have found that WC bars of more conventional length (0.5m long) and diameter (12.7 mm) have a very limited lifetime. Our miniaturised bar has, however, survived many hundred, if not thousands, of impacts. This is presumably due to the lower stresses imparted and the small intrinsic flaw size. Materials with lower Poisson ratio ν do exist (e.g. beryllium $\nu = 0.02-0.05$, diamond $\nu = 0.07$, and plutonium $\nu = 0.19$), but none of them are suitable for routine use in a normal laboratory. The only one of these three ever to be used as a bar material is beryllium (Jones 1966; Bateman *et al.* 1996). Safford (1988) suggested that a rod made from beryllium-2% copper (not to be confused with copper-2% beryllium) might be even more suitable, especially if nickel plated to contain the toxic dust and fumes, as its elastic properties are close to that of pure beryllium (Silversmith and Averbach 1970), but as far as we know no-one has acted on this suggestion.

According to the analysis of Pope and Field (1984), there are several quantities that need to be known accurately if a stress-strain curve is to be derived from the signal recorded from the output bar: (i) the initial dimensions of the specimen, (ii) the mechanical impedances Z_i ($= \rho_i c_i$), where ρ_i is the density and c_i the wavespeed

of the striker and output bars), (iii) the impact velocity v of the striker bar, and (iv) the force-time pulse $f(t)$ itself. To achieve this, the specimen dimensions are measured using a micrometer, the impedances (see Table 1.5) are determined from the density and wave speed (found from measuring the time for double transits of pulses in the output rod), the impact speed is measured using three light stations (this allows acceleration to be measured and allowed for), and the force pulse is recorded on a Tektronix scope.

TABLE 1.5
Mechanical properties of the materials used in the
miniature direct impact Hopkinson bar

Material	Density/kg m ⁻³	Wave speed/km s ⁻¹	Impedance/kg m ⁻² s ⁻¹
WC	13,920	6,900	9.607x10 ⁷

In recent years our miniaturised DIHB had not been used very often as we had developed a suite of conventional Hopkinson bars (SHPBs) with a range of mechanical impedances. As they are instrumented with high gain semiconductor gauges, we believed that they could also be used to obtain data from the very small specimen sizes necessary for the miniaturised bar and at similar strain rates. There have also been questions raised about the validity of performing tests with only one bar (Gray III *et al.* 1997; Gray III 2000; Gray III and Blumenthal 2000; Jia and Ramesh 2004), despite the very good agreement found between analysis and high-speed photography by Pope and Field (1984). These doubts had been raised because the use of a single bar does not allow analytical checks to be performed on specimen equilibrium, potentially a serious source of error especially at low strains and for soft materials such as polymers and PBXs.

However, work in our laboratory on polymers showed that specimen equilibrium issues are not as serious as we had been led to believe (Gary *et al.* 1995; Zhao *et al.* 1997; Siviour *et al.* 2001). Stress-strain curves obtained for polymers using conventional split Hopkinson bars with a wide range of impedances (all the way up to tungsten) were almost identical (see figure 1.6). The most unexpected feature of these graphs was the almost identical shape of the rising portion of the curves. This surprised us because specimens, particularly those made from soft materials such as polymers, are known not to be in equilibrium for the first few microseconds of loading in a Hopkinson bar (Gray III 2000; Gray III and Blumenthal 2000). We also detected initial specimen non-equilibrium by calculating the stress-strain curves two different ways from the three recorded stress waves (incident, transmitted, reflected); see figure 1.7. Note that the difference between the two stress-strain curves settles down to zero after around 20 μ s. We had therefore been expecting that this non-equilibrium would manifest itself in differences between the rising sections of the curves obtained from bars of different impedances.

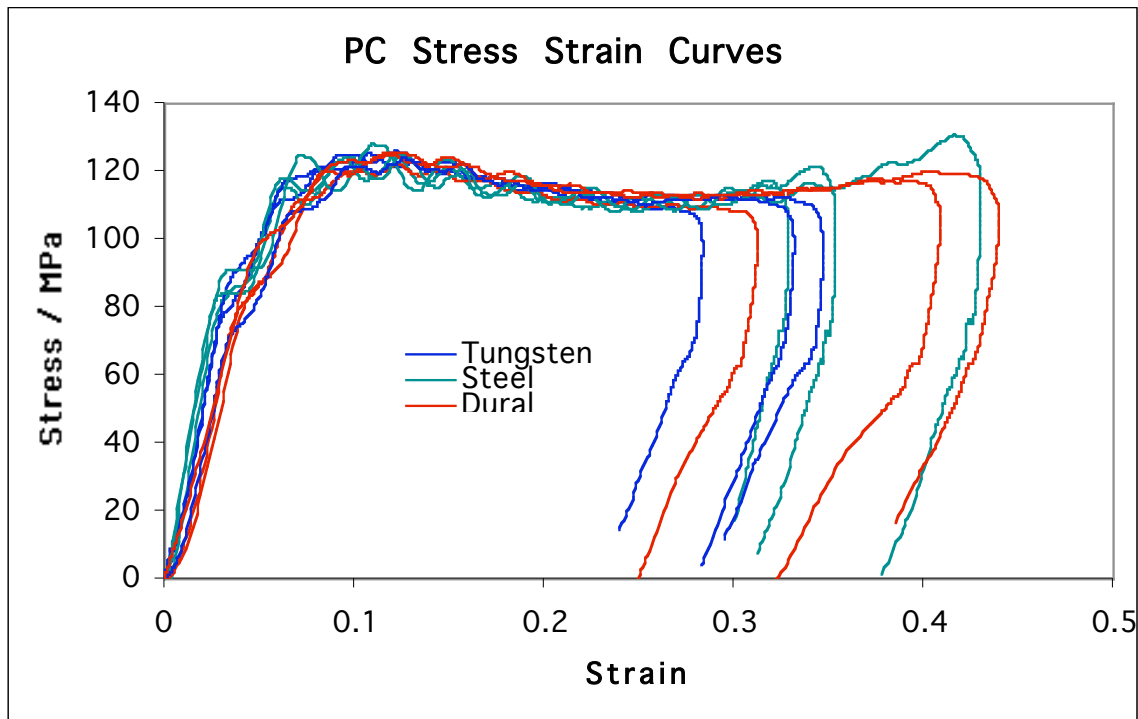


Figure 1.6. Stress-strain curves obtained for polycarbonate in our compression split Hopkinson pressure bars with a wide range of impedances.

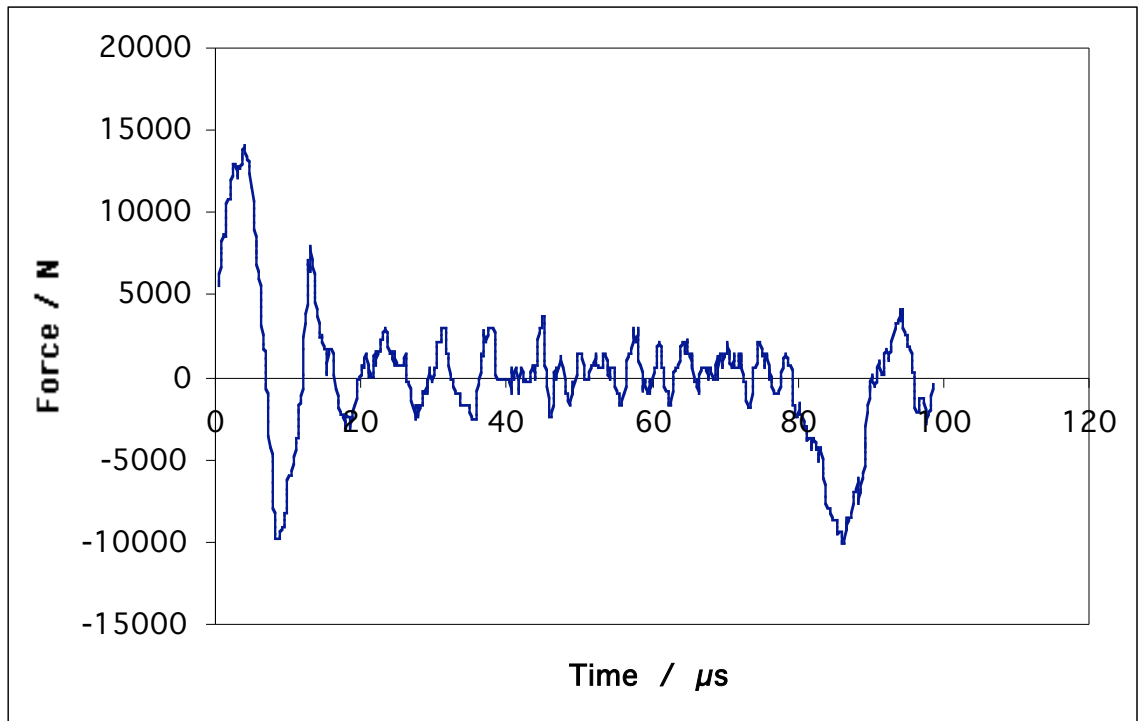


Figure 1.7. Plot of the difference between the stress-strain curves obtained for a polycarbonate specimen calculated two different ways.

We recommissioned our miniaturised direct impact Hopkinson bar for a project to obtain the stress-strain curves of copper specimens at very high rates of strain. Initially we believed we could do this using our low impedance dural SHPB and miniature specimens. But this bar material proved not to be hard enough. Steel bars were then used, with the disadvantage that the transmitted signal is smaller (see figure 1.8). But the maximum strain rate we could obtain was in the region of $15,000\text{ s}^{-1}$. The reason for this upper limit is that the impact speed of the striker bar must be kept below that which causes the strain gauges to spall off. It should be emphasised that this is a high strain rate for SHPB testing, but wasn't high enough for the particular application.

The main reason we can obtain such high strain rates with our conventional SHPBs is that we use semiconductor strain gauges which need no amplification. This means we can test very small specimens that only transmit a small signal into the output bar and still have a large signal-to-noise ratio (see figure 1.8).

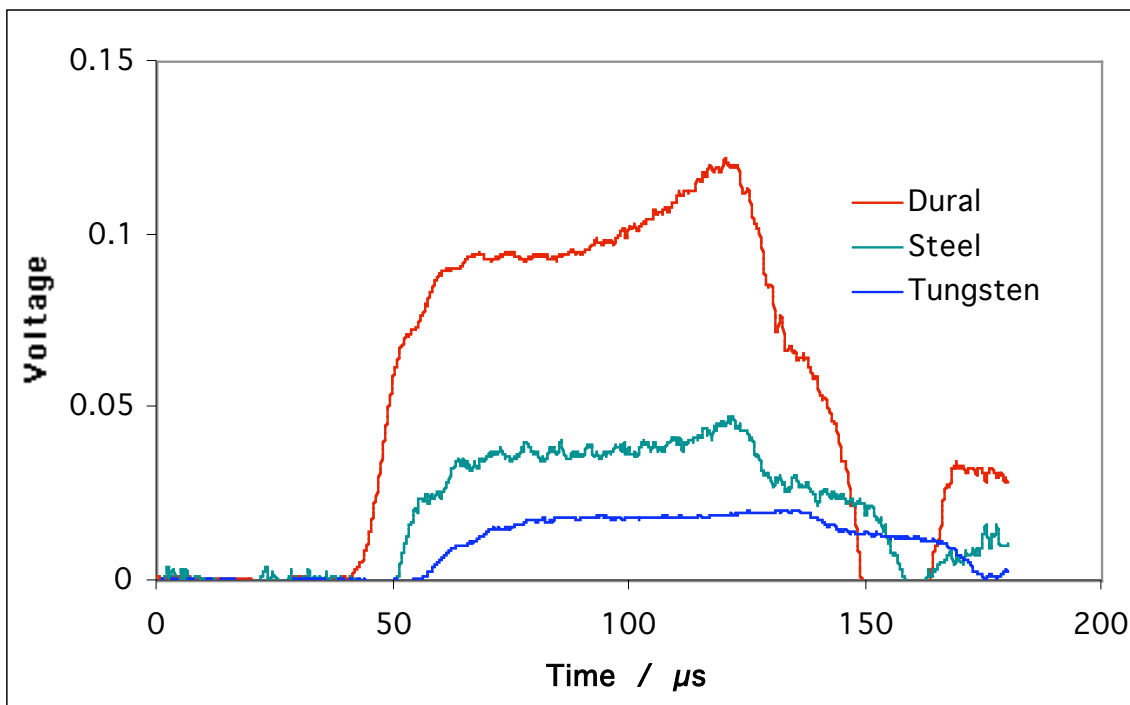


Figure 1.8. Output bar signals obtained for polycarbonate using three bars of widely varying impedances.

Two other experimental tests were performed to check that the strain in soft specimens was being calculated correctly. The first was to use an optical extensometer. An optical extensometer records the movement of a two black/white boundaries. For the SHPB, these boundaries can be simply created using black and white tape on the input and output bars (see figure 1.9). It can be seen (figure 1.10) that the agreement between the strains calculated from the strain gauge outputs using the standard Hopkinson bar equations and those calculated from the displacements measured using the optical extensometer is excellent. The second technique was high-speed photography (see figure 1.11). The camera used was an IMCO Ultranac. The strains calculated from the high-speed photographic

sequence are compared with those calculated from the strain gauge output are compared in figure 1.12. The scatter in the data can be seen to be worse than for the optical extensometer, but even so, the agreement is good.

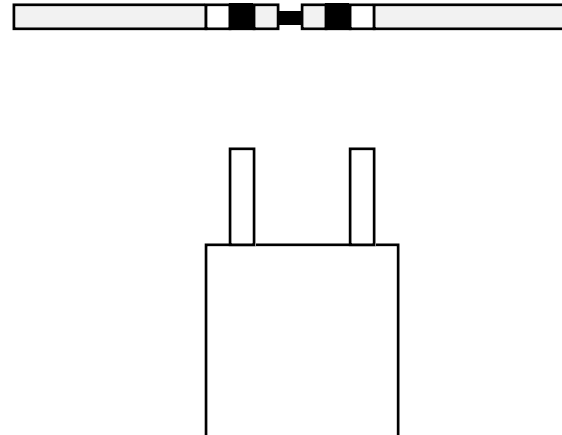


Figure 1.9. Schematic diagram of optical extensometer system set up to take measurements from a compression SHPB.

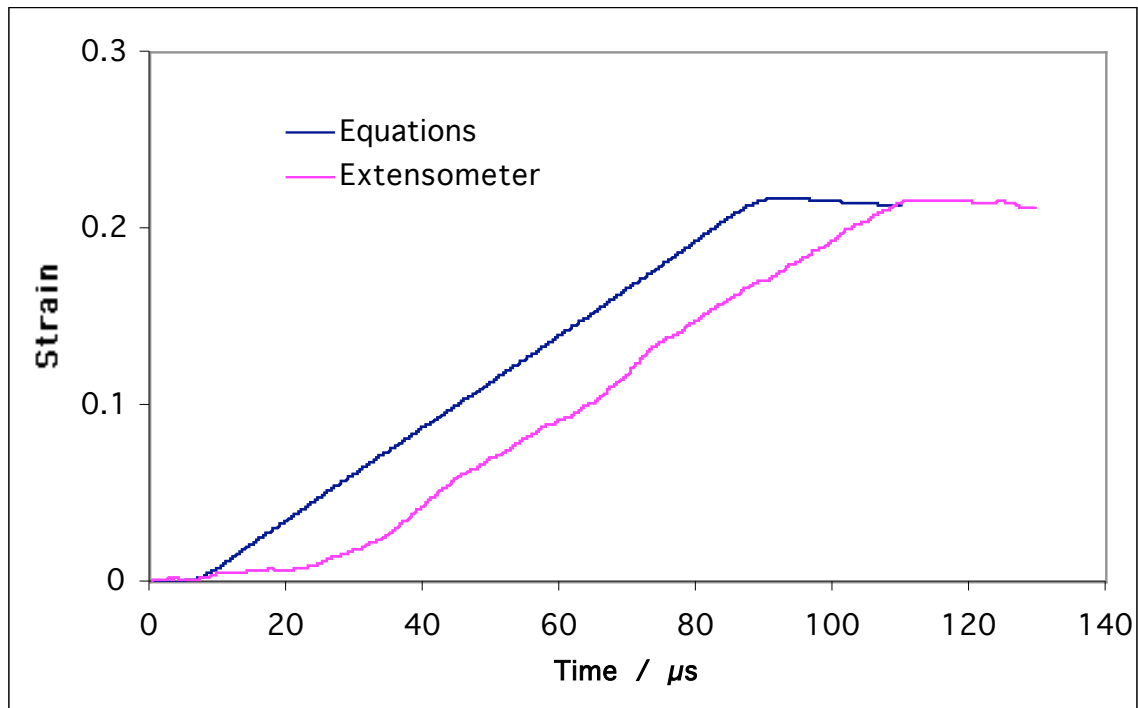
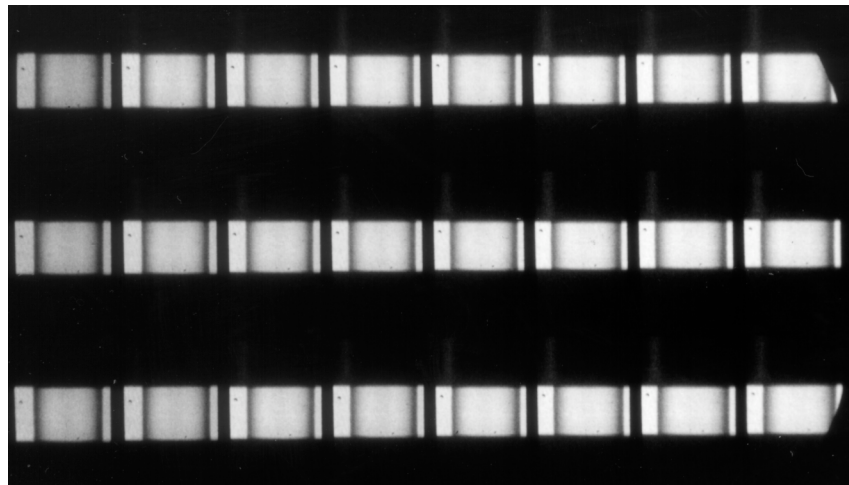


Figure 1.10. Comparison of strains calculated from SHPB strain gauge outputs and measured using the optical extensometer (traces are time-shifted for clarity).



Key to Frame Sequence

1 6 7 12 13 18 19 24

2 5 8 11 14 17 20 23

3 4 9 10 15 16 21 22

Figure 1.11. High-speed photographic sequence of the deformation of a 4mm long cylindrical PC specimen. Interframe time 5 μ s.

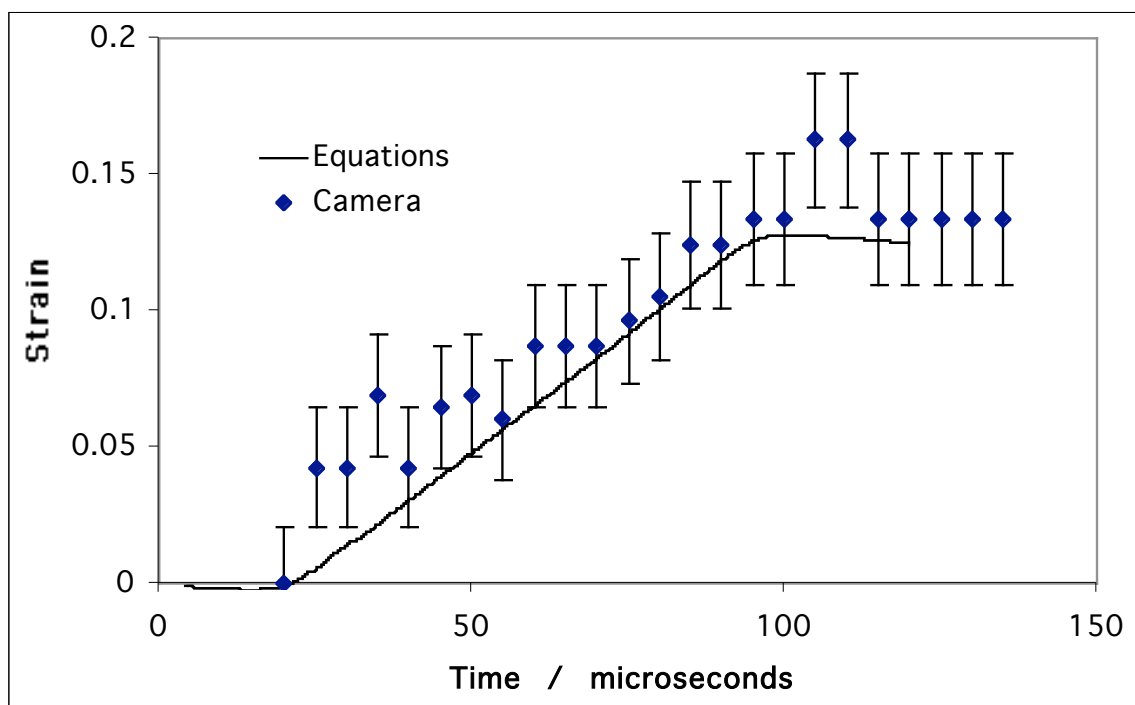


Figure 1.12. Comparison of strains measured from the sequence shown in figure 1.11 with that calculated from strain gauge output.

We discovered that the miniaturised tungsten carbide bar required regauging. We decided to use encapsulated semiconductor gauges (BLH Electronics type SPB1-03-12U1) as these are less prone to mechanical damage. They have, however, a longer gauge length than those originally used.

A series of experiments were then performed on 1mm diameter, 0.5mm thick copper specimens. The strain rate was increased in stages by firing the striker bar at increasingly higher velocities until a strain rate of $70,000\text{s}^{-1}$ was reached. Small specimens are required to ensure that inertial stresses do not dominate the measured response (see figure 1.13). These stresses are given by the following equation (Gorham 1991):

$$\square_i = \frac{a^2}{16} + \frac{b^2}{6} \frac{\partial^2 \square}{\partial t^2} + \frac{b^2}{6} \frac{a^2}{8} \frac{\partial^2 \square}{\partial t^2} \quad (1.1)$$

A plot of this for copper specimens of the size used is shown in figure 1.13.

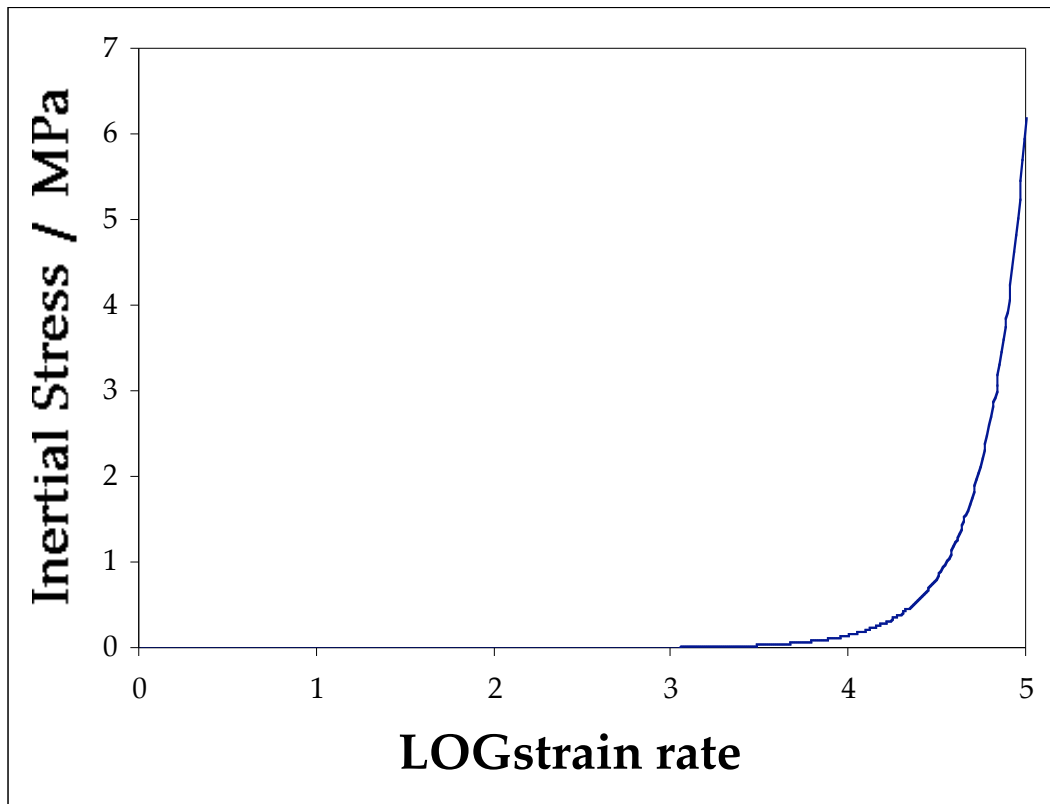


Figure 1.13. Graph of the inertial stress developed in copper when subjected to compressional deformation at various strain rates. Specimen dimensions: 1mm diameter x 0.5mm thick.

It can be seen that even at strain rates of $100,000\text{ s}^{-1}$ inertial stresses are only around 6 MPa, negligible compared to the flow stress of copper of around 1000 MPa (see figure 1.14). This demonstrates one of the major benefits of miniaturisation. It should be emphasised that inertial stresses are only active when material is being accelerated. When the specimen has reached steady flow conditions, inertial stresses drop back to zero.

Figure 1.14 presents the first direct comparison we have made between results obtained in one of our conventional SHPBs and our miniaturised DIHB. The agreement up to a strain of *ca.* 0.45 can be seen to be excellent. This gives us confidence that the DIHB can be used to obtain good data at strain rates approaching $100,000\text{ s}^{-1}$.

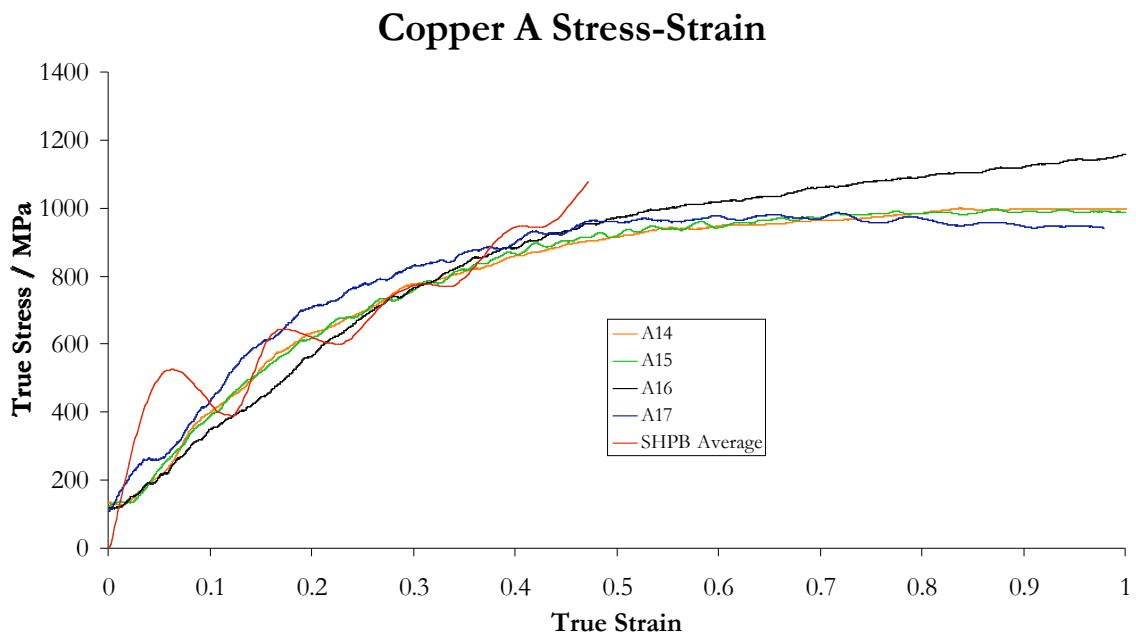


Figure 1.14. Comparison of stress-strain curve obtained in a conventional SHPB at a strain rate of *ca.* $15,000\text{ s}^{-1}$ with stress-strain curves obtained in our miniaturised DIHB at strain rates of between $45,000$ and $62,000\text{ s}^{-1}$.

1.4. DEVELOPMENT OF GAUGED DROPWEIGHT MACHINE

Background

The dropweight machine that we have used extensively for taking high-speed photographic sequences of the rapid deformation of energetic and inert materials (figure 1.15) has been operated for most of its history without any means of recording force-time data. Two recent attempts were made to instrument it: one with strain gauges attached to a metal ring below the glass anvil (Walley *et al.* 1995) and one with accelerometers attached to the dropweight itself. Accelerometers were found to output a very noisy signal due to reverberations within the dropweight: the oscillations were of similar amplitude to the signal. This has been a frequent observation in dynamic testing rigs of various types (Mooij 1981; Cain 1987; Sahraoui and Lataillade 1990, 1998; Aggag and Takahashi 1996). However, much cleaner signals were obtained using the instrumented ring (Walley *et al.* 1995).

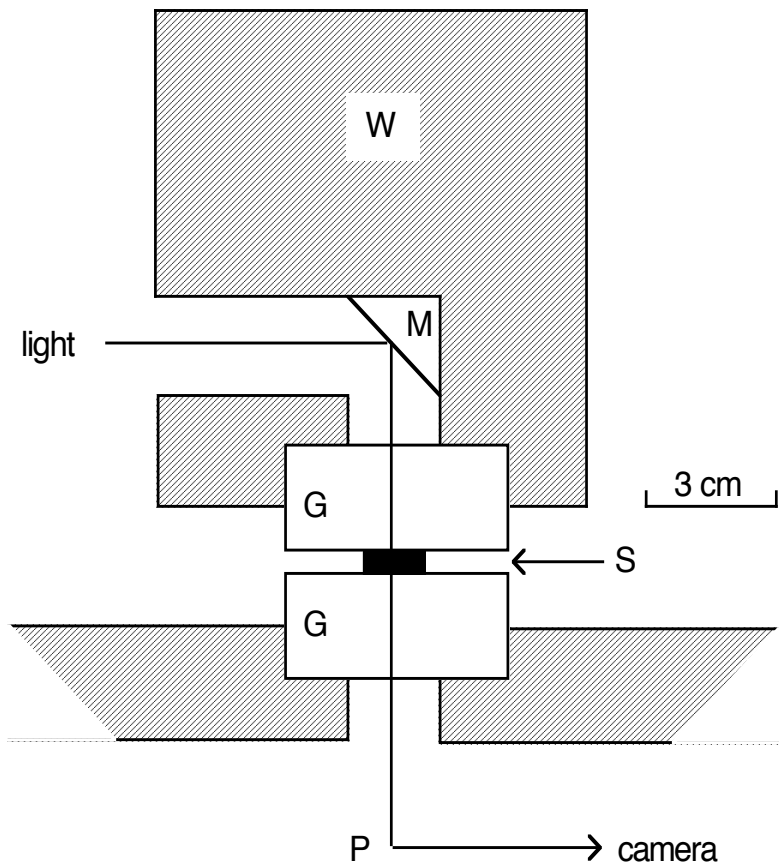


Figure 1.15. Schematic cross-section diagram of the high-speed photography dropweight apparatus. W weight; M mirror; G glass anvil; P prism; S specimen.

We have modified this apparatus so that it can also operate as a conventional dropweight machine. The stimulus for this is a project examining the rapid deformation and failure of hard metal cylinders of various aspect ratios. We found that specimens with diameters larger than 4mm could not be deformed in our

compression split Hopkinson pressure bars. They could, however, be deformed using our dropweight (mass 5.64 kg, impact speed *ca.* 4.9 m/s). As the specimens are hard metals, the anvils themselves also have to be fabricated from a hard, tough metal to avoid significant indentation of the surface and bulk plastic deformation. The anvils therefore were made from Maraging 300 steel. Their dimensions are 20 mm diameter, 30mm long. The experimental arrangement of the anvils plus specimen is shown in figure 1.16.

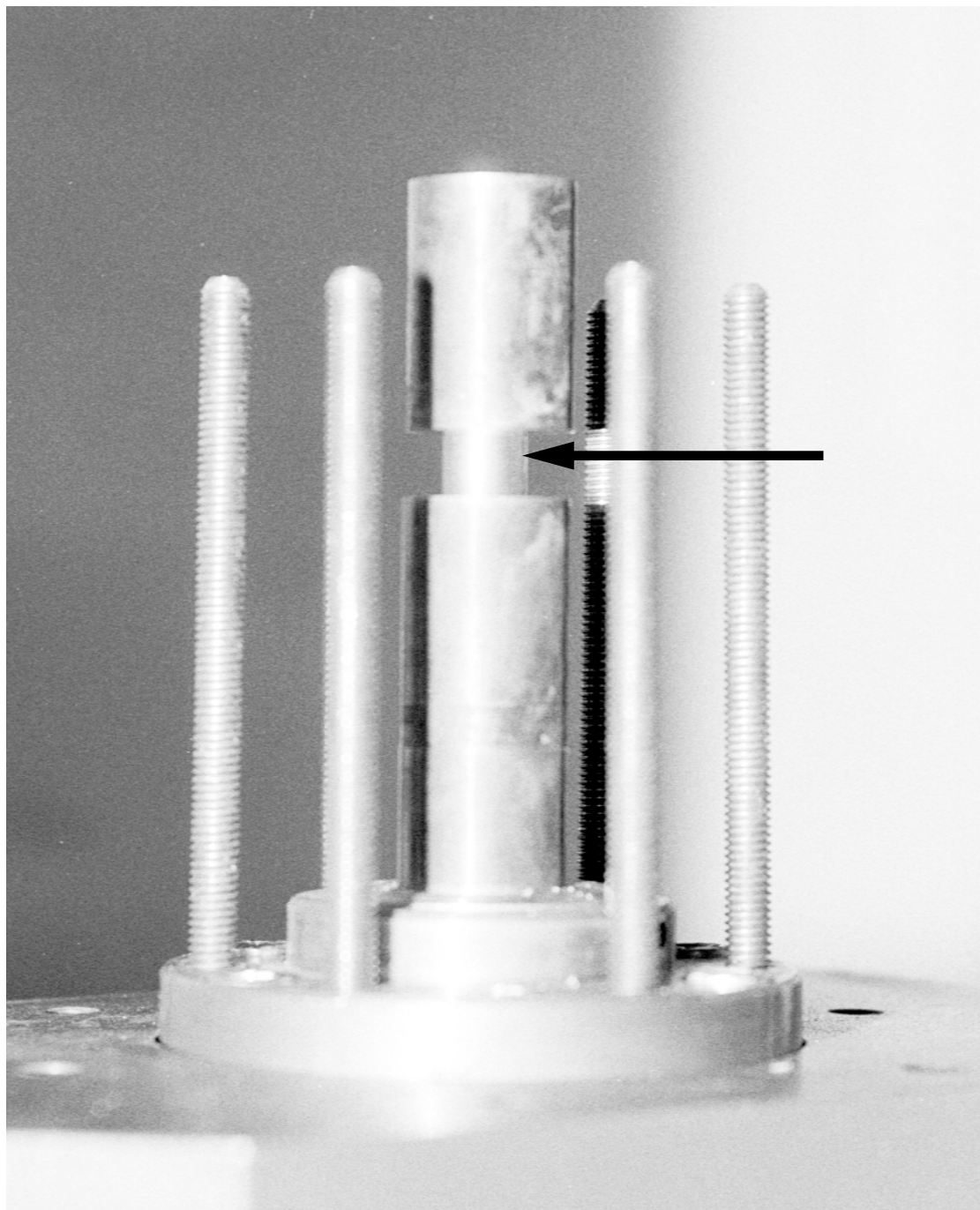


Figure 1.16. Photograph of anvil arrangement with specimen included (arrowed).

It can be seen in figure 1.16 that the dropweight loadcell consists of three maraging steel cylinders arranged in a stack. The specimen is sandwiched between the upper two. Foil strain gauges are attached to the lowest anvil. This arrangement ensures that the instrumented cylinder is not damaged by the deforming specimen and so can be used many times. It also ensures that the strain field in the gauged anvil is close to uniform (according to the St Venant Principle).

When in use, the stack is enclosed within a steel jacket with sections cut away to allow photography and recording of signals (figures 1.17 & 1.18).

The arrangement of figure 1.16 has been shown to give the best signal (Radford *et al.* 2003; see also figures 1.20 and 1.21). Closer examination of the signals near the origin shows that the first oscillation in the black and red traces has structure due to reflections within the block to which the force transducer is bolted (see figure 1.18). These may be eliminated by using a tapered block of metal that takes the elastic wave energy away and does not allow it to return (our previous dropweight apparatus sat on a blacksmith's anvil, the horns of which presumably have this function: Heavens and Field 1974). The other, more long-lived oscillations have a period commensurate with the elastic wave travel time within the stack of cylindrical anvils. Studies are in progress to determine the best method to reduce their magnitude.

Some soft Pb-Sn solder specimens were used as a check of the reproducibility of the transducer using configuration 1 of figure 1.19. This can be seen to be excellent, even out to long times.

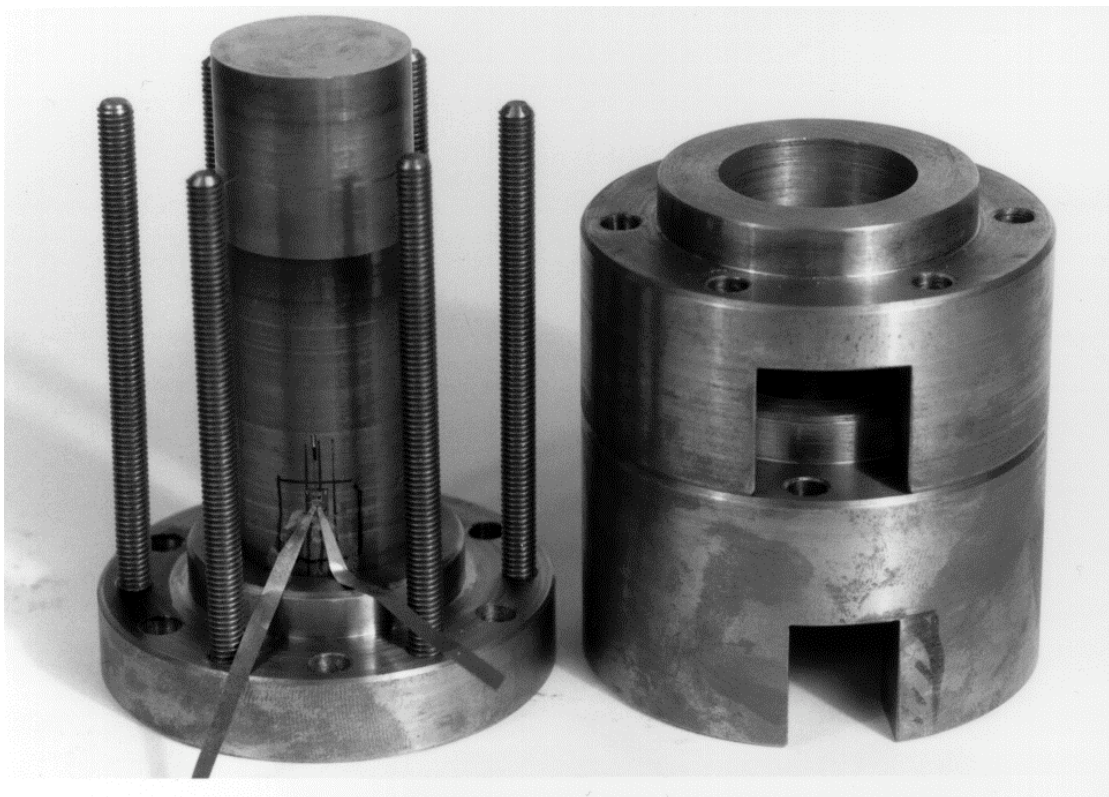


Figure 1.17. Photograph of the anvil force-transducer for the dropweight apparatus disassembled to show strain gauges on lower anvil and the steel jacket.

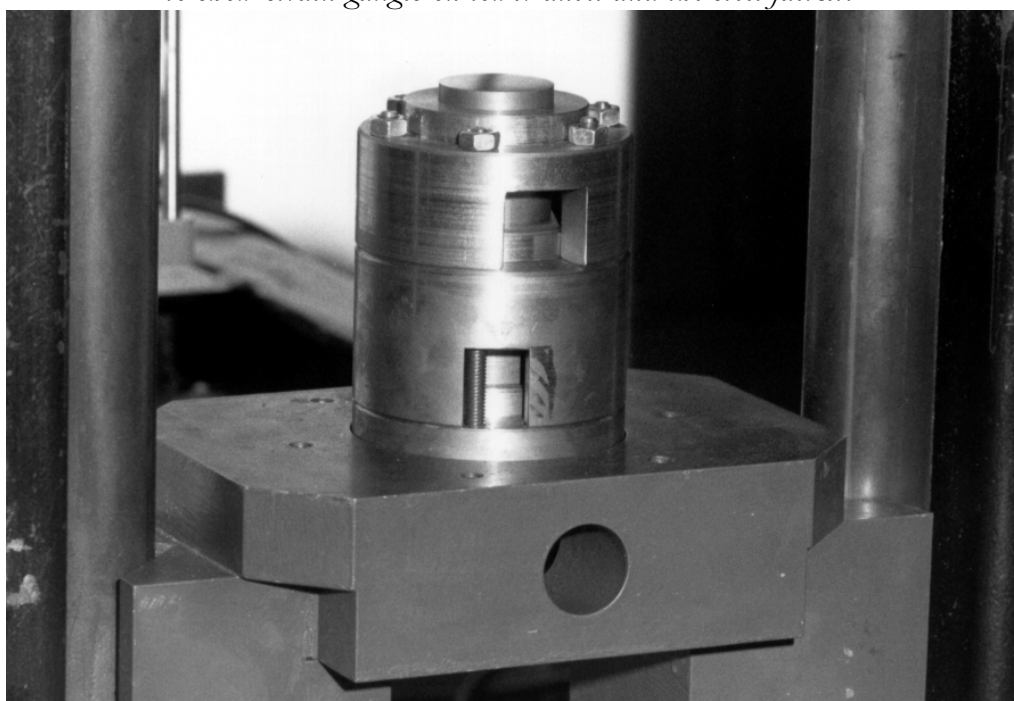


Figure 1.18. Photograph of the force-transducer in place in the dropweight apparatus

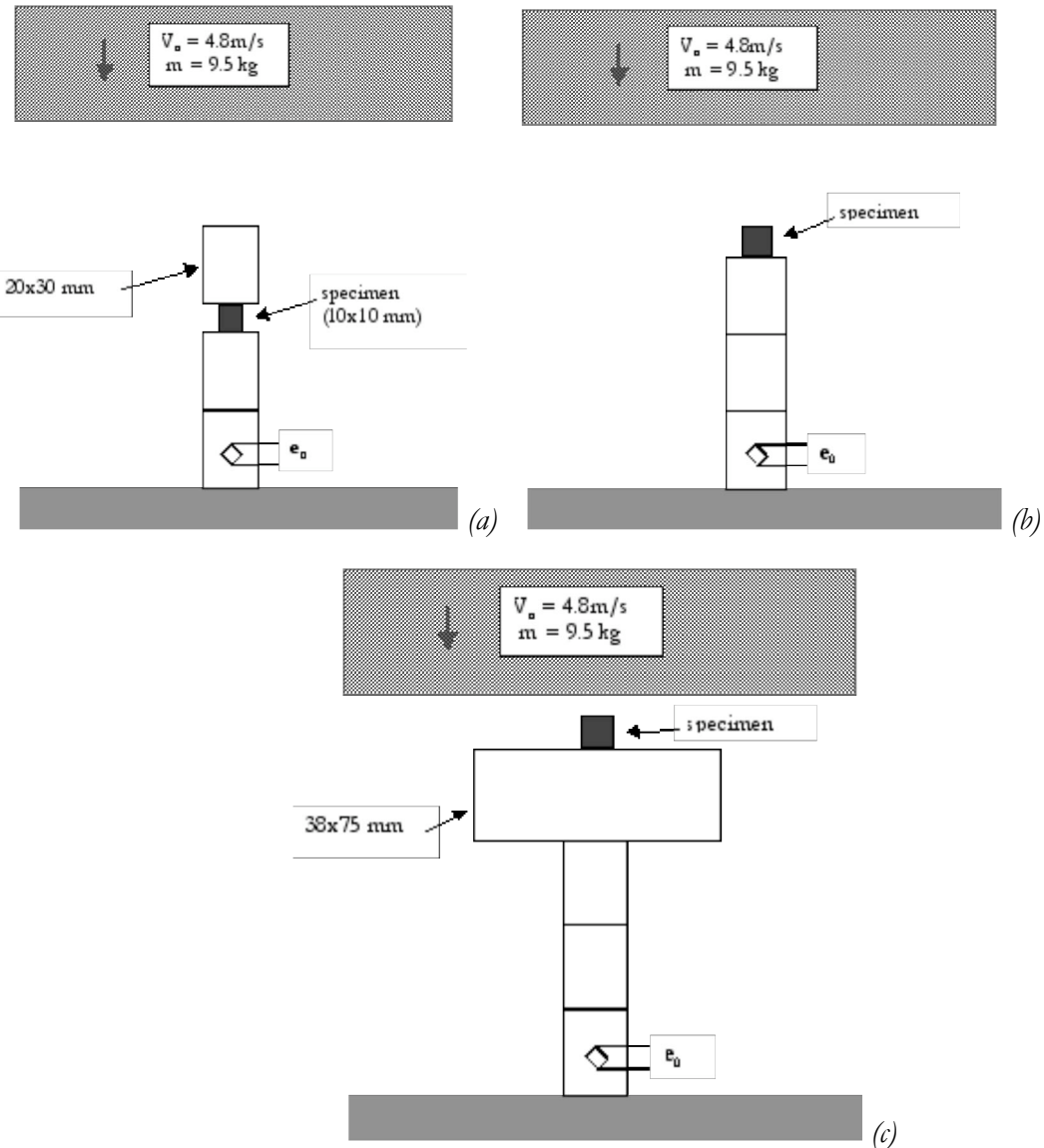


Figure 1.19. Three different configurations used to examine best location for specimen.

(a) Configuration 1; (b) configuration 2; (c) configuration 3.

Note that the falling mass was larger in these experiments compared to those reported later in this document.

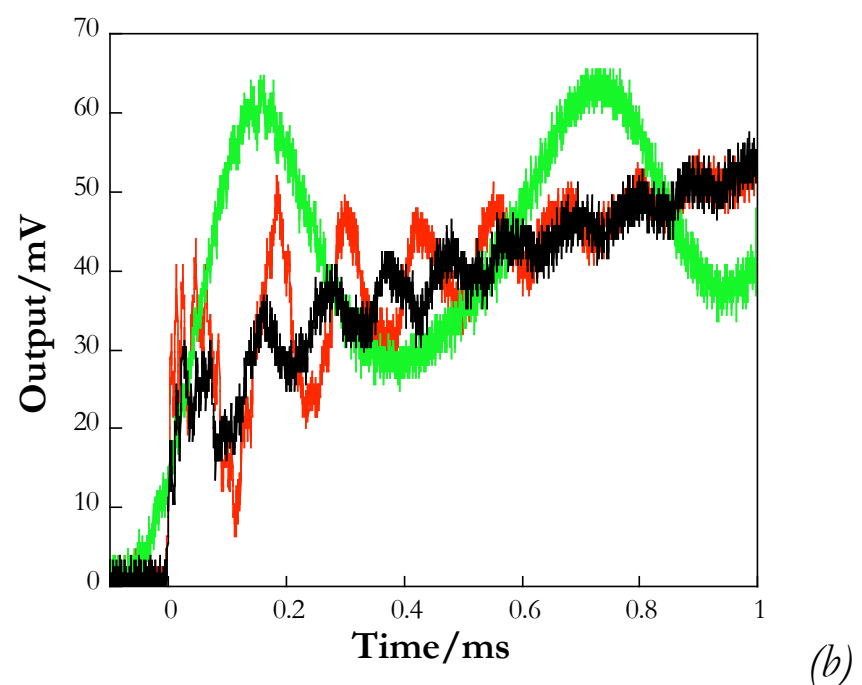
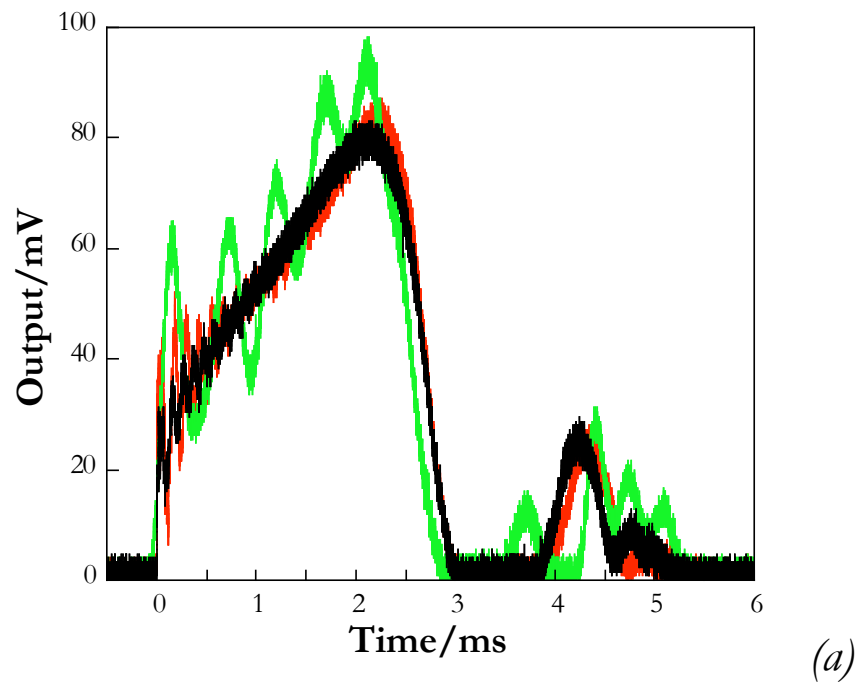
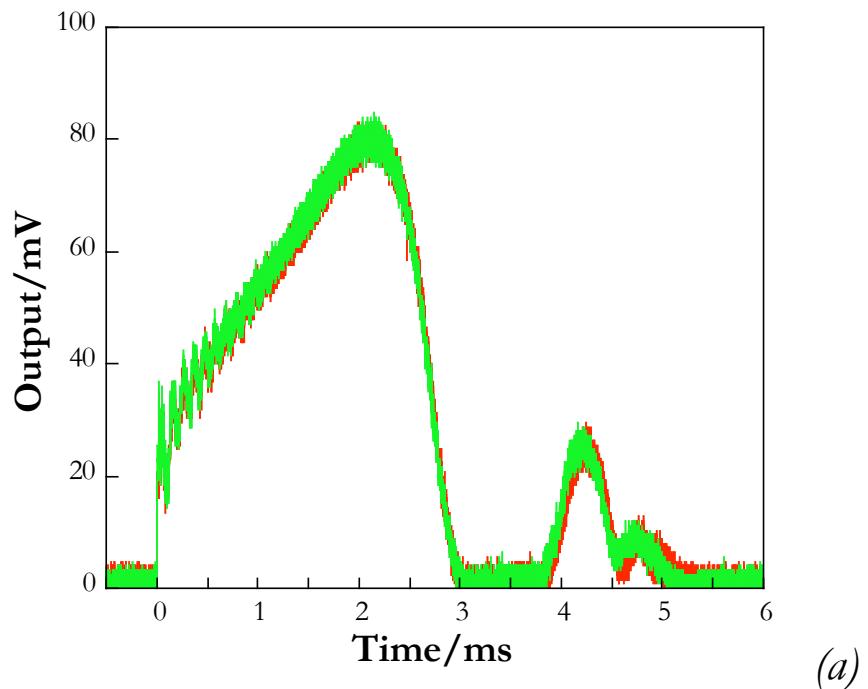
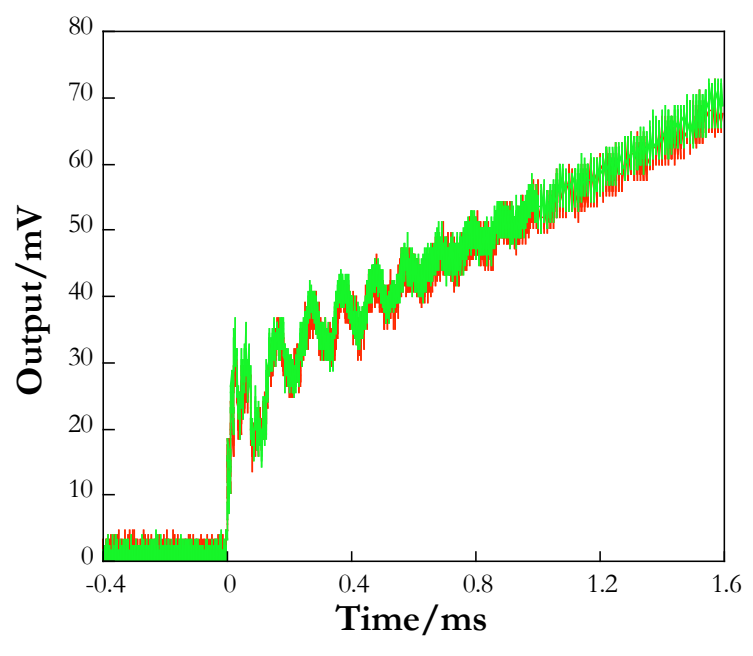


Figure 1.20. Transducer output for the three configurations shown in figure 1.19. Black line: configuration 1; Red line: configuration 2; Green line: configuration 3.
 (a) whole signals; (b) enlarged view of signals close to origin.



(a)



(b)

Figure 1.21. Check of reproducibility of output of dropweight force transducer.
(a) Whole traces; (b) enlarged view close to origin.

Gauge arrangement and calibration

Four foil strain gauges (type J2A-06-5033P-350, Measurement Systems Inc.) were used to instrument the lower cylinder. They were electrically connected in a full Wheatstone bridge (figure 1.22). Two of the gauges were glued parallel to the long axis of the cylinder. These therefore measure the compression of the lowest anvil when the transducer is struck. In order to ensure the bridge is not unbalanced by temperature differences between the longitudinally arranged gauges and the ‘dummy’ gauges needed to balance the bridge electrically, the dummy gauges were glued to the anvil at 90° to the other two i.e. circumferentially, the so-called Poisson orientation. This ensures they are in good thermal contact. The downside is that the Poisson gauges are also strained when the anvil is compressed lessening the sensitivity of the transducer. But because the Poisson ratio of steel is less than 0.5, the circumferential strain is always less than the compressional strain, the Wheatstone bridge outputs a voltage signal proportional to the force applied. As the signal is very small, an amplifier was used to magnify the signal before recording it using a Tektronix scope.

Any force transducer must be calibrated for use so that the recorded voltage can be converted to a force. Alternatively, the theory of the Wheatstone bridge is well-established. So if the properties of the gauges are accurately known, an algebraic expression appropriate for the arrangement of the gauges can be used to calculate the force.

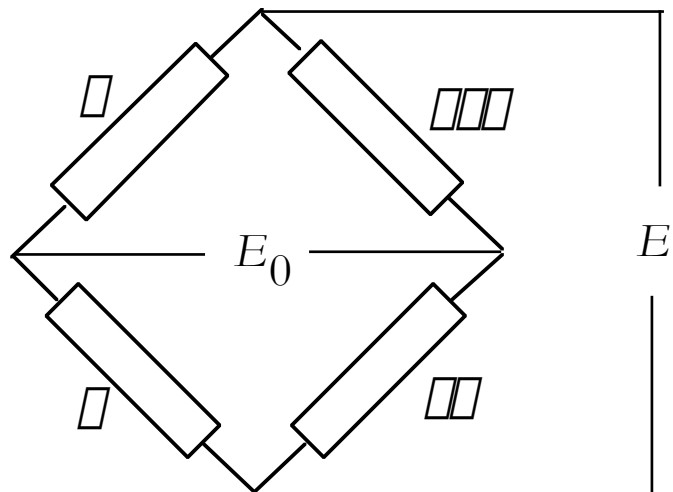


Figure 1.22. Schematic diagram of the electrical arrangement of the strain gauges in our force transducer. Two measure axial strain (labelled \square); two measure circumferential strain (labelled $\square\square$).

The output equation of the bridge circuit shown above in figure 1.22 is:

$$\frac{E_0}{E} = \frac{F \square (1 \square \square) \square 10^3}{2} \quad , \quad (1.2)$$

where F is the gauge factor of the gauges used and ϵ is the strain in the gauges (Anon. 1976). This particular configuration is linear.

We decided, however, to calibrate the instrumented anvil. This was done in two different ways: (i) the anvil was loaded statically in an Instron mechanical testing machine; (ii) the anvil was loaded dynamically in the rig by dropping the weight onto the transducer with no specimen present. The static calibration curve is presented in figure 1.23. The anvil was loaded and unloaded three times to check reproducibility.

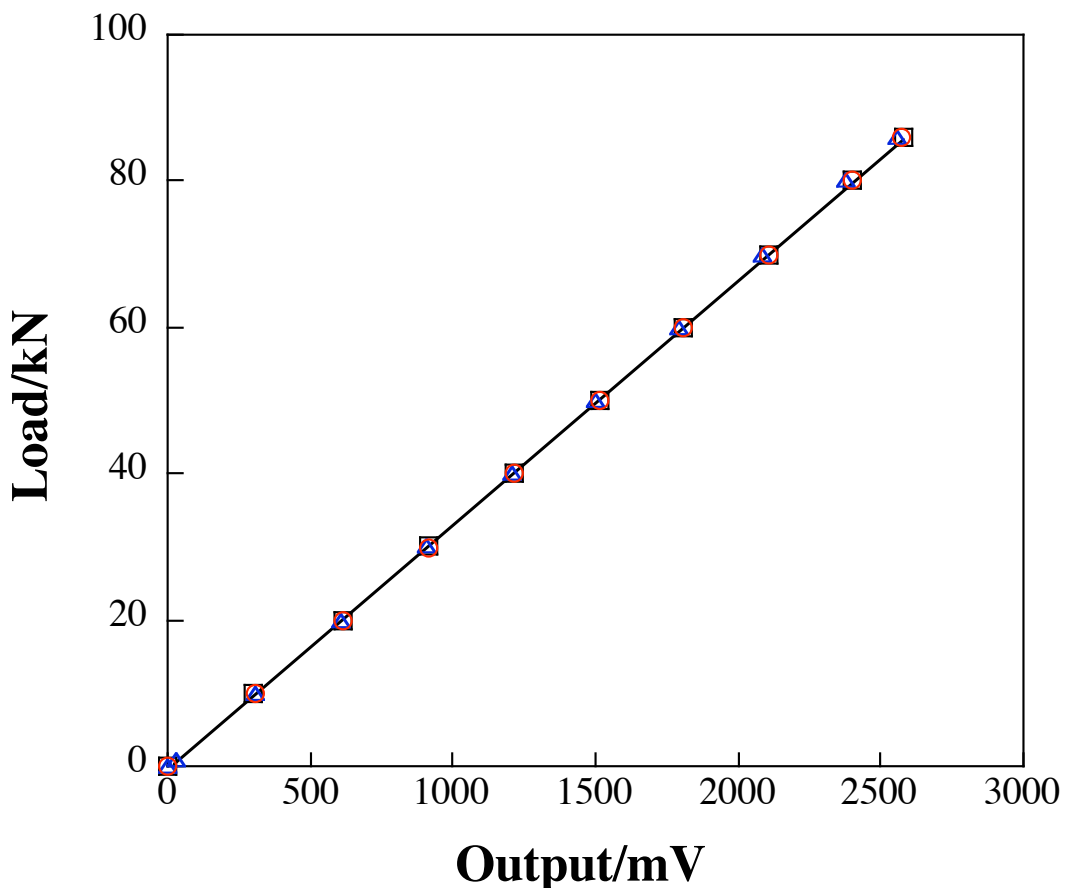


Figure 1.23. Static calibration curve of the instrumented anvil using the amplifier set to 100 \times amplification. The calibration factor is 33,380 N/V.

In order to perform a dynamic calibration, the mass of the dropweight needs to be known accurately, and also the impact and rebound speed. This is because the impulse imparted to the transducer is given by $m\int v \, dt$ Ns. The dynamic calibration factor k is given by:

$$k = \frac{m \int v}{\int V \, dt} \quad . \quad (1.3)$$

The impact and rebound speeds were measured by attaching a grating with a pitch of 2mm to the side of the dropweight. This passed between a diode laser and an optical fibre connected to a photodiode as the weight falls and rebounds. The measurement is taken as close as possible to the impact point. A typical signal recorded from this set-up is shown in figure 1.24. The corresponding voltage signal from the Wheatstone bridge is shown in figure 1.25.

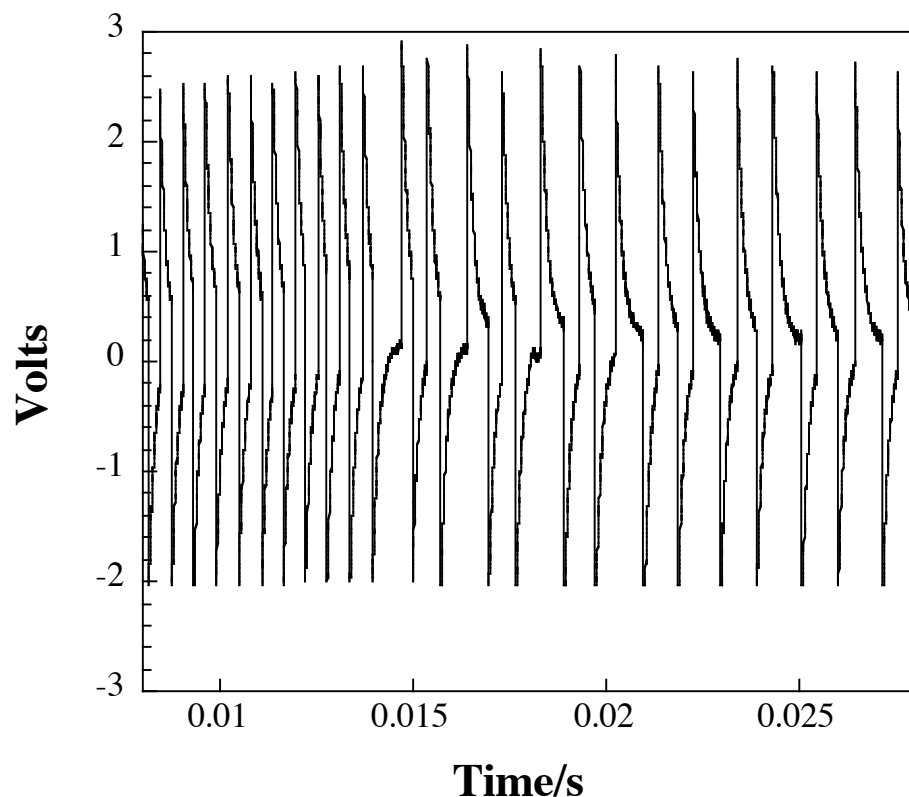


Figure 1.24. Output from the photodiode as the weight impacts and rebounds from the force transducer.

Calculated impact velocity = 3.419 m/s. Calculated rebound velocity = 1.964 m/s.

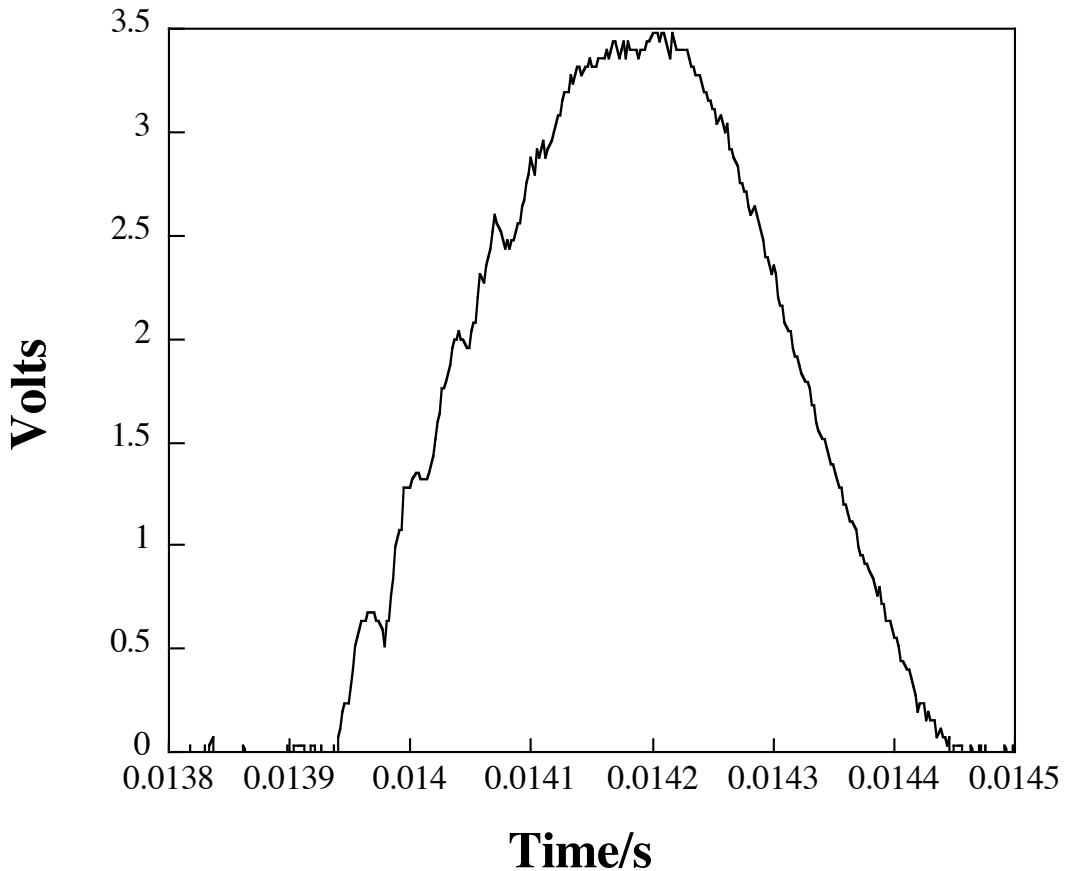


Figure 1.25. Voltage-time trace for the same impact as figure 1.7.
Area under the curve is $1.027 \times 10^{-3} \text{ s}^2$.

As the mass of the dropweight is 6.54 kg, k can be calculated using equation (1.3) as:

$$k = 6.54(3.419 - (-1.964)) / 1.027 \cdot 10^{-3} = 34,280 \text{ N/V} \quad .$$

Another dynamic experiment gave k as 33,760 N/V, bracketing the static value well.

Dropweights have a bad reputation for accuracy compared to Hopkinson bars. This is largely due to their often poor signal-to-noise ratio, especially if accelerometers are attached to the falling mass to measure force-time traces. The two machines are mechanically quite distinct. The Hopkinson bar is mechanically excited above its resonant frequency. One consequence of this is that the loading time is short, being given by the time for one elastic wave transit up and down the rod (although techniques have recently been developed for making use of data

from subsequent wave reflections: Bussac *et al.* 2002). The dropweight, by contrast, is excited below its resonant frequency. One consequence of this is that the loading time is long, governed by the time taken by elastic wave activity within the impacting mass to produce a net reversal of the momenta of its component parts. The mass, therefore, is subject to a very complex pattern of wave activity within it during impact. This is the reason that transducers should not be attached to it in order to measure the force on the specimen.

A check was then made that the dropweight gave the same stress-strain curve as our compression split Hopkinson pressure bar (figure 1.26): the agreement can be seen to be good despite the larger oscillations on the stress-strain curve obtained using the dropweight. Note that the dropweight curves go out to larger strains. The data is shown terminating at strains less than the specimens were actually taken to in the dropweight for two reasons: (i) it allows a clearer comparison with the Hopkinson bar data, and (ii) the true stress-true strain curves become less accurate at larger strains due to barrelling of the specimens.

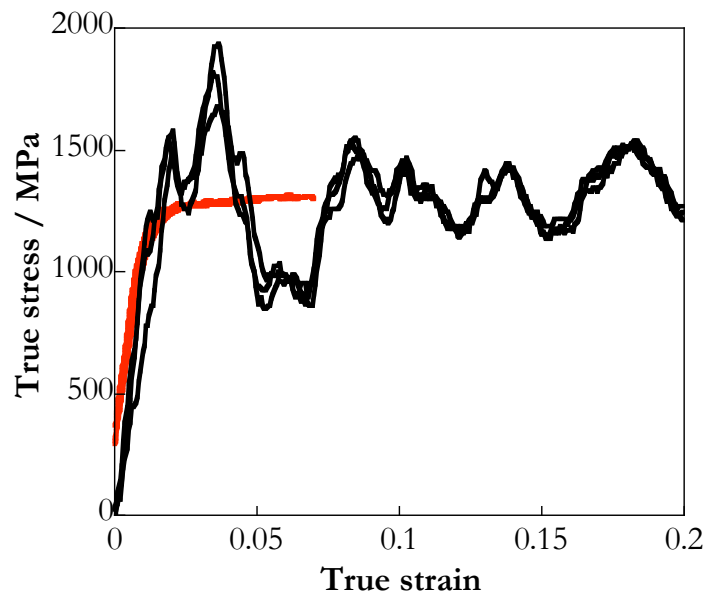


Figure 1.26. Comparison of stress-strain curves obtained using a compression split Hopkinson pressure bar (red lines) with that obtained using the dropweight (black lines) for Ti6Al4V specimens 4mm diameter, 8mm long.

If it is desired in future to combine high-speed photography with force-time measurement, the stack of steel cylinders would be replaced by the glass anvils (shown schematically in figure 1.15) and an instrumented annulus placed below the lower glass anvil. We already have experience of this constructing such a system (Walley *et al.* 1995).

Another check on the pressures developed during impact is to use a pressure-sensitive film (see figures 1.27 and 1.28). A photograph of a piece of this film that

was in contact with a polymer disc deformed in the dropweight machine is shown in figure 1.27. A false colour pressure-distribution map of this impact is shown in figure 1.28.

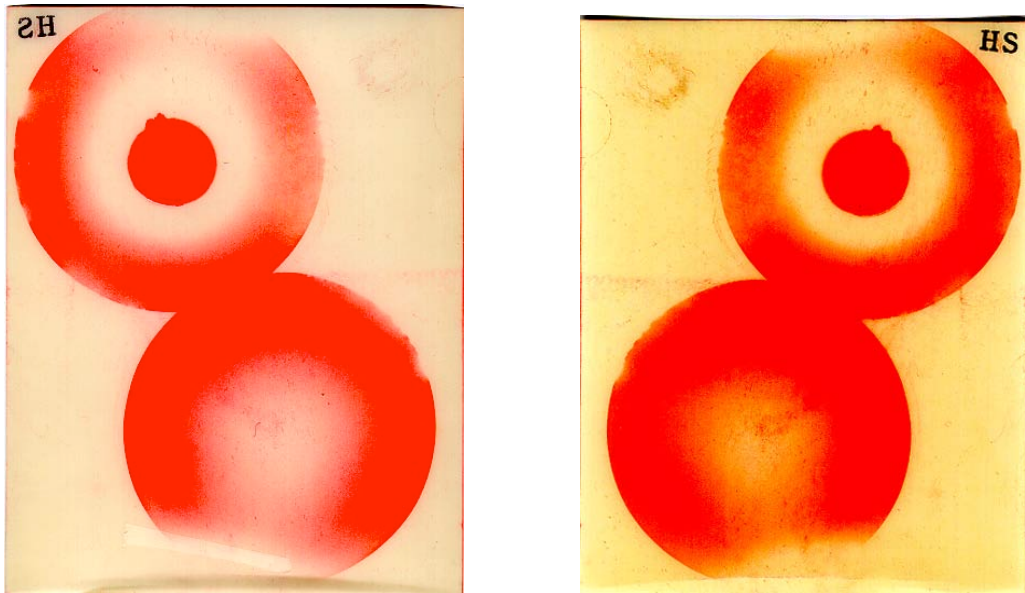


Figure 1.27. Photographs front and back of pressure-sensitive film after two drops in the dropweight machine using glass anvils. The top drop was onto a 5 mm diameter, 0.7 mm thick nylon 6 specimen. The bottom drop was glass anvil onto glass anvil. The red colour indicates high pressure.

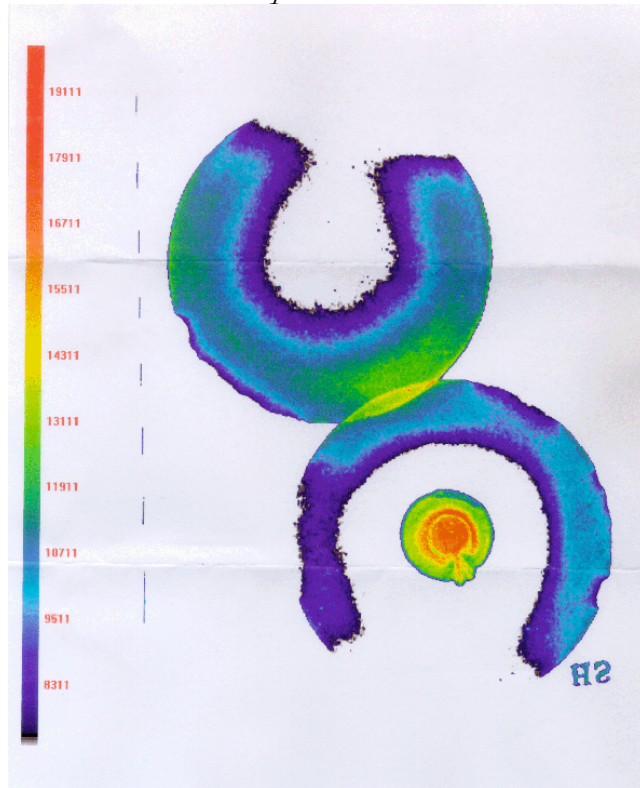


Figure 1.28. False-colour maps of pressure distribution computed by the manufacturer for the pressure sensitive film shown in figure 1.27. As the humidity and temperature were not measured in these experiments, the results are qualitative only.

1.5. DEFLAGRATION-TO-DETONATION (DDT) STUDIES

As part of an on-going programme to investigate the properties of ultrafine energetic materials a number of techniques have been developed to probe their response to different stimuli. A few of the different techniques that have been utilised will be outlined below together with some results that have originated from them. There is not the scope in this summary to outline all of the techniques in detail, some references are provided for further reading.

Materials

The materials that have been used are ultrafine PETN and RDX prepared by a proprietary method by ICI Nobel, Ardeer, U.K. The material is composed of approximately micron sized primary grains that form loose sponge-like secondary agglomerations. The density of the loose powder on delivery is $\sim 15\%$ of the theoretical maximum density (TMD). The ultrafine HNS that was used was HNS IV as supplied by Bofors, Sweden.

For comparison, conventional grain size materials were also provided by ICI and Bofors. These typically had a grain size of approximately $180\text{ }\mu\text{m}$.

Photographic studies of confined materials

A steel confinement (figure 1.29) with an inlaid polycarbonate window has been developed that allows the photographic study of materials as reaction travels along the column. For studying phenomena such as the deflagration-to-detonation transition, the level of confinement available in this set-up is essential for the mechanism to operate.

Typically an image converter camera operating in streak mode is used to view the passage of reaction along the column. Because this level of confinement has been found to be necessary when studying the deflagration-to-detonation transition the charge is usually ignited at the base of the column using a specially designed hot-wire pyrotechnic ignition system. This allows direct ignition of the charge of secondary explosive without the venting of gases given off in the early stages of the reaction.

The triggering of the high-speed camera is carried out using optical fibres positioned along the column. These can also be used to trigger fast responding detonators in order to send a detonation wave through the column prior to the charge undergoing a deflagration-to-detonation transition.

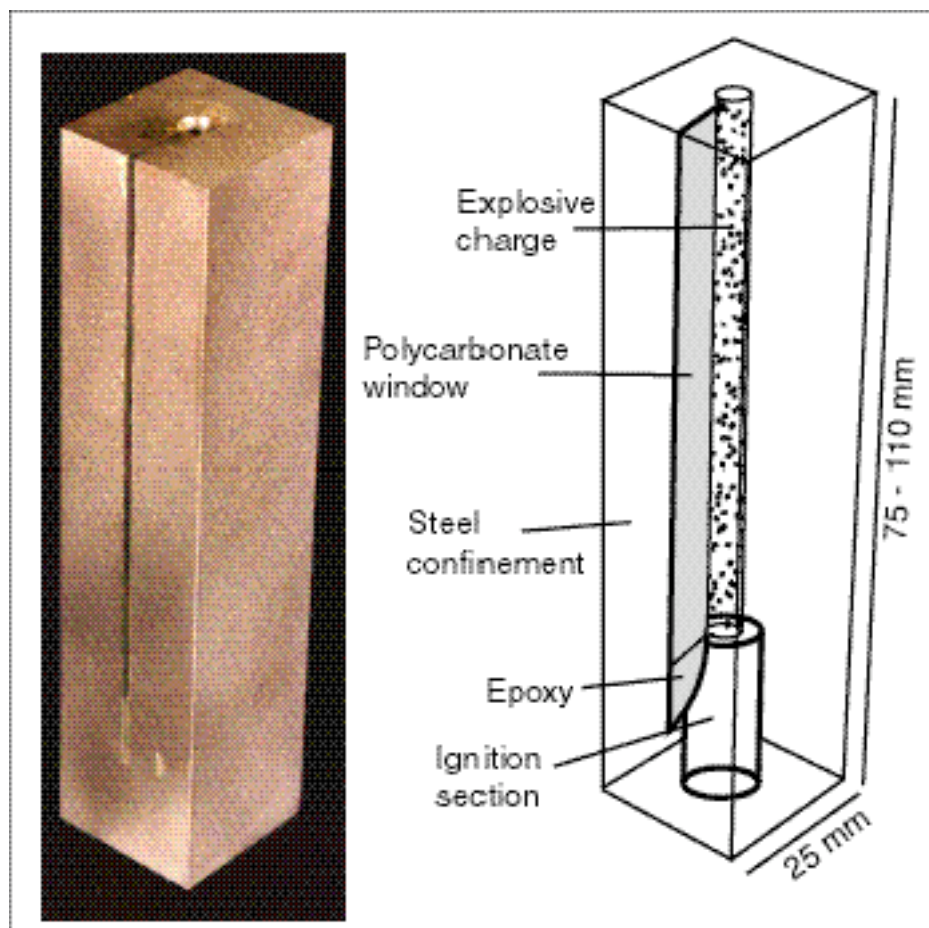


Figure 1.29. A photograph and a schematic of the windowed steel confinement.



Figure 1.30. Streak record of a type II deflagration-to-detonation transition in ultrafine PETN. A - Point at which initiation takes place; B - Detonation wave travelling at $5.6 \pm 0.3 \text{ mm } \mu\text{s}^{-1}$.

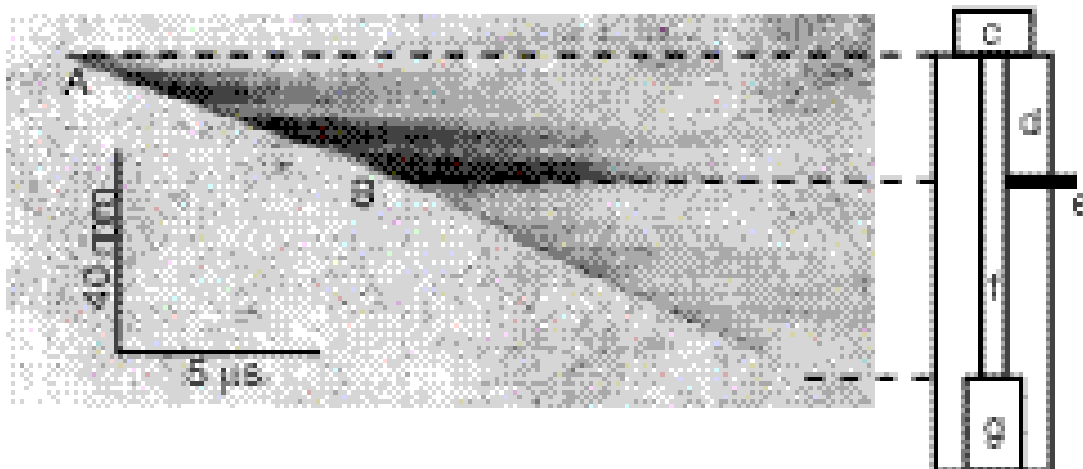


Figure 1.31. Negative streak record of an ultrafine PETN charge directly initiated after the reaction has reached an optical fibre placed along the column. A schematic of the charge is shown. A – point at which the charge is initiated; B – point reaction had reached when the detonation was initiated; c – EBW detonator; d – steel confinement; e – optical fibre; f – PETN charge; g – ignition section.

Directly initiated experiments – long duration shocks

Where the charges are directly initiated using a conventional detonator, polymethylmethacrylate (PMMA) confinements are used. These are typically 25 mm diameter, 25 mm long cylinders. PMMA offers visual access for high-speed photography. In their most basic guise, these confinements have been used for measuring detonation velocities in pressed charges of PETN.

A variation on this experimental set-up has allowed a ‘gap-test’ to be developed that uses a C8 detonator as the donor charge and a PMMA disc as the ‘gap’. The reproducibility of the results is particularly good with go/no-go boundaries being defined to within 0.01 mm providing the quality of the acceptor charge is good.

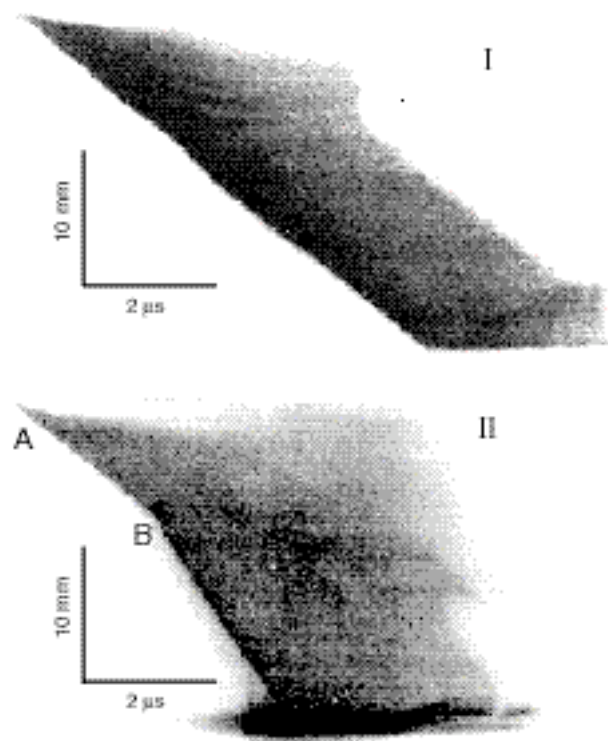


Figure 1.32. Negative streak records from two directly initiated charges of PETN. Charge I was a solid charge and has a steady detonation velocity of $4.1 \pm 0.1 \text{ mm } \mu\text{s}^{-1}$. Charge II had a 1.5 mm diameter axial channel drilled through it. At the point of initiation 'A' the detonation velocity is $3.9 \pm 0.1 \text{ mm } \mu\text{s}^{-1}$. At B this accelerates to $8.2 \pm 0.1 \text{ mm } \mu\text{s}^{-1}$.

Directly initiated experiments – short duration shocks

A laser-driven flyer plate system has been developed within the laboratory for imparting short duration high pressure shocks. The laser propels millimetre diameter metre flyers with a thickness of the order a few microns at velocities up to $10 \text{ mm } \mu\text{s}^{-1}$. It has been shown using this technique that only ultrafine materials are susceptible to initiation from shocks this thin. The system has been used for go/no-go studies of a range of materials to assess their suitability for use in system employing this type of initiator.

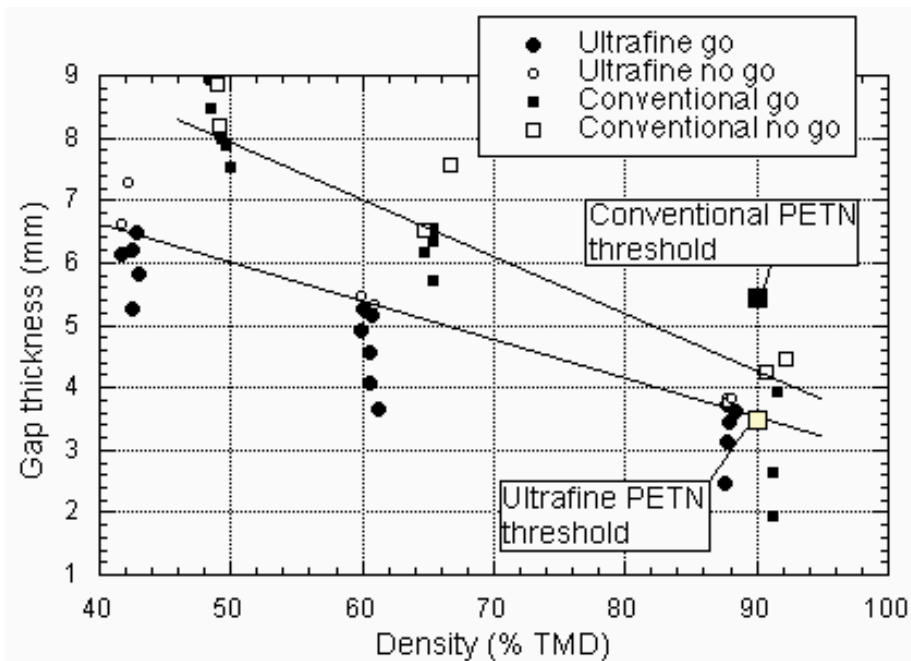


Figure 1.33. Plot of the results of gap testing comparing ultrafine and conventional RDX. Thresholds for PETN at a given density are also shown.

Thermocouples

Thin type K thermocouples have been used in a number of experiments involving energetic materials. Placed in columns during deflagration-to-detonation transitions they can only give an indication of the temperature during the fast reactions found later in the process. Due to their relatively low thermal mass the response time is sufficiently good to give temperature measurements during the slow build up prior to a type II DDT event. The confinements used for these experiments are cylindrical steel tubes.

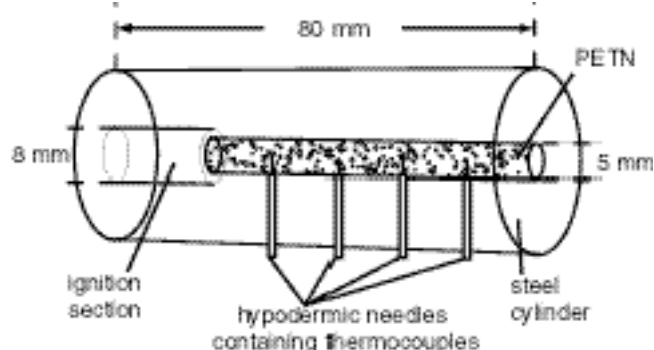


Figure 1.34. Schematic showing the way in which thermocouples have been inserted into the energetic column for monitoring the build-up to a type II DDT event.

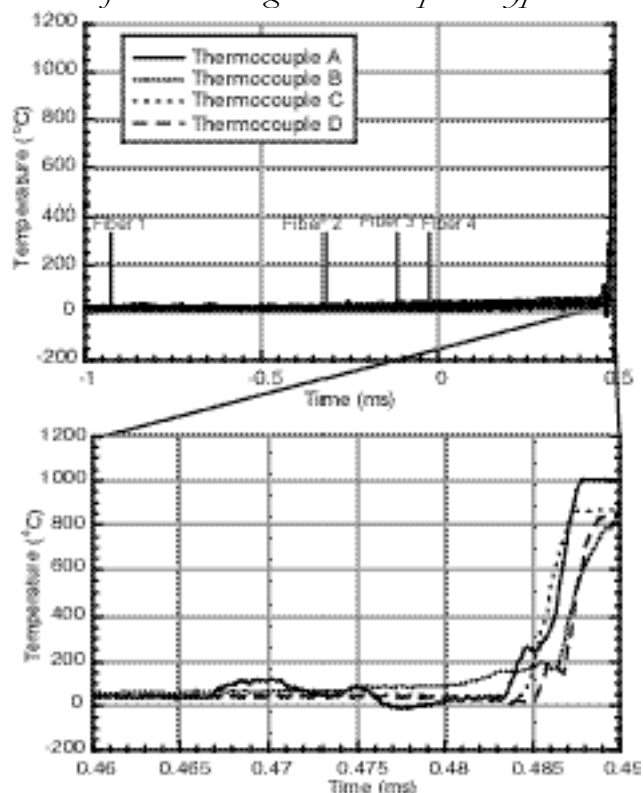


Figure 1.35. The output from four thermocouples placed in a column of ultrafine PETN during a type II DDT event.

The thermocouples have also been used for monitoring the temperature in an ignition cell that is used for critical hot-spot studies.

1.6 REFERENCES

Aggag, G. and Takahashi, K. (1996) "Study of oscillation signals in instrumented Charpy impact testing" *Polym. Engng Sci.* **36** 2260-2266

Anon. (1976) "Errors due to Wheatstone Bridge nonlinearity", Micro-Measurements Grouop, report no. TN-139-2

Armstrong, R.W., Codd, I., Douthwaite, R.M. and Petch, N.J. (1962) "The plastic deformation of polycrystalline aggregates" *Philos. Mag.* **7** 45-58

Armstrong, R.W. and Zerilli, F.J. (2001) "Dislocation aspects of shock-wave and high strain rate phenomena" in "Fundamental Issues and Applications of Shock-Wave and High-Strain-Rate Phenomena", ed. K.P. Staudhammer, L.E. Murr and M.A. Meyers, publ. New York, Elsevier: pp. 115-124.

Armstrong, R.W., Zerilli, F.J., Holt, W.H. and MockJr., W. (1994) "Dislocation mechanics based constitutive relations for plastic flow and strength of HY steels" in "High Pressure Science and Technology 1993", ed. S.C. Schmidt, J.W. Shaner, G.A. Samara and M. Ross, publ. New York, American Institute of Physics: pp. 1001-1004.

Bacon, C. and Brun, A. (2000) "Methodology for a Hopkinson bar test with a non-uniform viscoelastic bar" *Int. J. Impact Engng* **24** 219-230

Bacon, C., Guiliorit, E., Hosten, B. and Chimenti, D.E. (2001) "Acoustic waves generated by pulsed microwaves in viscoelastic rods: Modeling and experimental verification" *J. Acoust. Soc. Amer.* **110** 1398-1407

Balzer, J.E. (2001) "Low-level impact loading of explosives", PhD thesis, Univ. of Cambridge

Bancroft, D. (1941) "The velocity of longitudinal waves in cylindrical bars" *Phys. Rev.* **59** 588-593

Bardenhagen, S.G., Harstad, E.N., Maudlin, P.J., GrayIII, G.T. and FosterJr., J.C. (1998) "Viscoelastic models for explosive binder materials" in "Shock Compression of Condensed Matter - 1997", ed. S.C. Schmidt, D.P. Dandekar and J.W. Forbes, publ. Woodbury, New York, American Institute of Physics: pp. 281-284.

Bateman, V.I., Brown, F.A. and Davie, N.T. (1996) "Use of a beryllium Hopkinson bar to characterize a piezoresistive accelerometer in shock environments" *J. Inst. Environmental Sci.* **39** 33-39

Bernatskii, A.D. and Rabinovich, A.L. (1964) "Strain in certain crosslinked polymers" *Polym. Sci. USSR* **6** 1166-1175

Briscoe, B.J. and Hutchings, I.M. (1976) "Impact yielding of high density polyethylene" *Polymer* **17** 1099-1102

Briscoe, B.J. and Hutchings, I.M. (1978) "Impact yielding of high density polyethylene" *Polymer* **19** 1110

Briscoe, B.J. and Nosker, R.W. (1984) "The influence of interfacial friction on the deformation of high density polyethylene in a split Hopkinson pressure bar" *Wear* **95** 241-262

Bussac, M.-N., Collet, P., Gary, G. and Othman, R. (2002) "An optimisation method for separating and rebuilding one-dimensional dispersive waves from multi-point measurements: Application to elastic or viscoelastic bars" *J. Mech. Phys. Solids* **50** 321-249

Cain, P.J. (1987) "Digital filtering of impact data" in "Instrumented Impact Testing of Plastics and Composite Materials" (*ASTM STP 936*), ed. S.L. Kessler, G.C. Adams, S.B. Driscoll and D.R. Ireland, publ. Philadelphia, American Society for Testing and Materials: pp. 81-102.

Chou, P.C., Clark, W. and Liang, D.-S. (1995) "Blunt cylinder impact tests for the determination of constitutive equation of explosives" in "Proc. 15th Int. Symp. on Ballistics. Vol. 1", ed. M. Mayseless and S.R. Bodner, publ. Jerusalem: pp. 159-166.

Christopher, F.R., Foster Jr., J.C., Wilson, L.L. and Gilland, H.L. (2000) "The use of impact techniques to characterize the high rate mechanical properties of plastic bonded explosives" in "Proc. 11th Int. Detonation Symposium", ed. J.M. Short and J.E. Kennedy, publ. Arlington, Virginia, Office of Naval Research: pp. 286-292.

Davies, R.M. (1948) "A critical study of the Hopkinson pressure bar" *Phil. Trans. Roy. Soc. Lond. A* **240** 375-457

Dharan, C.K.H. and Hauser, F.E. (1970) "Determination of stress-strain characteristics at very high strain rates" *Exper. Mech.* **10** 370-376

Fugelso, E., Jacobson, J.D., Karpp, R.R. and Jensen, R. (1982) "Radiographic study of impact in polymer-bonded explosives" in "Shock Waves in Condensed Matter – 1981", ed. W.J. Nellis, L. Seaman and R.A. Graham, publ. New York, American Institute of Physics: pp. 607-612.

G'Sell, C. and Jonas, J.J. (1979) "Determination of the plastic behaviour of solid polymers at constant true strain rate" *J. Mater. Sci.* **14** 583-591

G'Sell, C. and Jonas, J.J. (1981) "Yield and transient effects during the plastic deformation of solid polymers" *J. Mater. Sci.* **16** 1956-1974

Gary, G., Klepaczko, J.R. and Zhao, H. (1995) "Generalization of split Hopkinson bar technique to use viscoelastic materials" *Int. J. Impact Engng* **16** 529-530

Goldrein, H.T. (1996) "Applications of optical strain measurement techniques to composite materials", PhD thesis, Univ. of Cambridge

Goldrein, H.T., Huntley, J.M., Palmer, S.J.P., Whitworth, M.B. and Field, J.E. (1995a) "Optical techniques for strength studies of polymer bonded explosives" in "Proc. 10th Int. Detonation Symposium", ed. J.M. Short and D.G. Tasker, publ. Arlington, Virginia, Office of Naval Research: pp. 525-535.

Goldrein, H.T., Palmer, S.J.P. and Huntley, J.M. (1995b) "Automated fine grid technique for measurement of large-strain deformation maps" *Optics Lasers Engng* **23** 305-318

Goldrein, H.T., Rae, P.J., Palmer, S.J.P. and Field, J.E. (2002) "Construction of a high-resolution moiré interferometer for investigating microstructural displacement fields in materials" *Phil. Trans. R. Soc. Lond. A* **360** 939-952

Goldrein, H.T., Synnergren, P. and Proud, W.G. (2000) "Three-dimensional displacement measurements ahead of a projectile" in "Shock Compression of Condensed Matter - 1999", ed. M.D. Furnish, L.C. Chhabildas and R.S. Hixson, publ. Melville, New York, American Institute of Physics: pp. 1095-1098.

Gorham, D.A. (1980) "Measurement of stress-strain properties of strong metals at very high strain rates" *Inst. Phys. Conf. Ser.* **47** 16-24

Gorham, D.A. (1991) "The effect of specimen dimensions on high strain rate compression measurements of copper" *J. Phys. D: Appl. Phys.* **24** 1489-1492.

Gorham, D.A., Pope, P.H. and Cox, O. (1984) "Sources of error in very high strain rate compression tests" *Inst. Phys. Conf. Ser.* **70** 151-158

Gorham, D.A., Pope, P.H. and Field, J.E. (1992) "An improved method for compressive stress-strain measurements at very high strain rates" *Proc. R. Soc. Lond. A* **438** 153-170

Grantham, S.G., Proud, W.G., Goldrein, H.T. and Field, J.E. (2000) "The study of internal deformation fields in granular materials using 3D digital speckle X-ray flash photography" *Proc. SPIE* **4101** 321-328

Gray III, G.T. (2000) "Classic split-Hopkinson pressure bar testing" in "ASM Handbook. Vol. 8: Mechanical Testing and Evaluation", ed. H. Kuhn and D. Medlin, publ. Materials Park, Ohio, ASM International: pp. 462-476.

Gray III, G.T. and Blumenthal, W.R. (2000) "Split-Hopkinson pressure bar testing of soft materials" in "ASM Handbook. Vol. 8: Mechanical Testing and Evaluation", ed. H. Kuhn and D. Medlin, publ. Materials Park, Ohio, ASM International: pp. 488-496.

Gray III, G.T., Blumenthal, W.R., Idar, D.J. and Cady, C.M. (1998) "Influence of temperature on the high strain-rate mechanical behavior of PBX 9501" in "Shock Compression of Condensed Matter - 1997", ed. S.C. Schmidt, D.P. Dandekar and J.W. Forbes, publ. Woodbury, New York, American Institute of Physics: pp. 583-586.

Gray III, G.T., Blumenthal, W.R., Trujillo, C.P. and Carpenter II, R.W. (1997) "Influence of temperature and strain rate on the mechanical behavior of Adiprene L-100" *J. Phys. IV France* **7** Colloq. C3 (EURODYMAT 97) 523-528

Gray III, G.T., Idar, D.J., Blumenthal, W.R., Cady, C.M. and Peterson, P.D. (2000) "High- and low-strain rate compression properties of several energetic material composites as a function of strain rate and temperature" in "Proc. 11th Int. Detonation Symposium", ed. J.M. Short and J.E. Kennedy, publ. Arlington, Virginia, Office of Naval Research: pp. 76-84.

Heavens, S.N. and Field, J.E. (1974) "The ignition of a thin layer of explosive by impact" *Proc. R. Soc. Lond. A* **338** 77-93

Huang, Q., Lu, T. and Liu, Y. (1997) "Study on the dynamic mechanical property of single base propellant" in "Proc 23rd Int. Pyrotechnics Seminar", ed. T. Yoshida and N. Kubota, publ. Chicago, IIT Research Institute: pp. 274-278.

Huntley, J.M. and Field, J.E. (1986) "Measurement of time-varying displacement fields by multiple-exposure speckle photography" *Appl. Opt.* **25** 1665-1669

Hutchings, I.M. (1978) "Estimation of yield stress in polymers at high strain rates using G.I. Taylor's impact technique" *J. Mech. Phys. Solids* **26** 289-301

Jia D. and Ramesh K.T. (2004) "A rigorous assessment of the benefits of miniaturization in the Kolsky bar system" *Exper. Mech.* **44** 445-454

Jones, I.R. (1966) "Beryllium pressure bar having submicrosecond risetime" *Rev. Sci. Inst.* **37** 1059-1061

Kukureka, S.N. and Hutchings, I.M. (1981) "Measurement of the mechanical properties of polymers at high strain rates by Taylor impact" in "Proc. 7th Int. Conf on High Energy Rate Fabrication", ed. T.Z. Blazynski, publ. Leeds, University of Leeds: pp. 29-38.

Mason, T.A. (1999) "Variation in the dispersion of axisymmetric waves in infinite circular rods with crystallographic wire texture" *J. Acoust. Soc. Amer.* **106** 1262-1270

Matheson, E.R., Drumheller, D.S. and Baer, M.R. (2000a) "A coupled damage and reaction model for simulating energetic material response to impact hazards" in "Shock Compression of Condensed Matter - 1999", ed. M.D. Furnish, L.C. Chhabildas and R.S. Hixson, publ. Melville, New York, American Institute of Physics: pp. 651-654.

Matheson, E.R., Drumheller, D.S. and Baer, M.R. (2000b) "An internal damage model for viscoelastic-viscoplastic energetic materials" in "Shock Compression of Condensed Matter - 1999", ed. M.D. Furnish, L.C. Chhabildas and R.S. Hixson, publ. Melville, New York, American Institute of Physics: pp. 691-694.

Mooij, J.J. (1981) "Instrumented flat-headed falling-dart test" *Polymer Testing* **2** 69-83

Murray, N.H., Bourne, N.K., Field, J.E. and Rosenberg, Z. (1998) "Symmetrical Taylor impact of glass bars" in "Shock Compression of Condensed Matter - 1997", ed. S.C. Schmidt, D.P. Dandekar and J.W. Forbes, publ. Woodbury, New York, American Institute of Physics: pp. 533-536.

Napadensky, H.S., Eichler, T.V., Kot, C.A. and Zaker, T.A. (1970) "Deformation of a cylinder of explosive material in unconfined impact" in "Proc. Fifth Symp. (Int.) on Detonation", publ. Arlington, Virginia, Office of Naval Research: pp. 313-320.

Nemat-Nasser, S., Isaacs, J.B. and Starrett, J.E. (1991) "Hopkinson techniques for dynamic recovery experiments" *Proc. R. Soc. Lond. A* **435** 371-391

Olsen, E.M., Rosenberg, J.T., Kawamoto, J.D., Lin, C.F. and Seaman, L. (2000) "XDT investigations by computational simulations of mechanical response using a new viscous internal damage model" in "Proc. 11th Int. Detonation Symposium", ed. J.M. Short and J.E. Kennedy, publ. Arlington, Virginia, Office of Naval Research: pp. 170-178.

Pope, P.H. and Field, J.E. (1984) "Determination of strain in a dynamic compression test" *J. Phys. E: Sci. Instrum.* **17** 817-820

Quidot, M. (1988) "Dynamic fragmentation of compact energetic materials" in "Impact Loading and Dynamic Behaviour of Materials", publ. Oberursel, Germany, DGM Informationsgesellschaft mbH: pp. 609-614.

Quidot, M., Racimor, P. and Chabin, P. (2000) "Constitutive models for PBX at high strain rate" in "Shock Compression of Condensed Matter - 1999", ed. M.D. Furnish, L.C. Chhabildas and R.S. Hixson, publ. Melville, New York, American Institute of Physics: pp. 687-690.

Radford, D.D., Church, P.D., Gould, P.J. and Eadington, E. (2001) "Deformation and failure during 'symmetric' Taylor impact tests" in "Plasticity, Damage and Fracture at Macro, Micro and Nano Scales", ed. A.S. Khan and O. Lopez-Pamies, publ. Fulton, Maryland, Neat Press: pp. 663-665

Radford, D.D., Walley, S.M., Church P. and Field J.E. (2003) "Dynamic upsetting and failure of metal cylinders: Experiments and analysis" *J. Phys. IV France* **110** 263-268

Safford, N.A. (1988) "High strain rate studies with the direct impact Hopkinson bar", PhD thesis, Univ. of Cambridge

Safford, N.A. (1992) "Materials testing up to 10^5 s⁻¹ using a miniaturised Hopkinson bar with dispersion corrections" in "Proc. 2nd. Int. Symp. on Intense Dynamic Loading and its Effects", ed. G. Zhang and S. Huang, publ. Chengdu, P.R. China, Sichuan University Press: pp. 378-383.

Sahraoui, S. and Lataillade, J.L. (1990) "Dynamic effects during instrumented impact testing" *Engng Fract. Mech.* **36** 1013-1019

Sahraoui, S. and Lataillade, J.L. (1998) "Analysis of load oscillations in instrumented impact testing" *Engng Fract. Mech.* **60** 437-446

Silversmith, D.J. and Averbach, B.L. (1970) "Pressure dependence of the elastic constants of beryllium and beryllium-copper alloys" *Phys. Rev. B* **1** 567-571

Siviour, C.R., Walley, S.M., Proud, W.G. and Field, J.E. (2001) "Are low impedance Hopkinson bars necessary for stress equilibrium in soft materials?" in "Proc. NEM-2001 Workshop on New Experimental Methods in Material Dynamics and Impact", ed. W.K. Nowacki and J.R. Klepaczko, publ. Warsaw, Poland, Institute of Fundamental Technological Research: pp. 421-427.

Synnergren, P. and Goldrein, H.T. (1999) "Dynamic measurements of internal three-dimensional displacement fields with digital speckle photography and flash X-rays" *Appl. Opt.* **38** 5956-5961

Synnergren, P., Goldrein, H.T. and Proud, W.G. (1999) "Application of digital speckle photography to flash X-ray studies of internal deformation fields in impact experiments" *Appl. Opt.* **38** 4030-4036

Vorthman, J.E. (1982) "Facilities for the study of shock induced decomposition of high explosives" in "Shock Waves in Condensed Matter – 1981", ed. W.J. Nellis, L. Seaman and R.A. Graham, publ. New York, American Institute of Physics: pp. 680-684.

Walley, S.M., Church, P.D., Townsley, R. and Field, J.E. (2000) "Validation of a path-dependent constitutive model for FCC and BCC metals using 'symmetric' Taylor impact" *J. Phys. IV France* **10 Pr. 9 (DYMAT 2000)** 69-74

Walley, S.M. and Field, J.E. (1994) "Strain rate sensitivity of polymers in compression from low to high strain rates" *DYMAT Journal* **1** 211-228

Walley, S.M., Field, J.E. and Palmer, S.J.P. (1992) "Impact sensitivity of propellants" *Proc. R. Soc. Lond. A* **438** 571-583

Walley, S.M., Field, J.E., Pope, P.H. and Safford, N.A. (1989) "A study of the rapid deformation behaviour of a range of polymers" *Phil. Trans. R. Soc. Lond. A* **328** 1-33

Walley, S.M., Field, J.E., Pope, P.H. and Safford, N.A. (1991) "The rapid deformation behaviour of various polymers" *J. Phys. III France* **1** 1889-1925

Walley, S.M., Xing, D. and Field, J.E. (1995) "Mechanical properties of three transparent polymers in compression at a very high rate of strain" in "Impact and Dynamic Fracture of Polymers and Composites", ed. J.G. Williams and A. Pavan, publ. London, Mechanical Engineering Publications Ltd.: pp. 289-303.

Zerilli, F.J. and Armstrong, R.W. (1990) "Description of tantalum deformation behavior by dislocation mechanics based constitutive equations" *J. Appl. Phys.* **68** 1580-1591

Zhao, H., Gary, G. and Klepaczko, J.R. (1997) "On the use of a viscoelastic split Hopkinson pressure bar" *Int. J. Impact Engng* **19** 319-330

2. THE EFFECT OF PARTICLE SIZE AND TEMPERATURE ON THE HIGH STRAIN RATE PROPERTIES OF AN AP/HTPB PBX

It was observed that lowering the temperature made the effect of particle size on the flow stress of an AP/HTPB PBX more prominent (Balzer 2001). We therefore performed a more thorough study of the high strain rate properties of this material at both room temperature (22 °C) and at –60 °C. The AP/HTPB PBX used consisted of 66% ammonium perchlorate and 33% HTPB by mass. This was available in four different grain sizes: M1=30μm, M2=80μm, M3=300μm and M4=200-300μm. The room temperature experiments were performed using our low impedance magnesium alloy Hopkinson bar. The low temperature study was carried out using our Inconel bar system (the mechanical impedance of Inconel is only a weak function of temperature, so the temperature gradient does not distort the elastic wave pulse travelling through it (Kandasamy and Brar 1994, 1995). Cooling was performed by surrounding the ends of the bars with a chamber into which helium gas was passed that had been cooled using liquid nitrogen. The temperature was monitored using chromel-alumel thermocouples.

The PBXs were available in blocks of typical size 10cm by 5cm by 2cm. In order to prepare the samples, strips of PBX approximately 2mm thick, were cut from the block using razor blades mounted 2mm apart. The specimens were taken from these strips using a vertical punch of 6mm diameter. The larger grain size materials were easier to prepare than the smaller grain ones: the cutting instrument moved through the samples much more readily, and the quality of the ends, and in particular the sides, was higher.

The results of this study are presented in figures 2.1-2.11. At least three experiments were performed for each grain size at each temperature. It can be seen from figures 2.1-2.5 that at room temperature all the compositions strain-hardened, the stresses rising from *ca.* 2 to *ca.* 10 MPa. The strain rates of each curve are tabulated in each figure where original data are presented, and as averages where the average stress-strain curves are given. The fall in stress at the end of each curve represents the unloading of the specimen rather than its failure or fracture. It can be seen from figure 5 that the material containing the largest AP particle size supported the lowest stresses. The dotted lines either side of the solid line in each case represents the standard deviation of the data.

The stress-strain curves at –60°C are different in shape: all the materials flow at constant stress varying between *ca.* 50 MPa for the largest particle size material and *ca.* 100 MPa for the smallest particle size material. Figures 2.10 and 2.11 confirm that lowering the temperature magnifies the effect of particle size: the curves are clearly separated by particle size.

References

Balzer, J.E. (2001) "Low-level impact loading of explosives", PhD thesis, Univ. of Cambridge

Kandasamy, R. and Brar, N.S. (1994) "Flow stress and material model study at high strain rate and low temperature" in "High Pressure Science and Technology 1993", ed. S.C. Schmidt, J.W. Shaner, G.A. Samara and M. Ross, publ. New York, American Institute of Physics: pp. 1031-1034.

Kandasamy, R. and Brar, N.S. (1995) "Low temperature and strain sensitivity of steel and aluminum" *Exper. Mech.* **35** 119-123

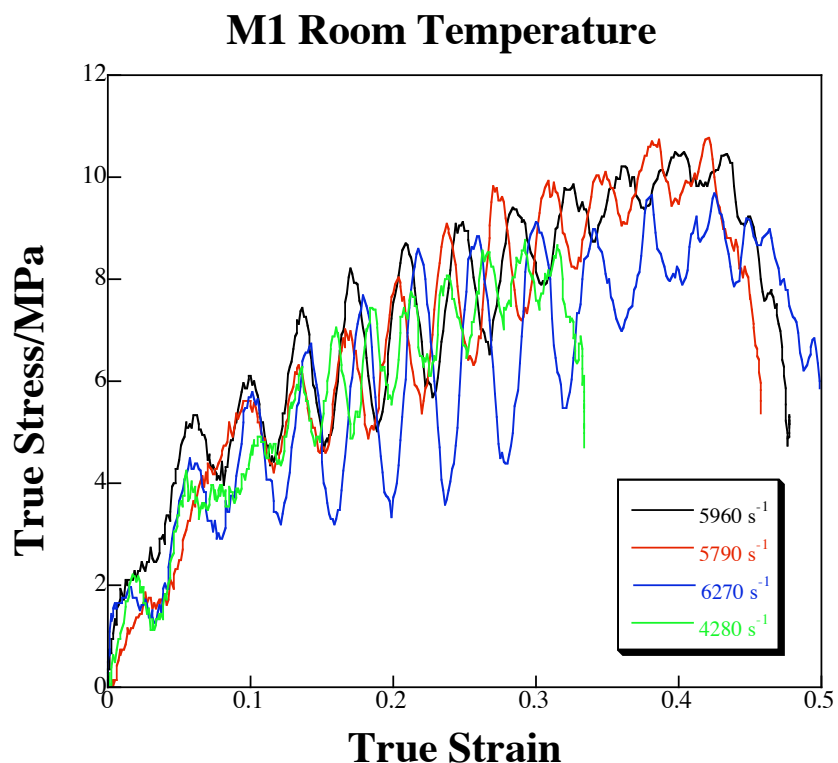


Figure 2.1. SHPB stress-strain curves for 3mm AP/HTPB at 22 °C.

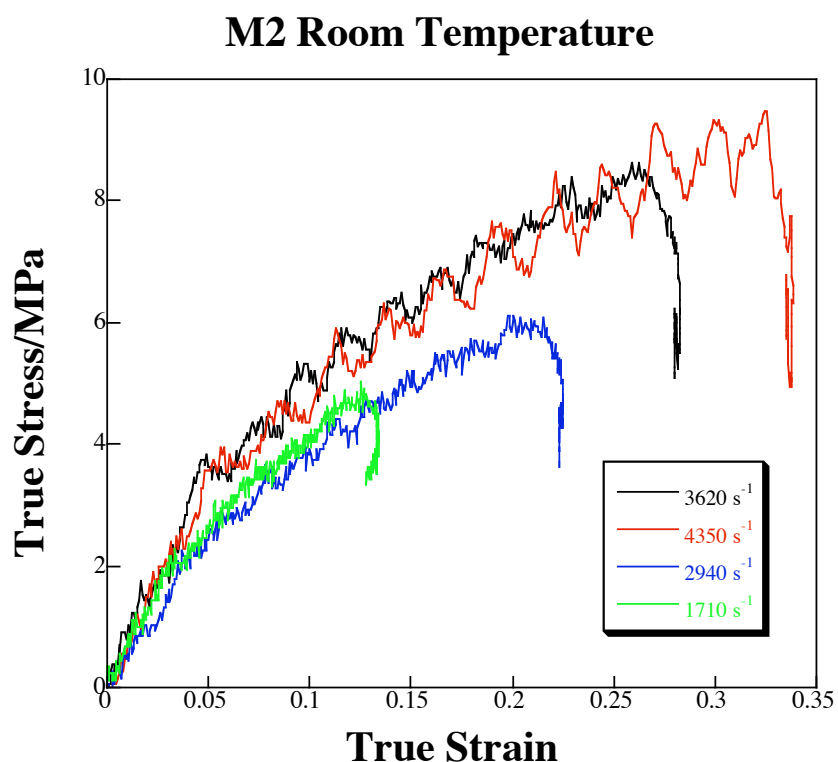


Figure 2.2. SHPB stress-strain curves for 8mm AP/HTPB at 22 °C.

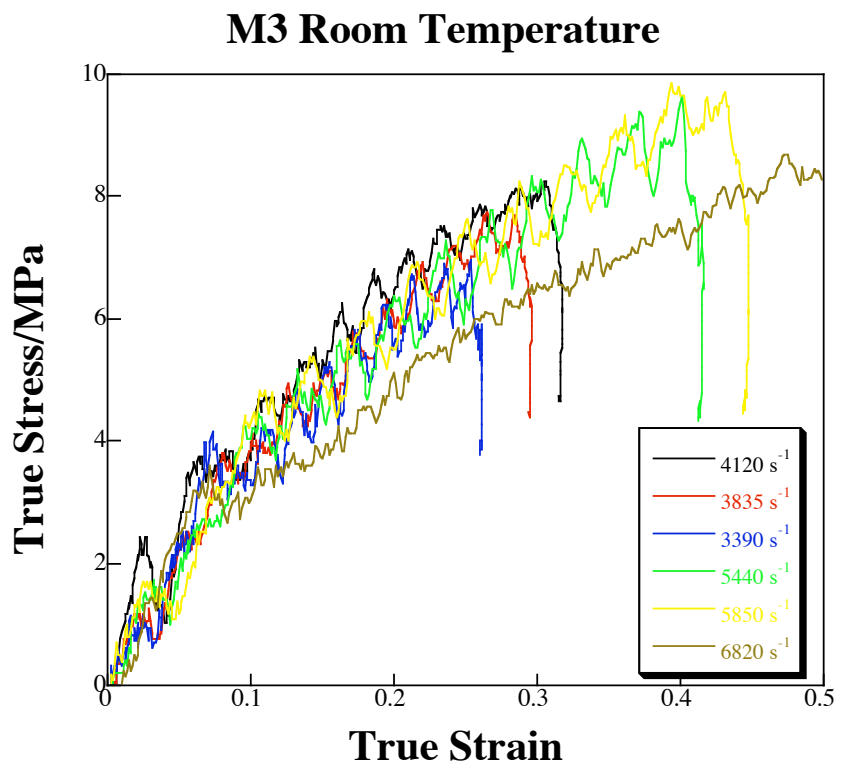


Figure 2.3. SHPB stress-strain curves for 30 μm AP/HTPB at 22 °C.

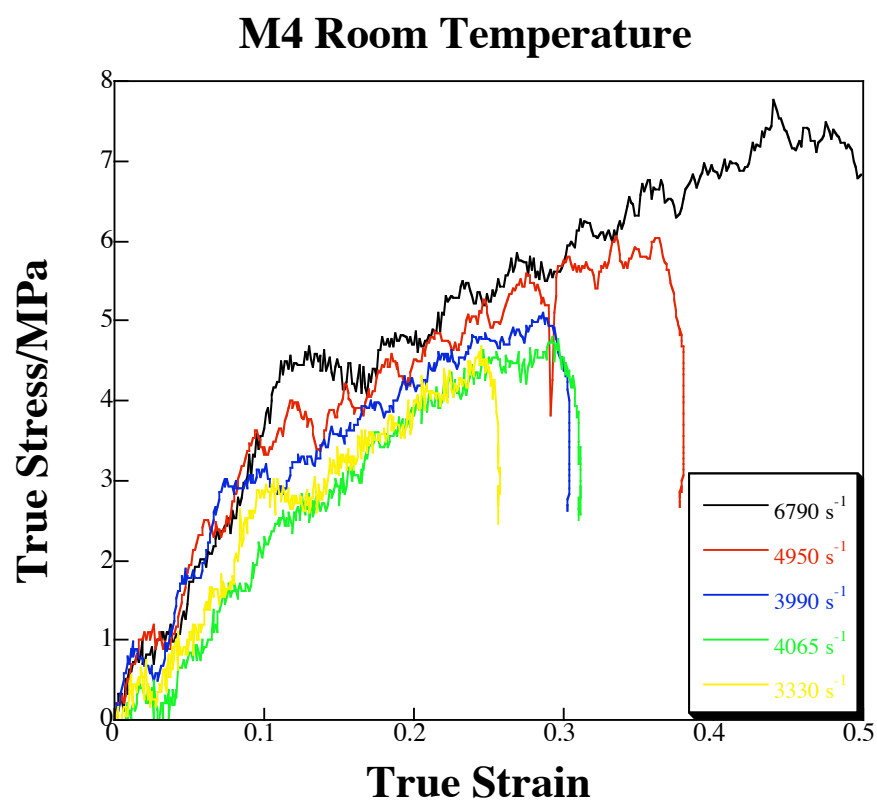


Figure 2.4. SHPB stress-strain curves for 200-300 μm AP/HTPB at 22 °C.

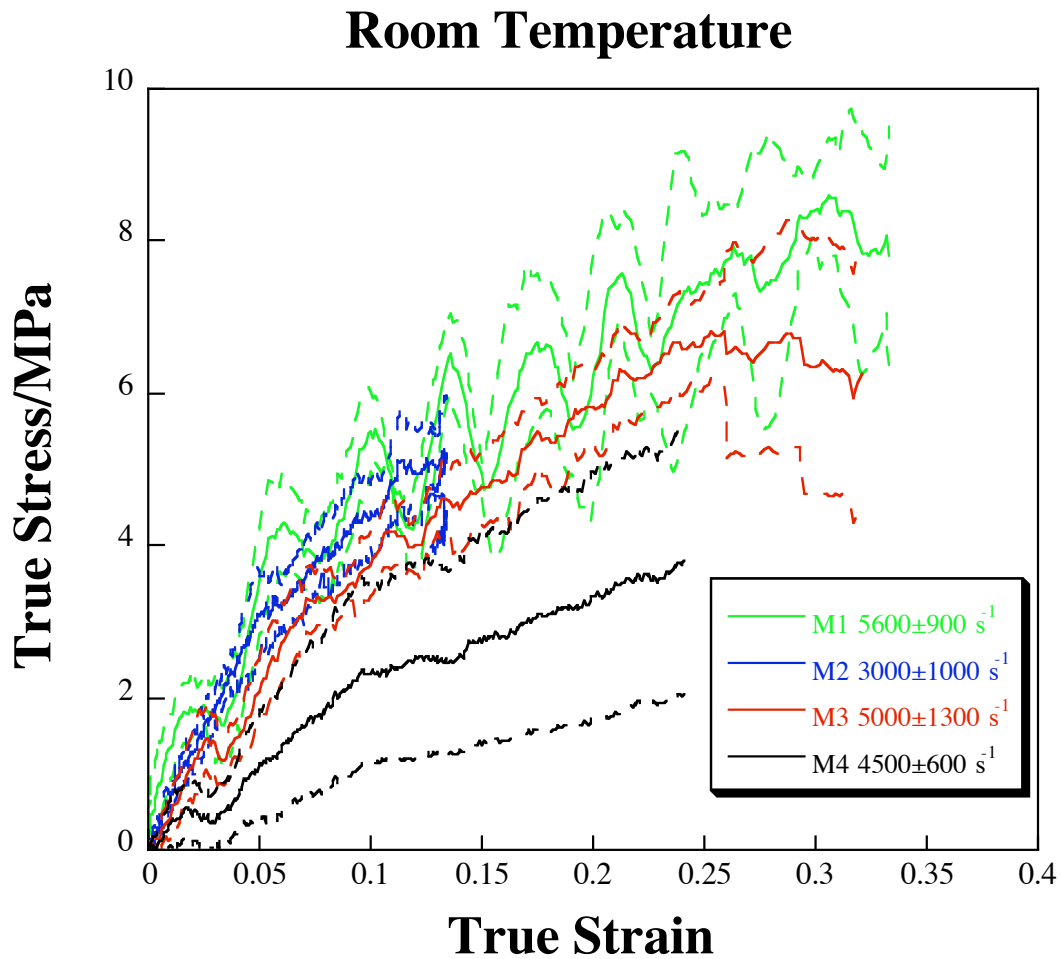


Figure 2.5. Average SHPB stress-strain curves for all the AP/HTPB compositions at 22 °C. Dotted lines indicate standard deviation of the data.

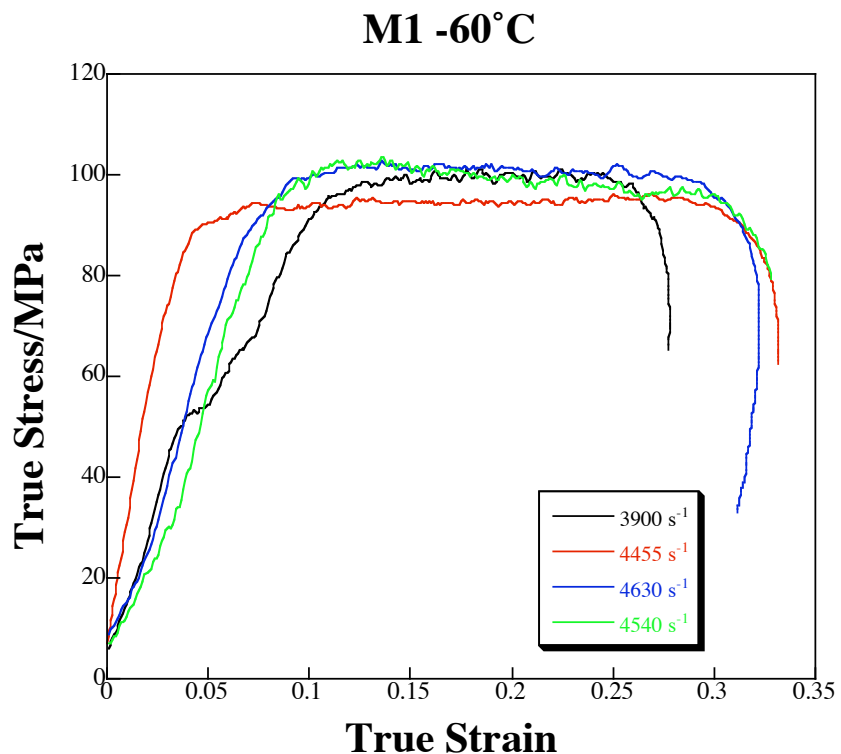


Figure 2.6. SHPB stress-strain curves for 3mm AP/HTPB at -60 °C.

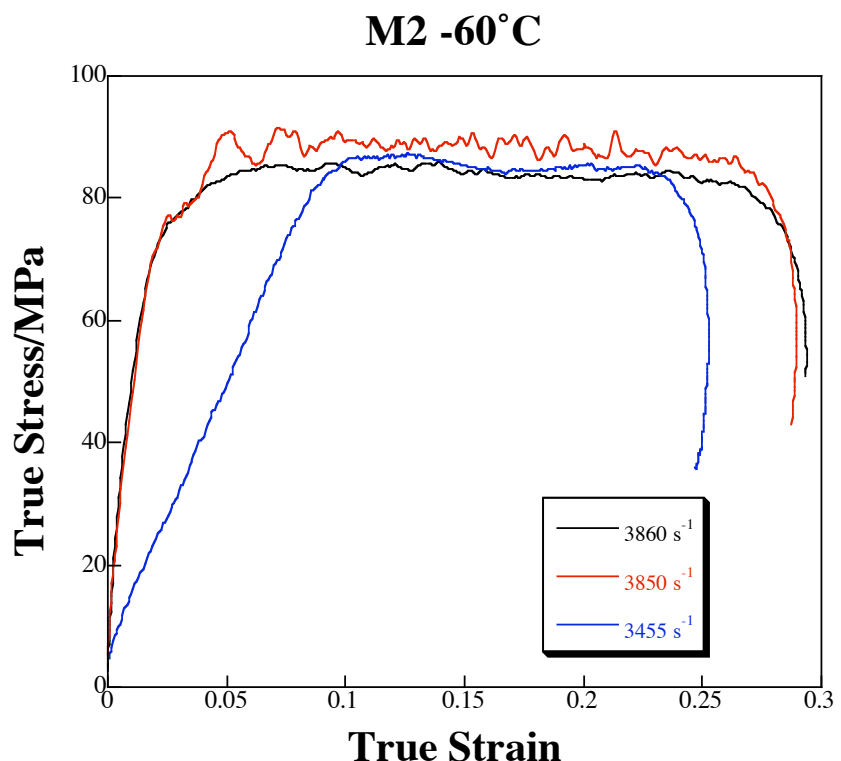


Figure 2.7. SHPB stress-strain curves for 8mm AP/HTPB at -60 °C.

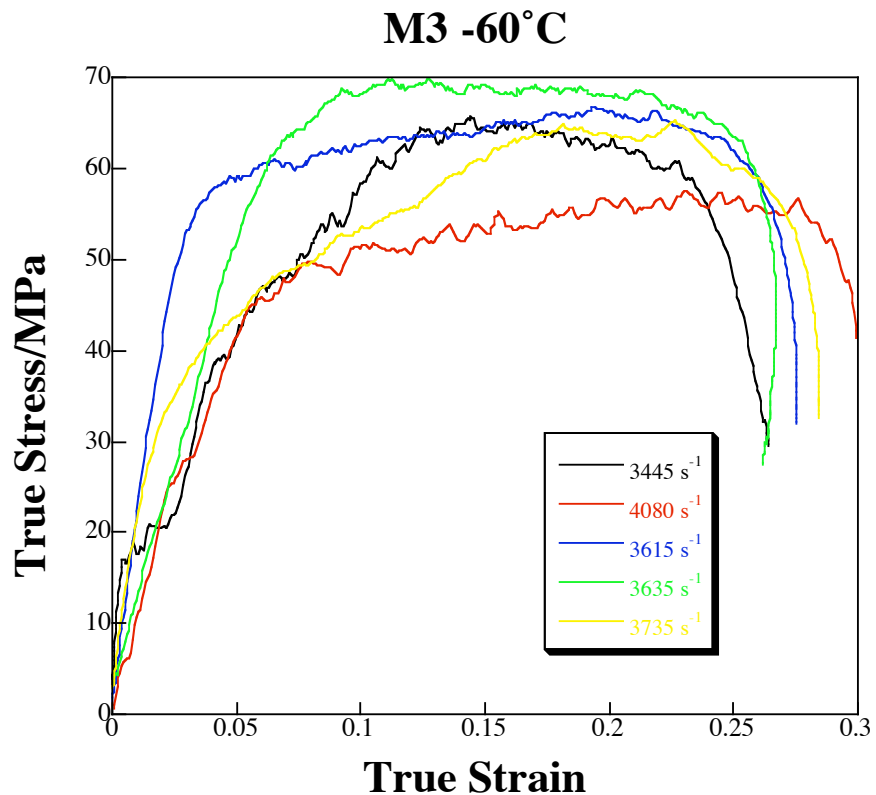


Figure 2.8. SHPB stress-strain curves for 30 μ m AP/HTPB at -60 °C.

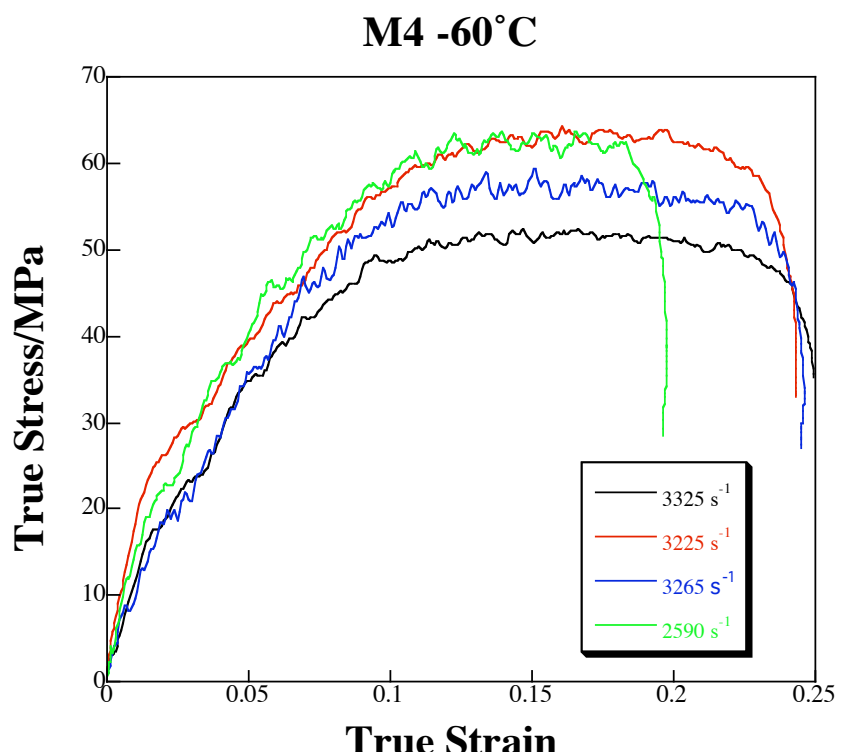


Figure 2.9. SHPB stress-strain curves for 200-300 μ m AP/HTPB at -60 °C.

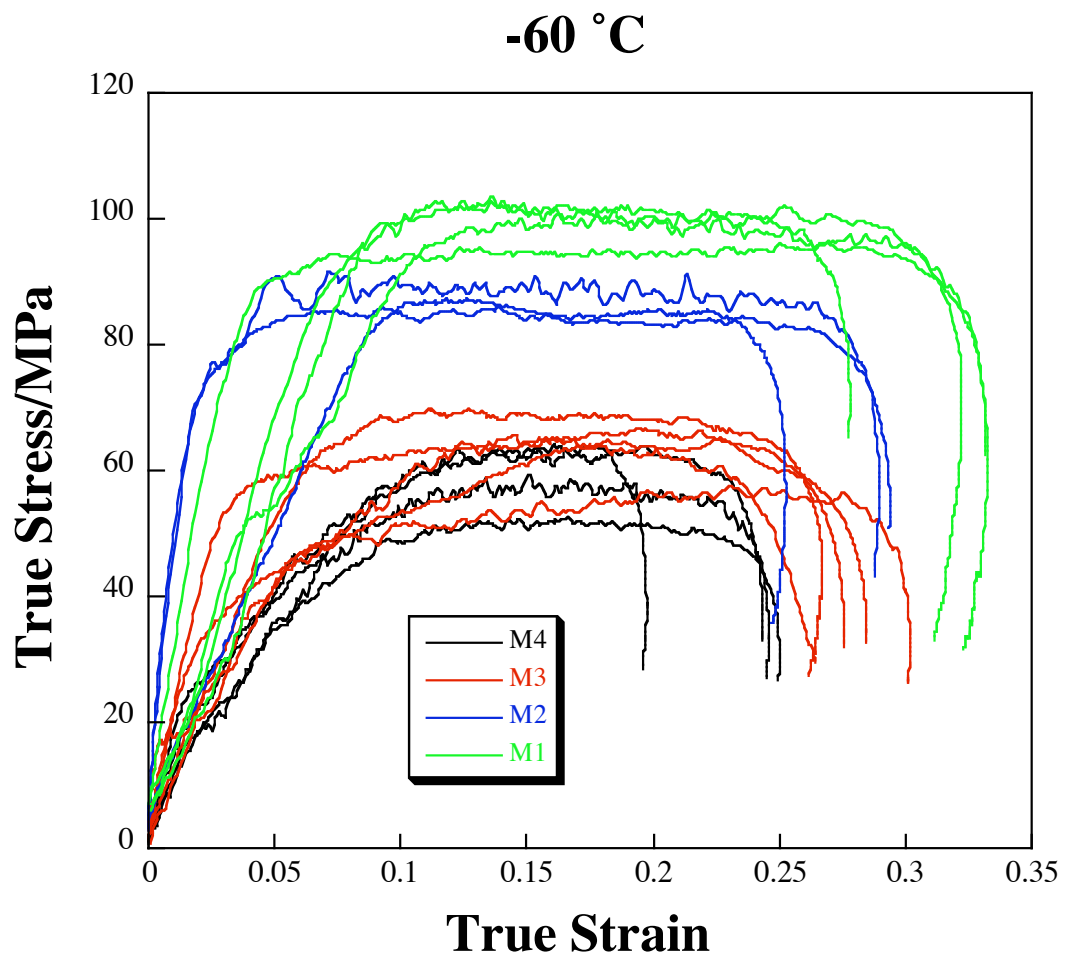


Figure 2.10. All the stress-strain curves for all four compositions at -60°C

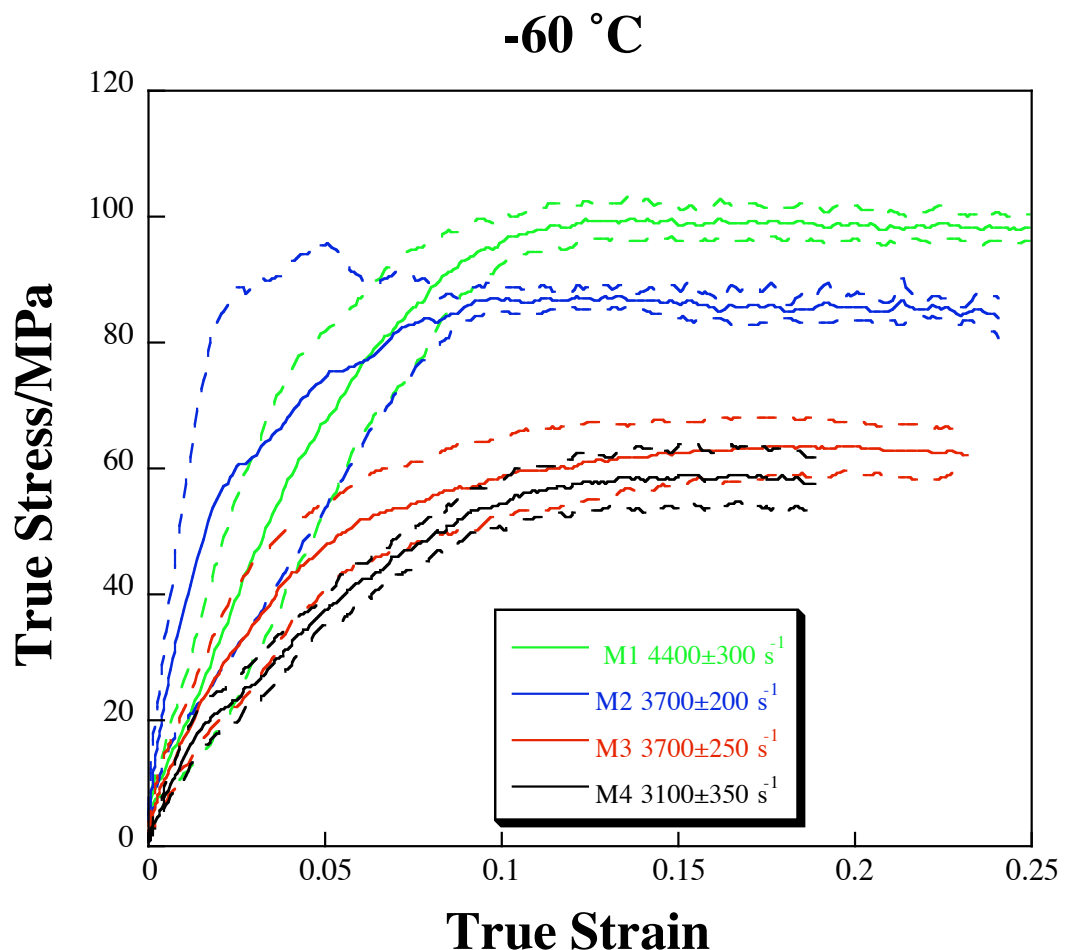


Figure 2.11. Average SHPB stress-strain curves for all the AP/HTPB compositions at -60 °C. Dotted lines indicate standard deviation of the data.

3. DEVELOPMENTS IN HOPKINSON BAR INSTRUMENTATION

3.1 INTRODUCTION

Two new techniques were applied for taking measurements on specimens in our split Hopkinson pressure bar (SHPB). These are: (i) Digital Speckle Metrology (DSM) for measurement of whole specimen deformation, and (ii) a line laser for measurements of specimen diameter.

This section is divided into three parts. The first part is a discussion of some aspects of Hopkinson bar testing, in particular the assumptions behind the Hopkinson bar equations and the limitations of these assumptions. The equations themselves will not be reproduced, they are available in a number of reviews e.g. Gray III (2000). Discussions of the problems of testing soft materials, and PBXs in particular are also available in the literature (Gray III and Blumenthal 2000; Sivior *et al.* 2003). The second part consists of a discussion for some new ideas for instrumenting the SHPB: these will address some of the issues raised. Examples of experiments carried out using the new instrumentation are then presented in the third part.

It should be remembered that the SHPB is an excellent, and versatile, piece of apparatus. The quality of results produced by the system is high, and if the limitations are known, then very useful data can be obtained. Some of these data are presented at the end of this chapter, and represent some of the recent results from PBX materials.

3.2 THE HOPKINSON BAR EQUATIONS

When the standard Hopkinson bar equations are used to calculate sample stress and strain from the output of gauges on the bars themselves, the values calculated have the following features:

The strain is calculated using the displacement of the sample/input bar interface. This means that the strain is effectively an average through the specimen thickness. No measurement of inhomogeneities in the specimen deformation is possible using this technique. Further assumptions of this method are that the specimen is in force equilibrium and that the lubrication is perfect so that there is no barrelling. Whilst equilibrium can be checked by comparing the input and output bar force-time traces, and lubrication is available that reduces friction of polymer-based materials to zero (Briscoe and Nosker 1984; Walley *et al.* 1989, 1991), it would be advantageous to be able to obtain data from inhomogeneous specimens, or those that are brittle or are foams, that do not necessarily reach a constant strain state during the experiment. It would also be useful to be able to measure strain fields so that elastic properties might possibly be determined.

The stress is measured using the force transmitted to the output bar. It should be noted that force is conserved at all the boundaries in the system (Parry *et al.* 1994). If the specimen is in mechanical equilibrium, and if also no barrelling occurs, the

force in the output bar is a direct measure of the force throughout the specimen and hence a measure of the stress in the material. These conditions are required for the calculations to be valid, and more importantly they are required if we are to measure a material property, rather than a specimen-specific property (geometry dependent). Of course, if the experiments are being used to validate finite element models, specimen-specific properties are just as valid as material properties.

The standard Hopkinson bar equations allow two types of stress calculation to be carried out. If the sample does not conserve volume, because, for example, it is a foam, then engineering stress may be calculated by dividing the transmitted force by the original area of the specimen (Zhao 1997; Zhao and Gary 2002). If the sample does conserve volume, the true stress may be calculated. Here the calculated strain is used to derive the new specimen area. Again, mechanical equilibrium, and zero barrelling is assumed (Gray III 2000). It should be remembered that elastic deformation does not usually conserve volume, even in materials where plastic deformation does. This introduces an inaccuracy in the stress measurements. However this will often be small (a few percent), since the yield point usually occurs at a low strain.

Currently it is not possible to measure elastic properties of samples accurately using the SHPB although there have been a number of recent attempts (Chen *et al.* 2003). This is for a number of reasons. Wave dispersion means that elastic strains measured at the gauge locations are not exactly the same as those actually at the sample. This has a negligible effect on the measured flow stress, but has a large effect on the slope of the initial rising part of the force-time curve (Gary 2001). Figure 3.1 shows the effect of dispersion on the incident and reflected force pulses in an Inconel Hopkinson bar with no specimen present. The slope of the initial rise can be seen to become less steep with increasing numbers of reflections (or increased distance travelled). It is possible to correct for dispersion, and a simple way to do this is to calculate the strain using first the incident and transmitted waves, and then the reflected wave, and finally to average the two values obtained. This produces a correction to the strain.

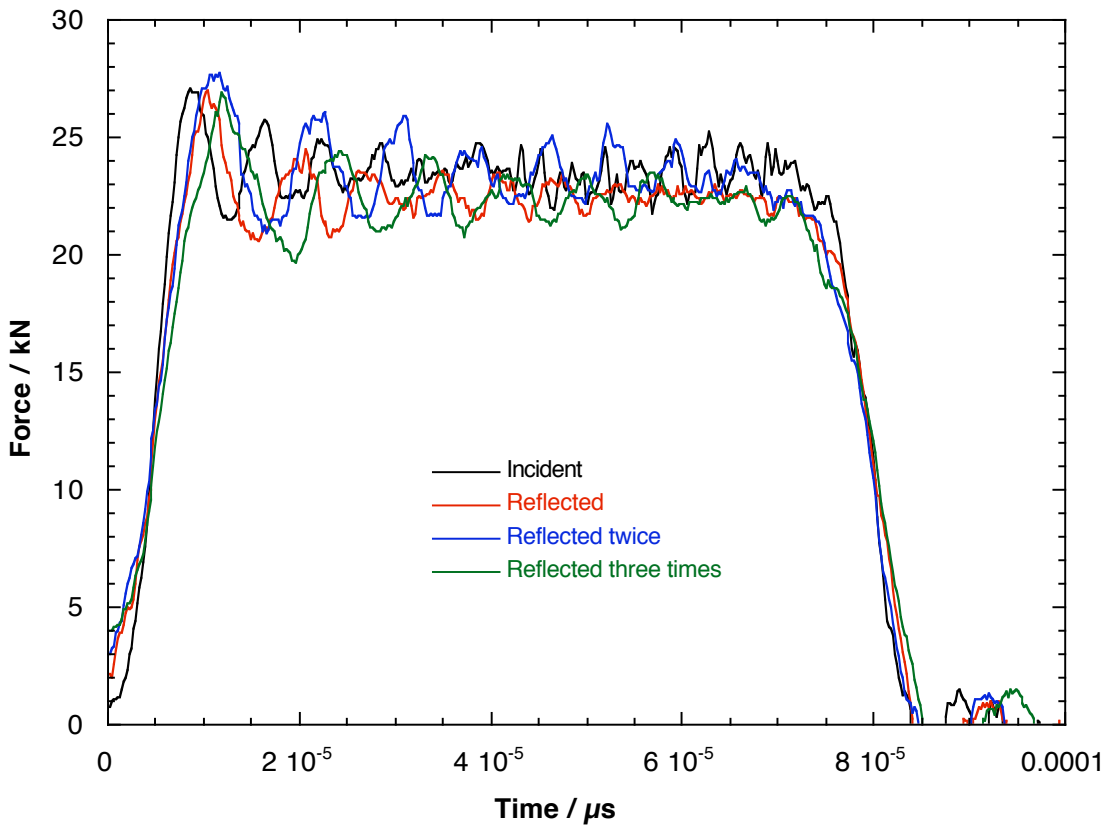


Figure 3.1. The effect of dispersion on the force pulse in an Inconel bar. The ‘reflected’ and ‘reflected twice’ pulses are tensile, and the others compressive, but all the pulses have been made positive for comparison.

However, there are further corrections required. It is always the case that the strain measured will be influenced by the thin layer of lubricant between the bars and the specimen and by any imperfections in the flatness of the specimen ends. These imperfections increase the apparent strain to a value greater than it should be for the stress applied/exerted. They also make it difficult to identify the start of the transmitted pulse accurately because the rise from zero is not sharp (figure 3.2). These will always introduce some error into the measured stress and strain. Also any misalignment between the bars and specimen would also affect the initial slope of the response curve and give an inaccurate modulus. Note though that a small amount of misalignment does **not** affect the measured yield or flow stress.

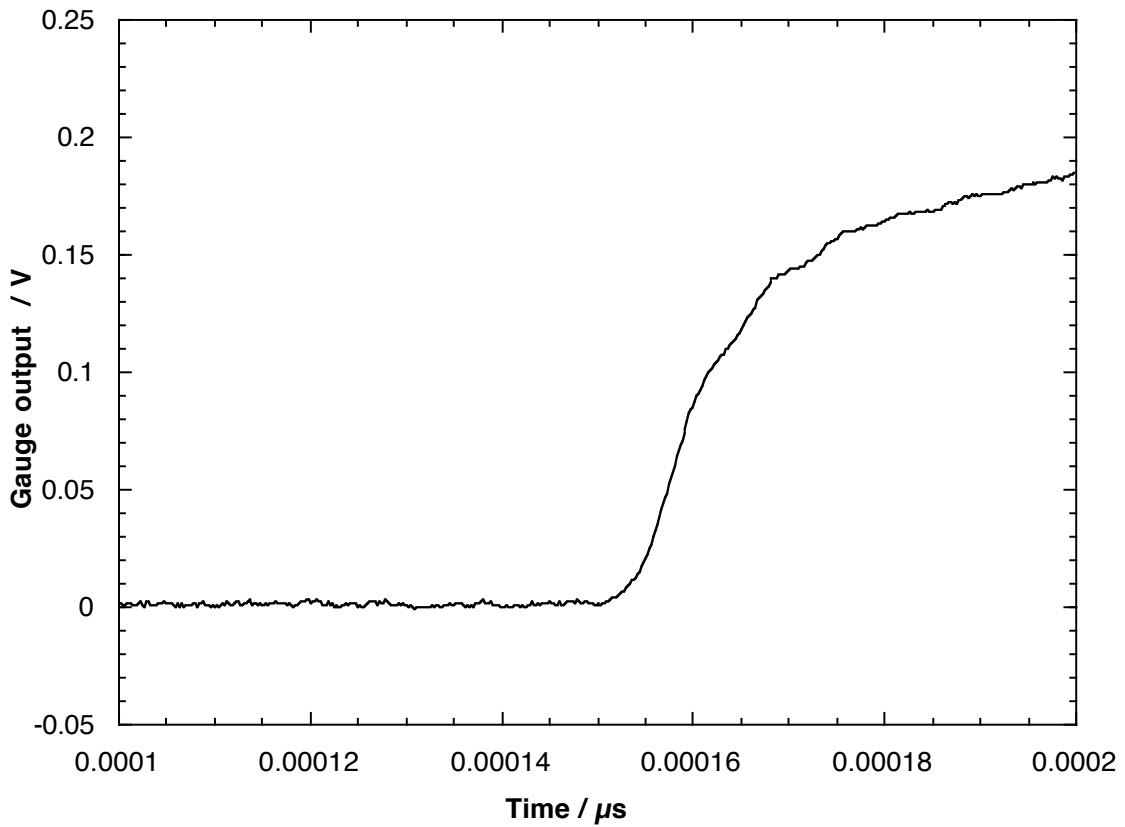


Figure 3.2. The start of the transmitted pulse from a polycarbonate specimen deforming between magnesium alloy bars.

Finally, the sample is not in force equilibrium during the initial rise of the force-time curve.

3.3 IMPROVED INSTRUMENTATION

(a) Digital speckle metrology.

1. Introduction

High-speed photography has often been applied to Hopkinson bar testing, for example to examine specimen deformation (Gorham 1980; Gary *et al.* 1996; Siviour *et al.* 2001). The use of an optical wedge can improve sensitivity for detecting barrelling and plastic wave activity (Gorham 1980). This method can give, for example, useful confirmation of strains calculated using the Hopkinson bar equations (figure 3.3). It can also give indications of failure mechanisms and sample diameter. However, this technique can only be used to measure overall deformations. Digital speckle metrology by contrast is a technique that allows surface deformation fields to be measured. Speckle techniques require a random pattern to be observed on a surface. The random pattern can then be tracked with time using a correlation algorithm providing a measure of both components of displacement between a reference and a deformed image. The resolution of the measurements depends on the size of the speckle pattern, and the resolution of the

camera. The correlation algorithm used in these experiments was originally developed by Sjödahl and Benckert (1993) and Sjödahl (1994).

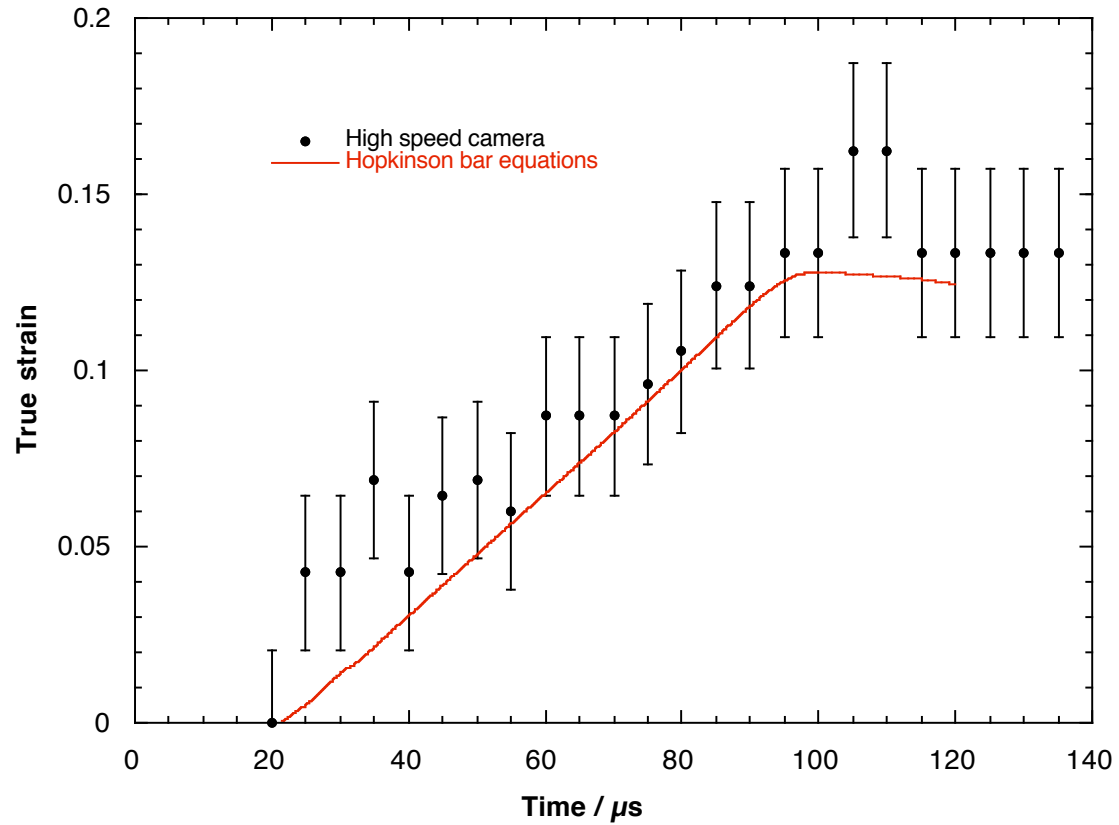


Figure 3.3. Comparison of true strain measurements from a high-speed camera and from the SHPB equations. From Sivior et al. (2001).

2. Experimental method

In the experiments reported here, the random speckle pattern was applied to the sample surface using an airbrush (Rae *et al.* 2002). Experiments were carried out on PBS 9501 in both a traditional compression configuration and in a high-speed Brazilian test. The Brazilian test produces tensile deformation in a compression apparatus. It has the advantage of requiring much smaller samples than a traditional tensile test, which is important when working with explosives. The disk shaped specimen is held between two curved anvils as shown schematically in figure 3.4. The curved nature of the anvils prevents localised strains at the points of contact, and instead ensures that the sample undergoes tensile strain along a line running down its centre.

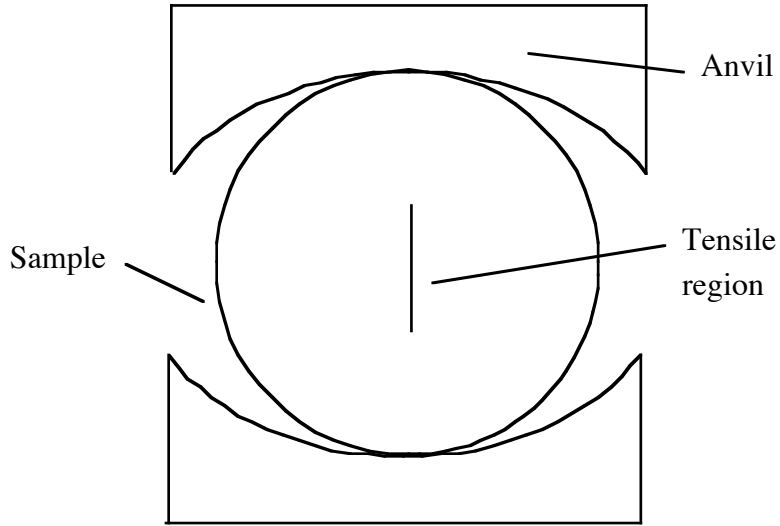


Figure 3.4. Brazilian test configuration

It has been established that if the ratio of the contact half width b between the sample and the anvils to the specimen radius R is greater than 0.27, then the tensile strength of the specimen is independent of b/R (Awaji and Sato 1979). In these experiments, the radius of the specimen is 10mm, that of the anvils is 12.7mm, and b/R has been established to be 0.3. The sample stress can be calculated using the Brazilian test equation:

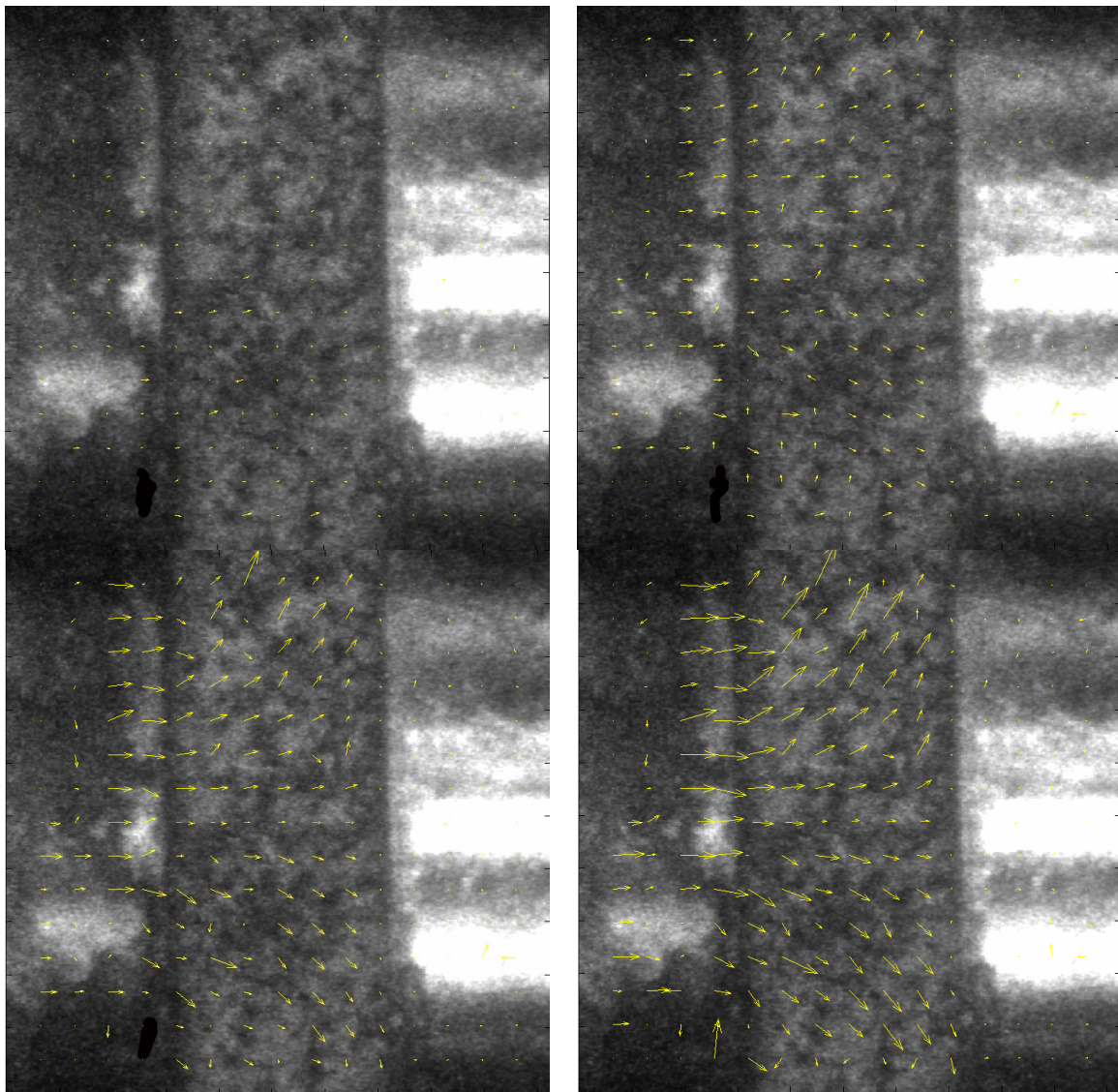
$$\sigma_x = \frac{2P}{D^2 t} \left(\frac{b}{R} \right)^2 , \quad (3.1)$$

where P is the load on the specimen, D its diameter and t its thickness (4mm in this case).

A Hadland Ultra-8 digital high-speed camera (Smith *et al.* 2001) was used for the experiments, with a Pallite VII radial light providing illumination. Use of a digital camera removes the need for fiducial markers to align the different photographs for comparison. The Ultra-8 duplicates the image onto 8 areas of a CCD array, each of which is sampled independently so that each of the 8 images can have completely different delays and exposure times. Before each experiment a set of reference images was taken. Each deformed image was compared to the reference image from the same part of the CCD array. This procedure removes the effect of any possible distortion in the images due to the internal optics of the camera. The exposure time and interframe time between the dynamic images were both set to 20 μ s.

3. Results

A set of displacement quiver plots is shown for PBS 9501 in compression in figure 3.5. Figure 3.6 shows a set of displacement quiver plots from a Brazilian test. These have been presented in the zero momentum frame, i.e. the specimen's frame of reference. The results are very encouraging: there is no strain concentration in the specimen, and the deformation is exactly as seen in a quasi-static experiment. In particular, if the values of strain are taken across the centre of the specimen perpendicular to the loading direction, then the strain across the centre of the sample should be twice the overall strain according to theory. This is shown indeed to be the case in figure 3.7. Values of stress against time are shown in figure 3.8, where it can be seen that the yield stress is about 8 MPa.



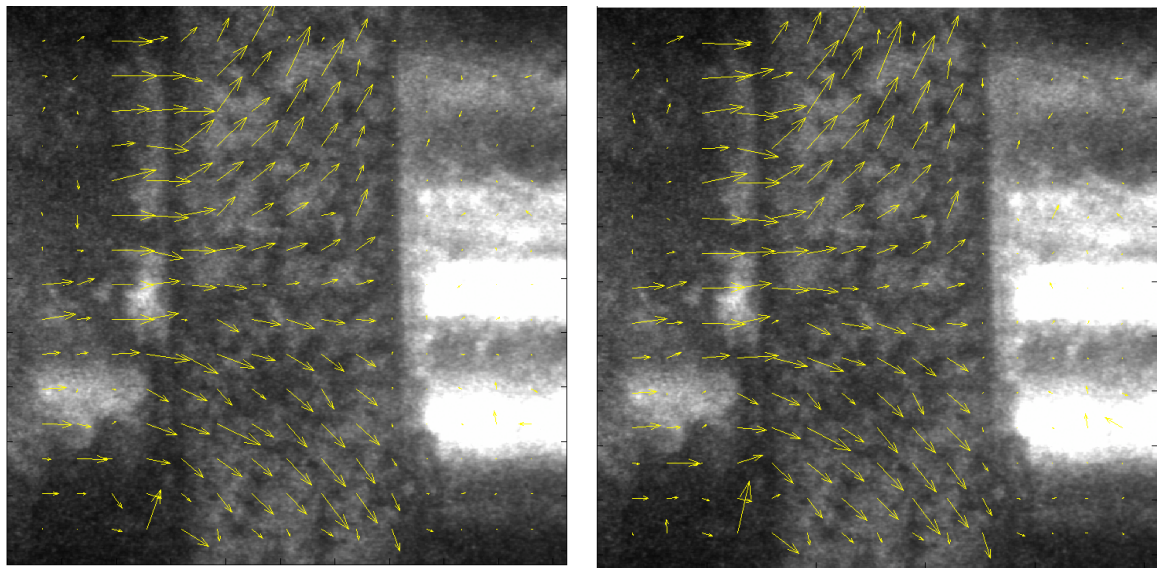


Figure 3.5. Displacement quiver plots for a compression experiment on PBS9501.

The length of the arrows is proportional to the displacement at their bases.

Note that there are arrows on both the input bar and the specimen.

In the sixth frame, the arrows right at the end of the bar
(third column of arrows from the left) are 0.67mm long.

Frame order is;

1	2
3	4
5	6

The first exposure was taken before the start of the loading, which was about 80 μ s in length, so the last exposure was taken at the end of the loading

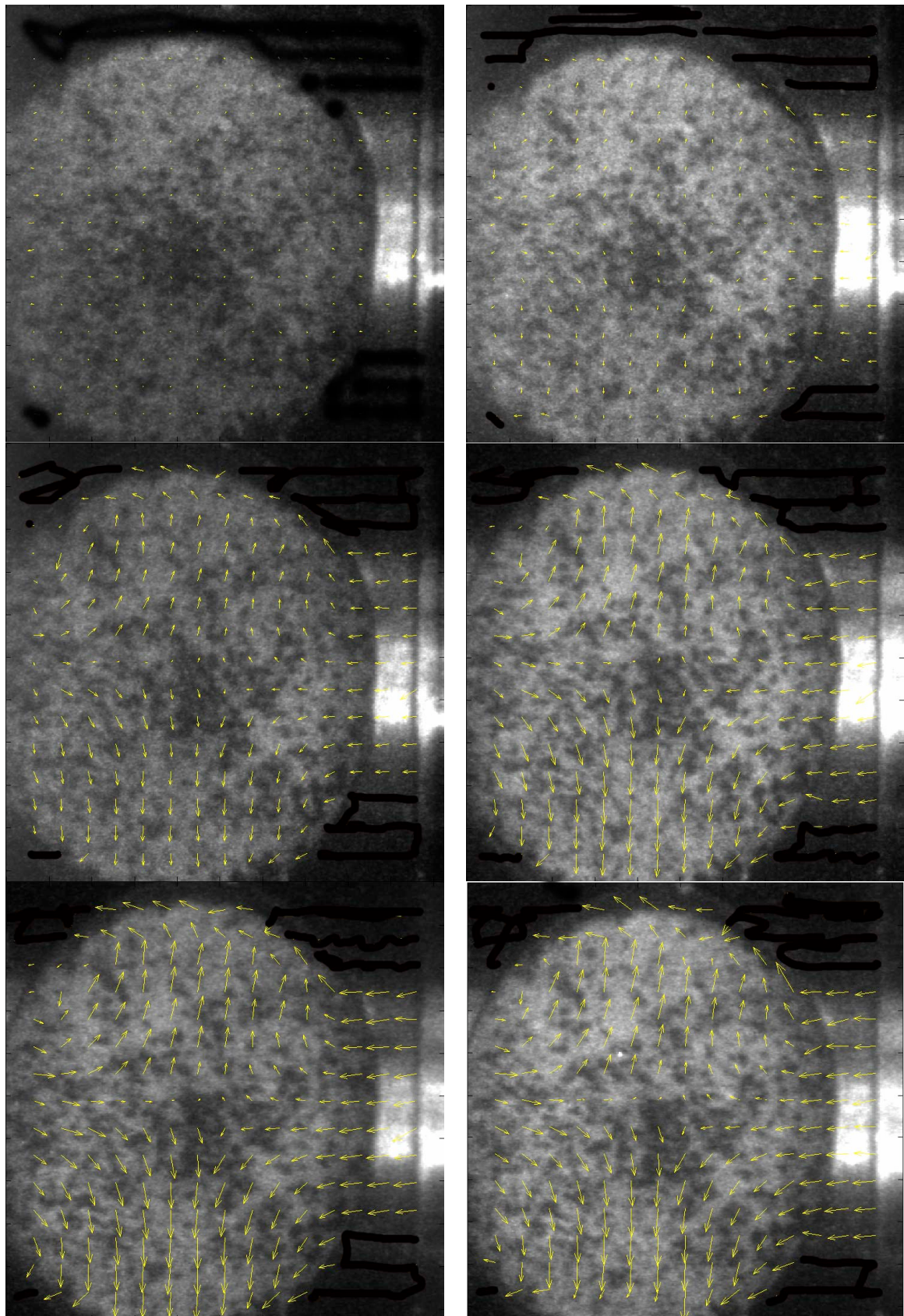


Figure 3.6. Displacement quiver plots for a Brazilian experiment on PBS9501.
Frame order as above.

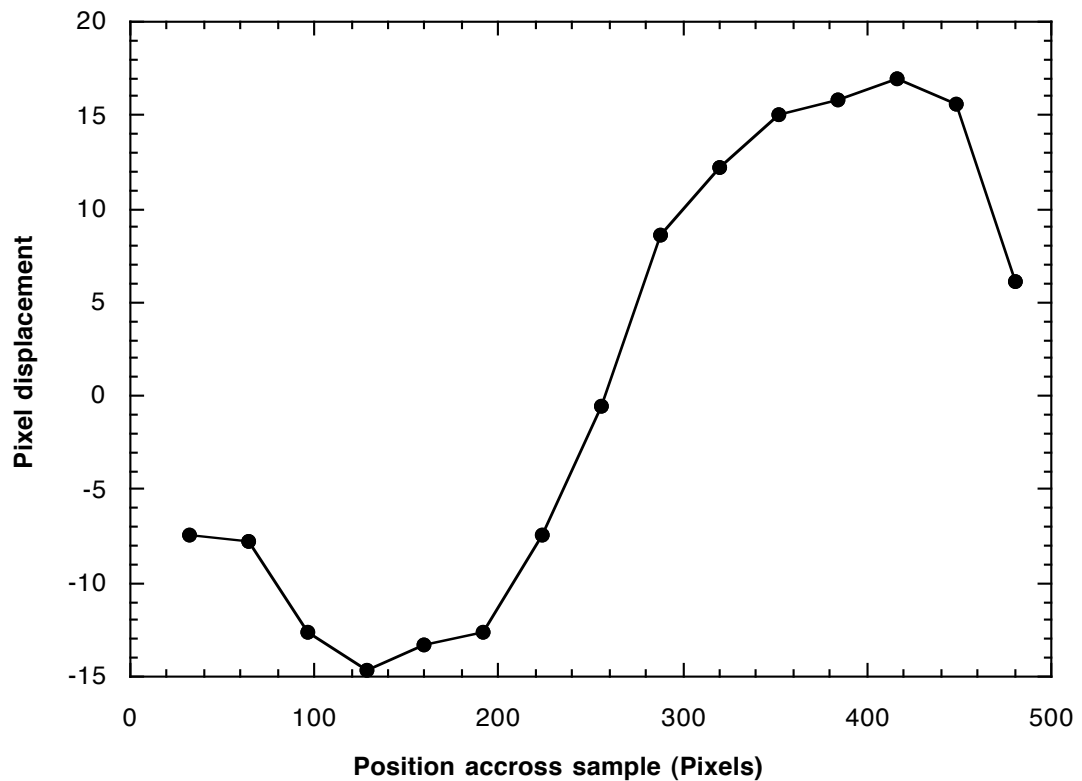


Figure 3.7. Displacement across the centre of Brazilian test sample, perpendicular to bar motion

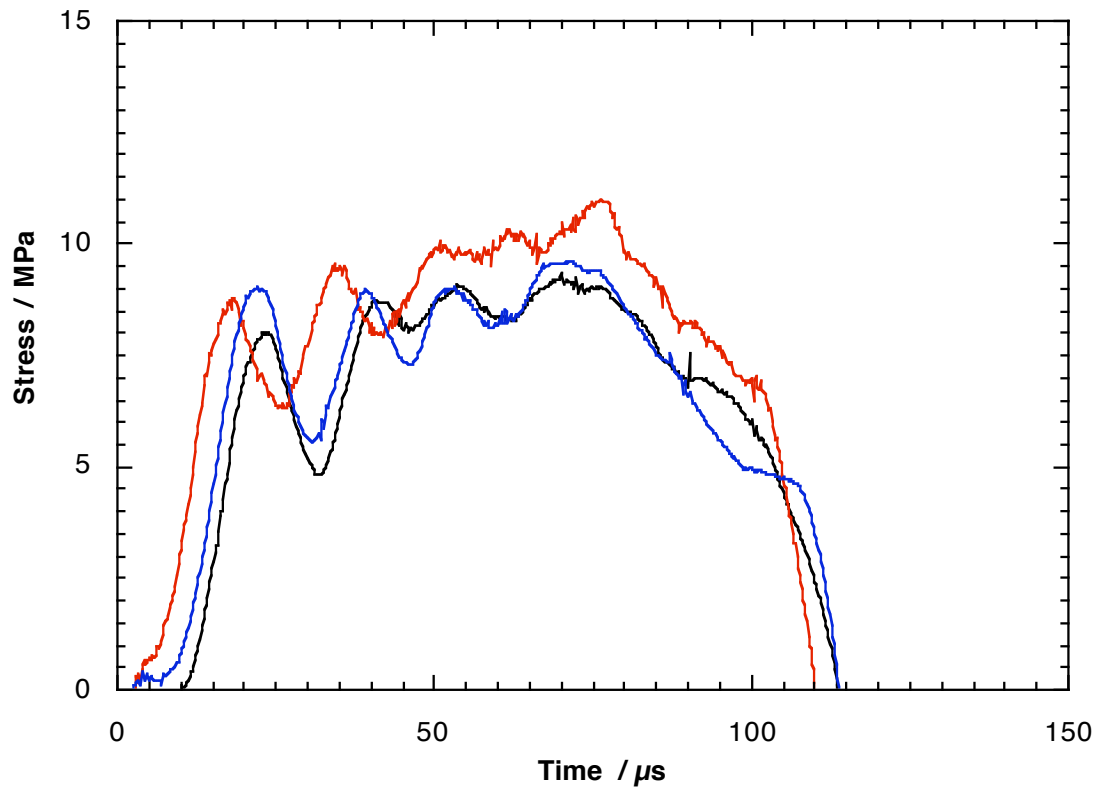


Figure 3.8. Tensile stress in three Brazilian test specimen, at a rate of 650 s^{-1}

4. Conclusions

PBS 9501

The results are very encouraging, showing uniform sample deformation throughout the sample. There were two major problems in performing these experiments. The first was illumination. In these experiments, the exposure time had to be 20 μ s. If a brighter light source were available, this could be dropped down to 5 μ s. It might then be possible to measure the elastic properties of long specimens by observing stress waves moving through them and comparing this to the output forces measured. Using longer specimens would also minimise the effects of friction and the roughness of the specimen ends. It is possible to calculate strain through a specimen by fitting a plane to a three dimensional plot of displacement against position in pixel space. However, there are difficulties with this at present due to the small number of measurements through the thickness of the specimen. By better use of the camera's image size, the number of measurements could probably be doubled in future experiments.

Brazilian test

The results from the Brazilian tests are very encouraging indeed. The first reference to such a test at high-speed was by Gomez *et al.* (2002) (we had earlier performed quasistatic Brazilian experiments on PBXs using curved anvils; Palmer *et al.* 1993). However, Gomez *et al.* (2002) used flat anvils and therefore found a large stress concentration at the edges of the specimen. In the present study, there was no such stress concentration in the specimen and all the results indicated that the test is valid. The sample shape is also ideal for optimal utilisation of the camera, and a large number of measurement points are possible. Extension of this test into the high strain-rate regime will permit a useful extension to the large amount of Brazilian testing that is currently performed at low strain rates. This work has now made it possible for tensile properties to be safely compared over a much wider range of rates than before. The problem of long exposures is not an issue for the Brazilian test as it is for uniaxial compression as there is no desire to obtain elastic properties by this method.

(b) Line laser measurements

This method was first described by Swantek *et al.* (2001). It allows the diameter of the sample to be measured directly during the experiment and removes the need to assume volume conservation to calculate true stress. Conversely, it also allows volume conservation to be evaluated. The original paper quotes an accuracy of 2% for the measurements. A line laser system has been developed in our laboratory, and some preliminary evaluation experiments have been carried out which are described here.

The system is shown in figure 3.9. A line laser and slit are used to produce a narrow, vertical line of light. The width can be adjusted, but is of the order 1mm. This line is then focused onto a photodiode by the lens. The specimen sits inbetween the slit and the lens, and causes a shadow. The size of the shadow and therefore the amount of light reaching the photodiode are determined by the diameter of the sample. The photodiode then gives an output voltage that depends on the amount of light, and this can be calibrated for different sample diameters, for a given slit width.

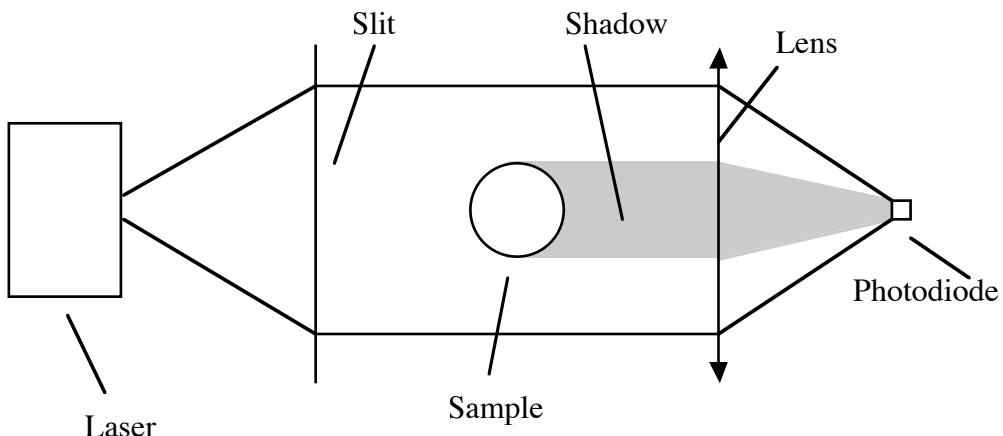


Figure 3.9. Schematic diagram of the use of a line laser to measure specimen diameter

Two calibration curves are shown in figure 3.10. Practically it is best to consider the voltage output relative to a baseline taken as that for the unobstructed case, i.e.

$d=0$. In fact, if the ratio $\frac{\text{voltage change}}{\text{unobstructed voltage}}$ is used, a master curve can be

obtained that is independent of slit width. Unfortunately, a best-fit line from this curve is less accurate than determining the curves for the different slit widths independently. Calibration is a simple process anyway and it is better to produce a calibration for the desired slit width. The radial true strain should be half that of the longitudinal strain if the sample conserves volume, and so the results from the photodiode were doubled for comparison with the Hopkinson bar equations.

Figure 3.11 shows typical curves obtained using a dural sample. The voltage output of the photodiode is shown in figure 3.11a, and then in 3.11b and c curves of measured sample strain against time are compared to that calculated from the

Hopkinson bar equations. The results are encouraging at this stage. However the sudden and very large increase in strain (figure 3.11*c*) has not been accounted for. It may be because the end of the bar protrudes into the laser beam or because of a problem with the photodiode. It is unlikely to be a true effect because the recovered specimen only showed 0.2 true strain. Further work will investigate the response of the photodiode and the possibility of narrowing the beam to prevent this problem.

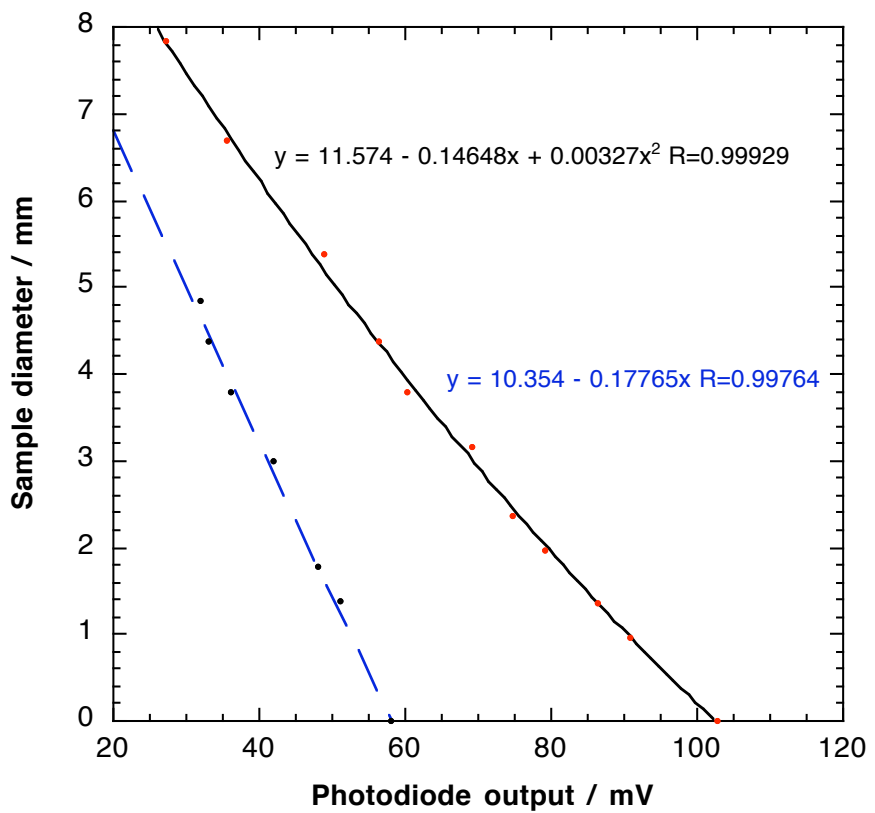


Figure 3.10. Calibration of the line laser. Two slit widths are shown.

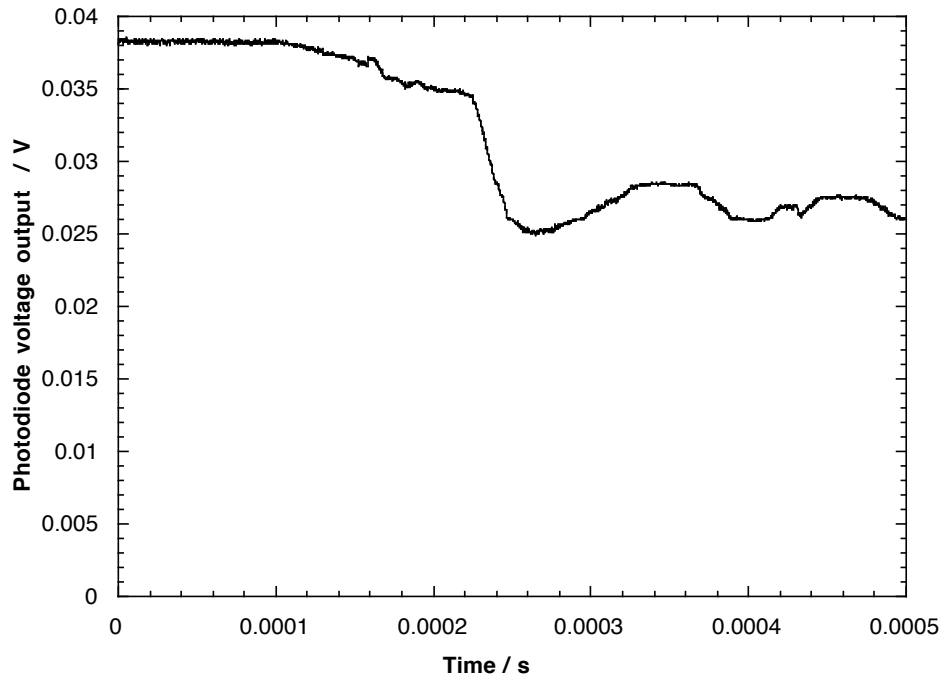


Figure 3.11a. Voltage output from the photodiode

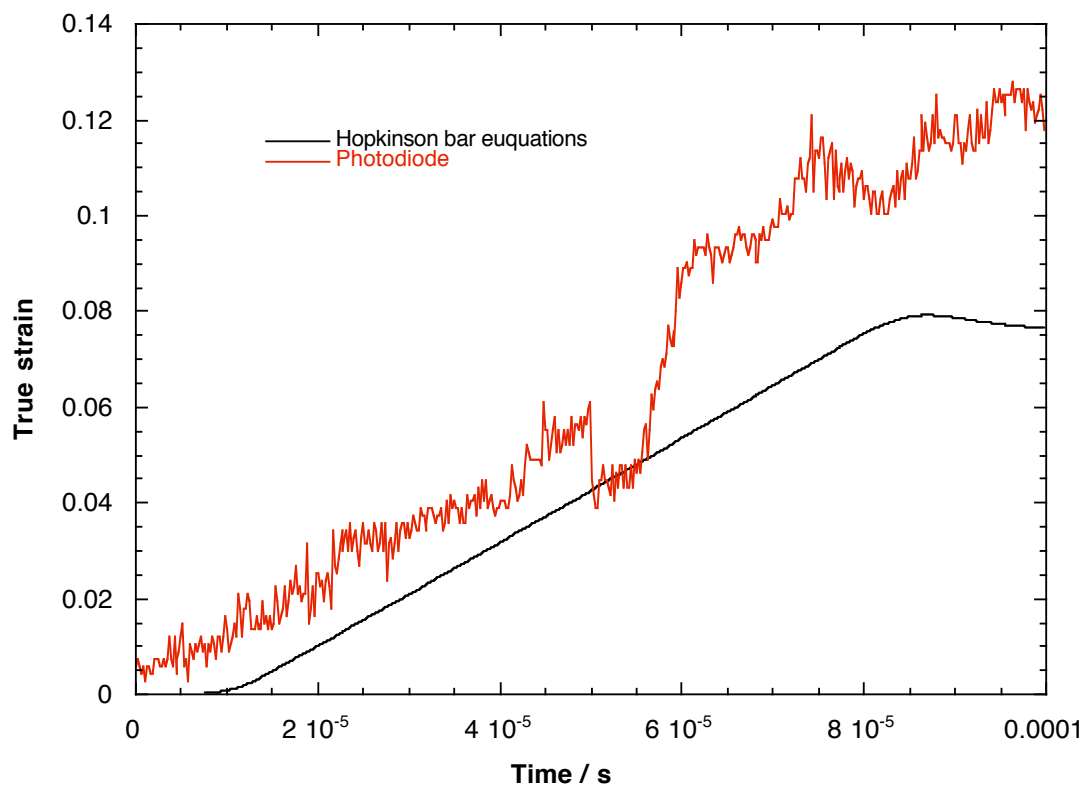


Figure 3.11b. Comparison of true strains calculated from the photodiode output and Hopkinson bar equations. Note that the radial strain calculated from the photodiode has been doubled for comparison with the equations.

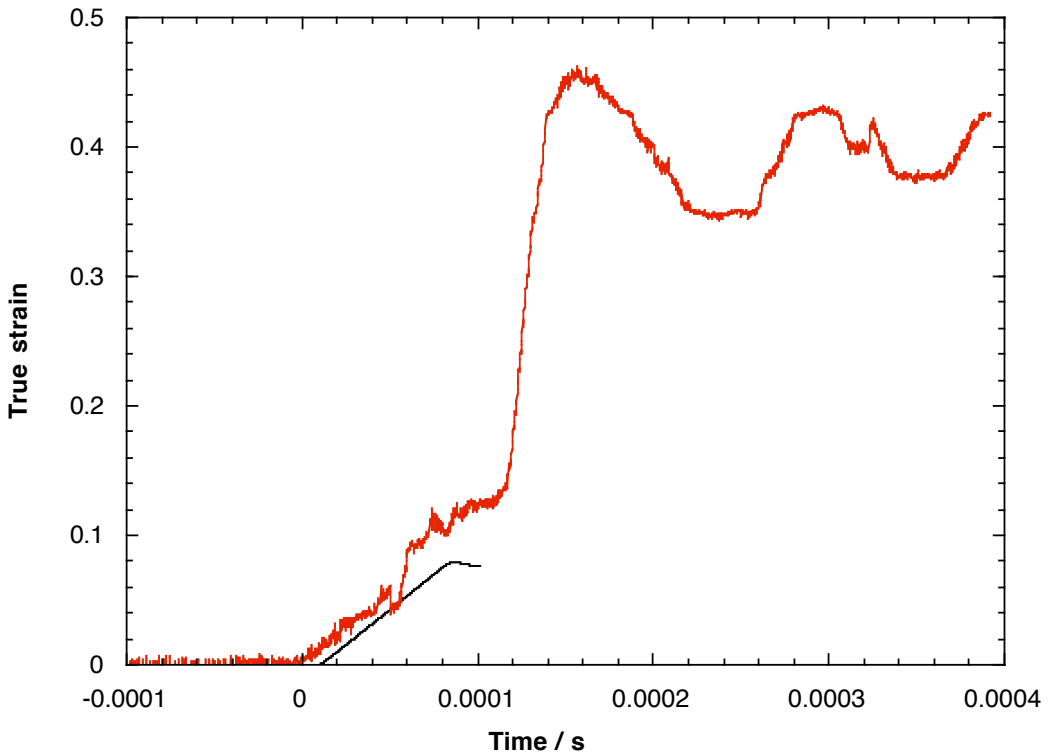


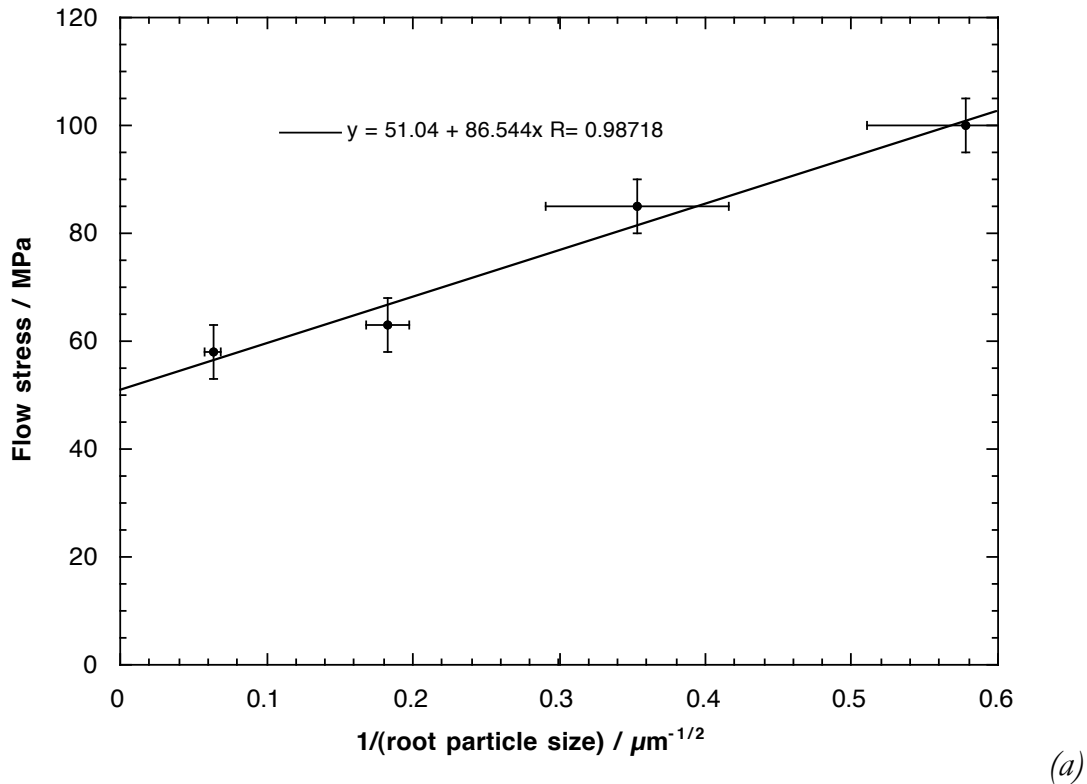
Figure 3.11c. True strain against time plot for the photodiode. Showing the large increase, possibly caused by the bars interfering with the laser beam.

(c) Results obtained on PBXs

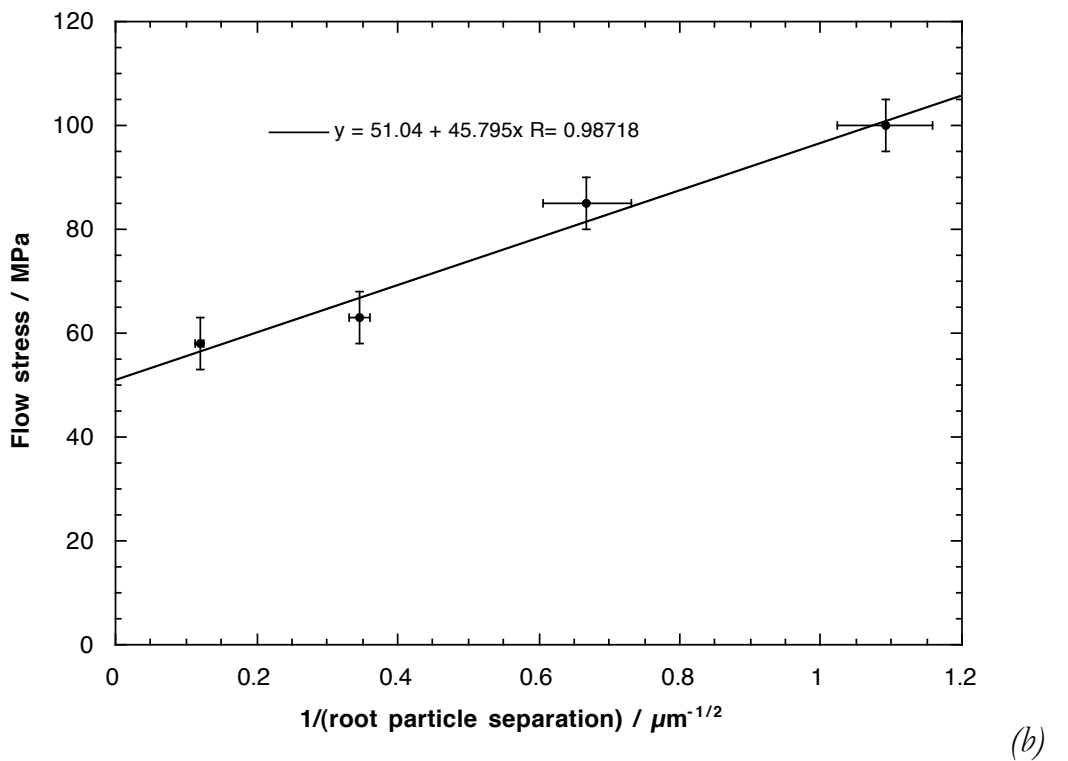
Over the last year, two major sets of experiments have been performed in the SHPB on PBX compositions. Further analysis has been performed on the results obtained from the AP/HTPB compositions. The AP/HPTB PBX in particular allowed an investigation of the effect of particle size/loading density on the mechanical properties of the PBX. The grain size effect in PBXs was first noticed by Field *et al.* (1985). Since that data was published, it has been observed that the effect is made more prominent by lowering the temperature at which the experiments are carried out (Balzer 2001; Balzer *et al.* 2003). The AP/HTPB PBX used consisted of 66% ammonium perchlorate and 33% HTPB by mass. This was available in four different grain sizes: M1=30 μ m, M2=80 μ m, M3=300 μ m and M4=200-300 μ m. The low temperature study was carried out using our Inconel bar system (the mechanical impedance of Inconel is only a weak function of temperature, so the temperature gradient does not distort the elastic wave pulse travelling through it; Kandasamy and Brar 1994, 1995). Cooling was performed by surrounding the ends of the bars with a chamber into which helium gas was passed that had been cooled using liquid nitrogen. The temperature was monitored using chromel-alumel thermocouples. The results of this study in the form of stress-strain curves were presented in chapter 2.

Figure 3.12 shows that the effect of particle size on the flow stress of the material is linear in either $1/\sqrt{d}$ or in $1/\sqrt{s}$ where d is the particle size, and s is the particle

separation. Note that these two parameters are connected for a given loading density, and in order to distinguish between them, experiments are required on materials with different loading densities.



(a)



(b)

Figure 3.12. (a) Relationship between flow stress and reciprocal of square root of particle size for AP/HTPB compositions at -60°C .

(b) Plot of flow stress against reciprocal of square root of particle separation for AP/HTPB compositions at -60°C

3.4 REFERENCES

Awaji, H. and Sato, S. (1979) "Diametral compressive testing method" *Trans. ASME: J. Engng Mater. Technol.* **101** 139-147

Balzer, J.E. (2001) "Low-level impact loading of explosives", PhD thesis, Univ. of Cambridge

Balzer, J.E., Sivior, C.R., Walley, S.M., Proud, W.G. and Field, J.E. (2003) "Behaviour of ammonium perchlorate-based propellants and a polymer-bonded explosive under impact loading" *Proc. R. Soc. Lond. A* (accepted for publication)

Briscoe, B.J. and Nosker, R.W. (1984) "The influence of interfacial friction on the deformation of HDPE in an SHPB" *Wear* **95** 241-262

Chen, W., Song, B., Frew, D.J. and Forrestal, M.J. (2003) "Dynamic small strain measurements of a metal specimen with a split Hopkinson pressure bar" *Exper. Mech.* **43** 20-23

Field, J.E., Palmer, S.J.P., Pope, P.H., Sundararajan, R. and Swallowe, G.M. (1985) "Mechanical properties of PBX's and their behaviour during drop-weight impact" in "Proc. Eighth Symposium (Int.) on Detonation", ed. J.M. Short, publ. White Oak, Maryland, USA, Naval Surface Weapons Center: pp. 635-644.

Gary, G. (2001) "Study of some aspects of dynamic testing with bars" in "New Experimental Methods in Material Dynamics and Impact", ed. W.K. Nowacki and J.R. Klepaczko, publ. Warsaw, Poland, Institute of Fundamental Technological Research: pp. 179-221.

Gary, G., Rota, L. and Zhao, H. (1996) "Testing viscous soft materials at medium and high strain rates" in "Constitutive Relation in High/Very High Strain Rates", ed. K. Kawata and J. Shioiri, publ. Tokyo, Springer-Verlag: pp. 25-32.

Gomez, J.T., Shukla, A. and Sharma, A. (2002) "Photoelastic evaluation of stress fields and fracture during dynamic splitting experiments" *J. Test. Eval.* **30** 186-196

Gorham, D.A. (1980) "Measurement of stress-strain properties of strong metals at very high strain rates" *Inst. Phys. Conf. Ser.* **47** 16-24

Gray III, G.T. (2000) "Classic split-Hopkinson pressure bar testing" in "ASM Handbook. Vol. 8: Mechanical Testing and Evaluation", ed. H. Kuhn and D. Medlin, publ. Materials Park, Ohio, ASM International: pp. 462-476.

Gray III, G.T. and Blumenthal, W.R. (2000) "Split-Hopkinson pressure bar testing of soft materials" in "ASM Handbook. Vol. 8: Mechanical Testing and Evaluation", ed. H. Kuhn and D. Medlin, publ. Materials Park, Ohio, ASM International: pp. 488-496.

Kandasamy, R. and Brar, N.S. (1994) "Flow stress and material model study at high strain rate and low temperature" in "High Pressure Science and Technology 1993", ed. S.C. Schmidt, J.W. Shaner, G.A. Samara and M. Ross, publ. New York, American Institute of Physics: pp. 1031-1034.

Kandasamy, R. and Brar, N.S. (1995) "Low temperature and strain sensitivity of steel and aluminum" *Exper. Mech.* **35** 119-123

Palmer, S.J.P., Field, J.E. and Huntley, J.M. (1993) "Deformation, strengths and strains to failure of polymer bonded explosives" *Proc. R. Soc. Lond. A* **440** 399-419

Parry, D.J., Dixon, P.R., Hodson, S. and Al-Maliky, N. (1994) "Stress equilibrium effects within Hopkinson bar specimens" *J. Phys. IV France* **4** Colloq. C8 (DYMAT 94) 107-112

Rae, P.J., Palmer, S.J.P., Goldrein, H.T., Field, J.E. and Lewis, A.L. (2002) "Quasi-static studies of the deformation and failure of PBX 9501" *Proc. R. Soc. Lond. A* **458** 2227-2242

Siviour, C.R., Walley, S.M., Proud, W.G. and Field, J.E. (2001) "Are low impedance Hopkinson bars necessary for stress equilibrium in soft materials?" in "New Experimental Methods in Material Dynamics and Impact", ed. W.K. Nowacki and J.R. Klepaczko, publ. Warsaw, Poland, Institute of Fundamental Technological Research: pp. 421-427.

Siviour, C.R., Walley, S.M., Proud, W.G. and Field, J.E. (2003) "Hopkinson bar studies on polymer bonded explosives" in "Proc. 6th Seminar on New Trends in Research of Energetic Materials", ed. J. Vágenknecht, publ. Pardubice, Czech Republic, University of Pardubice: pp. 338-349.

Sjödahl, M. (1994) "Electronic speckle photography: Increased accuracy by non-integral pixel shifting" *Appl. Opt.* **33** 6667-6673

Sjödahl, M. and Benckert, L.R. (1993) "Electronic speckle photography: Analysis of an algorithm giving the displacement with subpixel accuracy" *Appl. Opt.* **32** 2278-2284

Smith, G.W., Riches, M.J., Huxford, R.B., Smith, P.A., Seymour, C.L.G. and Bell, J.D. (2001) "Ultra: A new approach to ultrahigh-speed framing cameras" *Proc. SPIE* **4183** 105-118

Swantek, S.D., Wicks, A.L. and Wilson, L.T. (2001) "An optical method of strain measurement in the split Hopkinson pressure bar" *Proc. SPIE* **4359** 1471-1477

Walley, S.M., Field, J.E., Pope, P.H. and Safford, N.A. (1989) "A study of the rapid deformation behaviour of a range of polymers" *Phil. Trans. R. Soc. Lond. A* **328** 1-33

Walley, S.M., Field, J.E., Pope, P.H. and Safford, N.A. (1991) "The rapid deformation behaviour of various polymers" *J. Phys. III France* **1** 1889-1925

Zhao, H. (1997) "Testing of polymeric foams at high and medium strain rates" *Polymer Testing* **16** 507-516

Zhao, H. and Gary, G. (2002) "Behaviour characterization of polymeric foams over a large range of strain rates" *Int. J. Vehicle Des.* **30** 135-145

4. VISITS OF CLIVE R. SIVIOUR TO EGLIN AIRFORCE BASE AND STUDIES OF IMPACT-INDUCED SOLID-STATE PHASE CHANGE IN HMX

4.1. CONSTRUCTION OF A MINIATURISED HOPKINSON PRESSURE BAR AT EGLIN AFB

In July 2003 CRS visited Eglin AFB for two weeks as part of the contract arrangement to build a miniaturised Hopkinson pressure bar for their laboratory. Whilst there he worked closely with Dr Jennifer Jordan, to plan the bar itself, as well as planning the experiments that we hoped to work on together.

During the first week of the visit a two-day Hopkinson bar workshop was held. This included a number of interesting talks on Hopkinson bars, and was designed to give both an overview of latest thinking on the subject, but also to be useful as an educational tool for those who were not familiar with the technique. CRS also gave a seminar on research at the Cavendish Laboratory and had some useful discussions about the explosives work that goes on at Eglin.

The miniaturised Hopkinson bar has now been built and a report written by Jennifer Jordan and Clive Sivior has been issued (details may be found in Appendix 2).

3.2 mm diameter rods were used to construct the system. The input and output rods are 300 mm long, and the striker 100 mm. There is also a momentum trap. The input and output rods are instrumented half-way along their lengths with semiconductor strain gauges. Bars were made from the following materials: Ti6Al4V and tungsten carbide. The low impedance titanium alloy rods are intended for testing polymer-bonded explosives and their binders. The tungsten carbide rods allow testing of very hard metals. A 12.7 mm diameter gas gun is used to fire the striker rod carried in a sabot. A three-point velocity measurement system allows acceleration to be measured allowing the impact velocity to be calculated more accurately for both the calibration and direct impact configurations.

Experiments have been performed on copper and PTFE (see the Eglin AFB report listed in Appendix 2).

CRS visited Eglin AFB again in the summer of 2004 and gave training in the use of the gun, strain gauges and velocity measurements, calibration of the strain gauges and replacement of damaged strain gauges.

Jennifer Jordan visited Cambridge for two weeks in July 2004. During this time she gave a seminar to the PCS Fracture and Shock Physics Group.

4.2. SOLID-STATE PHASE CHANGE IN HMX DURING DROPWEIGHT IMPACT (WORK PERFORMED BY H. CZERSKI ON BEHALF OF DSTL)

HMX has at least three different crystalline phases, termed α , β , and γ . There has been considerable speculation in recent years about their different sensitivities and the possible role of a phase change in ignition processes. The stable form at room temperature and pressure is the α -phase. On heating this phase, a solid-state phase change to β -phase is seen, although the change is inhibited by high pressures. The β -phase has been observed to be more sensitive to impact than α -phase (although authors disagree about how much more sensitive it is) and so a phase change would have considerable implications in understanding and modelling ignition processes.

Until recently, the difficulty in addressing this question was the timescale of impact. Traditional techniques for elucidating crystal structure (Raman Spectroscopy and Fourier Transform Infra-red Spectroscopy) operate on much longer timescales than ignition processes (which usually last a few microseconds). In the past few years however, it has become apparent that the technique of second harmonic generation (SHG) has the required time resolution. Second harmonic generation is a non-linear optical phenomenon. By this is meant that when intense laser light is incident on an appropriate material, a significant proportion of the transmitted and reflected light is emitted at twice the original frequency. β -phase is a very efficient second harmonic generator, while the symmetry of the α -phase crystal structure means that it is only 2% as efficient. Using a Nd:YAG laser at its fundamental frequency of 1064nm, any second harmonics produced are at 532nm, which is very close to the peak spectral sensitivity of our visible-light high-speed cameras. Therefore, if a short (9ns) laser pulse is incident on a sample during impact, any resulting SHG can be isolated using a filter and recorded using a high-speed camera. This gives a snapshot of the location of any β -phase present at the time of the laser pulse. The laser used can only generate a single laser pulse during an impact so many experiments are necessary to build up the overall picture. It is also possible to follow visible light from reaction simultaneously with a second high-speed camera.

An apparatus has been designed and built at the Cavendish to carry out these experiments by modifying our existing transparent anvil dropweight system. A phase change from α to β was observed, approximately 10 μ s before ignition. It appeared in a narrow band, thought to correspond to an adiabatic shear band, but we were unable to correlate this with the ignition sites. This is the first time that such a phase change has been observed during low velocity impact loading. It appears that although the high pressure would be expected to inhibit the phase change the high temperatures reached along shear bands are sufficient to allow the phase change to occur. Ignition of HMX was previously thought to occur along shear bands and the higher sensitivity of β -phase seems likely to play a role in this. This research opens up the possibility of answering many questions about the role of the crystalline structure of HMX during failure and ignition.

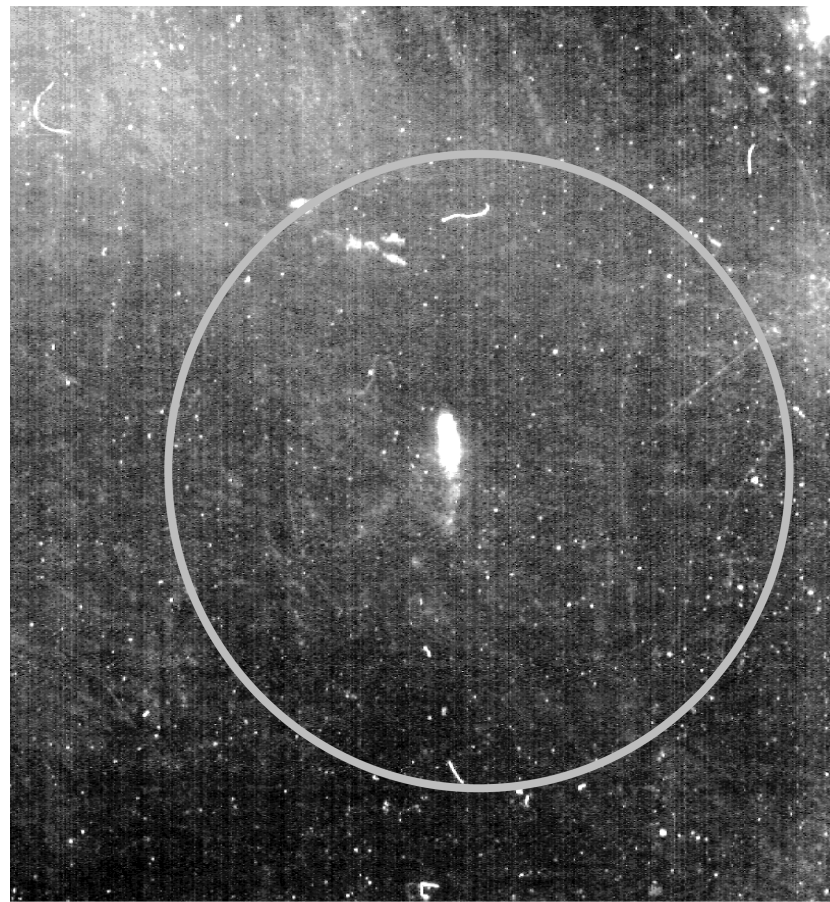


Figure 4.1. Image of SHG during impact on a 3mm diameter L-phase pellet. The HMX ignited 10ms after this photograph was taken. The circle marks the boundary of the field of view of the pellet (9mm diameter). The resolution of the photograph has been degraded in scanning - the line of SHG was far sharper in the original.

5. HIGH RATE MECHANICAL PROPERTIES OF PBXs

5.1. INTRODUCTION

Polymer bonded explosives (PBXs) are a family of composite materials that consist of explosive crystals held together by a polymer binder. They may also contain additives, such as oxidisers to improve explosive output, antioxidants to reduce ageing effects and plasticisers. The explosive content, by mass, may range from 60 % to 98 %, so a PBX may have a similar explosive output per unit mass to pellets of pressed explosive crystals. However, the mechanical properties of PBXs are very different from those of pressed explosives. Although the explosive makes up the bulk of the material, it typically has a much higher Young's modulus than the binder; when deformation takes place it is mainly accommodated by the binder. Hence the binder absorbs the energy dissipated in the deformation and also prevents crystal friction and fracture. The composite is therefore less sensitive to ignition via mechanical stimulus than pressed explosives.

The sensitivity of a PBX is dependent on its mechanical properties and composition. Because of this dependence, and because PBXs often have a structural role in modern applications, an understanding of their mechanical properties and how these relate to both internal and externally applied constraints is of great importance. Whilst a softer binder may reduce sensitivity, if it is too soft the material may not have the required structural strength. Ultimately one aim of PBX research is to be able to predict the mechanical properties of the materials from knowledge of their composition, and therefore allow them to be designed with specific properties. However, as with all models, experimental data are vital.

The main problem with currently published work on PBXs is that it does not form a cohesive body from which, for example, the effects of different constraints and stimuli can easily be extracted. This appears mainly to be due to the cost and difficulty of preparing explosives of non-standard composition. However, much important work has been published; this is described in section 5.2. Results from two sets of experiments follow. These are introduced in section 5.3 and the results are presented in sections 5.4 and 5.5. Whilst a discussion and conclusions are given at the end of each section there is also an overall discussion of deformation mechanisms in section 5.6, a summary of the conclusions in 5.7 and suggestions for further work in section 5.8.

5.2. DEFORMATION PROPERTIES OF PBXs

There are a number of different forms of stress-strain behaviour that can be exhibited by a polymer bonded explosive. These include all of those associated with polymers: elastic behaviour, yield and ductile flow and brittle behaviour; in addition to shear bands. An important aim of PBX research is to relate these types of behaviour to impact sensitivity, and to understand them terms of composition and deformation mechanisms.

If the PBX is treated as a two-component system - binder and crystals - there are a number of factors that may influence its mechanical properties. The most

important is the mechanical behaviour of the binder, in particular when in the form of thin layers, for these can show dramatically increased strength when compressed between anvils (Schroeder and Webster 1949; Heavens and Field 1974). The mechanical behaviour of the binder also depends on temperature, strain rate and structure. The latter often changes with age. The exact mechanical properties of the crystal are far less important. Because their elastic modulus may be 1000 times that of the binder these properties might only come into play when crystal-crystal interactions take place e.g. at low temperatures where the binder is stiffer, or at large deformations. In these cases, crystal shape is also important, since corners and protrusions can lead to stress concentrations. Otherwise, the crystals may be thought of as incompressible.

Crystal loading density and size also play a major role. It was clear when handling the PBX used in section 3 that the smaller particle sized composition was stiffer. This makes the PBX easier to machine, so specimen preparation was more straightforward. In addition, there was a tendency for crystals to fall out of the larger particle sized material. So clearly cohesion between the crystals and the binder is an important factor in the mechanical strength of the composite.

Unfortunately, it can be difficult to investigate these parameters in a coherent manner. As well as being expensive to produce small batches, it is also not always possible to produce novel formulations for experiments. PBXs with high loading densities tend to be produced by first coating the explosive crystals with binder, and then pressing them to form the composition. On the other hand, PBXs with lower loading densities are generally prepared by mixing the crystals and binder and then casting the mix. Whilst it might be interesting from a scientific point of view to reduce the loading density of an explosive formulation in order, say, to investigate the effect of particle spacing on strength, such a material would be soft and very difficult to machine or cast compared to its more heavily loaded counterpart. In addition, it would be difficult to achieve a constant loading density because the crystals tend to settle out as the binder cures. In practice, many of the compositions currently in use were chosen for their ability to be machined, cast and indeed formulated easily, as well as for other mechanical or explosive properties.

Ignition mechanisms and mechanical behaviour

It is generally accepted that explosive ignition is thermal in origin and that reaction begins at localised hot spots (Bowden and Yoffe 1952; 1958). The required size (critical size) of these hot spots is determined by their temperature and duration, and by the properties of the explosive itself. There are many proposed mechanisms for the production of hot spots (Field *et al.* 1982; 1992):

- Rapid collapse of gas spaces, or pores, which can be in or between crystals.
- Localised adiabatic shear
- Friction
- Dislocation motion

- Heating at crack tips
- Viscous flow

Not all of these mechanisms can produce critical hot spots on their own; however, they are additive, which is very important when considering mechanical deformation.

Before looking at PBXs some important observations from experiments on pure explosives must be mentioned. A number of authors have shown that sustained reaction in pure explosives during dropweight impact is usually associated with rapid radial expansion of the specimen (Heavens and Field 1974). A second feature of these experiments is the appearance of sudden drops in stress, which are often associated with ignition (Krishna Mohan and Field 1984; Afanasev and Bobolev 1971). Finally, there is evidence from both high-speed photography and heat sensitive film that adiabatic shear banding is an important contributor to hot-spot formation (Winter and Field 1975; Frey 1981; Coffey *et al.* 1981; Field *et al.* 1982; 1985; 1989; 1992; Krishna-Mohan *et al.* 1989; Coffey 1996).

There are relatively few studies of the ignition mechanisms of PBXs under impact. Field *et al.* (1985) and Walley *et al.* (1992) performed drop-weight and Ho (1992), direct impact Hopkinson bar, experiments. A number of different materials were investigated. The ignition mechanisms were found to depend on the high strain rate mechanical properties and the associated failure mode. Bulk heating by mechanical deformation does not raise the temperature of the material to the critical hot spot temperature, but the temperature may be enhanced locally by the following mechanisms:

- Heating through plastic deformation in regions of high shear stress. This could occur in shear bands, or in a boundary layer between the specimen and the anvils/bars (see also Guirguis 2000). In the drop weight experiments, shear bands were associated with a drop in strength of the specimen and shear in boundary layers with rapid radial expansion.
- Localised melting, and heating of the melt region though viscous flow.
- Energy released by brittle cracking.
- In drop weight experiments with large diameter anvils, adiabatic compression of trapped gas can occur if the specimen expands with jagged edges. This could not occur in Hopkinson bars since the ratio of bar to specimen area is not normally great enough,

Further measurements showed that materials containing larger crystals were more explosive (Field *et al.* 1985), even though they are mechanically weaker. They are also more sensitive to shock initiation (Moulard *et al.* 1985; 1989), even if the Young's modulus is the same (Schedlbauer and Kretschmer 1995). This was also observed in pressed pellets of pure explosives (Field *et al.* 1989; Balzer *et al.* 2002). Armstrong *et al.* (1990) showed that the impact sensitivity of RDX crystals increases with increasing crystal size: the HD_{50} (drop height at which half the samples initiate) of the crystals was found to be linearly dependent on a negative power of the crystal size. A number of mechanisms have been proposed for this effect in pure explosives:

- The more open structure allows the burning front to propagate more easily (Field *et al.* 1989). This is supported for PBXs by the work of Berghout *et al.* (2000a; b; 2002) who observed a faster rate of burning in damaged rather than pristine PBX 9501, the damaged material also having a more open structure. Damaged materials are also expected to be more sensitive because they contain air gaps that can be adiabatically compressed.
- The thermal conductivity of explosive pellets with large crystals is larger.
- The greater size of the collapsing gas pores in the larger particle size material (Balzer *et al.* 2002), although this could not be the case in a PBX.
- Dislocation mechanisms (Armstrong *et al.* 1982, 1986, 1990; Coffey and Sharma 1999; Armstrong and Elban 2004). Whilst dislocation pile-up has been proposed as a hot-spot mechanism (Coffey 1984; 1985), Field argues that is it not a ‘critical’ mechanism (Field 1992b).

It should be straightforward experimentally to distinguish between pore collapse and dislocation processes by finding the sensitivity of mixed particle size materials, where the pores between the large particles are filled by smaller material. This would affect the pore collapse, but not the dislocation motion.

Composition and mechanical behaviour

There are very few studies on the effects of composition on the properties of a PBX. As discussed earlier in this section, the strength of the binder plays a major role in determining the overall strength of the material. This has not been investigated systematically by using different binders, but can be deduced from experiments performed at different temperatures (presented later in section 2.4), and ageing studies (see section 2.3).

The effect of explosive particle size on mechanical strength was first reported by Field *et al.* (1985). Mechanical strength measurements from Hopkinson bar and Brazilian tests showed that the dynamic strength of a PBX containing only large particles is less than that of a similar PBX containing both small and large particles. A more recent study on the effect of composition on a trimodal system of aluminium, ammonium perchlorate (AP) and Hydroxyl-Terminated Polybutadiene (HTPB) was reported by Göçmez *et al.* (1998). Each material contained two unimodal distributions of AP and one of Al. The effect of changes in the loading densities of these materials on both mechanical properties at low strain rates and burning rate was investigated. These results are very interesting but unfortunately it is difficult to extract a trend from them.

Ageing

Age is likely to affect the properties of the binder more than the crystals. de la Fuente and Rodríguez (2003) investigated thermal ageing on the properties of an HTPB-based propellant. The exact composition of the material is complicated, but included 12% HTPB and 2 % dioctyl adipate as a plasticiser. The specimens were characterised using dynamic mechanical analysis (DMA), which showed that the unaged propellant had a distinct phase change at about -70 °C: the glass transition

temperature of the binder. This characterisation was repeated after ageing at 40, 60 and 80 °C for 1000, 3000 and 5000 hours. Various parameters were presented, e.g. the modulus at 0.1 Hz, as a function of age. An unexpected feature was that the modulus decreased, and then increased again, as the specimen aged. Judge (2003) also looked at the effect of storage at elevated temperatures (33, 43 and 60 °C) over a period of two years on an HTPB-based propellant. Over this long period of ageing the modulus of the propellant increased, the increase being much more dramatic for ageing at 60 °C than at the other two temperatures. The data from the two studies imply that whilst short-term ageing might decrease the modulus of the composition, longer-term ageing causes it to increase. The weakening may be explained by chain scission and absorption of water, whilst the strengthening may be due to additional cross linking of the polymer by oxidation, and loss of plasticiser, which tends to diffuse out of the material.

A number of authors have studied the effect of age on mechanical properties measured over large deformations. Goldrein *et al.* (2001) carried out Brazilian tests on aged and unaged specimens of a nitrocellulose-based PBX. They found that aged specimens were weaker, but could not find a change in the failure mechanism. Idar *et al.* (2001) also investigated the effect of binder ageing on the Estane-based PBX 9501. In these experiments, the Estane was degraded before the composite was formulated, reducing the molecular weight of the Estane. In quasistatic experiments there were clear changes of the strength and elastic modulus of the composite as the age of the Estane increased. And as in the studies of de la Fuente & Rodríguez (2003) and Judge (2003) the composite initially became stronger and then weakened. At high strain rates this was only observed at low temperatures and was a small effect even then. One would expect that reducing the molecular weight of a polymer would have less effect at high strain rates because less of the polymer chain is sampled on the timescale of the deformation. However, it is odd that the effects of ageing should be seen in the *cold* dynamic and *room temperature* quasi-static, experiments. Usually it is thought that *increasing* the temperature of a polymer is equivalent to *decreasing* the rate of deformation. These results might give an interesting insight into the different deformation mechanisms at work.

In summary:

- HTPB-based propellants show an increased modulus after an extended period of ageing at elevated temperatures. There is a small decrease during the initial stages of ageing.
- Ageing of the estane binder in PBX 9501 and of a nitrocellulose-based PBX weakened the material. The mechanism that causes this is uncertain. As expected the effect is more marked at low strain rates; unexpectedly it is observed at high strain rates, if the temperature is reduced.

Strain rate and temperature

A number of studies have looked at the effect of strain rate and temperature on the mechanical properties of various service explosives, measured using quasistatic devices as well as the SHPB (Gray III *et al.* 1998; 2000 Idar *et al.* 1998; John Jr. *et al.*

1998; Tasker *et al.* 1998; Blumenthal *et al.* 2000; John Jr. and Alamo 2000; Joshi and Lee 2001).

Generally it is found that:

- The strength of the material increases with decreasing temperature, or increasing strain rate. However, within the range of strain rates accessible using the SHPB, the change is small.
- The mode of failure may depend on the composition, strain rate and temperature. Materials with low loading densities tend to behave elastically, whilst those which are more heavily loaded may yield, then rapidly strain soften, and often form shear bands.

Figure 5.1 reproduces stress strain curves from experiments on PBX 9501 over a range of quasi-static strain rates at room temperature, and a range of temperatures at high strain rates obtained by Gray III *et al.* (2000).

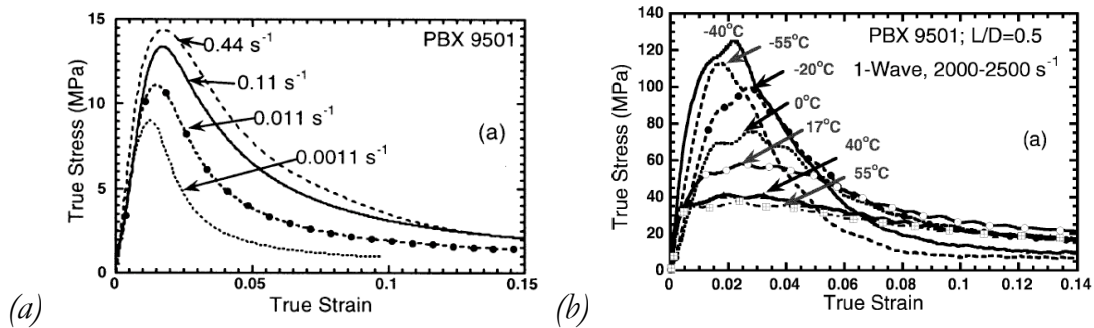


Figure 5.1. Stress-strain curves for PBX9501 (from Gray III *et al.* 2000).

- (a) Over a range of quasi-static strain rates.
- (b) In the Hopkinson bar, over a range of temperatures.

Deformation mechanisms

Careful studies of deformation mechanisms in PBXs have been carried out in quasistatic Brazilian tests using moiré interferometry, speckle metrology, environmental scanning electron microscopy (ESEM), and optical microscopy. There appear to be three observed deformation mechanisms (Palmer *et al.* 1993): debonding (between the crystal and binder), crystal fracture, and deformation twinning within the crystal. Cavitation has also been postulated as a fourth mechanism. Debonding was the main mechanism: both Palmer *et al.* (1993) and Rae *et al.* (2002a, b) found that in quasi-static experiments crystal fracture was rare and often associated with prior flaws or crystal-crystal contact. Twinning is important in HMX based composites: whilst HMX is very brittle, twinning allows large elastic distortions before fracture develops (Palmer and Field 1982).

In drop-weight experiments, HMX fracture during loading was seen (Field *et al.* 1985), despite the fact that the critical flaw size at the stresses developed is larger than the crystals themselves. It was suggested that where a twin meets a crystal boundary the sharp step that is developed acts as a stress concentrator which may initiate crystal fracture at lower global stresses. This ties in with the microscopic work of Coffey and Sharma (1999). Fracture of explosive crystals alone is unlikely

to produce a critical hot spot due to the low fracture surface energy of the crystals which is only of the order of tens of mJ (Palmer and Field 1982; see also Field *et al.* 1982). However it can be an important mechanism when tough contaminant grits are added to pure explosives. Grits such as particles of certain polymers are indeed found to sensitise explosives (Swallowe and Field 1982). The polymer has to fail catastrophically and have a low specific heat, latent heat and thermal conductivity if it is to act as a sensitiser.

Some interesting research by Wiegand (e.g. Wiegand 1998; 2000; 2003a; b) has indicated that there may be two sets of mechanisms in play during PBX deformation. He measured the Young's moduli (E), the failure stresses (σ_f) and failure strains (ϵ_f) of a number of PBXs over a range of temperatures and strain rates. For low values of E , σ_f was proportional to $E\epsilon_f$ and ϵ_f varied with E , whilst at large values σ_f was proportional to $E^{0.5}$ and ϵ_f was approximately constant. The value of E at which the changeover occurred depended on the material in question. The loading densities of the materials ranged from 80 % to 95.5 % by mass of explosive crystal.

5.3 EXPERIMENTS: AN INTRODUCTION

From the above review it is clear that the mechanical properties of PBXs play an important role in determining their sensitivity to impact, and their subsequent deflagration behaviour. Their deflagration behaviour is also affected by their composition, in particular the crystal size. In addition, the composition of the material also affects the mechanical properties, the main contributions coming from the binder strength and the crystal size. Finally, the binder properties can be altered by strain rate, temperature and age: these strongly affect the mechanical properties of the material as a whole.

Unfortunately most studies of the mechanical properties of PBXs have been phenomenological studies of service materials which are not necessarily comparable. Therefore, in order to systematically compare the effect of composition, further more controlled experiments are required. Recently it has been possible to obtain materials with the same binder and loading density, but different particle sizes, and experiments on these materials will be presented in the next two sections.

In section 4 results from a study of two PBX compositions with different particle size distributions at four different temperatures are presented. Reducing the particle size of the explosive was found to increase the strength of the material. The study also gave a good guide to the way that the deformation properties of PBXs are modified by changes in temperature.

After the difference in strength caused by different particle sizes had been observed, it was quantified using a second set of compositions. These had four different particle size distributions whose means spanned 2 decades of size (3 to 300 μm). By testing these materials within the glass transition region, the

dependence of flow stress on particle size was measured. This is presented in section 5.

5.4 RDX/HTPB COMPOSITIONS WITH TWO PARTICLE SIZES

Description of materials used

The materials investigated were designated RF 38-09 and RF 38-22, and were manufactured by RO Defence, Glascoed, UK. Both materials are polymer bonded explosives consisting of 88% cyclotrimethylene trinitramine (RDX) and 12% HTPB. RF 38-09 has a median RDX particle size of 710 μm . RF 38-22 has median particle diameter of 159 μm .

Specimen preparation

The materials were supplied as cylinders of 10 cm diameter and 5 cm thickness. From these, 2 mm thick strips were cut. Discs of 6 mm diameter were then punched out from these strips. Since the preparation process did not produce specimens of exactly reproducible size, each one was individually measured to ± 0.01 mm before testing. The samples were checked carefully to ensure that they had parallel faces; those that did not were rejected for use except for 'setting-up' experiments.

A problem in specimen preparation was loss of explosive crystals from the polymer binder: they were easily brushed from the free surfaces. This was especially true for RF 38-09, as the loss of large surface grains has an effect deeper into the material, and there were fewer grains in each sample to start with. Care was taken to reject samples that had lost surface grains.

It should be noted that for the larger grain sized material there were not 5 characteristic units (in this case average grain diameters) along the length of the specimens. It was, however, decided that using specimens of 5 mm length, which would meet this criterion, would not enable the specimen to reach equilibrium quickly enough during the experiment. This is especially important for this very soft material because it was not possible to compare the one- and two-wave analyses to check for equilibrium at either room temperature or 70 °C. Therefore, there was a chance that the specimens tested were not representative of the bulk material. However, a number of tests were carried out and it will be seen that the results were very consistent with each other. Therefore it is felt that the specimens did represent the bulk material.

Experimental conditions

The experiments were carried out at a strain rate of approximately 5000 s^{-1} , and at four different temperatures; +70, +20, -60 and -100 °C. The final temperature was chosen to ensure that it was below the glass transition temperature of the binder (which is approximately -70 °C). The experiments are room temperature

were carried out using magnesium bars, and those at other temperatures using Inconel.

Results

Figure 5.2 shows stress-strain curves for samples of RF 38-22 and RF 38-09 at room temperature. The RF 38-22 (smaller particle size) material showed continual strain-hardening throughout the loading. The RF 38-09 material showed some strain-hardening at high strains, but yielded at a true strain of approximately 5%.

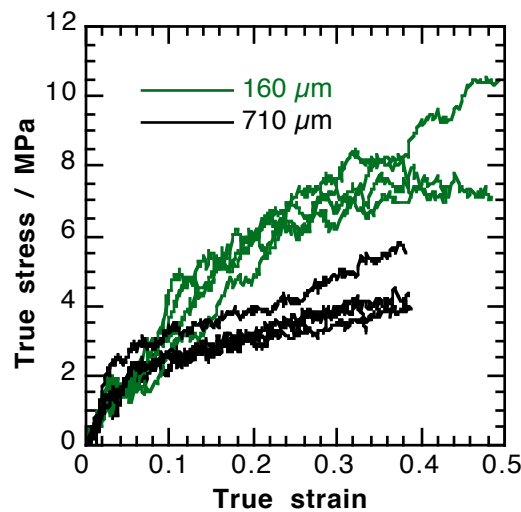


Figure 5.2. Stress-strain curves for the two RDX / HTPB compositions, with median particle sizes of 710 and 160 μm , at room temperature. The strain rate was approximately 5400 s^{-1} .

The stress-strain curves for the two materials at 70 °C are shown in figure 5.3, where they are compared to the room temperature results. The curves are noisy, since the output of the potential divider on the output bar was only a few mV in amplitude. In these experiments the weakness of the materials was compounded by the use of high modulus Inconel bars, chosen the low temperature sensitivity of their mechanical properties.

At -60 °C the materials are stronger, as expected. The stress-strain curves are shown in figure 5.4. RF 38-09 has a distinct yield and level flow stress, whilst the RF 38-22 (smaller particle size) material exhibits strain softening after yield, behaviour that is strongly indicative of the formation of strain localisations. A comparison with room temperature data is given in figure 5.5.

Below the glass transition temperature the materials behave in a brittle manner (see figure 5.6, which plots engineering stress, rather than true stress, against time). In this case it would be unrealistic to assume that the specimens conserve volume, or even that it is possible to define material-specific, rather than specimen-specific, values of stress and strain.

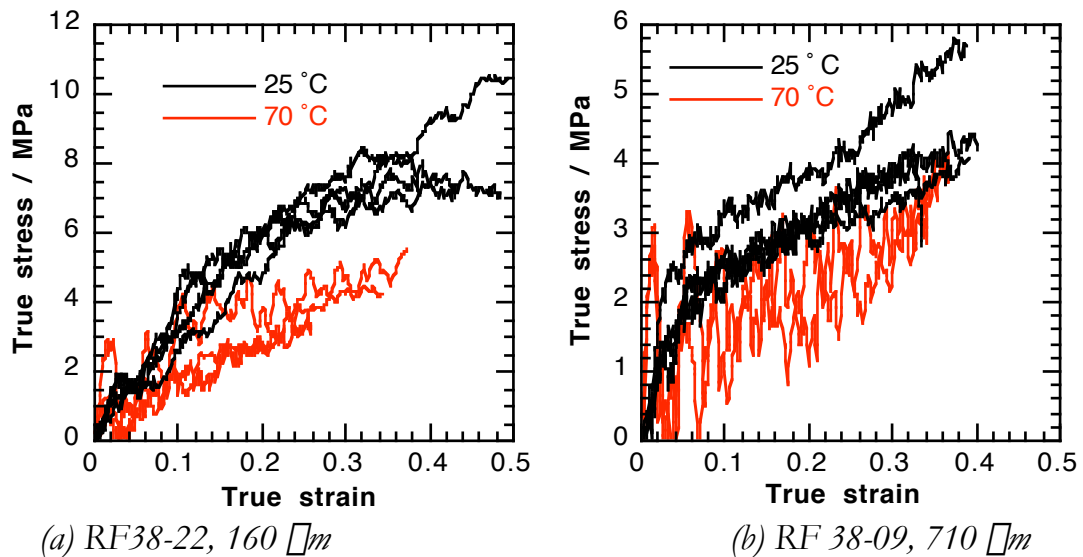


Figure 5.3. Stress-strain curves for RDX / HTPB compositions at 70 °C, compared to those at room temperature, the strain rate was 5400 s^{-1} .

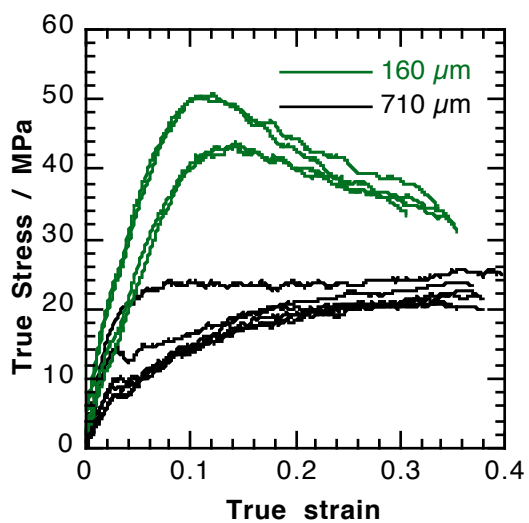


Figure 5.4. Stress-strain curves for RDX / HTPB compositions at -60 °C, strain rate of 4000 s^{-1} for the 160 μm median particle size, and 4400 s^{-1} for the 710 μm median particle size.

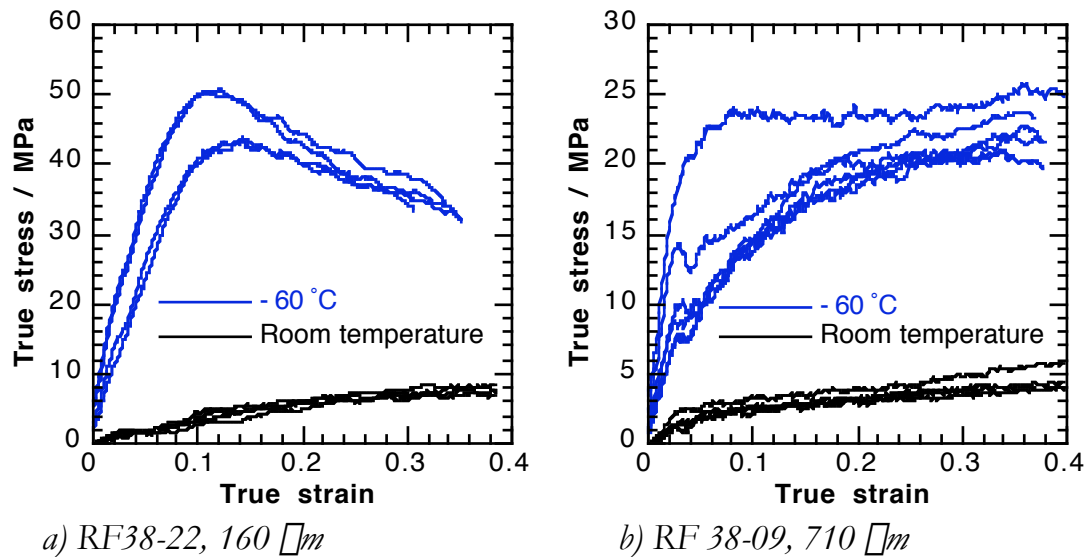


Figure 5.5. Comparison of stress-strain curves at room temperature and $-60\text{ }^{\circ}\text{C}$ for the two different RDX / HTPB compositions.

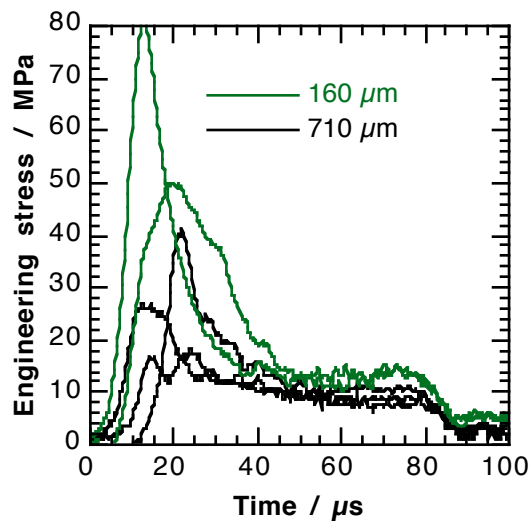


Figure 5.6. Stress-strain curves for the RDX/HTPB compositions at $-80\text{ }^{\circ}\text{C}$. The nominal strain rate is $5400\text{ }\mu\text{s}^{-1}$.

Discussion

At room temperature, RF 38-22 deforms at a higher stress than RF 38-09 but does not have a distinct yield point and strain-hardens more rapidly. RF 38-22 also shows a greater dependence on temperature than the larger particle size RF 38-09, evident in the experiments at both 70 °C and –60 °C. The experiments at –60 °C also indicate that particle-particle interactions are more important in the smaller grain size material, causing the strain localisation. This is expected, for if the particle size is reduced but the loading density remains the same, the particle separation is also reduced. It is suggested that the thinner regions of binder allow the particles to interact more quickly as the temperature is reduced, partly because of the smaller distance between particles, but also because a thin film of polymer compressed between two harder materials is more rigid. This increased dominance of the particle-particle interaction affects the material properties.

In the experiments below the glass transition temperature both materials shattered at a high stress, before settling down to a constant ‘flow’ stress. The stress of the initial peak is not reproducible, as it depends on the pre-existing flaws in each sample. The later part of the stress curve is probably governed by the strength of the mixture of binder material and crystals and is slightly higher for the RF 38-22 (small particle size) material.

Conclusions

Changing the particle size in a PBX alters its response to dynamic loading in both a quantitative and a qualitative way. In particular, for a given loading density, the strength decreases with increasing particle size, as does the temperature dependence of this strength. Increasing the temperature of the material also reduces its strength, but if both of the temperatures in question are above the glass transition of the binder the overall nature of the response does not change. As the temperature is reduced, however, the response first changes to a yield and flow process for large grain sizes and to that associated with strain localisations for small grain sizes. Below the binder glass transition temperature* the material becomes brittle.

* Because of the spread of molecular weights present in the binder this is not a single temperature, but a temperature range. This will be referred to as the glass transition region. The experiments at –60 °C were also carried out in this region.

5.5 AP / HTPB COMPOSITIONS WITH FOUR PARTICLE SIZES

Materials used and specimen preparation

The material used was an AP-HTPB propellant, designated CPX-372. It was made up of 66 % ammonium perchlorate (AP), and 33 % HTPB, and was supplied with 4 AP particle size distributions. The median particle sizes were:

- i. $\sim 3 \mu\text{m}$
- ii. $\sim 8 \mu\text{m}$
- iii. $\sim 30 \mu\text{m}$
- iv. $200 - 300 \mu\text{m}$.

Specimen preparation was carried out in the same manner as the previous section, the nominal specimen sizes were 2.3 mm thick, and 5.7 mm diameter.

Experimental conditions

The materials were tested at room temperature, over a range of rates from about 2000 s^{-1} to about 6000 s^{-1} . Because they were very weak it was decided that raising the temperature would not be of interest. In the previous section it was seen that the sensitivity to particle size is increased by decreasing the temperature. So further experiments were carried out at a temperature of -60°C . This temperature was chosen because it is within the glass transition region of the binder and was observed to give yield and flow behaviour in the larger particle separation RF material.

Results

Figure 5.7 shows stress-strain curves for all four different particle sizes, over a range of strain rates. So that the sizes can be compared to each other, a typical result from each size is shown in figure 5.8. The equivalent results at -60°C are shown in figure 5.9.

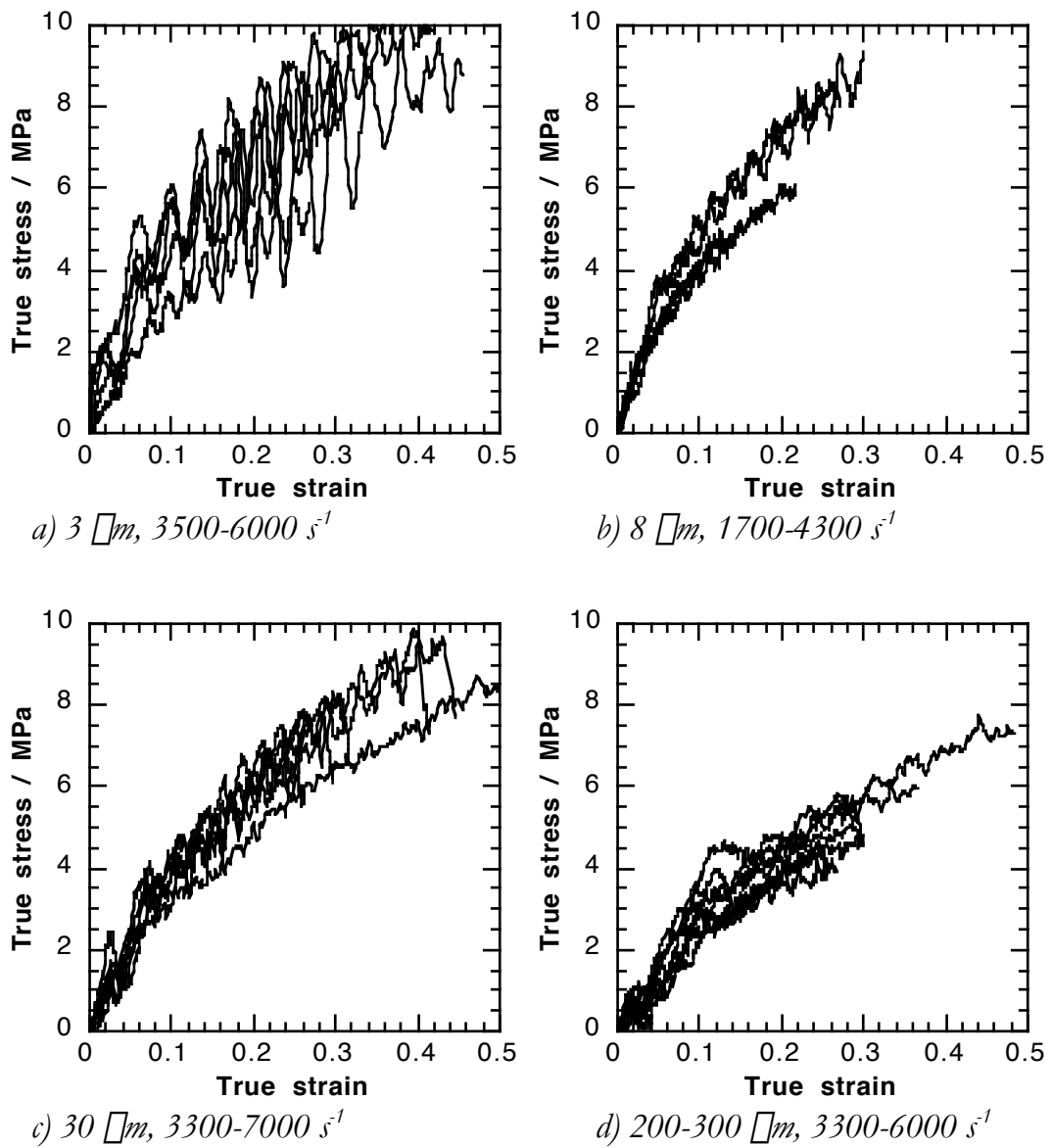


Figure 5.7. Stress-strain curves for four AP/HTPB compositions obtained at room temperature, with median particle sizes as given in the figure captions. Ranges of strain rates are also given in the figure captions. There is no observable dependence of strength on strain rate.

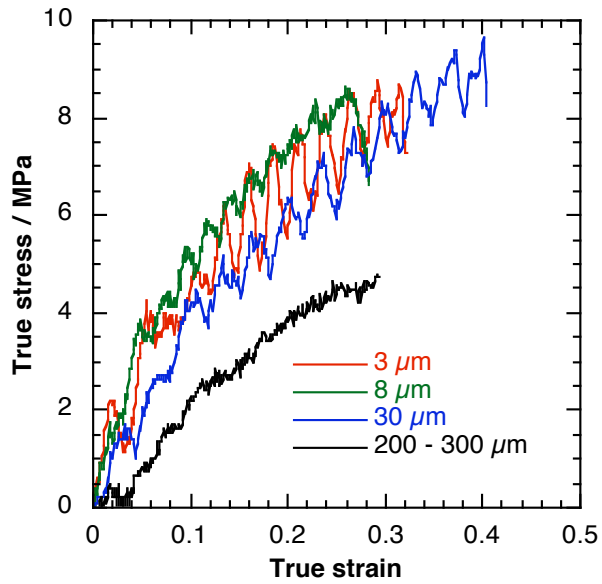


Figure 5.8. Comparison of typical (not average) stress-strain curves for the four AP/HTPB compositions at room temperature.

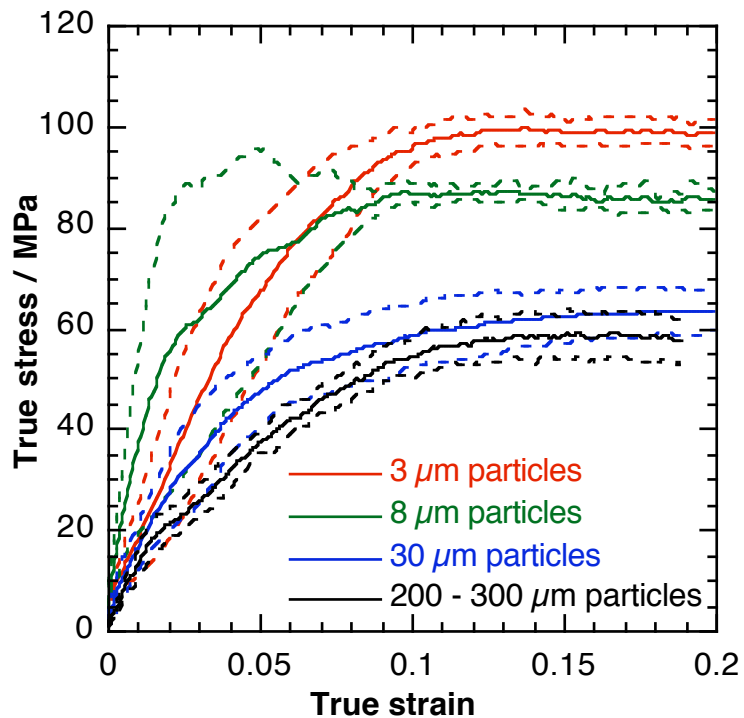


Figure 5.9. Comparison of stress-strain curves for the four AP/HTPB compositions at -60°C . Between four and six experiments were performed on each type. The mean stress strain curve is shown as a full line, the dotted lines give spread, as defined by the standard deviation of the results. The strain rate is $4100 \pm 300 \text{ s}^{-1}$.

Discussion

As observed for the RF materials in section 5.4, the strength of the AP/HTPB compositions decreases with increasing particle size, this being more pronounced in the low temperature experiments. At -60°C the materials yield and then flow at constant stress giving a quantitative measure (the flow stress) that can be compared across the particle sizes. It was found that the flow stress is linearly dependent on the reciprocal square root of the particle size, figure 5.10. This is of the same form as the well-established Hall-Petch relationship for metals (Hall 1951; Petch 1953). However, it is important not to read too much into this similarity. The Hall-Petch relationship is based on the movement of dislocations in metals and whilst the bulk failure mechanism in PBXs is not well understood, it is unlikely to be the same. We also note that, because the loading density of AP was the same for all the compositions, the particle spacing is proportional to the particle size, which means that the results in figure 5.10 can equally be represented as in figure 5.11. An appreciation of whether it is particle size, or particle spacing, that affects the strength is important to fully understand the properties of these materials.

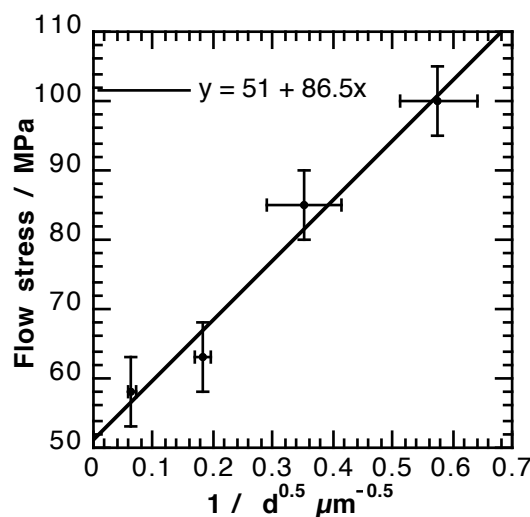


Figure 5.10. Dependence of flow stress at -60°C on the reciprocal square root of particle size.

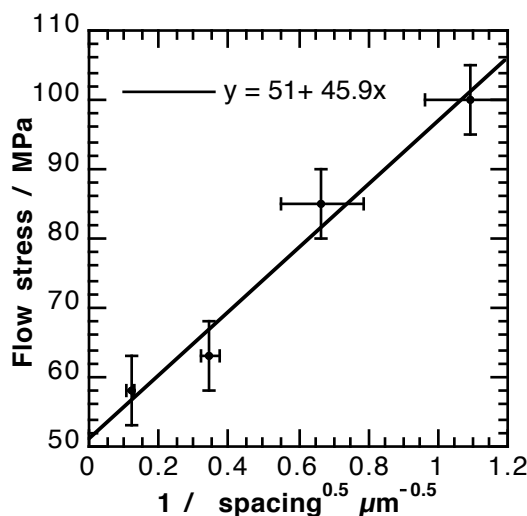


Figure 5.11. Dependence of flow stress at -60°C on the reciprocal square root of mean particle spacing. Because particle size and spacing are proportional to each other, the graphs in figures 5.10 and 5.11 are identical except for scale.

Conclusions

The dependence of the flow stress of a PBX on particle size has been investigated at room temperature and at -60°C . The low temperature was chosen so that the material was deformed under conditions that favour clear yield and flow behaviour. It is seen that for a 66%AP, 33% HTPB propellant the flow stress depends on the reciprocal square root of both the particle size and the particle spacing.

5.6 STRAIN LOCALISATION AND CHANGES IN DEFORMATION MECHANISMS

Figure 5.12 shows stress-strain curves from Hopkinson bar experiments on a highly loaded and fairly strong PBX composition, EDC37 (91 wt% HMX, 8 % K-10 and 1 % nitrocellulose (Gustavsen *et al.* 2000). If these are compared with those shown in figure 5.1 for PBS 9501 (94 % sugar crystals, 3.0 % Estane and 3.0 % BDNPA-F (Idar *et al.* 1998), it can be seen that while the stress-strain curves are quantitatively different, they have the same shape: i.e. a distinct failure stress is followed by rapid weakening which gradually reaches a plateau. This plateau stress is generally not as consistent as the failure stress. The shape is associated with strain localisation, or shear bands. The existence of shear bands was confirmed by high-speed photography, figure 5.13. Both sets of experiments were carried out at room temperature. This behaviour can be compared with the measurements presented in sections 5.4 and 5.5, where the materials behaved approximately elastically at room temperature. All these results show that the mode of deformation is heavily dependent on the composition of the material, and in particular the loading density.

The deformation mechanism is also strongly dependent on temperature, through the temperature dependence of the binder. Reducing the temperature of the AP/HTPB compositions to -60°C changed their behaviour so that instead of being elastic they showed a distinct yield and constant flow stress. This was also the case for the larger particle size RDX/HTPB composition RF 38-09. However, the smaller particle size (and therefore smaller particle spacing) RF 38-22 strain softened after yield and behaved similarly to EDC37 and PBX9501 do at room temperature. In addition, increasing the temperature of PBX 9501 reduced the height of the failure peak whilst maintaining the height of the plateau (figure 5.1), giving a yield and flow similar to that of the AP/HTPB composition at room temperature. When the temperature was reduced there was some increase of the failure stress down to -40°C , but not between -40 and -50°C . This is consistent with the behaviour of polymers below their glass transition temperature, where the strength is much less temperature dependent. In addition, as the temperature was reduced the drop in strength after the peak became more dramatic. In fact from the shape of the stress-strain curves shear bands appear just to be the transition region between truly ductile and truly brittle behaviour.

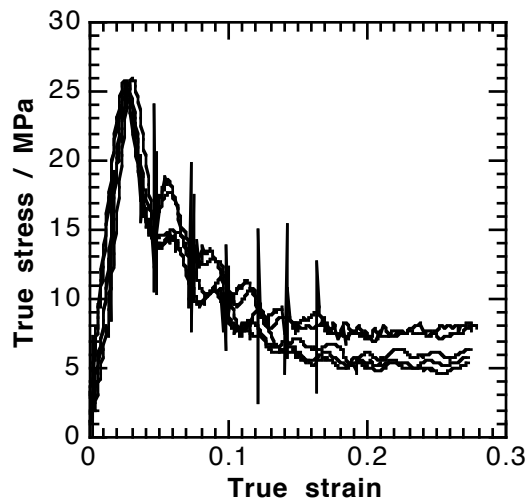


Figure 5.12. Stress-strain curves for EDC 37 at room temperature, and a strain rate of $3900 \pm 50 \text{ s}^{-1}$. The distinct yield and the post-yield drop in stress are associated with shear bands. The large black spikes are electrical noise caused by the trigger used for a high speed camera. From Sivior et al. (2004).

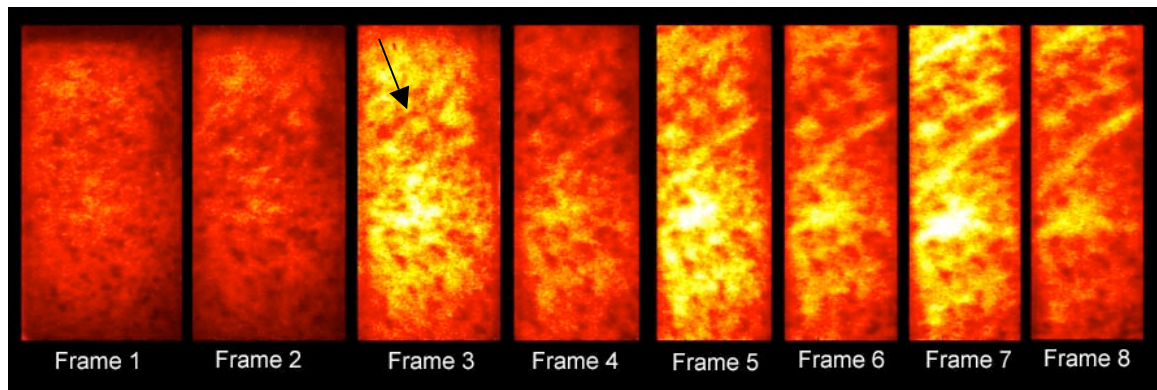


Figure 5.13. High-speed photographic sequence of an EDC 37 specimen, compressed at 3900 s^{-1} . The original image is in black and white; however, false colour shows up shear bands more clearly. They initially develop in frame 3 (arrowed). The stress pulse arrived between frames 1 and 2. The exposure time was $20 \mu\text{s}$, and the interframe time was $0 \mu\text{s}$.
From Sivior et al. (2004).

This shear band behaviour is repeated for many other PBXs with high loading densities: PBX 9502 (95 % crystal by mass) (Blumenthal *et al.* 2000), X0242-92-0-04 (92%) and PBXN-9 (92%) (Gray III *et al.* 2000). Conversely, yield and flow or elastic behaviour is often seen for lower density materials: PBXC-29 (89%) (John Jr. and Alamo 2000) and PBXW-128 (60%) (Tasker *et al.* 1998)*.

These results indicate that the appearance of macroscopic shear bands is associated with the onset of particle-particle interactions, and that these interactions can be increased with either a stiffer binder, a higher loading density or smaller particles, the last two parameters reducing the particle spacing. This seems a logical result. Once the crystals begin to interact with each other there are a limited number of modes of deformation available to them. Because the critical flaw size at the stresses in these experiments is much larger than the crystal size, fracture cannot normally occur. This is supported by observations reported in section 5.2. Yield and flow of the crystals, even if possible, would be unlikely to allow sufficient movement to accommodate the large strains being applied. Therefore, the only alternative is for crystal planes to slide past each other, leading to localised deformation.

A further important observation is that the changes in behaviour that occur when the test temperature was increased in the Hopkinson bar (strain rate held constant) were not replicated when the strain rate was decreased at room temperature. This is supported by modelling work that suggests that the two main mechanisms leading to shear bands are mechanical softening due to microcracking and a quasi-granular constitutive response (Dey and Kamm 2000), which are not binder dominated responses.

Previous research examined in section 5.2 showed that the specific deformation mechanism plays an important part in determining the sensitivity of an explosive; in particular, shear bands or strain localisations are an important initiation mechanism. However, both the link between sensitivity and mechanism and that between mechanism and composition are not yet fully understood. It would appear that further experiments are required to rigorously establish these relationships. For example, it would be useful to create a deformation behaviour map, similar to an Ashby plot (Frost and Ashby 1982) showing how the behaviour changes for different combinations of particle spacing and binder stiffness. The studies by Wiegand may provide a useful foundation for this.

One of the problems with the SHPB, which is shared with other systems that remotely measure the load on a specimen, is that they only produce values that are averages over the whole specimen. This is a particular problem with materials that produce shear bands or to deform in some other inhomogeneous manner, and

* The materials listed here have a range of different binders, and it may appear from these results that there is a threshold loading density of about 90 % at which the behaviour changes. However, this is very unlikely, as evidenced by the change in behaviour with temperature. It is much more likely that the behaviour depends on a combination of the loading density and binder properties, and that for practical reasons manufacturers have chosen binders which give similar properties.

limits the investigation of these phenomena. For this reason it is important to investigate other methods of interrogating the experiment. These are discussed and developed in chapter 6.

5.7 CONCLUSIONS

- The strength of a PBX composition decreases with increasing particle size (or spacing) for materials whose loading density and binder properties remain the same. This effect is more pronounced if the temperature is reduced, thereby stiffening the binder.
- If the material is compressed under conditions that allow a distinct yield and flow, the flow stress is dependent on the inverse square root of the particle size (or spacing).
- The deformation mechanisms present when the explosive is deformed at high strain rates are dependent on the particle size, loading density, binder type and temperature. It appears that these parameters can be reduced to particle spacing and binder stiffness.

5.8 SUGGESTIONS FOR FURTHER WORK ON PBXs

- Isolate the effects of particle size and spacing from each other by measuring the properties of materials with a range of loading densities.
- Further investigate the effect of different temperatures on the properties of the CPX material. By combining these results with experiments on the binder alone, produce a map of behaviour as a function of particle spacing and binder stiffness. Investigate whether these can be combined to a single strength parameter.
- Investigate the effects of the mechanical properties and composition of PBXs on their energetic properties. How are these related? There are two simple ways to produce a mechanically weaker PBX: increase the particle size or use a weaker binder. The weaker binder could be of a different material, or the same material with a smaller molecular weight (either through production or ageing). In addition, the stiffness of the binder alters with changes in temperature.
- Introduce methods of measuring stress and strain fields in the specimen, rather than average specimen properties. Some optical methods for further interrogating the SHPB system are developed in chapter 6.
- Introduce recovery methods, or develop means of observing the evolution of the material during deformation, in order to better understand the microscopic deformation mechanisms. This may be helped by the development of the dynamic Brazilian test (see chapter 6).

5.9 REFERENCES

Afanas'ev, G.T. and Bobolev, V.K. (1971). "Initiation and Growth of Explosions in Liquids and Solids", publ. Israel Program for Scientific Translations, Jerusalem.

Armstrong, R.W. and Elban W.L. (2004). "Dislocations in Energetic Crystals" in "Dislocations in Solids", eds. F. R. N. Nabarro and J. P. Hirth publ. Elsevier B.V. pp 405-446.

Armstrong, R. W., Coffey, C. S., DeVost, V. F. and Elban, W. L. (1990). "Crystal size dependence for impact initiation of cyclotrimethylenetrinitramine explosive." *J. Appl. Phys.* **68** 979-984.

Armstrong, R. W., Coffey, C. S. and Elban, W. L. (1986). "Dislocation pile-up mechanism for initiation of energetic crystals" in "Advances in Chemical Reaction Dynamics", ed. R. M. Rentzepis and C. Capellos, publ. New York, D. Reidel: pp. 469-474.

Armstrong, R.W., Coffey, C.S. and Elban W.L (1982) "Adiabatic heating at a dislocation pile-up avalanche" *Acta metall.* **30** 2111- 2116.

Awaji, H. and Sato, S. (1979). "Diametral compressive testing method." *Trans. ASME: J. Engng Mater. Technol.* **101** 139-147.

Balzer, J.E., Field, J.E., Gifford, M.J., Proud, W.G. and Walley, S.M. (2002) "High-speed photographic study of the drop-weight impact response of ultrafine and conventional PETN and RDX." *Combust. Flame* **130** 298-306.

Berghout, H. L., Son, S. F. and Asay, B. W. (2000a) "Convective burning in gaps of PBX 9501" in "Proc. 28th Int. Symp. on Combustion", publ. Edinburgh, U.K.: pp. 911-917.

Berghout, H. L., Son, S. F. and Asay, B. W. (2000b) "Measurement of convective burn rates in gaps of PBX 9501" in "Shock Compression of Condensed Matter - 1999", ed. M. D. Furnish, L. C. Chhabildas and R. S. Hixson, publ. Melville, New York, American Institute of Physics: pp. 841-844.

Berghout, H. L., Son, S. F., Skidmore, C. B., Idar, D. J. and Asay, B. W. (2002). "Combustion of damaged PBX 9501 explosive." *Thermochim. Acta* **384** 261-277.

Blumenthal, W. R., Gray III, G. T., Idar, D. J., Holmes, M. D., Scott, P. D., Cady, C. M. and Cannon, D. D. (2000) "Influence of temperature and strain rate on the mechanical behavior of PBX 9502 and Kel-F 800" in "Shock Compression of Condensed Matter - 1999", ed. M. D. Furnish, L. C. Chhabildas and R. S. Hixson, publ. Melville, New York, American Institute of Physics: pp. 671-674.

Bowden, F. P. and Yoffe, A. D. (1952) "Initiation and Growth of Explosion in Liquids and Solids" (republ. 1985), publ. Cambridge, Cambridge University Press.

Bowden, F. P. and Yoffe, A. D. (1958) "Fast Reactions in Solids", publ. London, Butterworth.

Coffey, C. S. (1996) "Energy dissipation and the initiation of explosives during plastic flow" in "Shock Compression of Condensed Matter 1995", ed. S. C.

Schmidt and W. C. Tao, publ. Woodbury, New York, American Institute of Physics: pp. 807-810.

Coffey, C. S., Frankel, M. J., Liddiard, T. P. and Jacobs, S. J. (1981) "Experimental investigation of hot spots produced by high rate deformation and shocks" in "Proc. Seventh Symposium (Int.) on Detonation", ed. J. M. Short, publ. Dahlgren, Virginia, Naval Surface Weapons Center: pp. 970-975.

Coffey, C. S. and Sharma, J. (1999). "Plastic deformation, energy dissipation, and initiation of crystalline explosives." *Phys. Rev. B* **60** 9365-9371.

Coffey, C. S. (1985). "Energy localization in rapidly deforming crystalline solids." *Phys. Rev. B* **32** 5335-5341.

Coffey, C. S. (1985). "Hot-spot production by moving dislocations in a rapidly deforming crystalline explosive." in "Proc. Eighth Symposium (Int.) on Detonation", ed. J. M. Short. White Oak, Silver Spring, Maryland, Naval Surface Weapons Center pp. 62-67.

dellaFuente, J. L. and Rodríguez, O. (2003). "Dynamic mechanical study on the thermal aging of an HTPB-based energetic composite." *J. Appl. Polym. Sci.* **87** 2397-2405.

Dey, T. N. and Kamm, J. R. (2000) "Numerical modeling of shear band formation in PBX 9501" in "Proc. 11th Int. Detonation Symposium", ed. J. M. Short and J. E. Kennedy, publ. Arlington, Virginia, Office of Naval Research: pp. 725-734.

Field, J. E., Bourne, N. K., Palmer, S. J. P. and Walley, S. M. (1992). "Hot-spot ignition mechanisms for explosives and propellants." *Phil. Trans. R. Soc. Lond. A* **339** 269-283.

Field, J. E. (1992b). "Hot spot ignition mechanisms for explosives." *Accounts Chem. Res.* **25** pp. 489-496.

Field, J. E., Palmer, S. J. P., Pope, P. H., Sundararajan, R. and Swallowe, G. M. (1985) "Mechanical properties of PBX's and their behaviour during drop-weight impact" in "Proc. Eighth Symposium (Int.) on Detonation", ed. J. M. Short, publ. White Oak, Maryland, USA, Naval Surface Weapons Center: pp. 635-644.

Field, J. E., Parry, M. A., Palmer, S. J. P. and Huntley, J. M. (1989) "Deformation and explosive properties of HMX powders and polymer bonded explosives" in "Proc. Ninth Symposium (Int.) on Detonation", publ. Arlington, Virginia, Office of the Chief of Naval Research: pp. 886-896.

Field, J. E., Swallowe, G. M. and Heavens, S. N. (1982). "Ignition mechanisms of explosives during mechanical deformation." *Proc. R. Soc. Lond. A* **382** 231-244.

Frey, R. B. (1981) "The initiation of explosive charges by rapid shear" in "Proc. 7th Symp. (Int.) on Detonation", ed. J. M. Short, publ. White Oak, Maryland, Naval Surface Weapons Center: pp. 36-42.

Frost, H. J. and Ashby, M. F. (1982) "Deformation-Mechanism Maps", Oxford, Pergamon Press.

Göçmez, A., Erisken, C., Yilmazer, U., Pekel, F. and Ozkar, S. (1998). "Mechanical and burning properties of highly loaded composite propellants." *J. Appl. Polym. Sci* **67** 1457-1464.

Goldrein, H. T., Rae, P. J., Palmer, S. J. P. and Lewis, A. L. (2001) "Ageing effects on the mechanical properties of a polymer bonded explosive" in "Ageing Studies and Lifetime Extension of Materials", ed. L. G. Mallinson, publ. Plenum, New York: pp. 129-136.

Gray III, G. T., Blumenthal, W. R., Idar, D. J. and Cady, C. M. (1998) "Influence of temperature on the high strain-rate mechanical behavior of PBX 9501" in "Shock Compression of Condensed Matter - 1997", ed. S. C. Schmidt, D. P. Dandekar and J. W. Forbes, publ. Woodbury, New York, American Institute of Physics: pp. 583-586.

Gray III, G. T., Idar, D. J., Blumenthal, W. R., Cady, C. M. and Peterson, P. D. (2000) "High- and low-strain rate compression properties of several energetic material composites as a function of strain rate and temperature" in "Proc. 11th Int. Detonation Symposium", ed. J. M. Short and J. E. Kennedy, publ. Arlington, Virginia, Office of Naval Research: pp. 76-84.

Guirguis, R. H. (2000) "Ignition due to macroscopic shear" in "Shock Compression of Condensed Matter - 1999", ed. M. D. Furnish, L. C. Chhabildas and R. S. Hixson, publ. Melville, New York, American Institute of Physics: pp. 647-650.

Gustavsen, R. L., Sheffield, S. A., Alcon, R. R., Hill, L. G., Winter, R. E., Salisbury, D. A. and Taylor, P. (2000) "Initiation of EDC-37 measured with embedded electromagnetic particle velocity gauges" in "Shock Compression of Condensed Matter - 1999", ed. M. D. Furnish, L. C. Chhabildas and R. S. Hixson, publ. Melville, New York, American Institute of Physics: pp. 879-882.

Hall, E. O. (1951). "The deformation and aging of mild steel. III: Discussion of results." *Proc. Phys. Soc. Lond. B* **64** 747-753.

Heavens, S. N. and Field, J. E. (1974). "The ignition of a thin layer of explosive by impact." *Proc. R. Soc. Lond. A* **338** 77-93.

Idar, D. J., Peterson, P. D., Scott, P. D. and Funk, D. J. (1998) "Low strain rate compression measurements of PBXN-9, PBX 9501, and mock 9501" in "Shock Compression of Condensed Matter - 1997", ed. S. C. Schmidt, D. P. Dandekar and J. W. Forbes, publ. Woodbury, New York, American Institute of Physics: pp. 587-590.

Idar, D. J., Thompson, D. G., Gray III, G. T., Blumenthal, W. R., Cady, C. M., Peterson, P. D., Roemer, E. L., Wright, W. J. and Jacquez, B. (2001) "Influence of polymer molecular weight, temperature, and strain rate on the mechanical properties of PBX 9501" in "Shock Compression of Condensed Matter - 2001", ed. M. D. Furnish, N. N. Thadhani and Y. Horie, publ. Woodbury, New York, American Institute of Physics: pp. 821-824.

John Jr., H. J. and Alamo, M. F. (2000) "High strain rate testing of HMX-based explosive" in "Shock Compression of Condensed Matter - 1999", ed. M. D.

Furnish, L. C. Chhabildas and R. S. Hixson, publ. Melville, New York, American Institute of Physics: pp. 679-682.

John Jr., H. J., Hudson III, F. E. and Robbs, R. (1998) "High strain rate testing of AP/Al/HTPB solid propellants" in "Shock Compression of Condensed Matter - 1997", ed. S. C. Schmidt, D. P. Dandekar and J. W. Forbes, publ. Woodbury, New York, American Institute of Physics: pp. 603-606.

Joshi, V. S. and Lee, R. J. (2001) "High strain rate behavior of explosives containing polymeric binders" in "Fundamental Issues and Applications of Shock-Wave and High-Strain-Rate Phenomena", ed. K. P. Staudhammer, L. E. Murr and M. A. Meyers, publ. New York, Elsevier: pp. 43-46.

Judge, M. D. (2003). "An investigation of composite propellant accelerated ageing mechanisms and kinetics." *Propell. Explos. Pyrotech.* **28** 114-119.

Krishna Mohan, V., Jyothi Bhasu, V. C. and Field, J. E. (1989) "Role of adiabatic shear bands in initiation of explosives by drop-weight impact" in "Proc. Ninth Symposium (Int.) on Detonation", publ. Arlington, Virginia, Office of the Chief of Naval Research: pp. 1276-1283.

Krishna Mohan, V., Field, J. E. (1984) "Impact ignition of hexanitrostilbene" *Combus. Flame* **56** 269- 277.

Moulard, H. (1989) "Particular aspect of the explosive particle size effect on shock sensitivity of cast PBX formulations" in "Proc. 9th (Int.) Symp. on Detonation", publ. Arlington, Virginia, Office of the Chief of Naval Research: pp. 18-24.

Moulard, H., Kury, J. W. and Delclos, A. (1985) "The effect of RDX particle size on the shock sensitivity of cast PBX formulations" in "Proc. Eighth Symposium (Int.) on Detonation", ed. J. M. Short, publ. White Oak, Silver Spring, Maryland, Naval Surface Weapons Center: pp. 902-913.

Palmer, S. J. P. and Field, J. E. (1982). "The deformation and fracture of \square -HMX." *Proc. R. Soc. Lond. A* **383** 399-407.

Palmer, S. J. P., Field, J. E. and Huntley, J. M. (1993). "Deformation, strengths and strains to failure of polymer bonded explosives." *Proc. R. Soc. Lond. A* **440** 399-419.

Petch, N. J. (1953). "The cleavage strength of polycrystals." *J. Iron Steel Inst.* **174** 25-28.

Rae, P. J., Goldrein, H. T., Palmer, S. J. P., Field, J. E. and Lewis, A. L. (2002a). "Quasistatic studies of the deformation and failure of \square -HMX based polymer bonded explosives." *Proc. R. Soc. Lond. A* **458** 743-762.

Rae, P. J., Palmer, S. J. P., Goldrein, H. T., Field, J. E. and Lewis, A. L. (2002b). "Quasi-static studies of the deformation and failure of PBX 9501." *Proc. R. Soc. Lond. A* **458** 2227-2242.

Schedlbauer, F. and Kretschmer, A. (1995) "The influence of particle size and mechanical properties on the sensitivity of high explosive charges (PBX)" in "Proc. 10th Int. Detonation Symposium", ed. J. M. Short and D. G. Tasker, publ. Arlington, Virginia, Office of Naval Research: pp. 876-881.

Schroeder, W. and Webster, D. (1949). "Press-forging thin sections: Effect of friction, area and thickness on pressures required." *J. Appl. Mech.* **16** 289 - 294.

Siviour, C. R., Williamson, D. M., Grantham, S. G., Palmer, S. J. P., Proud, W. G. and Field, J. E. (2004) "Split Hopkinson bar measurements of PBXs" in "Shock Compression of Condensed Matter - 2003", ed. M. D. Furnish, Y. M. Gupta and J. W. Forbes, publ. Melville NY, American Institute of Physics: pp. 804-807.

Swallowe, G. M. and Field, J. E. (1982). "The ignition of a thin layer of explosive by impact: The effect of polymer particles." *Proc. R. Soc. Lond. A* **379** 389-408.

Tasker, D. G., Dick, R. D. and Wilson, W. H. (1998) "Mechanical properties of explosives under high deformation loading conditions" in "Shock Compression of Condensed Matter - 1997", ed. S. C. Schmidt, D. P. Dandekar and J. W. Forbes, publ. Woodbury, New York, American Institute of Physics: pp. 591-594.

Walley, S. M., Field, J. E. and Palmer, S. J. P. (1992). "Impact sensitivity of propellants." *Proc. R. Soc. Lond. A* **438** 571-583.

Wiegand, D. A. (1998) "Mechanical failure properties of composite plastic bonded explosives" in "Shock Compression of Condensed Matter - 1997", ed. S. C. Schmidt, D. P. Dandekar and J. W. Forbes, publ. Woodbury, New York, American Institute of Physics: pp. 599-602.

Wiegand, D. A. (2000) "Mechanical failure of composite plastic bonded explosives and other energetic materials" in "Proc. 11th Int. Detonation Symposium", ed. J. M. Short and J. E. Kennedy, publ. Arlington, Virginia, Office of Naval Research: pp. 744-750.

Wiegand, D. A. (2003a). "Changes in the mechanical properties of energetic materials with aging." *J. Energ. Mater.* **21** 125-140.

Wiegand, D. A. (2003b). "Constant strain criteria for mechanical failure of energetic materials." *J. Energ. Mater.* **21** 109-124.

Winter, R. E. and Field, J. E. (1975). "The role of localized plastic flow in the impact initiation of explosives." *Proc. R. Soc. Lond. A* **343** 399-413.

6. OPTICAL TECHNIQUES

6.1 INTRODUCTION

The standard Hopkinson bar equations use the input, reflected and transmitted strain pulses in the input and output bars to calculate stress and strain in the specimen. These measurements are averages over the whole specimen volume. This means that in order to produce a representative specimen from inhomogeneous materials the size of the specimen must be large enough for the effects of inhomogeneity to even out. However, whilst a specimen may be structurally homogeneous, during the initial stages of the experiment it does not deform in mechanical equilibrium. Specimens may also exhibit strain localisations, such as shear bands. Furthermore, calculation of true stress requires the area of the specimen to be known. If the specimen does not conserve volume this cannot be calculated from the longitudinal strain and other techniques must be applied.

High-speed photography has been used for many years to record the deformation of Hopkinson bar specimens. Pope and Field (1984) used a high-speed camera to confirm their analysis of direct impact Hopkinson bar experiments. This was assisted by the 'optical wedge', developed by Gorham (1982) to look for barrelling in specimens. Barrelling is a sign of friction between the ends of the specimen and the bars. The optical wedge cut out the centre of the specimen from the image so that movement of the edges could be observed at higher magnification, and hence greater accuracy. High-speed photography may now be regarded as a standard technique when applied to the Hopkinson bar system: to confirm the specimen dimensions during an experiment, to observe bar movement, or to measure the diameter of a specimen that does not conserve volume, allowing true stress to be calculated. A further technique that has been applied is high-speed thermal imaging to measure the surface temperature changes in a deforming specimen (Walley *et al.* 2000; Zehnder *et al.* 2000). Optical extensometry has also been used (Bussac *et al.* 2002).

This chapter will present results from various optical techniques.

The first is a commercial Zimmer optical extensometer system. This measures the separation between two light/dark boundaries.

The second is a line laser, which can be used to measure the specimen diameter. This technique was first reported by Ramesh and Narasimhan (1996) and developed subsequently by Swantek *et al.* (2001). A line laser is used to provide a beam of light, which is shone across the specimen and then focussed onto a photodiode. The output from the photodiode depends on the amount of light that reaches it, and therefore on the size of the shadow cast by the specimen.

The third is a speckle technique. Modern computers allow detailed finite element models of the Hopkinson bar to be run. These models can predict the motion of regions of the specimen, as well as the forces expected on the strain gauges. In order to confirm these models more accurately, full-field measurements of specimen displacement are required. These can be provided by Digital Image

Cross Correlation (DICC), otherwise known as Speckle Metrology (e.g. Sjödahl 2001; Gåsvik 2002), the final technique examined, where the motion of a random speckle pattern on the surface of the specimen is tracked between photographs. This technique provides a high data density, and allows accurate, quantitative, measurements from high-speed photographs. It has previously been applied to flat, dog-bone specimens in a tensile Hopkinson bar (Kajberg and Sjödahl 2000; Kajberg 2002). Another suitable technique that has been applied to measure longitudinal strains only is moiré interferometry (Verleysen and Degreick 2003; 2004).

Once the methods have been discussed, three applications are presented: measurement of dynamic Poisson's ratio, the dynamic Brazilian test, the compressive behaviour of PBS 9501. An overall discussion and conclusions are presented at the end of this chapter.

6.2 OPTICAL EXTENSOMETER

Experimental

Measurements were made of strain in Hopkinson bar specimens using a Zimmer OHG 200X extensometer. This is a high accuracy, 0.008% of viewing distance (manufacturer's data), high-speed (response time $<1\mu\text{s}$) device for measuring the movement of two light/dark boundaries. There are two lenses, both of which can be moved perpendicular to their optical axis, and pointed directly at their respective boundaries. This ensures that there is no parallax. A schematic diagram of the arrangement is shown in figure 6.1.

In the Hopkinson bar experiments, the boundaries consisted of black and white tape. This was placed on the bars about 20 mm from the specimen end, and illuminated by a white spot lamp. Each extensometer lens is focused on one of the boundaries using a viewfinder. This has a black crosshair in the centre of the view from each lens, which allows the camera to be lined up so that the boundaries are vertical and in the centre of the view. The extensometer provides three voltage outputs, two of them are proportional to the displacement of the two boundaries, and the third is proportional to the change in distance between the boundaries. This provides the length change required for the strain calculation.

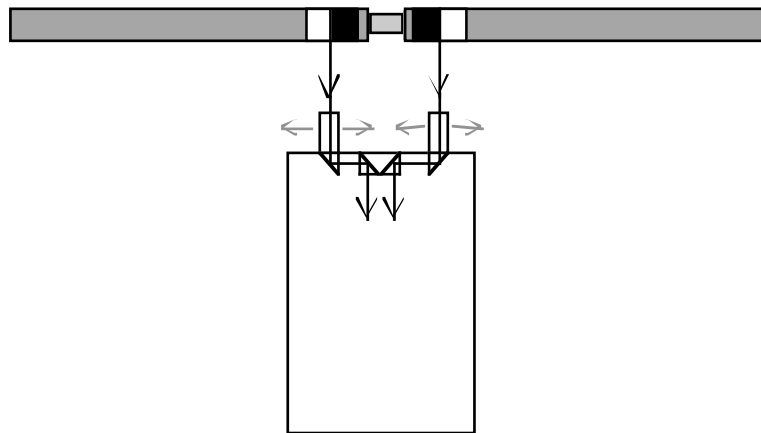


Figure 6.1. Schematic diagram showing the layout of the optical extensometer and Hopkinson bars.

Before performing the experiments, the extensometer was calibrated for the boundary size and lighting conditions that were to be used. It was found that the extensometer was so sensitive to light intensity that it could not be used with the flash required for high-speed photography. It was therefore not possible to use the two techniques on a single experiment. It also meant that the positions of the ends of the bars could not be measured directly by backlighting the specimen and measuring the dark boundaries formed by the bar ends. Also because the specimen expands sideways, the distance between the bars reduces, so the amount of light reaching the extensometer decreases upsetting the calibration.

The extensometer was calibrated by recording the voltage output for different bar separations, which were achieved by placing feeler gauges between the bars. Figure 6.2 shows the calibration curve obtained.

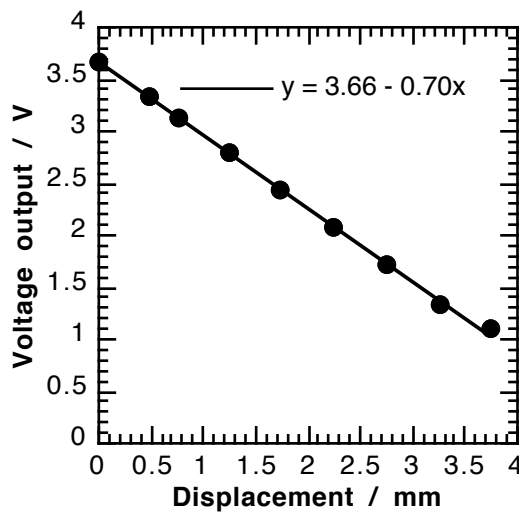


Figure 6.2. Calibration curve for the optical extensometer.

Results

The following figures and calculations refer to results obtained from a 2 mm thick, 5 mm diameter specimen of polycarbonate deformed in tungsten bars.

Figure 6.3 shows voltage traces from the extensometer and the input and output bar strain gauges. The noise on the extensometer trace had two sources: uncertainty in the boundary position, and electrical noise. The uncertainty in the boundary position could be reduced by increasing the light intensity, whilst a 100 point smoothing process was used to remove the random electrical noise. Note that the extensometer pulse rises halfway between the rising edges of the incident and reflected pulses: this is when the stress wave reaches the specimen. The calibration coefficient is then used to calculate the length change in the specimen, and the usual formula

$$\epsilon = \ln \frac{l_o}{l_i} = \frac{V_o - V_i}{V_o + V_i}, \quad (6.1)$$

was used to calculate the true strain as a function of time, figure 6.4. The strain rate and final strain measured by the extensometer are in excellent agreement with those calculated using the Hopkinson bar equations.

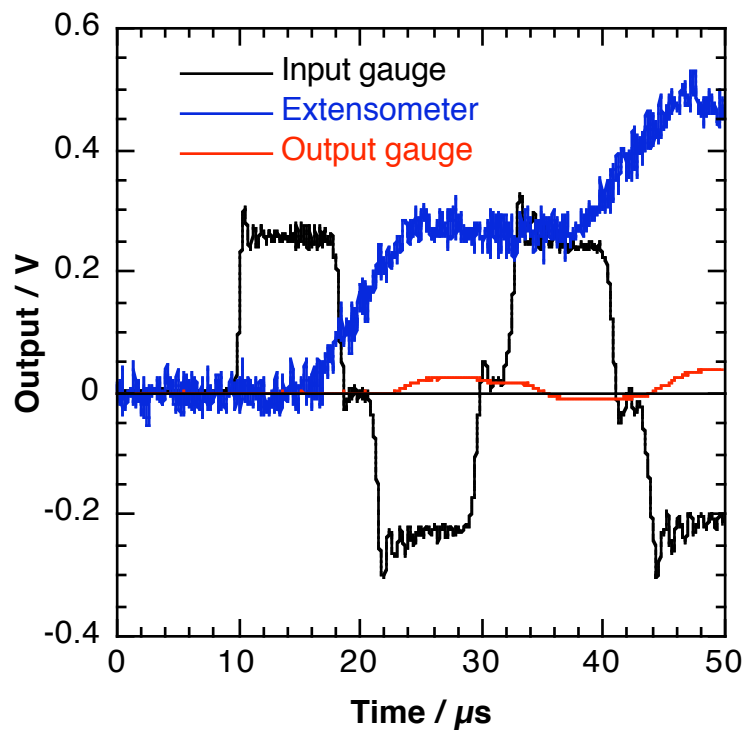


Figure 6.3. Comparison of extensometer voltage output with those from the Hopkinson bar strain gauges.

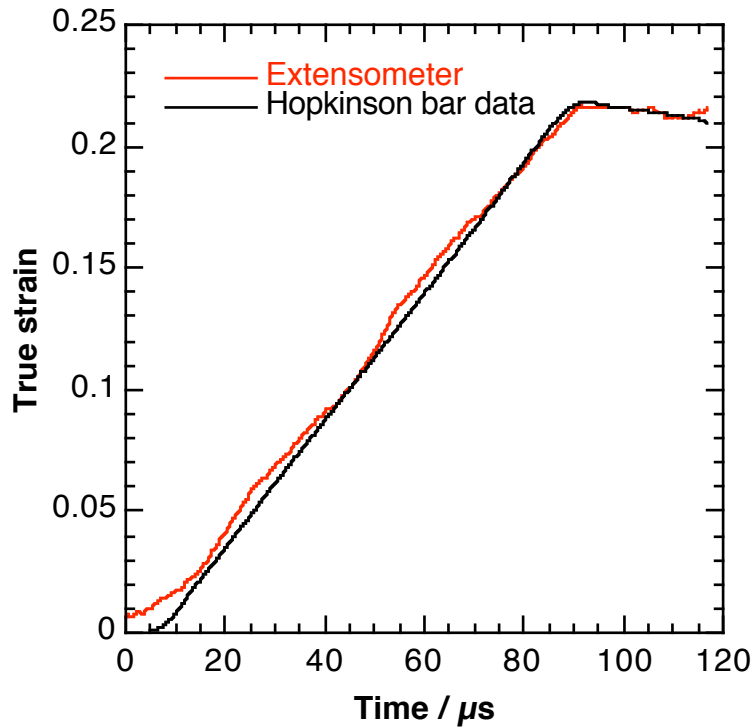


Figure 6.4. Comparison of the strain time curves obtained from the extensometer and the Hopkinson bar equations.

6.3 LINE LASER

Experimental

A diode line laser was mounted with the plane of the line perpendicular to the direction of the bars. A slit of variable width was then mounted in front of the laser, so that a thin line of light was projected across the specimen. On the other side of the bar, a lens was used to focus the light onto a photodiode. The electrical current output from the photodiode was passed through a resistor producing a voltage which was recorded using an oscilloscope. Because the specimen casts a shadow, the photodiode output decreased in proportion to increasing specimen diameter, allowing the diameter to be calculated. A schematic diagram of the experimental optical arrangement is shown in figure 6.5.

The slit was used to increase or decrease the width of the line. A wide slit decreases the spatial resolution along the specimen, but increases the accuracy of the measurements of the specimen diameter. A narrow slit allows thinner specimens to be used without the bar ends interfering with the measurements.

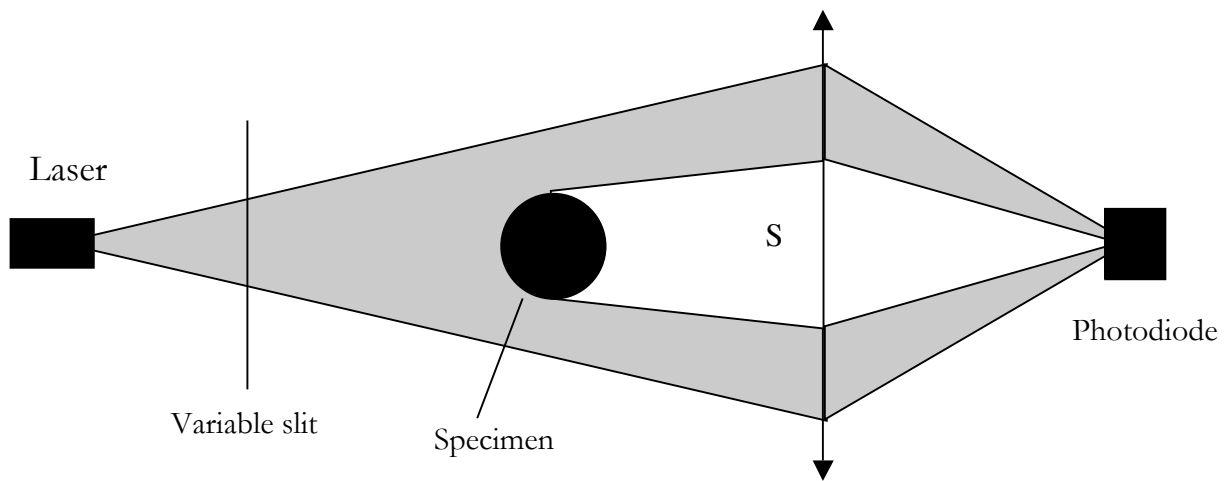


Figure 6.5. Schematic diagram of the laser and photodiode arrangement for measuring the specimen radius.

Before use, the apparatus was calibrated using a metal rod machined to have a series of steps in its diameter attached to the end of one of the bars. Whilst it was possible using this method to produce a curve relating the diameter to the normalised photodiode output (photodiode output divided by unobstructed output), it was found to be more accurate to perform a calibration for each line width used (defined by the unobstructed output). A typical calibration curve is shown in figure 6.6.

If the specimen conserves volume, then the true strain measured using the diameter is half of the longitudinal true strain, so a plot of $2 \times$ (diametric strain) can be compared to the compressive strain calculated from the Hopkinson bar equations.

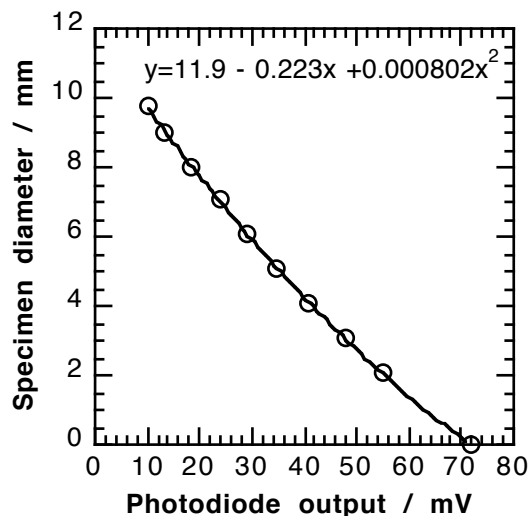


Figure 6.6. Calibration curve for the laser diameter measurements.

Results

Initially, results were complicated by interference produced by the ends of the bars. By decreasing the slit width, and moving the line closer to the output bar, this could be removed. Figure 6.7 shows one of the successful results that were then obtained. Although the voltage traces could be very noisy, a suitable smoothing algorithm allows them to be compared with the Hopkinson bar equations. In this case, the dural specimen did not compress, which is in agreement with the expected results, and also the work of Ramesh and Narasimhan (1996). Most of the noise was digital noise from the oscilloscope; although this was set to its highest possible voltage resolution the signals were often very small. This method is now used for checking and correcting the stress measurements from the Hopkinson bar equations. In particular, if the diametric strain is half of the compressive strain calculated from the equations, this gives confidence in the true stress calculations. Application 1 also gives a comparison between the line laser, and Digital Speckle Photography for measuring a high-rate Poisson's ratio for a few materials.

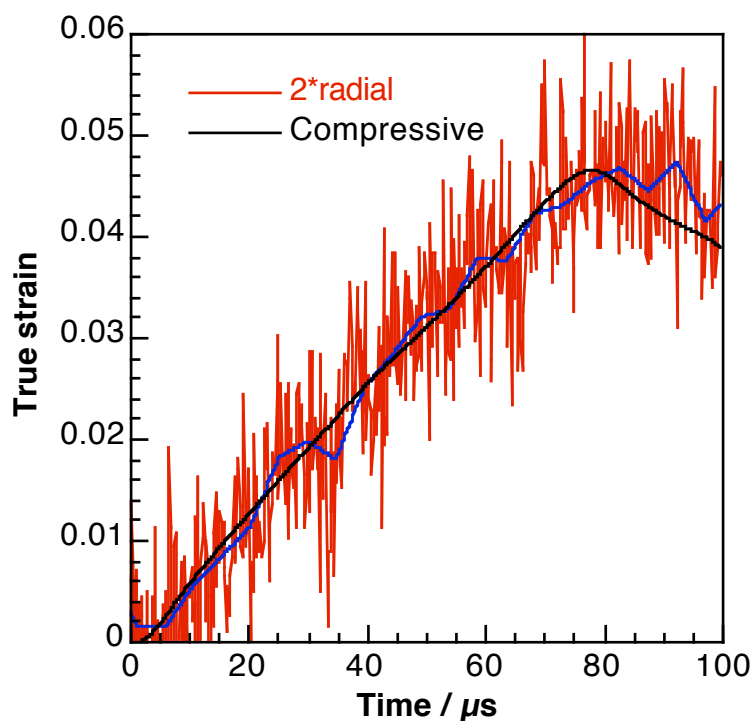


Figure 6.7. Comparison of the compressive strain calculated from the Hopkinson bar equations, and the radial strain from the line laser. The blue line shows a weighted average of the line laser data. These data are consistent with conservation of volume in the specimen.

Possible improvements

There is a major problem that can make the line laser difficult to use in practice: uneven light intensity along the line. The centre of the line is brightest, with the intensity decreasing towards the edges. This means that the specimen had to be centred very accurately in the bars for the calibration to be valid. Since the

experiments in this chapter were carried out, an even light intensity line laser has been obtained, and it is hoped that this will make the experiments easier.

Another important observation about the optical system used in both this experiment and previous systems regards the production of the line. A so-called 'line laser' is actually a fan laser: the light originates at the opening of the laser (which has a finite, but small, size), and then fans out at a given angle. This means that the shadow cast by the specimen does not have parallel sides but continues to spread out along with the fan. As long as the calibration has been carried out under the same conditions, this does not necessarily produce an inaccuracy. However, another improvement to the system would be to use a collimating lens between the laser and the specimen.

6.4 DIGITAL SPECKLE PHOTOGRAPHY

Background

High speed photography is a commonly used technique, and can give quantitative information about the movement of specimen and bar boundaries. If we need to know the movement of another point on a specimen, we might put a dot on its surface of a different colour to the specimen material. It would then be possible to follow the motion of this dot between photographs. The error in the measurement would be limited to either the size of the dot or the resolution of the camera, whichever is greater. If, instead of measuring the movement of just one position, we wanted to measure displacements point-to-point over a whole surface the process would be far too time consuming. Moreover, it would be impossible to know which dot in the first image corresponded to which in the later images. If, however, a random pattern of dots is applied to the surface there would be no repetition of the pattern, and hence no two regions on the surface would look the same. By analysing the patterns of dots in the sequence of images, it is possible to measure the motion of the dots and hence the surface deformation of the specimen, as long as the pattern is known to move with the surface. This technique is known as speckle metrology (Gåsvik 2002; Sjödahl 2001).

Early methods of making these measurements used so-called 'double exposure speckle photography'. A photograph was taken before the deformation of the specimen, and another during the deformation, on the same film. This produced a picture consisting of the two speckle patterns slightly displaced from each other. In order to extract the displacement information the film was illuminated using a laser beam. The diffraction pattern produced by this illumination contained fringes whose spacing represented the displacement between the two images at the illuminated point. The process can then be repeated to produce a displacement field across the negative. However it is very tedious, and in the 1980s the increased use of desktop computers led to methods of automating the process (Huntley 1989).

Computers also allowed a new method of comparing the two images to be developed. The images are first digitised. Then a region (subimage) is selected from

the first photograph and compared sequentially to subimages from the second. These subimages are selected from the second photograph by moving around pixel by pixel. For each position a correlation value is calculated, which is effectively a measure of how similar the two subimages are to each other. The maximum of this correlation value corresponds to the displacement between the two images, at the position of the first subimage. This method was first used by Peters and Ranson (1982), and then developed further by Sutton *et al.* (1983). By choosing a small enough subimage, it is possible to account for distortion and rotation, basically by assuming that for a sufficiently small region straight lines deform to straight lines. The calculations can be performed more quickly by the computer by performing the correlation in the frequency domain rather than the spatial. The calculation of the Fast Fourier Transform (FFT) of the image allows very efficient evaluation of the correlation coefficient. This is the method used in the algorithm adopted in this research, developed originally by Sjödahl and Benckert (1993; 1994) and Sjödahl (1994). The basic points of this algorithm are now described.

The two images are denoted b_1 and b_2 , and from these subimages b_{s1} and b_{s2} are selected. These subimages are squares with sides n_1 and n_2 respectively (one of the consequences of using the FFT is that n_1 and n_2 must be integer powers of 2). The Fourier transforms of these images are defined as

$$H_{s1}(r, s) = \mathcal{F}(b_{s1}) = \frac{1}{m} \sum_{k=0}^{m-1} \sum_{l=0}^{m-1} (b_{s1}(k, l) \exp(-2\pi i(rk + sl)/m)), \quad (6.2)$$

where $m = n_1 + n_2$, and similarly for H_{s2} . Note that the two subimages must be padded out with zeros or greyscale to have sides of length m . The correlation coefficient is then

$$c(k, l) = \mathcal{F}^{-1}(H_{s2}^H H_{s1}), \quad (6.3)$$

and has a maximum at the values of k and l corresponding to the x- and y-displacements between the two images (call these k_x and k_y). At this point k_x and k_y are integers. This operation can be considered as equivalent to sliding the two subimages over each other in the spatial domain.

If there is no distortion between the two images, then the value of c at the maximum is 1. If there is distortion it will be less than one, and the peak of the surface described by c may not be sharp. In practice, b_{s1} is initially made larger than b_{s2} to increase the chance of successful peak detection. The size of b_{s1} is then reduced to be the same as that of b_{s2} , and it is re-centred according to the previously estimated translation. This increases the similarity between the two images, and therefore the size of the correlation peak, which is also now centred on the origin. By repeating the shifting, calculation and re-centring, an accurate value of displacement (to the nearest pixel) can be found.

In order to increase the accuracy of the displacement measurement to less than a pixel, it is possible to expand the correlation surface c in Fourier space to give a continuous correlation function

$$u(a, b) = \frac{1}{P^2} \prod_{k=0}^{P-1} \prod_{l=0}^{P-1} c(k, l) \frac{\sin[\Box(a \Box k)] \sin[\Box(b \Box l)]}{\sin[\Box(a \Box k)/P] \sin[\Box(b \Box l)/P]}, \quad (6.4)$$

where P is odd. Increasing the value of P increases the accuracy of the approximation, but also increases the computing time. In practice, a value between 5 and 10 is sufficient. The maximum value of u is then found using a maximum search routine known as Brent's method, to give new non-integral values of k_x and k_y . The random error in this value is given by

$$\epsilon \Box 0.66 \frac{\Box}{n\Box^2}, \quad (6.5)$$

where the error ϵ , the speckle size \Box and the subimage size n are all in pixels, and \Box is the degree of correlation, which ranges from 1 for perfect correlation to zero for no correlation.

It is important to note that even if there is no distortion of the object, there may still be some random error in the result. This is because of the way digital cameras work. If the displacement between the two images is not an integral number of pixels in both directions, what appeared on one pixel in the original image will appear spread over two in the final image. Because the value of each pixel is an average of what it 'sees', this means that a perfect overlap between the two images cannot be found. The solution to this is to again shift and re-centre one of the subimages, but this time by non-integral pixel values, as indicated by the non-integral part of k_x and k_y . This is again performed iteratively and increases the size of the correlation peak, as well as centring it more accurately and making it symmetrical about the origin (Sjödahl 1994)

The random error is now zero for a perfect correlation. In practice, this is not the case; the random errors in the new algorithm are given by

$$\epsilon = 0.7 \frac{\Box^2}{n} \sqrt{\frac{1 \Box \Box}{\Box}}, \quad (6.6)$$

In good experimental conditions this can be as low as 0.01 of a pixel (Sjödahl 1997).

It is important to note that the error in the displacement calculation decreases as the size of the subimage increases. However, choosing a very large subimage will increase the computing time and also decrease the correlation if there is a lot of

distortion between the images. In addition for a large subimage, no correction for distortions is possible, which makes the correlation peak more difficult to find and potentially decreases the accuracy. A useful feature of the implementation used in this research is that it does not produce a displacement measurement if the decorrelation is large, and it also outputs σ for each displacement measurement calculated. A further limitation of using the FFT is that the spatial resolution of the technique is limited by the Nyquist criterion. Because one measurement of average displacement is produced per correlation, the highest spatial frequency is half the subimage size. Therefore, it is usual to move the sampling window by half the subimage size between correlations: producing extra displacement values does not increase the resolution. This distance is called the step size. Overall, there is a balance between spatial resolution and displacement accuracy, which also needs to be taken into account when choosing sub-image sizes.

Experimental and speckle analysis

A number of techniques can be used to produce the required speckle pattern. Some materials have features, such as the explosive grains in a PBX, which can be resolved in the images (Rae 2002). Otherwise a good speckle pattern can be produced using the laser speckle effect, or by spray painting a pattern onto the specimen surface. High-speed cameras usually have a lower resolution than video or still cameras and, because the exposure times are very small, more contrast is needed between features that are to be resolved. Ideally, laser speckle would be used. However this requires a high power pulsed laser. And images of sufficient quality can be produced using an artist's airbrush, filled with either black paint or a thinned solution of silver dag.

In order to image the experiments, a high-speed camera is required. For these experiments a Hadland Ultra-8 camera was used. This is a digital camera that produces 8 independently triggered frames arranged into a single image as shown in figure 6.8. To allow completely independent triggering, the camera splits the incoming light into eight beams. Each of these beams is imaged on a different area of an intensified CCD array; the camera outputs a single picture that contains these 8 images, from which the individual frames are cut out. The obvious disadvantage of this system is that the light intensity is divided by 8, and more illumination is required than would otherwise have been the case. The intensification on the CCD can be set by the user, so that low light levels are overcome. However, this introduces some noise into the image and has to be kept to a minimum (between 30 and 50 on a scale of 0 to 100).

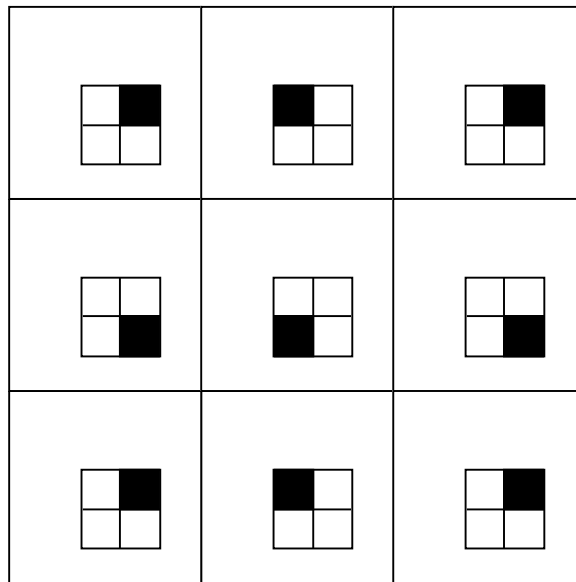


Figure 6.8. Schematic diagram showing the arrangement of the frames from the Ultra-8 camera. Also showing the relative reflections of the image between the frames. Frame 1 is actually a mirror of the object.

The main advantage of using a digital camera is that the frames can be cut out of the image very accurately, so that fiducial markers are not required in the pictures. The resolution of the Ultra-8 is 512 x 512 pixels. This is equivalent to that which is obtained if a polaroid image from an analogue camera, such as the Imacon 790 or Ultranauc 501, were scanned using a 1200 dpi scanner. However, images from analogue cameras can be photographically enlarged to increase the scanned resolution, and therefore using the Ultra-8 did sacrifice some resolution.

Illumination was initially provided by a Pallite-VIII lamp. This consists of 8 high-power (400W) halogen bulbs, arranged in a ring. The camera lens points through the ring, which means that the illumination is axial and no shadows are formed. Unfortunately, the very high power means that the specimen rises in temperature by about 10 K in about 30 s, so the lamps had to be turned on just before performing the experiment. Later it was found that using two flashes, one above and one below the specimen, provided better illumination.

When taking images for quantitative analysis, it is important to align the camera correctly. This was achieved *in situ* by making cross hairs on either side of a 50 mm diameter polycarbonate cylinder. The cylinder had endcaps with 12.7 mm diameter holes in their centre. This allowed it to be mounted on the ends of the input and output rods, where the specimen would eventually sit. The camera was then adjusted until the cross hairs in the viewfinder were aligned with the cross hairs on both the front and rear faces of the cylinder. At this point, the camera was looking down a radius into the specimen, achieving an accuracy of about 0.1°. It will be shown in Appendix 1 that only the longitudinal alignment was important, and radial strains could be calculated accurately for any alignment.

The flash and camera were triggered using a make-trigger consisting of two thin copper strips stuck to the front of the input bar, where they were shorted by the impact of the striker bar. The camera has an internal timer that was used to send a trigger immediately to the flashes. These take about 80 – 100 μ s to warm up to full brightness, and so the first photograph was set to start 100 μ s after the initial trigger. The input rod has a length such that an elastic wave takes about 100 μ s to traverse it, but the trigger ‘makes’ i.e. shorts about 10 μ s before the incident pulse is actually introduced into the rod. This delay ensures that the first photograph was taken before the incident pulse arrives at the specimen. An output was sent to the oscilloscope at the same time as the first photograph was taken, allowing the individual photographs to be related to the specimen strain-time or stress-time curves. The interframe and exposure times were varied for the different experiments, but the exposure times were eventually reduced to 1 μ s (the loading pulse being between 80 and 100 μ s long).

Once the photographs had been taken, a Matlab routine was used to extract the 8 frames from the image, and also to rotate and reflect them to the correct orientation*. They were then analysed using an implementation of the Sjödahl algorithm described above. The program outputs a number of two-dimensional data arrays, of which the most important are the x-displacement, y-displacement and correlation factor. There is also an error output, which is zero if the algorithm was able to find a suitable correlation, and 1 if it was not. In the latter case the displacement returned is exactly zero.

These values are given at a series of co-ordinates, the distance between them being set by the user: this is called the step size. The user is also able to select the subimage size. As described above, there is a trade-off between the two. In practice, most of the experiments reported here were first analysed with a subimage size of 64 pixels and a step size of 32, and then re-analysed with a subimage size of 32 and a step size of 16. These values were found to be appropriate for the overall image size of 512 x 512 pixels, the coarser one giving 5 or 6 measurements over a specimen, and the finer one usually working, but sometimes not. Using a window size of 16 pixels very rarely worked.

When performing the calculations it is important to correct distortions of the image between the 8 frames, which are introduced by the optical system of the camera. These are shown in figure 6.9, where the larger quivers represent movements of approximately 4 pixels, or strains of approximately 1.5 μ m on a 256 pixel long specimen. In many of the experiments, these were large relative to the displacements measured. However, they are consistent between images, and can therefore be subtracted from the results. In order to allow the correction to be made, a static image was taken before the experiment, and a moving image during it. Two different comparisons can be used; these are illustrated in figure 6.10, and proceed as follows:

* DM Williamson wrote this algorithm and the Matlab interface for the speckle correlation. The computer program for the analysis was provided by M Sjödahl.

- In the first, each static frame was compared to the corresponding dynamic frame. This gave the displacement field as a function of time, and also removed distortions due to the optical system of the camera. However, at large strains the algorithm was unable to work because the correlation became too small.
- For large strains the correlations were carried out between the dynamic frames and between the static frames. Any distortion due to the optical system in the camera was calculated by the correlation between the static frames. Therefore by subtracting the static displacements from the dynamic ones the actual movement of the specimen between frames was calculated. These displacements could then be added to give the overall displacement at any time. This allows larger overall displacements to be measured, because the distortion between individual dynamic images is small.

The first method was used in all of the results presented in this chapter, with the exception of the Brazilian test data.

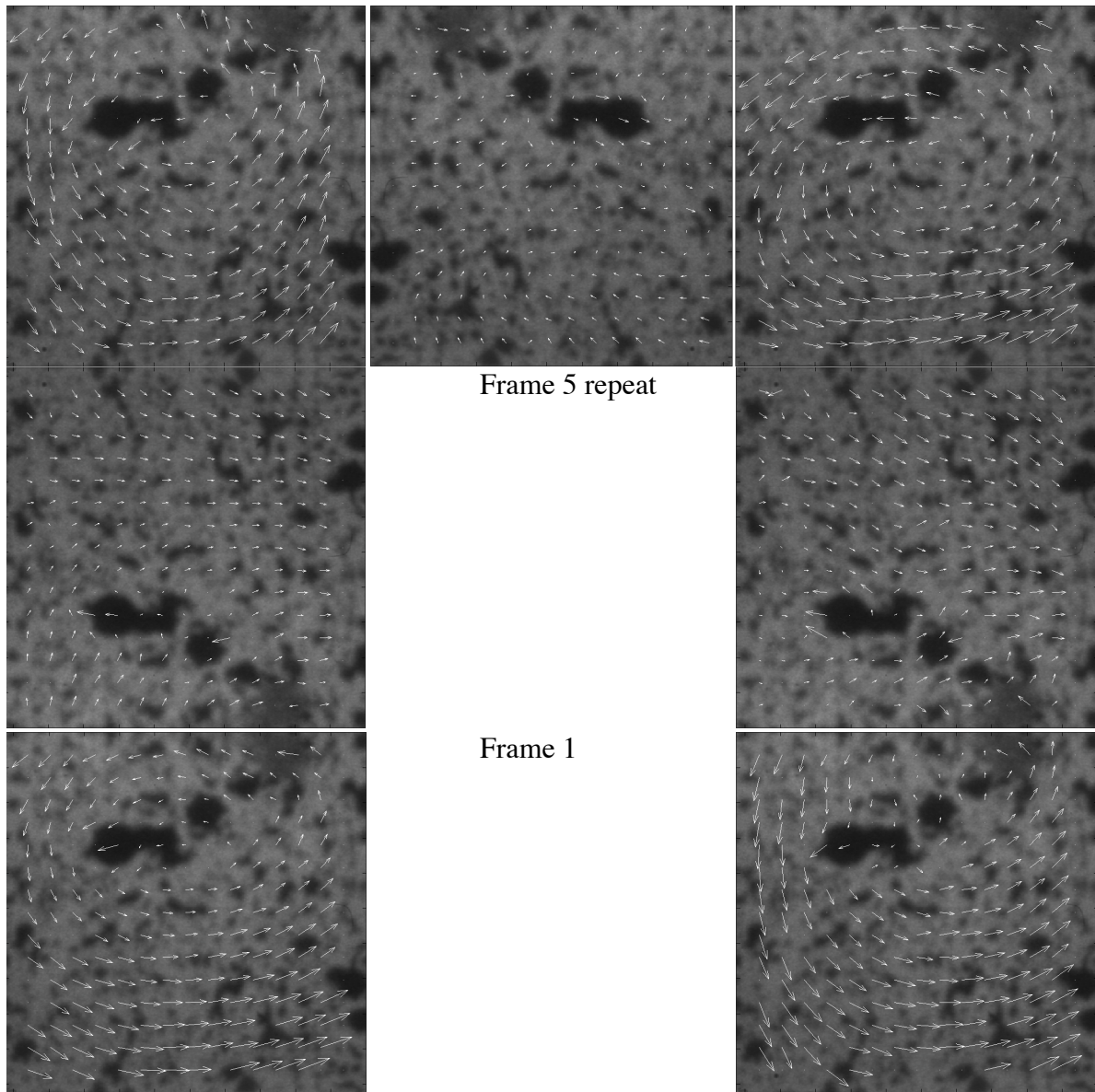
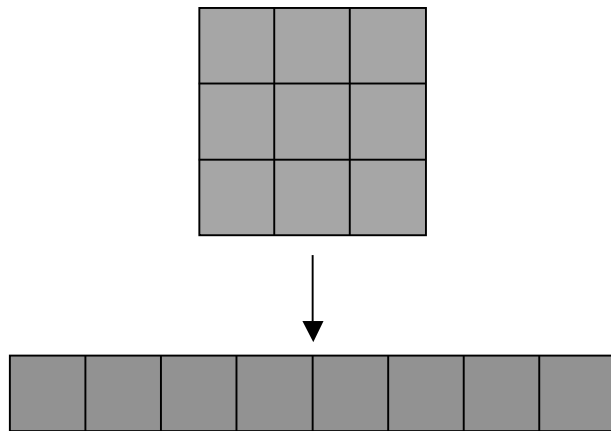


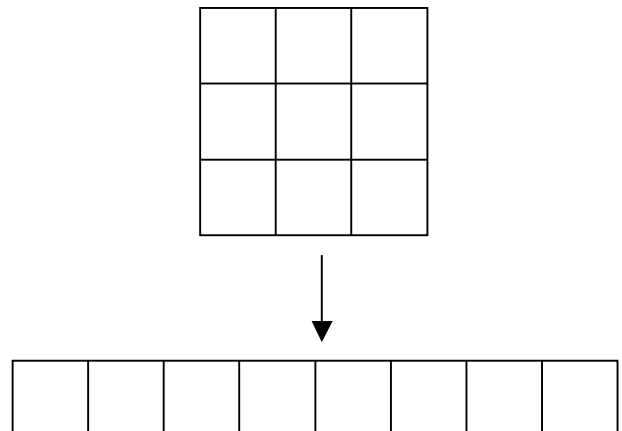
Figure 6.9. Quiver plot illustrating the distortion in each of the Ultra-8 frames relative to frame 1. The scale of the quivers is magnified 5 \times .

Figure 6.10. *Following page*. Schematic diagram showing how the speckle images can be processed to give displacement fields.

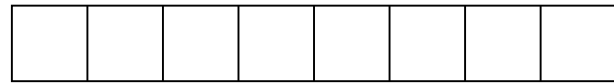
Dynamic Image



Static image



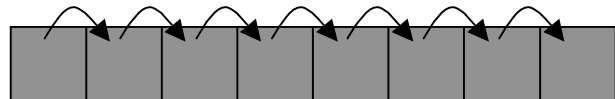
Method 1



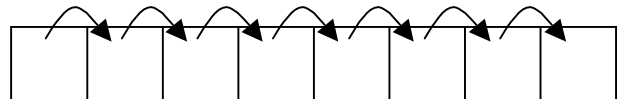
$Disp_1$ $Disp_2$ $Disp_3$ $Disp_4$ $Disp_5$ $Disp_6$ $Disp_7$ $Disp_8$



d_1 d_2 d_3 d_4 d_5 d_6 d_7



s_1 s_2 s_3 s_4 s_5 s_6 s_7



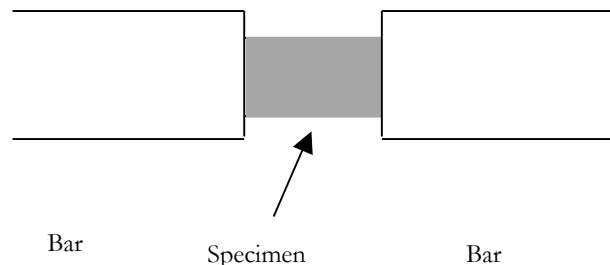
Method 2

$$D_1 = d_1 - s_1$$
$$D_2 = d_2 - s_2 \text{ etc}$$

$$Disp_1 = D_1$$
$$Disp_2 = D_1 + D_2$$
$$Disp_3 = D_1 + D_2 + D_3 \text{ etc}$$

Initial results, analysis of displacement information and errors

Figure 6.11 shows the first speckle image taken with the system. The specimen was made from polybutylene terephthalate (PBT). It sits between the bars (which cannot be seen in the picture) which are oriented horizontally thus:



This material was chosen because it is white and readily available in 10 mm diameter rods, allowing large specimens to be machined. It is a polymer with a similar strength to polycarbonate, and a low sound speed ($1.3 \text{ mm } \mu\text{s}^{-1}$). The quality of the images has been improved since this picture was taken, firstly by improving the speckle quality, figure 6.12, and then by improving the lighting by using flashes, figures 6.13 and 6.14. The exposure time is now typically 1 or 2 μs . From these photographs of specimens in the Hopkinson bar sensible estimates of specimen strain can be made, both longitudinally and radially.

In order to calculate radial strain, the first requirement is a relationship between the strain measured on the photograph and that in the specimen. The photograph used in the speckle analysis is a two-dimensional projection of a three-dimensional, cylindrical, object. Fortunately the geometry is such that the diametral strain in the specimen is the same as the strain measured in the y direction on the photograph. This is shown in Appendix 1.

The first step in calculating the strain is to remove spurious data points. There are two causes of such data. The first is the zero displacement returned if the algorithm was unable to find a match for a specific region (this usually occurs for large distortions, but can also happen if a region leaves the field of view). Since strain calculations involve determining a gradient, zero values in a region of large displacements will have much more effect than those in regions of small displacement, and cause the gradient to be too small. This then appears as too small a strain. In addition, Rae (2000) found that if there are regions of low contrast on the undeformed and deformed images (these occurred in his case because of the large crystals in his PBXs) the algorithm can find a faint correlation peak in a random direction and return a spurious displacement value. He removed these by neglecting any displacement values that were more than three standard deviations from the mean, and this approach is used here.

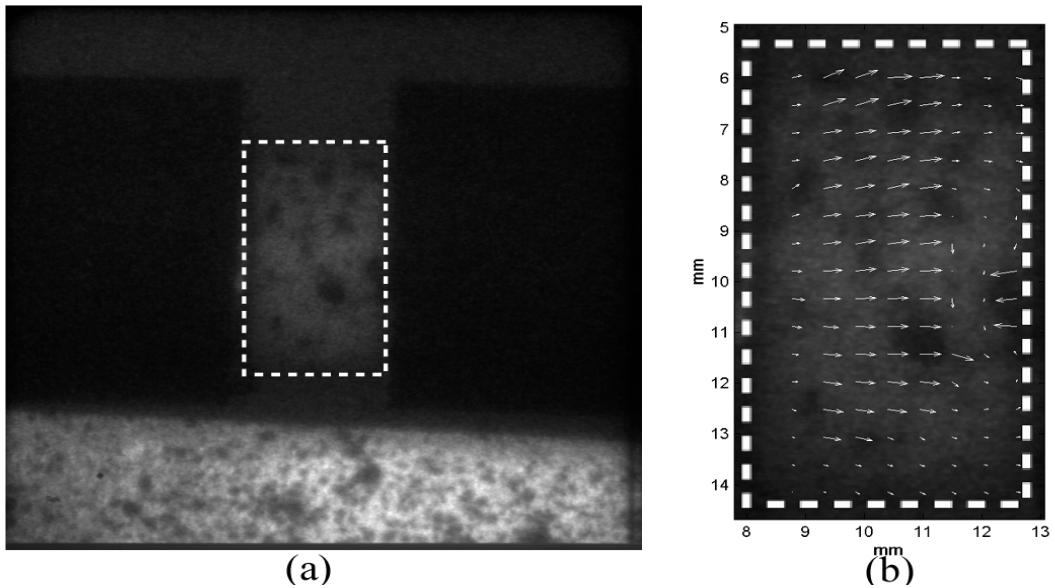


Figure 6.11. An early speckle image of a specimen of PBT. The low light levels and large speckle size meant that the image was poor, (a). However the algorithm is very robust, and sensible displacement measurements could be made (b). The ideal speckle pattern would have very evenly sized speckles. Illumination was provided by a Pallite-VIII radial lamp, and the exposure time was 20 μ s. The speckle pattern at the bottom of (a) is a fiducial marker, which was not strictly required. The specimen was positioned between the Hopkinson bars as shown schematically above.

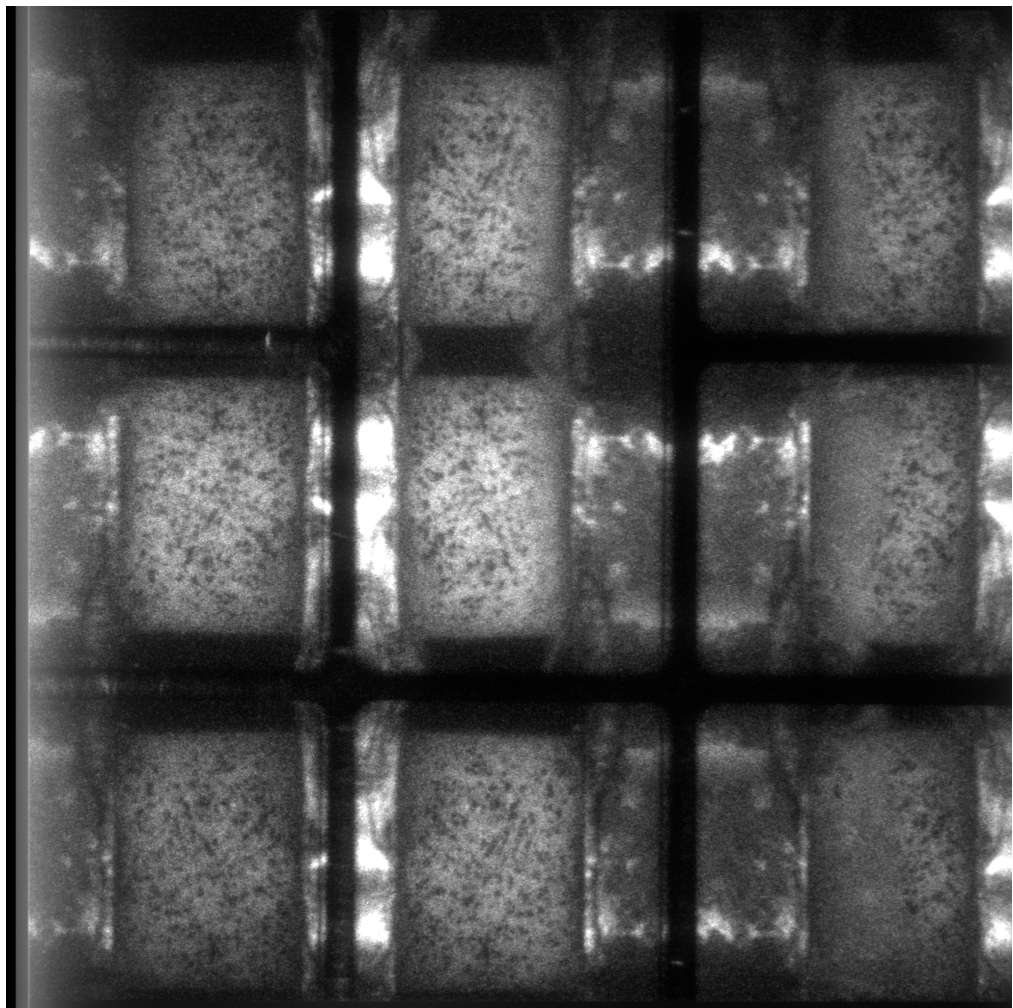


Figure 6.12. A series of images of deforming PBT. The exposure time is 20 μ s and the interframe time 0 μ s. Jetting of the lubricant can be seen in the later frames. This obscures the speckle measurements.

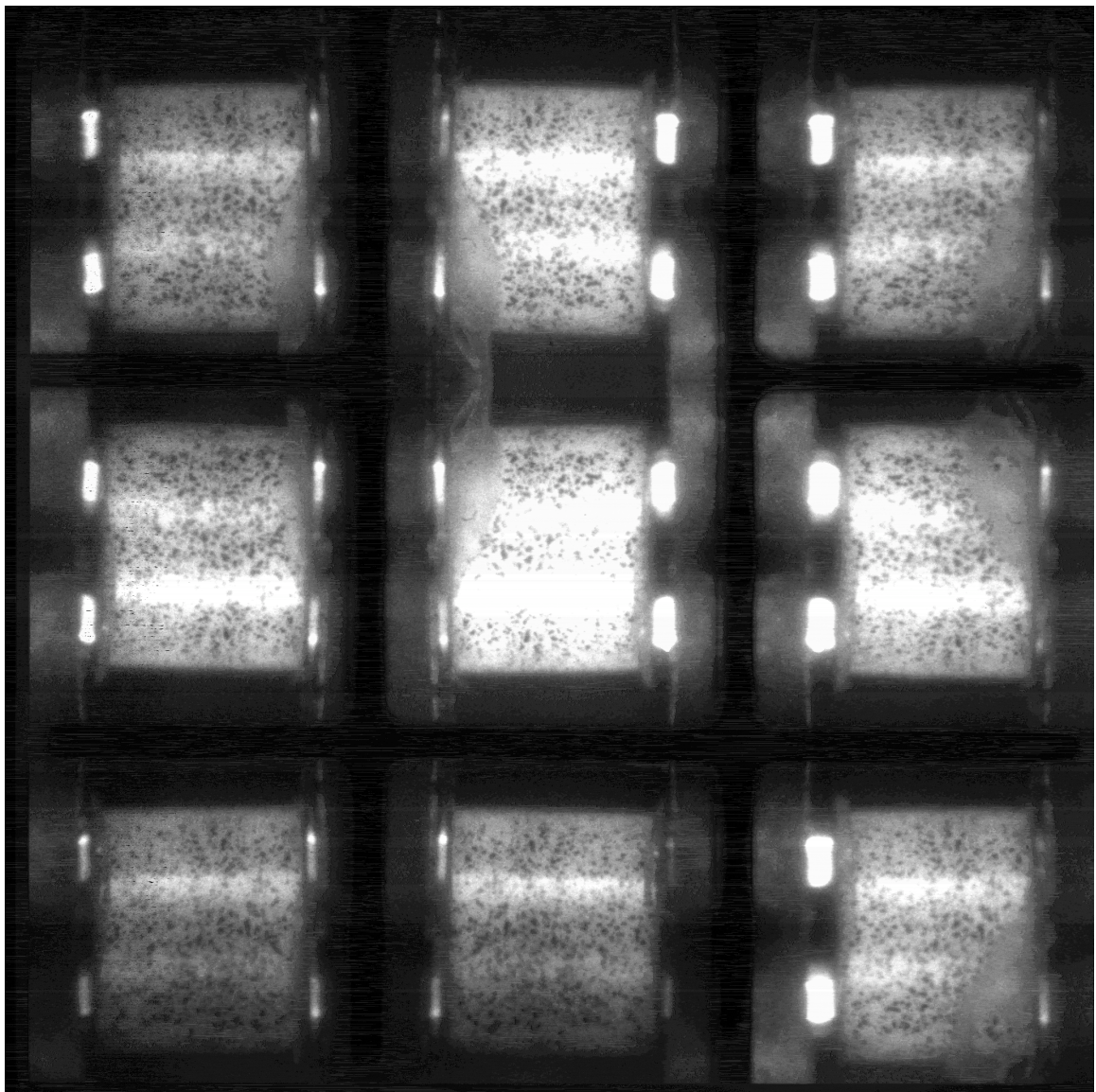


Figure 6.13. A second series of images of PBT. Here the exposure time is 1 μ s and the interframe time 14 μ s. The increased amount of light also gives more depth to the images. Note that the specimen was a right cylinder; however, the camera distorts the image slightly to make it appear like a parallelogram in cross-section.

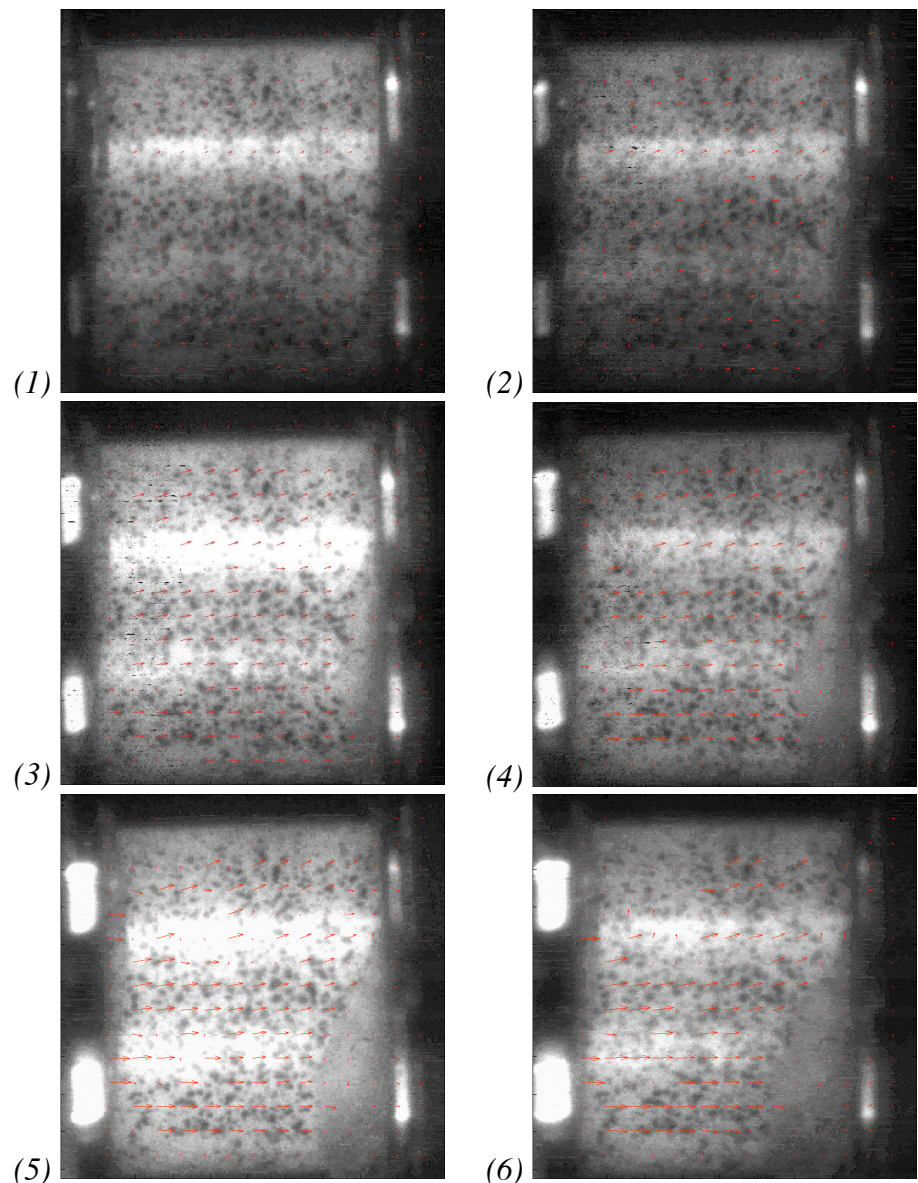


Figure 6.14. Quiver plot for the PBT specimen shown in figure 6.13.
The quivers are unscaled.

The most obvious approach to calculating the gradient of the displacements is to fit a plane to each of the two surfaces defined by the x- and y- displacements within the specimen area. The gradients of the plane in the two directions gives the two corresponding engineering strains. The units are pixels / pixels, but the numerical value is the same as for mm / mm. If the image is noisy, this method may be less accurate. It is also difficult for the user to understand and to make good judgements of the accuracy of the result.

It was generally found that the most accurate, but time consuming, way to evaluate the data was to examine each line down the specimen independently. The procedure is illustrated in figure 6.15 and described as follows: at each x -position, the average x -displacement is calculated (i.e. the average over the y -positions) along with the standard deviation. The gradient of the plot of average x -displacement against x -position gives the strain for each individual picture, figure 6.16. Repeating this for the y -displacements gives the radial strain. The final result for the specimen under consideration is shown in figure 6.17.

x_{11}	x_{12}	$x_{13} \dots \dots \dots x_{1n}$
x_{21}	x_{22}	$x_{23} \dots \dots \dots x_{2n}$
...		
x_{m1}	x_{m2}	$x_{m3} \dots \dots \dots x_{mn}$
$\square x_{i1}$	$\square x_{i2}$	$\square x_{i3}$
i	i	i
\square_1	\square_2	\square_3
$\square x_{in}$		
i		
\square_n		

Figure 6.15. Illustration of the methodology used to calculate the average x -displacements and their errors from the x -displacement values. This is repeated for every frame. The subscripts represent quiver numbers, which are related to position by the step size.

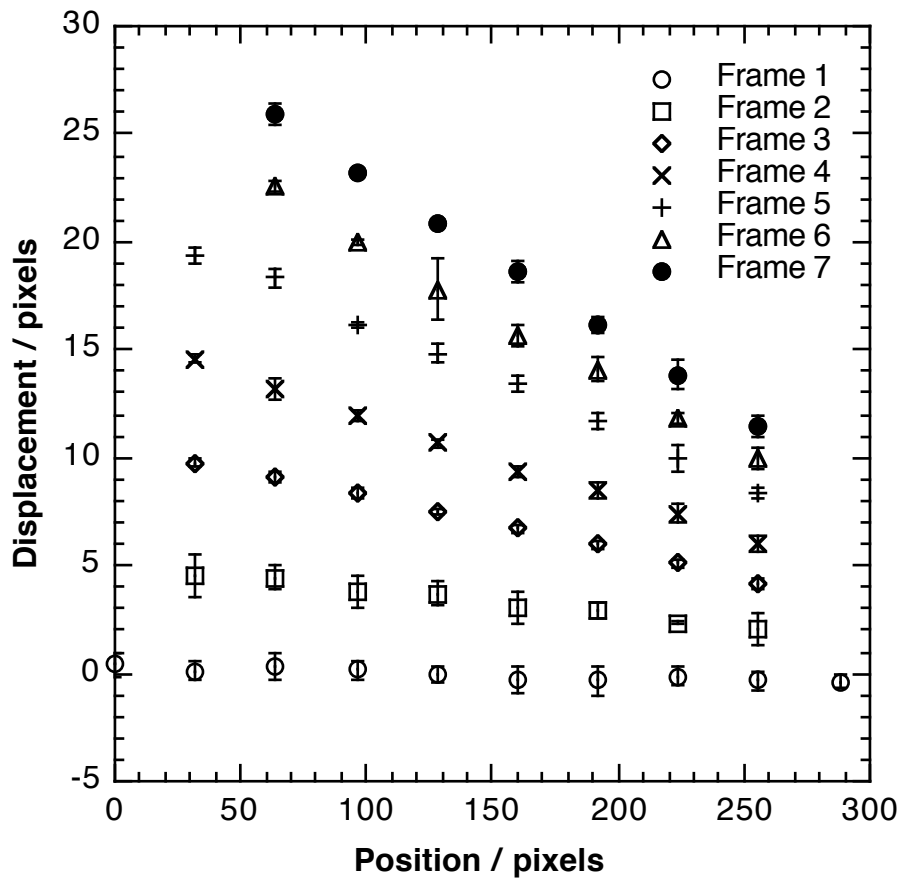


Figure 6.16. Displacement position plots for the specimen of PBT from figure 6.13, in the x direction. The gradients of the data series are equivalent to the engineering strain e in the specimen, which can be converted to true strain ϵ using $\epsilon = \ln(1 + e)$. The error bars shown on the points are the standard deviations calculated as indicated in figure 6.15.

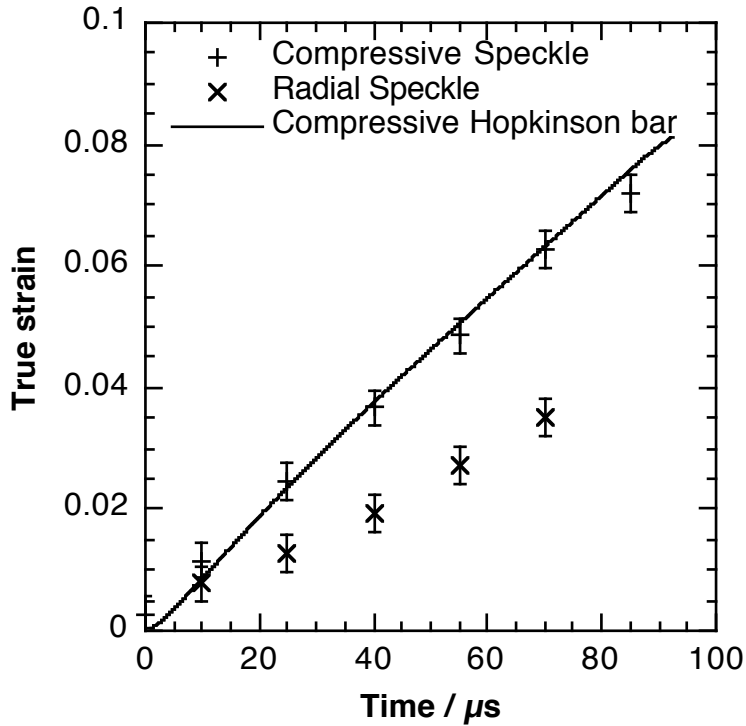


Figure 6.17. Comparison of the compressive and radial strains calculated from the speckle measurements on the PBT specimen, and the compressive strain from the Hopkinson bar equations. The error bars on the points are the errors in the gradients from the displacement position plots.

Figures 6.15–6.17 provide a good illustration of the sources of error in the measurements. Initially, there is error in the individual displacement measurements. This comes across in the standard deviation (σ) values that are shown as error bars in figure 6.16. These have two causes: the random error in the algorithm (equations 6.5 and 6.6) and inhomogeneity in the specimen movement.

In principle, it is possible to estimate the error introduced by the correlation using equations (6.5) and (6.6). However, finding the appropriate speckle size σ for each individual object would be very difficult. An approach adopted by Rae (2000) is to create a typical speckle pattern and move it by known amounts using a translation stage. The displacement values returned by the algorithm can then be compared to the known displacements. This has the advantage of allowing the whole optical system to be assessed as well as the algorithm. However, since there is no distortion of the specimen, it is an unnecessary exercise. In addition, the quality of the speckle patterns for the high-speed research was found to be more variable than for quasistatic work. It is therefore more useful to have a system for evaluating the errors on each individual set of results.

In much of this research, the speckle measurements were reduced to a single value (strain) for the whole specimen. The error in this value can be calculated as follows. Initially, the errors in the average strains calculated down and along each of the lines are given by the appropriate values of σ , which are effectively the errors in equation (6.6). This error is therefore of the order of one pixel or less.

When the averages are then plotted against position, the standard least-squares method can be used to find the error in the gradient. This is the error that is quoted in this research. Whilst in principle \square should be independent of the amount of displacement, this was found not always to be the case because of reduced correlation as the specimen deforms. In practice, this increase in \square is compensated for by the increase in displacement in such a way that the error in the final gradient calculated (and therefore the strain) is nearly always approximately constant for an individual experiment.

Of course, if individual displacement measurements are required for comparison with computer models, this is not an effective approach. In this case, we suggest two methods for calculating the approximate error in these values. If there is a region or line of constant displacement on the specimen, the standard deviation of measurements made in that region can be calculated. Otherwise, an image of the specimen can be displaced a known amount using a computer, and then compared to the undisplaced original. If desired, some 1D strain could also be imposed. The random error in these measurements, when compared to the known displacement, would give a reasonable estimate of the error in the experimental values.

Finally, there is also a time error due to the finite exposure time of the camera. In all of these data the time given for a datum point is the time at the middle of the exposure (if strains are used it will be the equivalent strain). Effectively, an error bar in the time exists stretching to the edge of the exposure time in each direction. However, comparison of the speckle data to the Hopkinson bar equations shows that in fact, displacements measured from the photographs behave as if they were taken at the middle of the exposure.

6.5 APPLICATIONS

Application 1: Measurement of dynamic Poisson ratio

When conservation of volume is used to calculate the true stress in the Hopkinson bar specimen it is assumed that Poisson's ratio is 0.5 throughout the experiment. However, this is not necessarily the case. Certainly, if the material is brittle, or a foam, then it is obvious that volume conservation will not hold. But in fact all materials are compressible to some extent. With the application of the line laser and DSP measurements, we now have two methods for calculating the radial strain in the specimen, and therefore making more accurate measurements of the true stress in the specimen. This also allows a measurement of the dynamic Poisson's ratio to be made.

The procedures for calculating the specimen radius from both methods were described earlier in this chapter. This section looks at results from three materials, dural, polycarbonate and PVDF. For the initial work on dural specimens, it was found that the line laser gave a much more useful result than the speckle for these calculations. So only the line laser was used on the polymer specimens.

Dural

Figure 6.18 shows a series of photographs from a dural specimen; the exposure and interframe times were 20 μ s. The method of calculating the average x-displacement for each x-position was found to give very good results, figure 6.19. The displacement-position plots had very little scatter throughout the experiment, and therefore the error on the calculated strains was small. The values for the y strains were relatively less accurate because the measured displacements are much smaller. There was also more scatter in the y data.

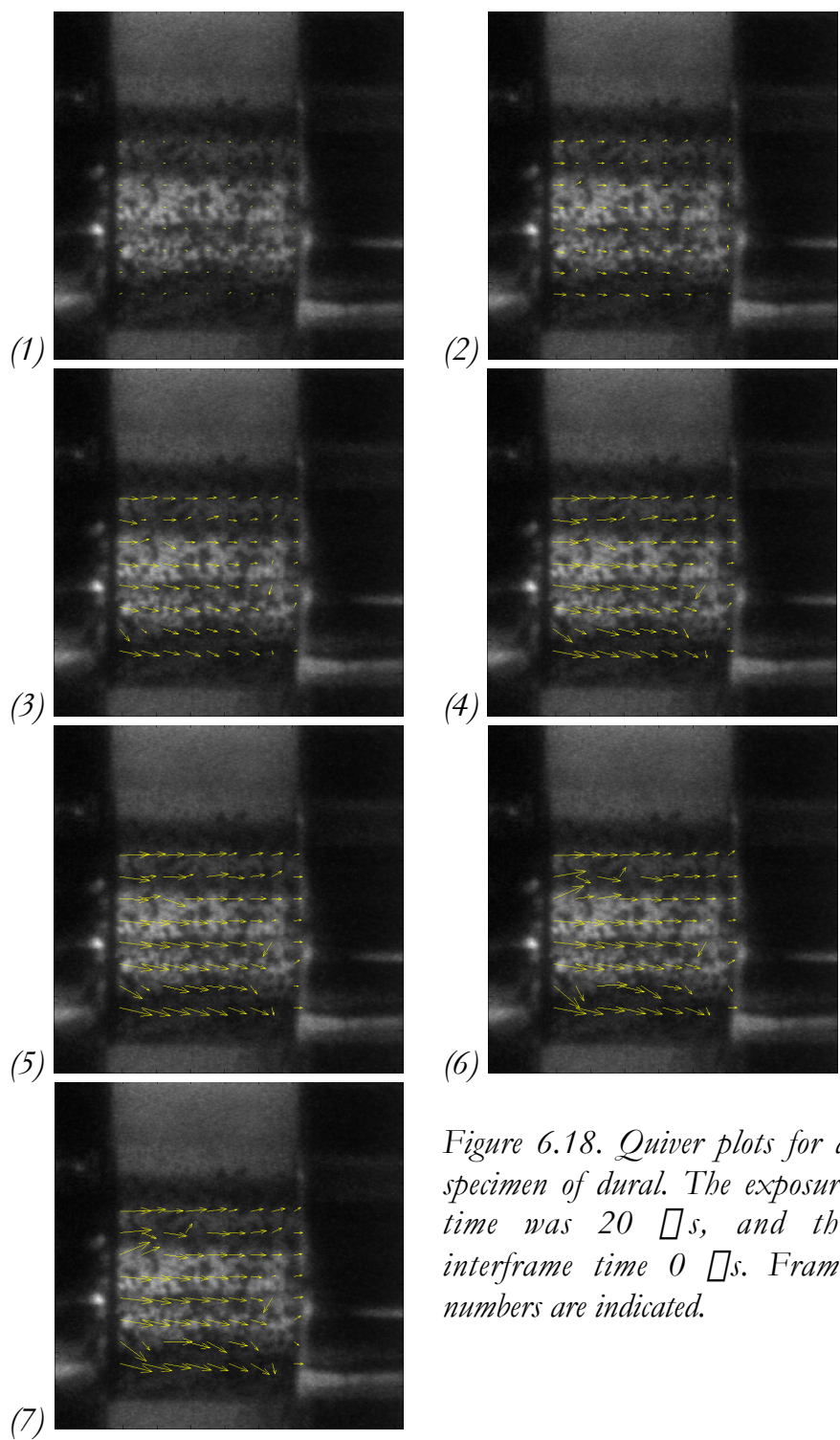
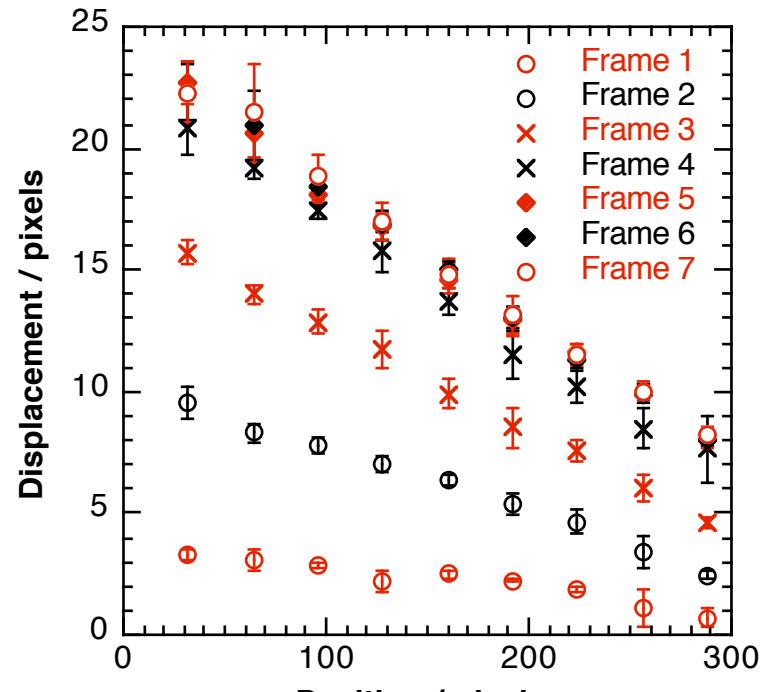
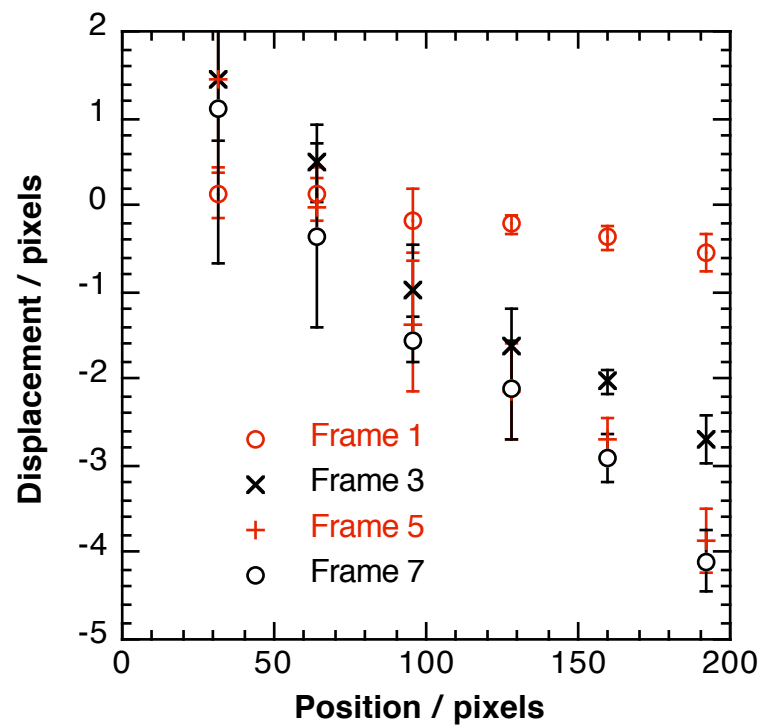


Figure 6.18. Quiver plots for a specimen of dural. The exposure time was $20 \mu s$, and the interframe time $0 \mu s$. Frame numbers are indicated.



(a)



(b)

Figure 6.19. Displacement-position plots for a specimen of dural in (a) the longitudinal direction and (b) the radial direction. Note that there is more scatter in the radial data. This is reflected in the increased error on the strain-time plot, figure 6.20.

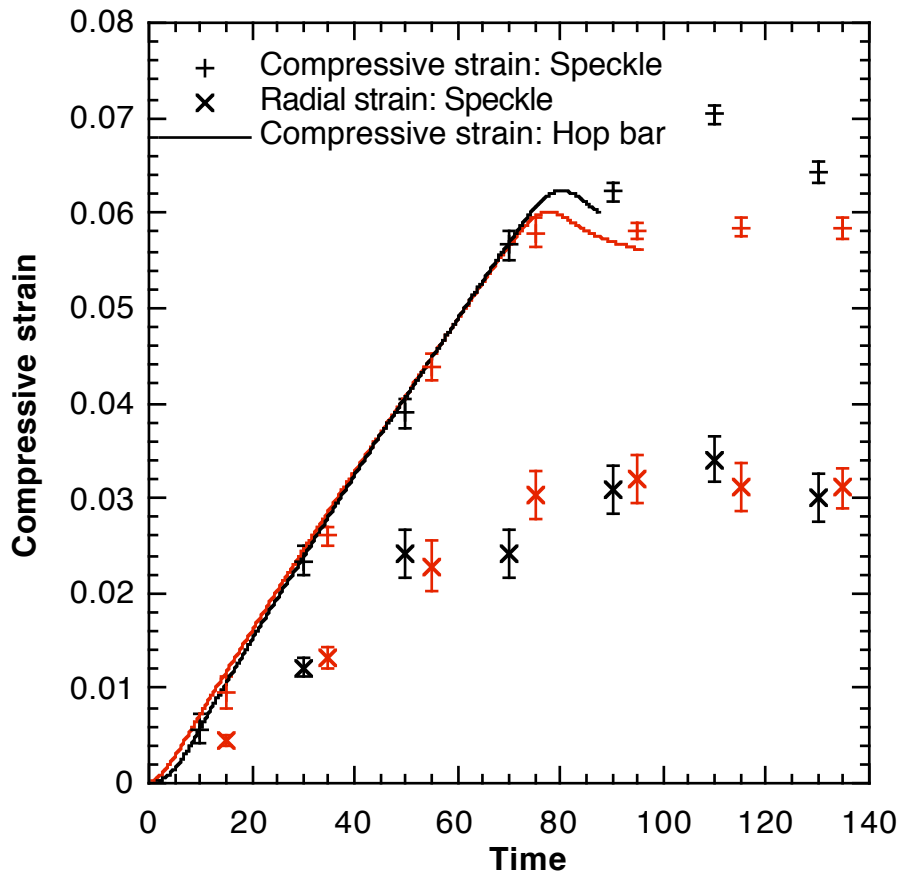


Figure 6.20. Strain time data for compressive and radial strains calculated from the speckle measurements for dural. The strain-time curve from the Hopkinson bar equations is also shown. The two different colours represent two specimens.

Results from the strain calculations are shown in figure 6.20. The longitudinal strains calculated from the speckle agreed very well with those calculated from the Hopkinson bar equations and the radial strains were approximately consistent with volume conservation, although one of the specimens (plotted red) gave better results than the other (black). When Poisson's ratio is calculated from these experiments and plotted against compressive strain, Figure 6.21, the results show a lot of scatter, probably mostly due to that in the radius calculations. The average values of Poisson's ratio are 0.52 ± 0.03 for the 'red' results, and 0.50 ± 0.07 for the 'black' results.

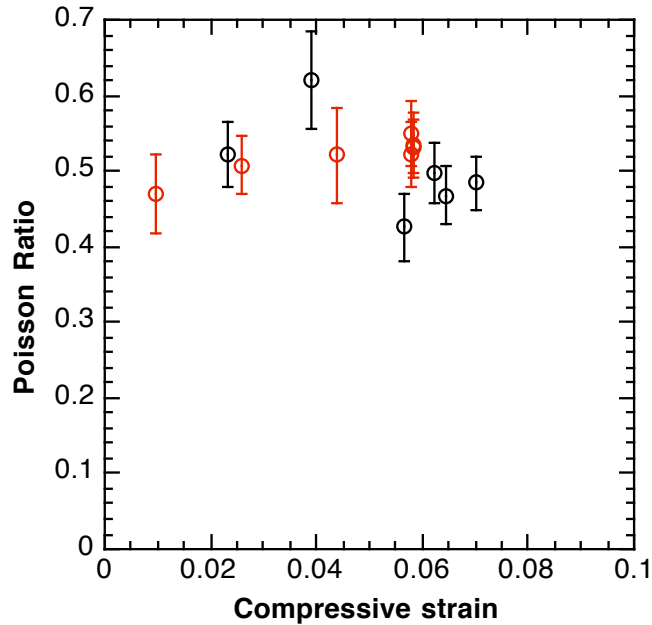


Figure 6.21. Poisson's ratio calculated for each frame of the two dural experiments presented in figure 6.20. The mean values are 0.52 ± 0.03 for the red results, and 0.50 ± 0.07 for the black results.

A result from using the line laser was shown in figure 6.7. Here the radial strain calculated from the line laser measurements is doubled, to make comparison with the longitudinal strain from the Hopkinson bar equations easier. Whilst the results from the line laser are noisy, they are consistent with volume conservation in the specimen. The two strain values, as functions of time, were used to calculate Poisson's ratio. A plot of Poisson's ratio against compressive strain is shown in figure 6.22. The corresponding stress-strain curve is given on the same plot. The data at the beginning of the curve are especially noisy, since the denominator in the division is very close to zero. Although the data look to lie mainly above the $\square = 0.5$ line, the line of best fit shows that a value of 0.5 is appropriate during the plastic section of the stress-strain curve. A value of 0.5 is in agreement with the observation of Ramesh and Narasimham (1996) that dural conserves volume in Hopkinson bar experiments. It should be noted that whilst the accepted value of \square is 0.345 for dural this is a low strain 'elastic' value, and plastic deformation usually conserves volume.

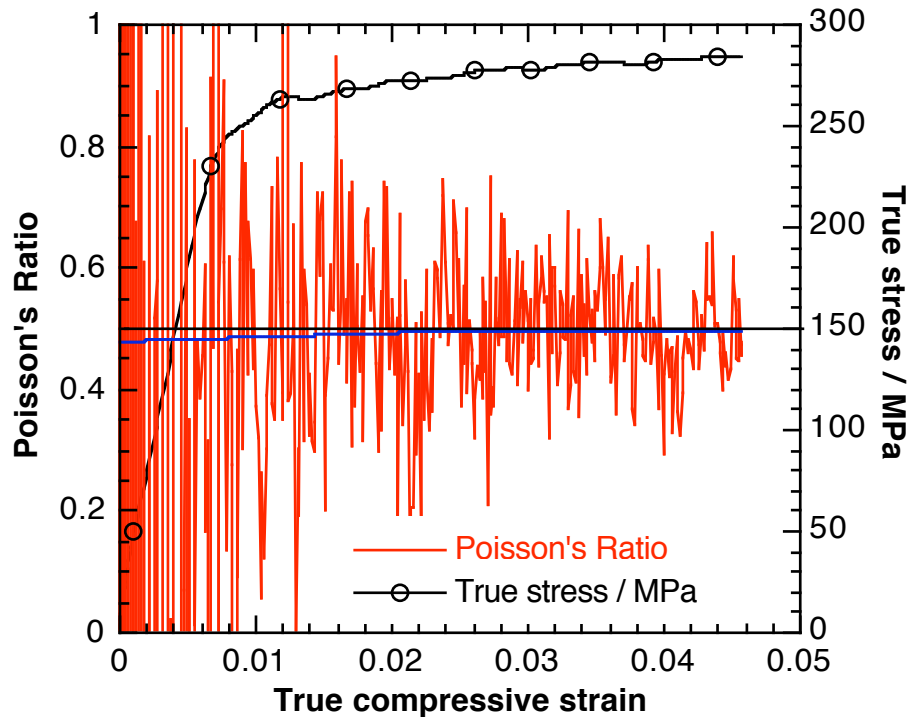


Figure 6.22. Poisson's ratio for a specimen of dural, calculated from line laser results, compared to the stress-strain curve for the same specimen. The blue line is a heavily weighted smooth of the Poisson's ratio data.

Polycarbonate

In chapter 5, data are presented from Hopkinson bar experiments on polycarbonate and PVDF over a wide range of temperatures, and strain rates. It was therefore natural to apply the new line laser technique to these two materials. An initial, noisy, result from polycarbonate is given in figure 6.23. An improvement to the line laser measurement was made by increasing the intensity of the laser (simply by increasing the supply voltage slightly). This led to the results shown in figure 6.24. The small strain value of Poisson's ratio, calculated using elasticity theory from the manufacturer's data for elastic modulus and density was 0.39. It is important to note that this is a *small strain* value, rather than a *quasistatic* value: if the elastic modulus is calculated using ultrasonic measurements the strain *rate* may be very high even though the strains are small.

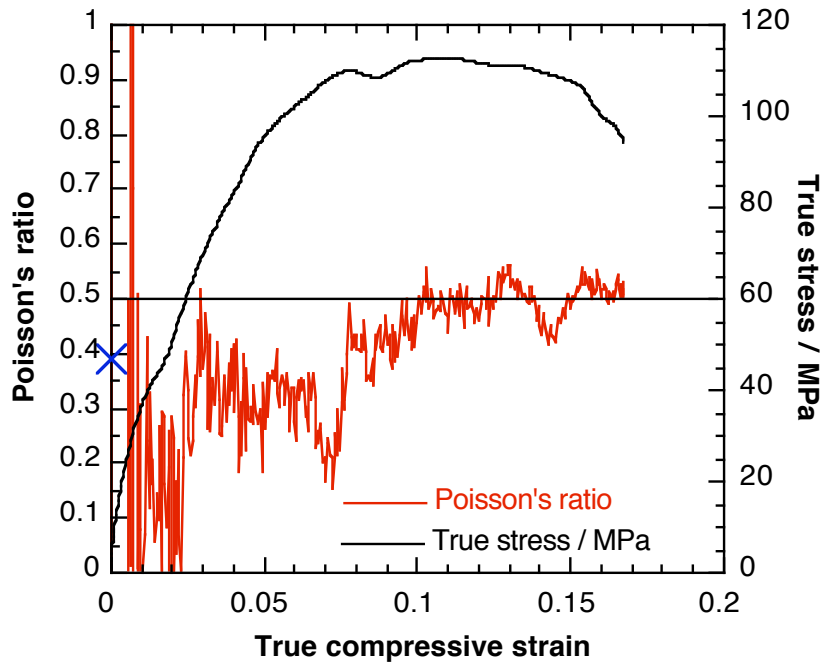


Figure 6.23. Poisson's ratio for a specimen of polycarbonate, calculated from line laser results, plotted along with the stress-strain curve for the same specimen. The strain rate was 2230 s^{-1} .

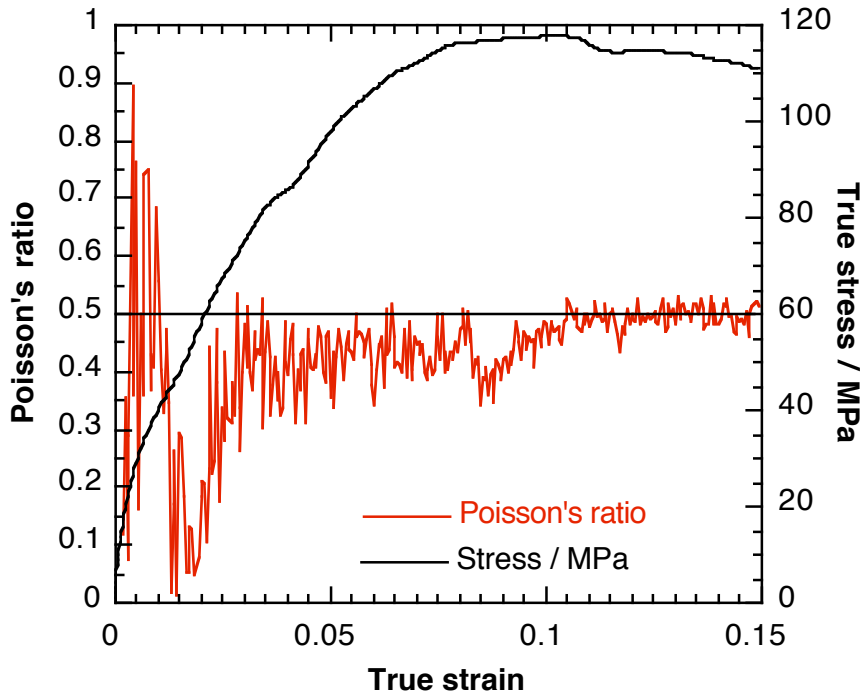


Figure 6.24. Poisson's ratio for another specimen of polycarbonate. By increasing the voltage input to the laser diode it was possible to increase the light output and therefore reduce the noise. Of course this cannot be done indefinitely! The strain rate was 2240 s^{-1} . The dip at a true strain of 0.03 may be due to inertia.

When these results are compared to the stress-strain curve a very interesting feature emerges. Once the initial noise settles down, the Poisson's ratio has a steady value, which then drops suddenly before rising to 0.5. This drop and rise coincides with the yield on the stress-time curve, and may give a clue as to the processes occurring at yield. Note that because true strains are used, the strain relative to the undeformed specimen is the same as the incremental strain.

PVDF

Unfortunately the results for PVDF were not as encouraging as those for polycarbonate. Figure 6.25 shows a typical example. In all cases the line laser initially showed a small initial change after which the diameter appeared to increase dramatically. It is very likely that this is because of interference from the bars, since the specimens were relatively thin (approximately 3.2 mm). However, if the line laser measurement were correct it would mean that the true stress values calculated for PVDF are wrong. A further problem with some of the PVDF experiments was that the recovered specimen was cone shaped, one end of the specimen having expanded laterally dramatically more than the other.

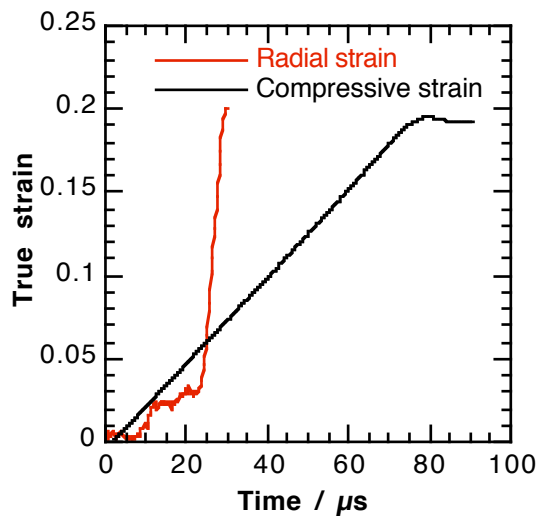


Figure 6.25. Comparison of the line laser radius measurement and the Hopkinson bar diameter calculation for a specimen of PVDF.

In order to resolve these problems, high-speed photographs were taken of a PVDF specimen as it deformed. The experiment was lit from behind and as this produces a high contrast between the shadow of the specimen and the light, it was easy to use an exposure time of 1 μ s. The interframe time was 15 μ s. The photographs are shown in figure 6.26. Measurements of the specimen diameter were made, and from these the true radial strain was calculated. A comparison of the radial strains from the photographs and the longitudinal true strains from the Hopkinson bar equations is shown in figure 6.27. This comparison supports the use of volume conservation, and the photographs themselves show that the specimen radius is deforming homogeneously along its length, at least through the first loading pulse.

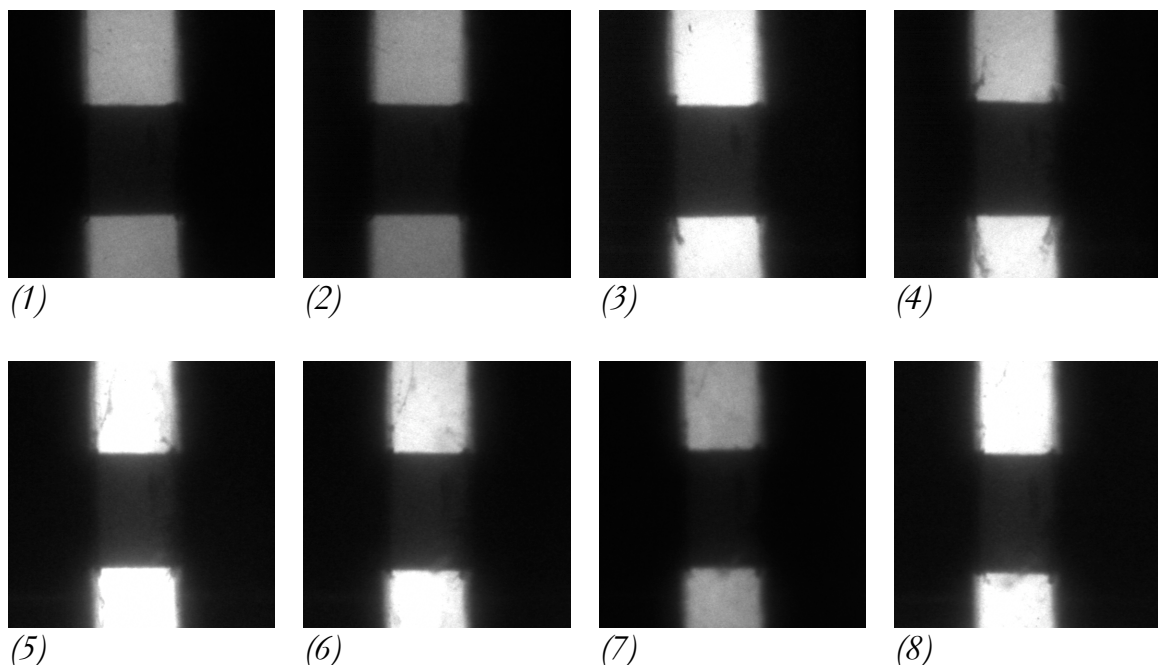


Figure 6.26. Sequence of photographs showing the deformation of a specimen of PVDF in the Hopkinson bar. The exposure time was 1 μ s and the interframe time was 15 μ s. The specimen was 3.2 mm long and 4 mm in diameter. Lubricant can be seen jetting from between the specimen and the bar from frame 3 onwards.

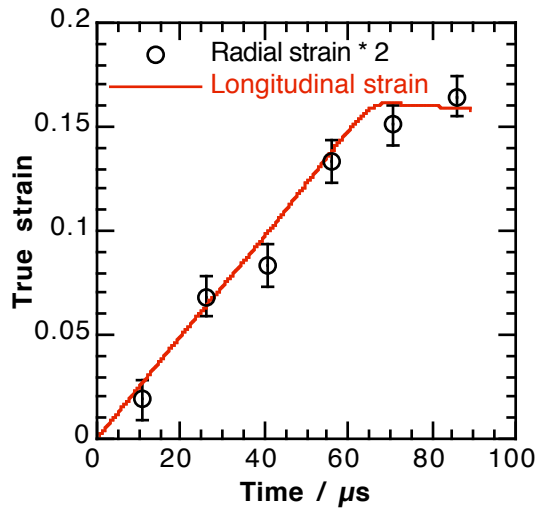


Figure 6.27. Comparison of the radial strain calculated from the photographs in figure 6.26 to the longitudinal strain from the Hopkinson bar equations for a specimen of PVDF. The strain rate was 2450 s^{-1} .

Application 2: The dynamic Brazilian test

The Brazilian test is a well-established technique for evaluating the tensile stress-strain properties of materials using compressive loading devices. It involves the compression of a disc along a diameter as illustrated in figure 6.28. This introduces a tensile stress and failure in the centre of the specimen, perpendicular to the axis of loading. By using curved anvils, it is possible to lower the shear stresses near to the anvil contact points, preventing premature edge failure (Awaji and Sato 1979). The tensile stress at the centre of the specimen is then given by equation (6.7)

$$\sigma_y = \frac{2P}{D t} \frac{b}{R^2}, \quad (6.7)$$

where b is the contact half-width between the specimen and the anvils, R is the radius of the specimen, D is the diameter and t is the thickness. P is the magnitude of the compressive load on the specimen. It has been established that if the ratio b/R is greater than 0.27, then the experiment is purely tensile, and tensile strength of the specimen is independent of b/R .

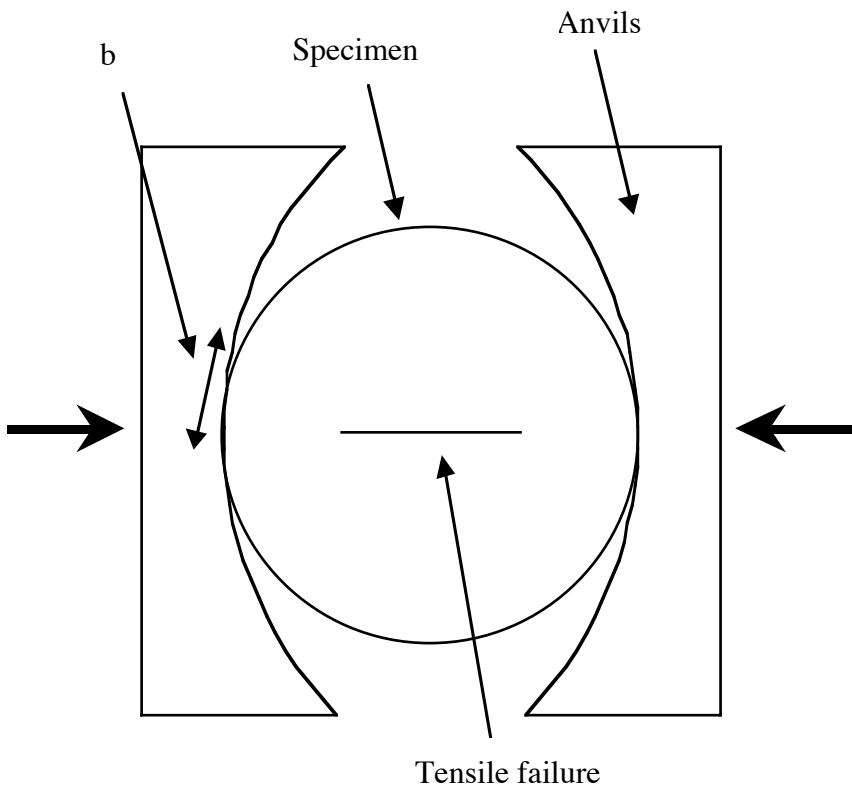


Figure 6.28. Schematic diagram of the Brazilian test arrangement. The thick arrows indicate the direction of the load, P . The contact half-width, b , between the specimen and anvils is indicated. Of course, this width only becomes finite because of plastic deformation between the specimen and anvils.

The advantage of this method compared to standard tensile experiments is that smaller amounts of material is used and the specimen geometry is very simple. This is particularly important for the testing of energetic compounds where large quantities of material can present safety problems. Extensive quasistatic studies have been carried out on explosives using various high-resolution optical techniques including moiré interferometry (Goldrein *et al.* 2002; Rae *et al.* 2002a; b) and image correlation (Grantham and Field 2003) to measure the tensile strain at the centre of the sample up to failure. However, whilst a high strain rate Brazilian test has been used by a few researchers (Nowacki 1994; Quidot 2003), measurements of the tensile strain were not attempted. In addition, these experiments used flat, rather than curved, anvils, which would have led to strain concentrations at the loading points.

These experiments used the same specimen and anvil radii (10 mm and 12 mm respectively) as in previous quasistatic work by Palmer *et al.* (1993) who established a value of $b/R = 0.3$. The nominal specimen thickness was 4 mm. The curved anvils were machined out of discs of steel, which were attached to the Inconel bars using double-sided adhesive tape. The thickness of the disc between the specimen

and bar was kept small (2 mm) to reduce the time taken for the steel end-caps to reach mechanical equilibrium.

Specimen equilibrium is an interesting issue in these experiments, because of the combined effect of the changing area at the ends of the bars and the longer than usual specimen, although it is important to remember that no assumptions of equilibrium are made in the analysis. By far the most important factor is probably the specimen length, which is effectively 10 mm. The longitudinal sound speed in this material is $3145 \pm 15 \text{ m s}^{-1}$, so the transit time in the specimen is approximately 3 μs , or 10 μs for three transits. However, because the area that the specimen presents to the wave is not constant, the mechanical impedance of the specimen changes, and the stress does not progress through it as a rectangular wave. This should actually reduce the time taken to achieve equilibrium. In any case, equilibrium was confirmed in each specimen tested, from both the Hopkinson bar outputs and the displacement measurements (which should be constant if the specimen is in stress equilibrium). Equilibrium occurs after about 20 μs which is the same time as the specimen yields.

Figure 6.29 shows the high-speed photographic sequence obtained for one of the experiments on PBS9501, with a speckle displacement quiver plot superimposed. The dashed circle indicates the specimen, with one of the curved anvils visible to the right of the sample in each frame. The inter-frame and exposure times were both 20 μs . The displacements also show the same strain behaviour as that observed in quasistatic Brazilian experiments.

The tensile strains measured at the centre of the specimen using the optical technique were in this case calculated using a plane fit to the x - and y -displacement components, where the compressive, tensile and shear strains are given by the gradients of the plane fits. A plot of the tensile strain across the centre of the specimen as a function of time during the experiment for three separate experiments on PBS9501 is shown in figure 6.30.

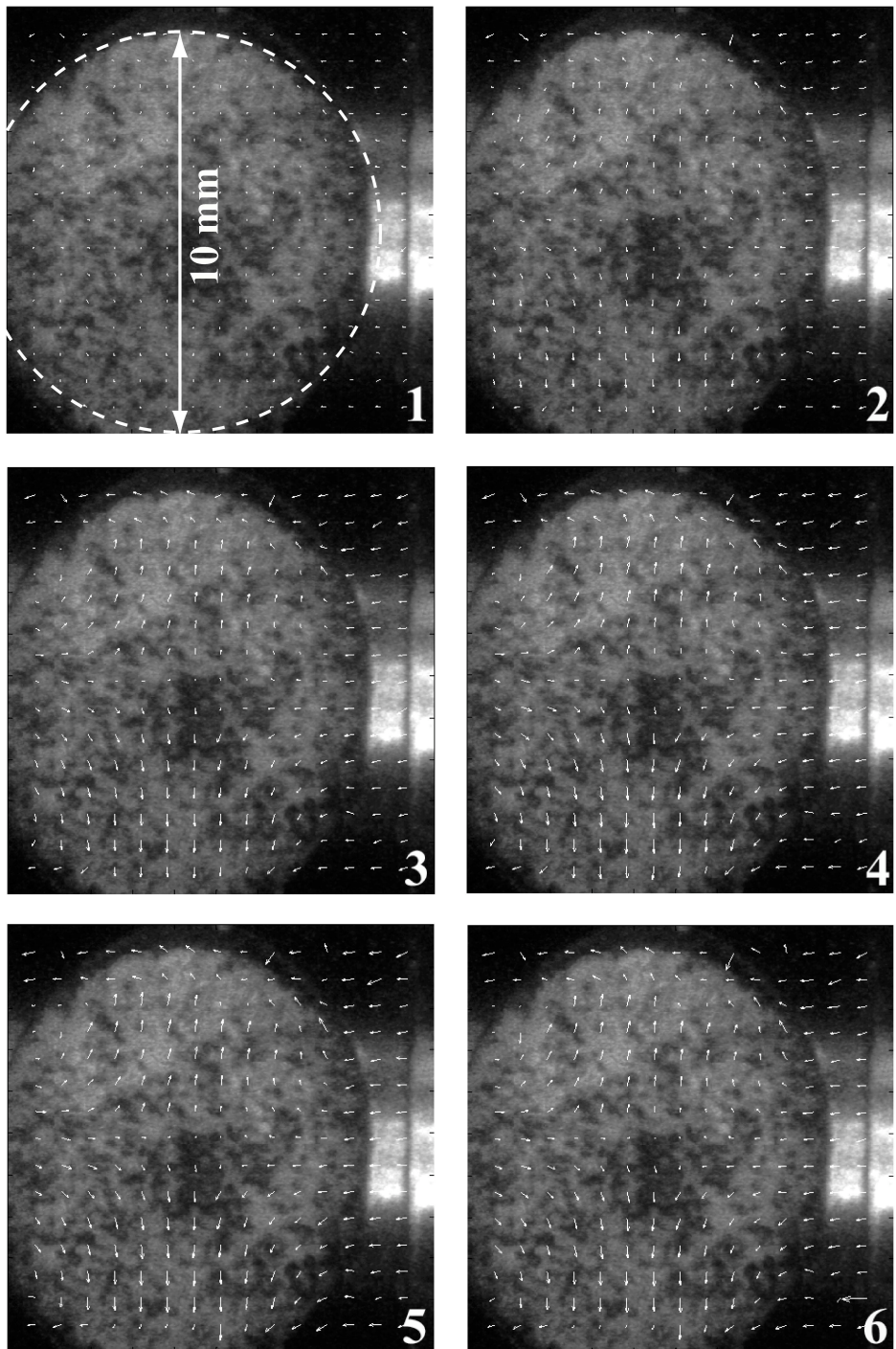


Figure 6.29. A sequence of quiver plots from one of the Brazilian experiments on PBS 9501. The quivers are not scaled. The exposure time was 20 μ s.

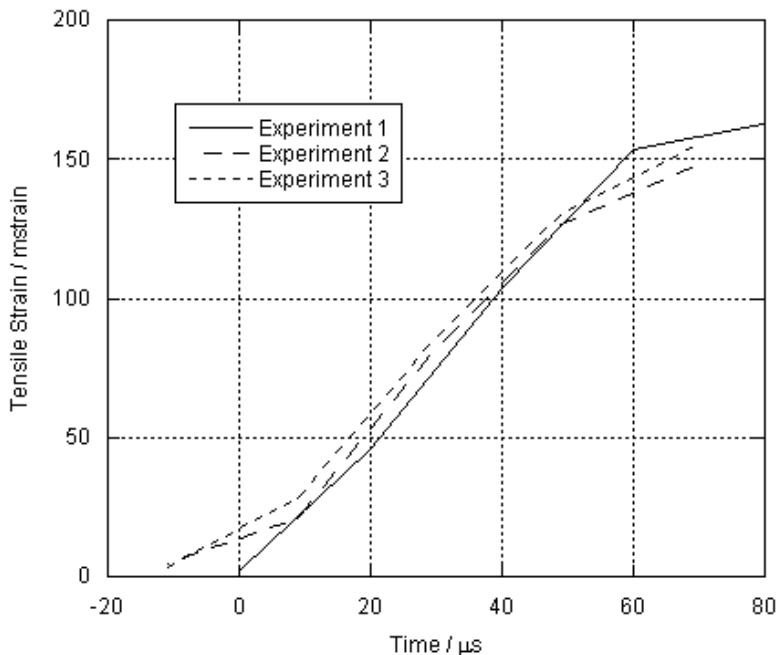


Figure 6.30. Tensile strain-time plots for three Brazilian tests. The linear region represents a strain rate of $2300 \pm 100 \text{ s}^{-1}$.

Taking the linear region from each of these curves gives a tensile strain rate of $2300 \pm 100 \text{ s}^{-1}$. Combining the stress (calculated using equation 6.7 from the applied load) and strain rate data gives the tensile stress-strain curve shown in figure 6.31. The oscillatory behaviour seen in the curves is most probably due to some oscillation of the stress wave in the specimen. These figures show that good consistency in the strain rate and the stress-strain curves was achieved.

From these plots the ultimate tensile stress in PBS9501 was found to be approximately 7.5 MPa. This parameter has been measured a number of times for quasistatic loading of PBS 9501 and been found to be approximately $0.75 \pm 0.1 \text{ MPa}$ at strain rates of about $1.7 \times 10^{-5} \text{ s}^{-1}$. Whilst this is much lower than the value measured in these dynamic tests, the quasistatic compressive strength is also lower. The maximum compressive stress is approximately 4 MPa at $1.7 \times 10^{-5} \text{ s}^{-1}$ ^{*}, and approximately 45 MPa at 2000 s^{-1} ^{**}. Therefore the ratios between the compressive and tensile strengths of the material at the two strain rates were similar: between 5 and 6.

^{*} This value has been extrapolated from measurements taken by DM Williamson $10^4 - 10^3 \text{ s}^{-1}$.

^{**} See application 3 in this chapter.

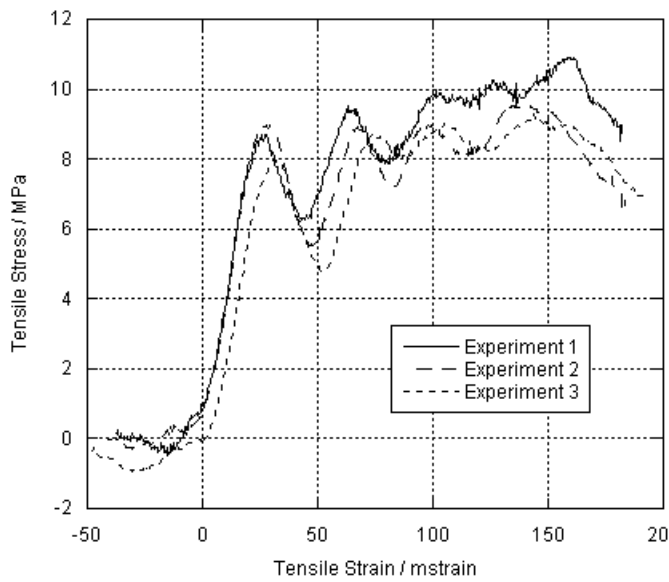


Figure 6.31. Tensile stress-strain curves for three Brazilian tests.

Application 3: The compressive behaviour of PBS 9501 at high strain rates

PBS 9501 is an inert simulant of the explosive composition PBX 9501, which consists of 95 % HMX crystals in a plasticised estane binder. The simulant has a number of features that make it an attractive candidate for applying speckle photography to the Hopkinson bar. As well as the general interest in PBXs and their simulants, PBS 9501 has specific properties that are conducive to speckle work. Firstly, it is a relatively stiff material that can be machined easily and accurately. The surface of the material is pink and matt, which means that either black or silver speckles give good contrast. In addition, its high loading density also encourages the formation of shear bands, which make photography more interesting and useful than it would be on a homogeneously deforming specimen. There has been very little previous, published, work on the mechanical properties of PBS 9501 at high strain rates, although the properties of PBX 9501 have been measured by Gray *et al.* (1998; 2000), over a range of rates and temperatures. The strength of the material is strongly dependent on both parameters. Some of his results were presented in figure 5.1.

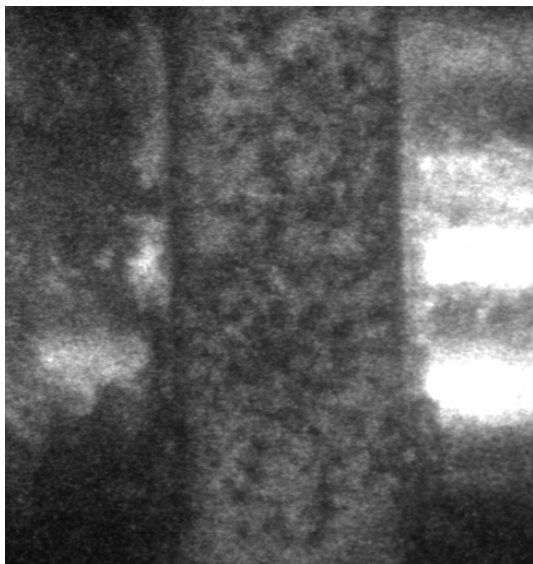


Figure 6.32. Example of an image taken of PBS 9501 speckled with black paint. The exposure time was 20 μ s.

Initial experiments used specimens of PBS 9501 that had been machined to nominal lengths of 3.8 mm and diameters of 10 mm. The speckles were introduced using black ink in an artist's airbrush, and illumination was provided by the Pallite VIII. Exposure and interframe times were 20 μ s. The exposure time was very long, but could not be shortened without compromising image quality. A typical frame from one of these experiments is shown in figure 6.32. Later on, the use of silver dag to produce speckles, and flashes for illumination allowed exposure times of 2 μ s to be used instead. In fact, it was possible to use 1 μ s exposures, but as this required increasing the gain setting on the camera, a 2 μ s exposure time with a gain of 30 was thought to be better. A typical frame from one of these experiments is shown in figure 6.33. These later experiments used specimens of nominal length 5 mm and diameter 8 mm, to allow better frame filling in the camera. This was found to make no difference to the stress-strain measurements.

The specimens were lubricated with paraffin wax lubricant. Stress-strain curves are shown in figure 6.34.

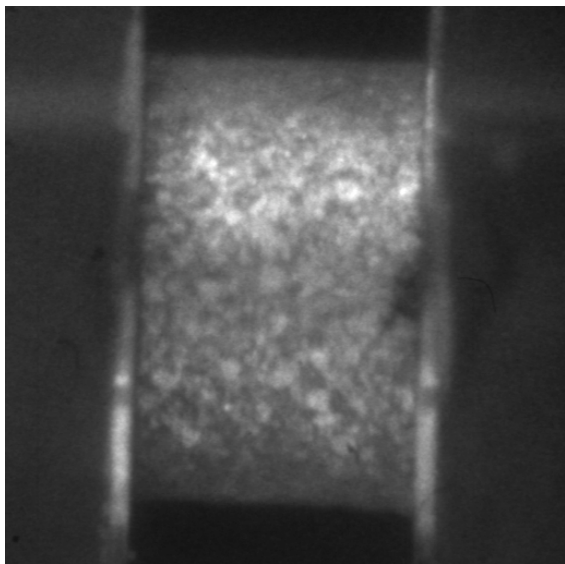


Figure 6.33. Example of an image taken with a 2 μ s exposure time of PBS 9501 speckled with silver dag.

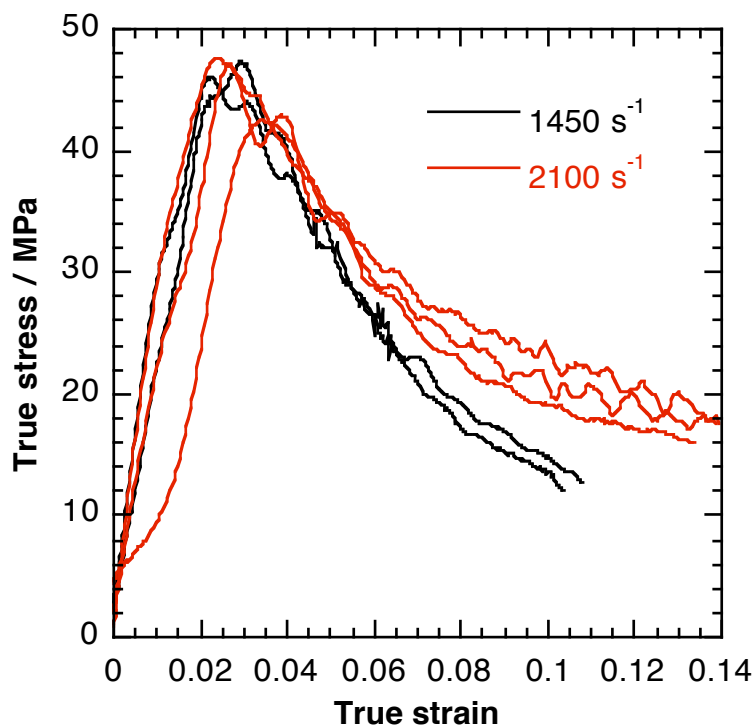
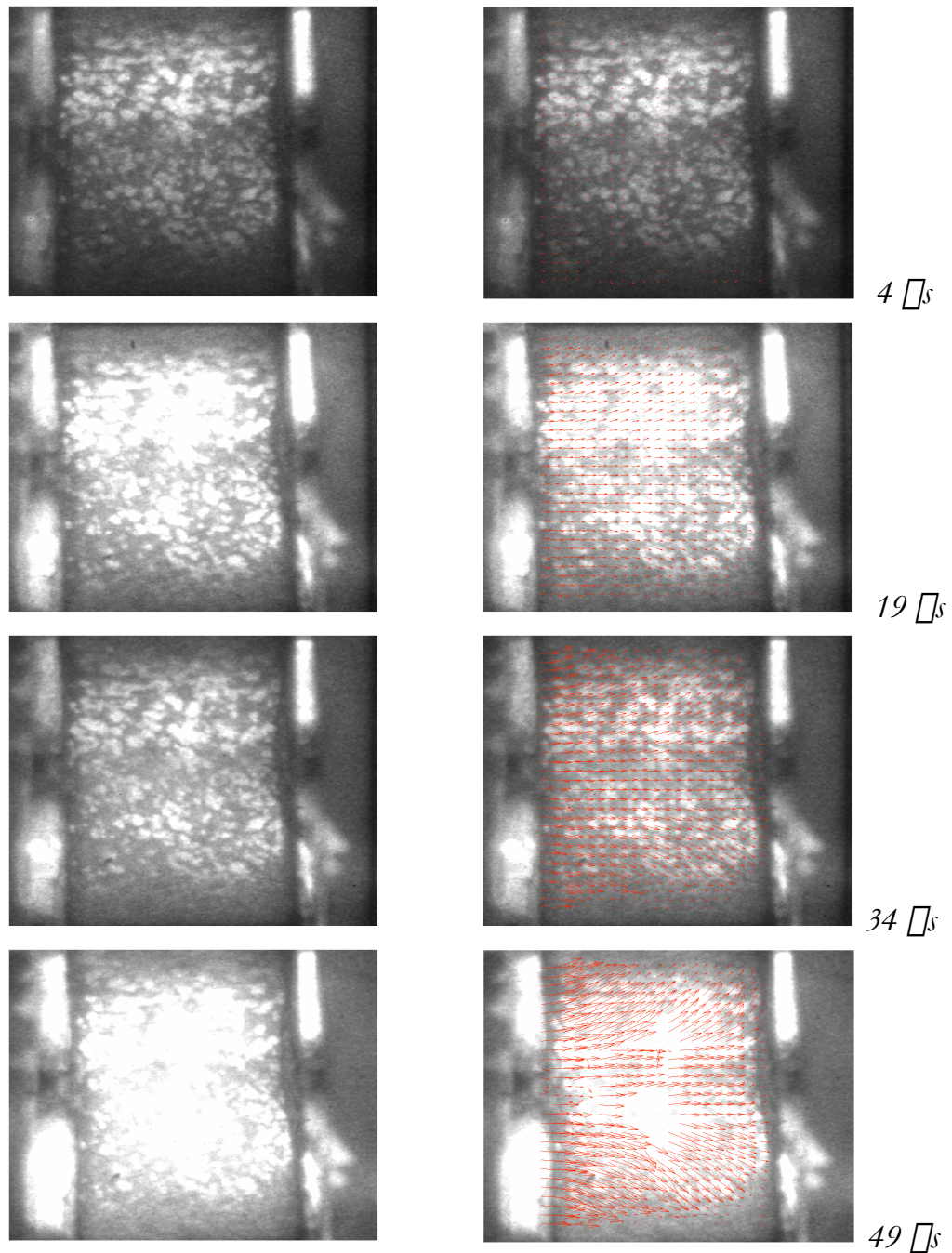


Figure 6.34. Stress-strain curves for PBS 9501 at two Hopkinson bar strain rates.

Photographs of the deforming specimens were used as before to give displacement matrices. A typical set of quiver plots is presented in figure 6.35a, with a corresponding stress-time plot in 6.35b. There are two areas of interest that were addressed with the photographs: the formation of cracks and strain localisations in the specimen and the evolution of longitudinal and radial strain.

The benefit of using speckle to observe crack formation in the specimen is shown in the following example, which is typical of the results obtained. Figure 6.36a shows raw photographs and quiver plots of a second specimen as it deformed; the stress-time curves are given in figure 6.36b. It was quite common to observe strain

discontinuities in the speckle quiver plots before they became visible in the raw photographs. Here the strain discontinuities associated with the formation of cracks appear in the second frame, which is equivalent to the peak in the stress-strain curve. However, the cracks themselves are not visible until one frame later, well after the peak.



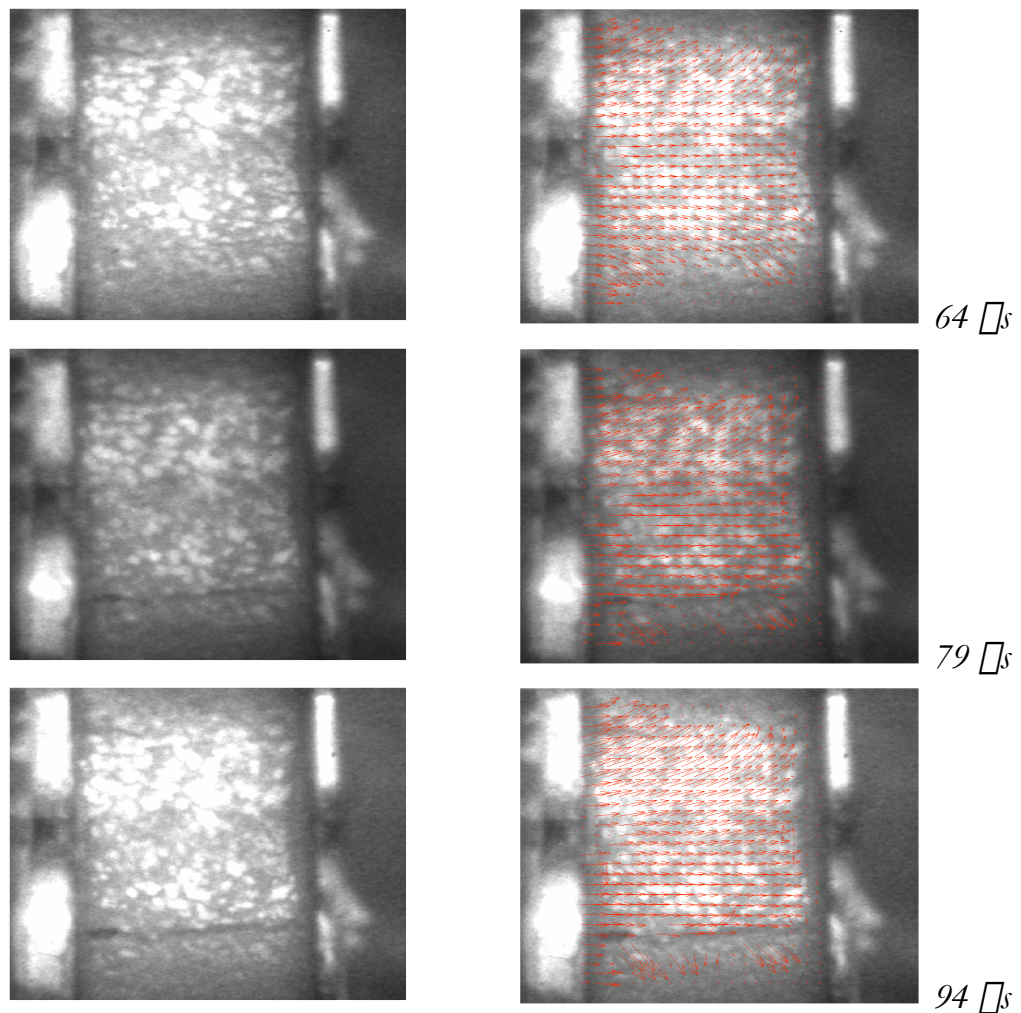


Figure 6.35a. High speed photographs (left) and quiver displacement plots (right) of 'specimen J', deformed at $745\mu\text{s}^{-1}$. The exposure time was $2\mu\text{s}$. The frame times are shown relative to the arrival of the stress wave at the specimen.

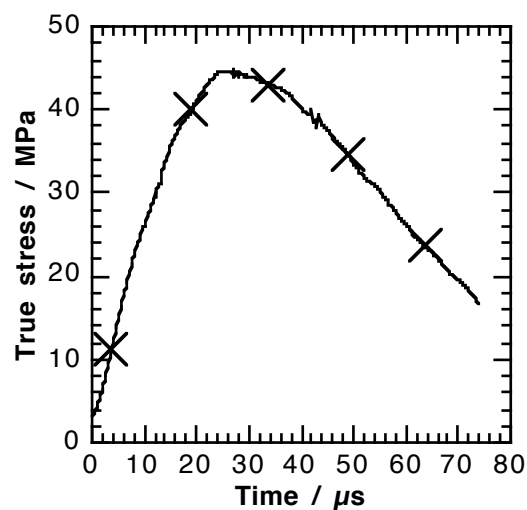
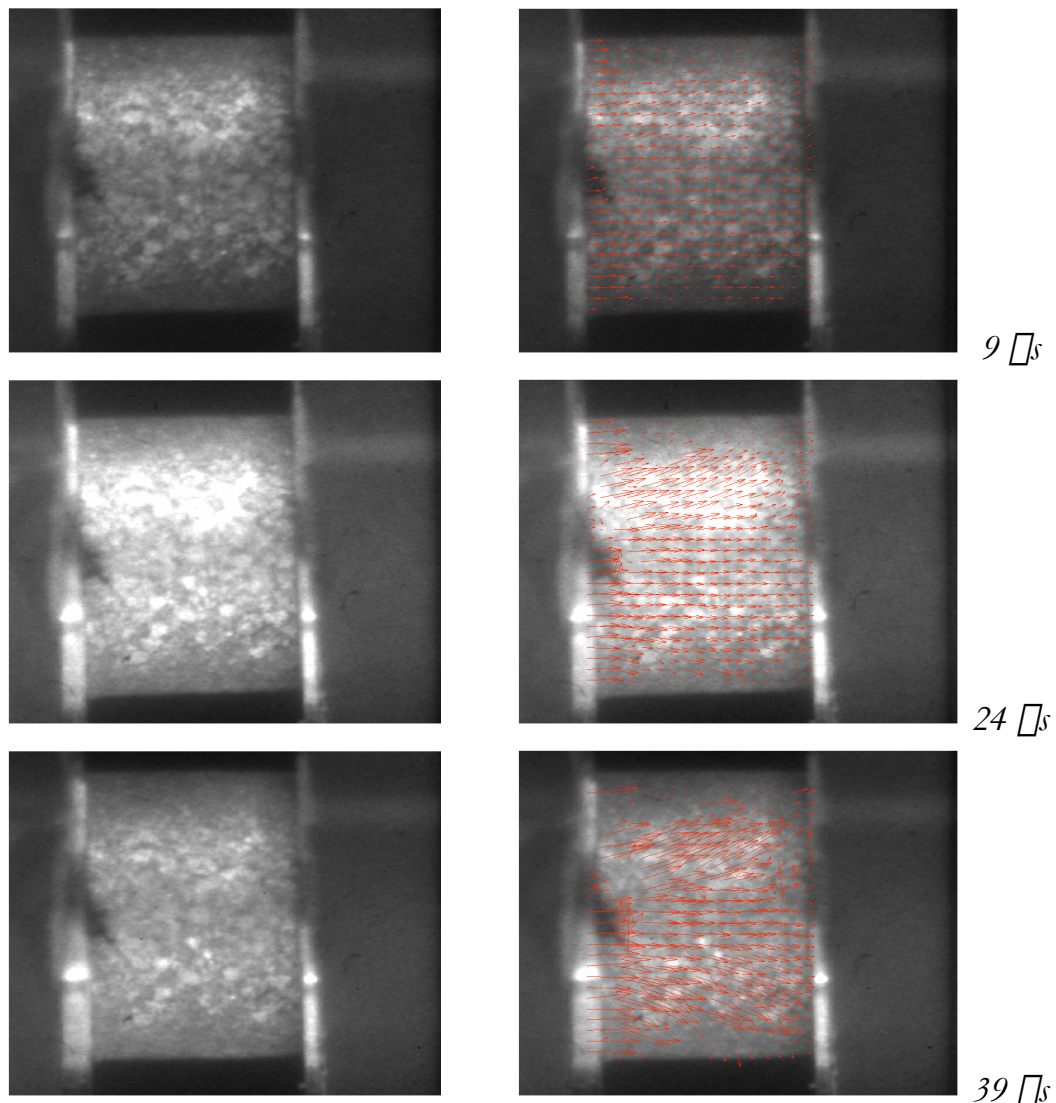


Figure 6.35b. Strain-time plot corresponding to the photographic sequence in figure 6.35a. The times the photographs were taken are indicated with crosses; note that some of them were taken after the end of the loading pulse.



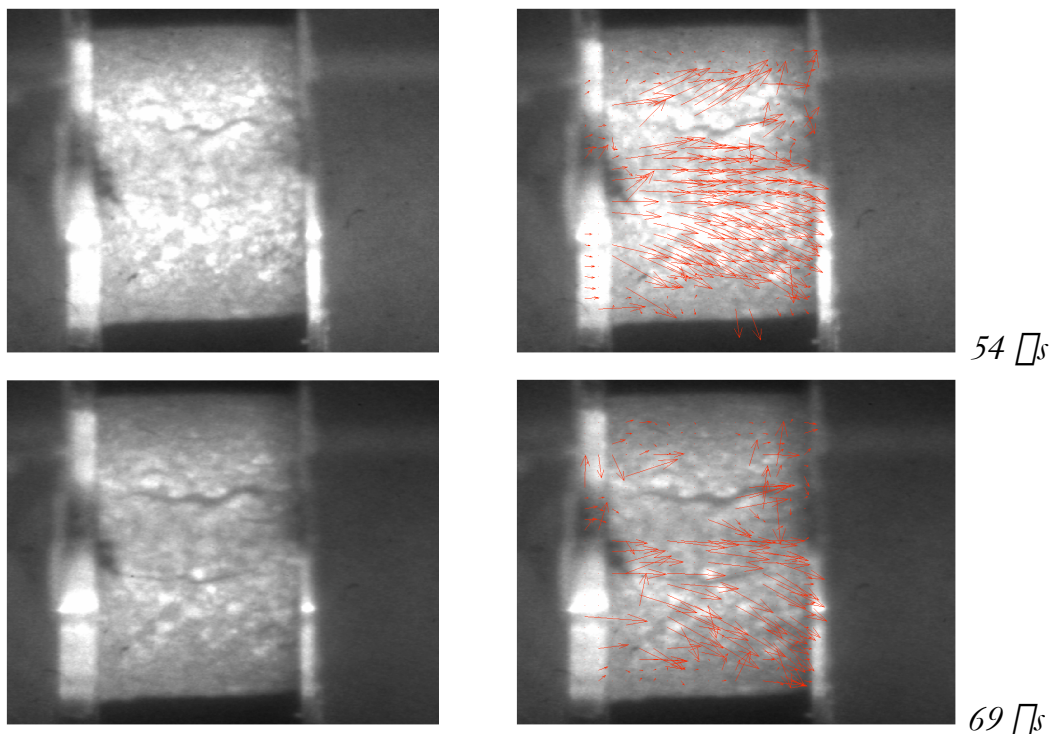


Figure 6.36a. High speed photographs (left) and quiver displacement plots (right) of 'specimen D', deformed at 1420 s^{-1} . The exposure time was $2\ \mu\text{s}$. The frame times are shown relative to the arrival of the stress wave at the specimen. Subsequent frames were too decorrelated to be of use.

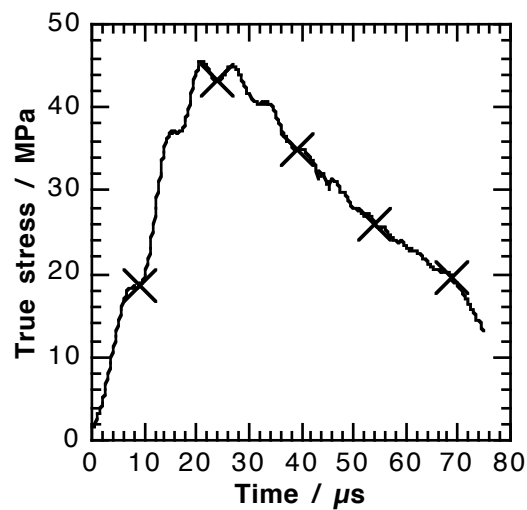


Figure 6.36b. Strain time plot corresponding to the photographic sequence in figure 6.36a. The times the photographs were taken are indicated with crosses; note that some of them were taken after the end of the loading pulse.

This behaviour was observed in a number of the experiments, and indicates that strain localisation and damage in the specimen are the causes, rather than the result, of the drop in strength of the material, because they occur before this drop. Specimen J, see figure 6.35, did not exhibit such obvious discontinuities, but it is likely that this is because the crack formed towards the edge of the specimen where speckle resolution is poorer.

Having shown that the material does not deform homogeneously, it is now necessary to examine the assumption of volume conservation in the Hopkinson Bar equations for true stress.

Speckle measurements were used to calculate the longitudinal and radial strains in a number of specimens, using the calculation method described earlier. A comparison of the speckle measurements of compressive strain to those from the Hopkinson bar equations is given in figure 6.38 for experiments over a range of different strain rates. Calculations of Poisson's ratio were performed for all of the frames in which reasonable measurements of radial strain could be made (i.e. those frames in which the radial displacements were significant compared to the noise). The results of these calculations are presented in figure 6.39. Measurements were made of the longitudinal and shear sound speeds in the material ($c_L = 3150 \text{ m s}^{-1}$ and $c_S = 1680 \text{ m s}^{-1}$ respectively), from which a value of $\nu = 0.30$ is calculated. The natural quadratic relationship between strain and ν has an intercept of 0.31, as shown in the figure.

Further measurements of radial strain were now performed using the line laser, and the results of these measurements are given in figures 6.40 and 6.41. These data agree with the sound speed measurements at low strains; however it is of some concern that the Poisson's ratios calculated from the line laser are very different to those from the speckle measurements.

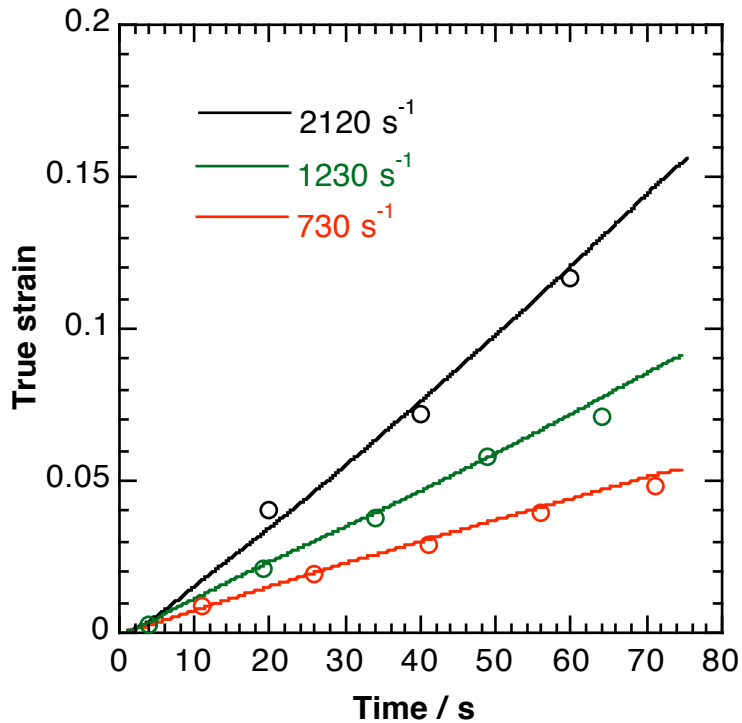


Figure 6.38. Comparison of compressive strain-time calculations from the Hopkinson bar and speckle. The strain rates of the three specimens are shown in the figure. The lines represent results from the Hopkinson bar equations, whilst the circles represent speckle results. The strain errors in the speckle results are similar in size to the circles. The exposure time was 20 μ s for the specimen at 2130 s^{-1} and 2 μ s for the other two experiments. The time position represents the middle of the exposure.

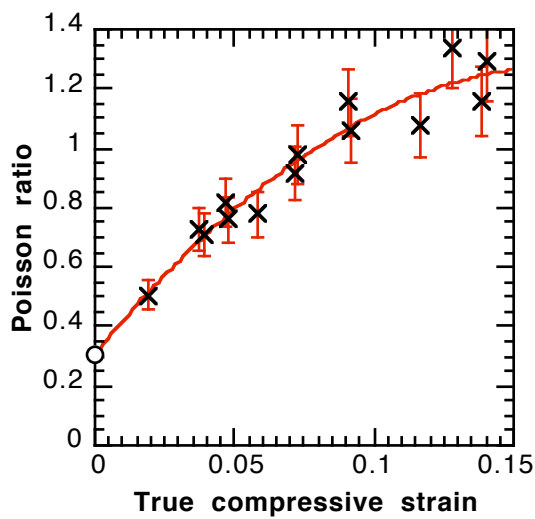


Figure 6.39. Plot of Poisson's ratio against longitudinal compressive strain, calculated from speckle measurements on the three specimens presented in figure 6.40. The red line is a quadratic line of best fit through the data. The circle on the y-axis represents the low strain Poisson's ratio calculated from sound-speed measurements.

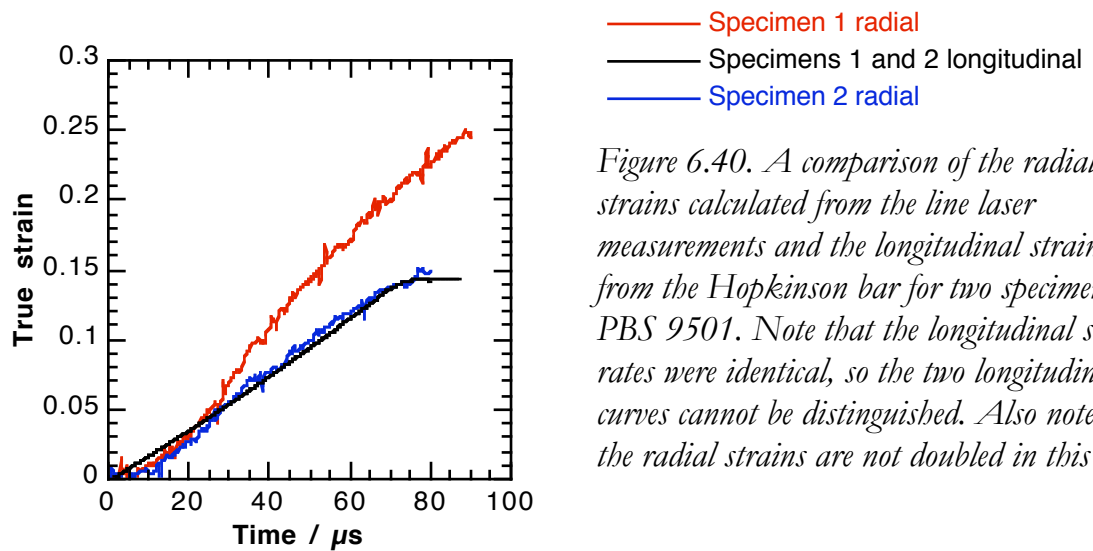


Figure 6.40. A comparison of the radial strains calculated from the line laser measurements and the longitudinal strains from the Hopkinson bar for two specimens of PBS 9501. Note that the longitudinal strain rates were identical, so the two longitudinal curves cannot be distinguished. Also note that the radial strains are not doubled in this case.

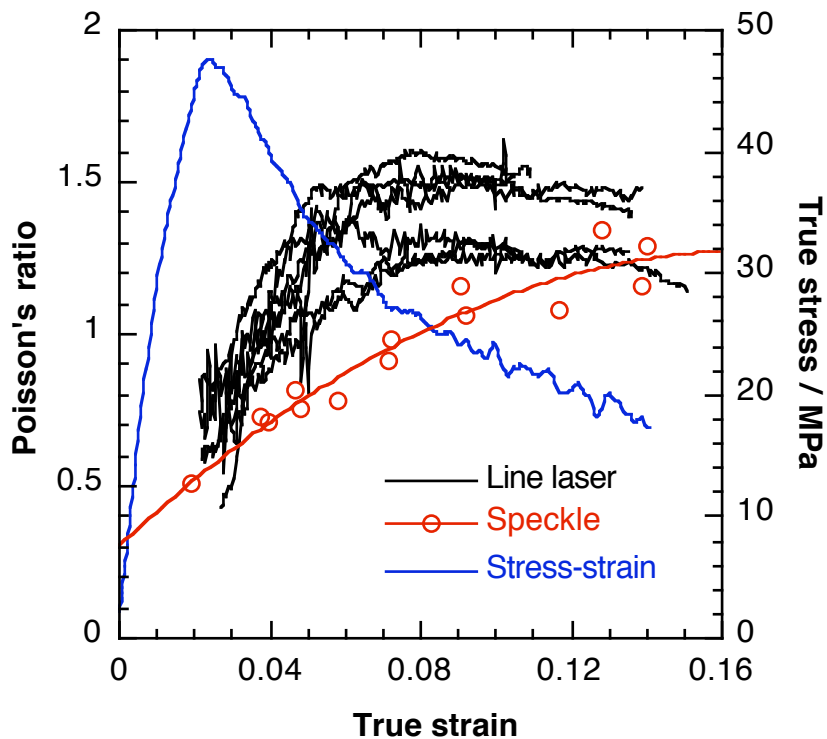


Figure 6.41. Poisson's ratio calculated from the line laser measurements as a function of longitudinal compressive strain for six specimens of PBS 9501. Results from the speckle calculations are also shown. These are compared to a typical stress-strain curve.

In order to investigate this difference, measurements of specimen diameter were made by hand directly from the photographs. These indicated that in specimens where there was a lot of cracking (such as that shown in figure 6.35) the measurements agreed with the line laser, whilst in specimens where there was little cracking they agreed with the speckle. In order to obtain good global strain measurements, the speckle technique is biased towards specimens with little surface cracking. It is also biased towards the centre of the specimen, which is facing the camera and therefore gives better image quality. On the other hand, whilst the line laser is not biased towards any particular specimen, it is more likely to be affected by cracking of the specimen. Both of these techniques effectively treat a three-dimensional object as a two-dimensional projection. When cracking occurs, it tends to increase the radius of the specimen to a value that is larger than the actual material strain. This means that the edges of the specimen move apart, whilst the centre of the specimen merely moves towards the camera, with no apparent increase in strain in the centre.

Therefore, careful consideration needs to be given to which of the measurements are valid. It would appear that speckle measurements give a good indication of *material* strains, whilst the line laser gives information about the *specimen* radius. For many materials these are the same, but in cases where they are not the line laser is effectively giving a measure of the effect of specimen damage.

How much effect does this have on the stress-strain curve measurements? Poisson's ratio is a first order effect on the change in radius, and therefore a second order effect on the radius itself. For example: if an 8 mm diameter specimen is assumed to have a Poisson's ratio of 0.5, whilst it actually has a ratio of 1.5, and the specimen is taken to 10% longitudinal strain, the assumed diameter would be 8.4 mm, whilst the real diameter was 9.2 mm. The ratio of area differences is 1.2:1. This means that at 10% strain the stress calculated from volume conservation would be 1.2 times too large. Therefore, it is important to check the assumption of volume conservation wherever possible. This can usually be done in a straightforward manner with high-speed photography.

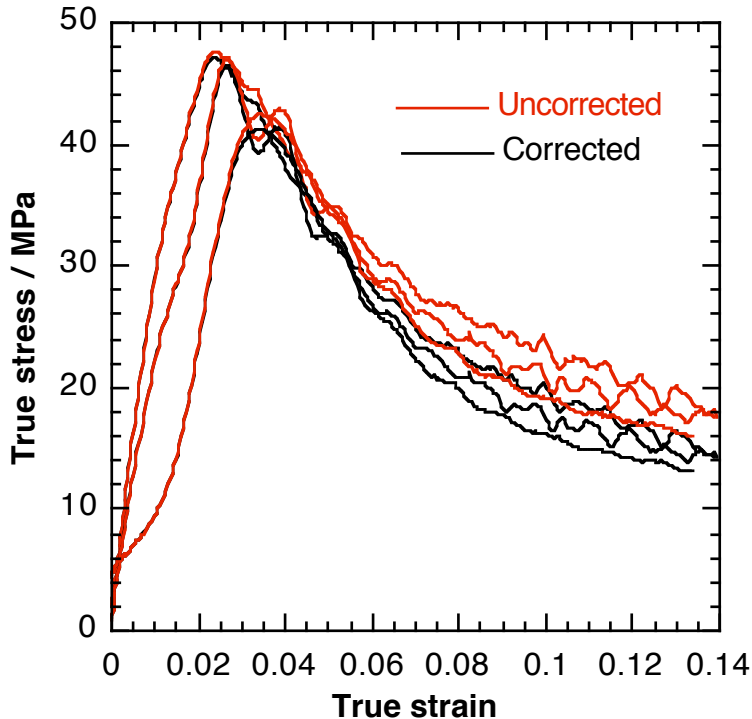


Figure 6.42. Stress-strain curves for PBS 9501 corrected for the dependence of Poisson's ratio on strain measured by the line laser. These are compared to the uncorrected curves.

Since the assumption of volume conservation definitely does not hold here, it is possible to correct the stress-strain curves using the line laser measurements, figure 6.42. The interpretation of these results is difficult. It is likely that the two sets of curves shown in figure 6.42 are upper and lower bounds on the *material* properties. In particular, when the specimen forms longitudinal cracks the area of the specimen, defined by a radius that contains all of the specimen material, is not the same as the area of load-supporting material. The cracks split the specimen into a number of smaller fragments, and the gaps between these fragments do not support load. In addition, the radial strains of these pieces are not the same as the radial strain of the specimen, since the gaps contribute to the specimen radius but not to the fragment radius. In effect, if the change in volume is due to cracking, then volume conservation would effectively still hold for the *material*.

Furthermore, a very important observation from the line laser data presented in figure 6.41 is the peak in, and gradual decrease of, Poisson's ratio. This plateau coincides with the start of the plateau at the end of the stress-strain curve. These observations indicate that the Poisson's ratio measurement can be used as a quantification of the degree of damage inside the specimen. We would expect increasing damage to cause the Poisson's ratio to increase, and also cause the strength of the specimen to decrease. Since both of these stop happening at the same time, it seems likely that the amount of damage stops increasing at this time. Interrupted tests should be performed to investigate whether this is the case.

Finally, these results indicate why materials that behave in this way (e.g. EDC37, in figure 5.12) have consistent maximum stresses, but unload to inconsistent tails at

high strains, since the measurements from the Hopkinson bar equations do not take into account the degree of fragmentation of the specimen. In the 24 experiments performed as part of the work presented in this chapter there appeared to be no relationship between the strain rate and the amount of visible fragmentation at a given strain (although, of course, higher rate experiments did go to higher strains).

6.6 CONCLUSIONS

Techniques

This chapter reports on the application of two optical techniques to the SHPB system: line laser and speckle.

Line lasers can be used to make accurate continuous measurements of the specimen diameter, which allows continuous measurements of Poisson's ratio. Because it measures the positions of the specimen edges it is most useful for homogeneously deforming specimens. However experiments on PBS9501 indicate that it might also be useful as an assessment of damage within a material as it expands. Interrupted tests would be required to investigate whether this is the case. The speckle technique allows calculation of displacement fields in the specimen, for which accuracies of better than one pixel have been achieved in the displacement measurements. Global strain calculations can then be performed in both the longitudinal and radial directions. These are about as accurate as those calculated using the Hopkinson bar equations. In addition, strain localisations can be observed in the displacement field before they become apparent in the raw photographs. Finally, dynamic Brazilian tests with measurements of tensile strain within the specimen are now possible. In the future, such data will allow much better comparison of models to experiment.

Material properties

The dynamic, high strain, Poisson's ratio of dural (figure 6.22) was measured as being 0.5 ± 0.1 . Of more interest is the Poisson's ratio of polycarbonate (figure 6.24). At low strains this is the same as the literature value of 0.39. However, as the material yields, it jumps to 0.5. As the polycarbonate is strained it initially loses volume, but this is quickly restored upon yield. This observation may provide important understanding of the processes that govern yield in polycarbonate and other polymers.

A number of observations have been made on the properties of PBS 9501. Brazilian tests conducted at high strain rate showed that the ultimate tensile stress is 7.5 MPa at strain rates of 2300 s^{-1} . The equivalent at $1.7 \times 10^{-5} \text{ s}^{-1}$ is 0.75 MPa. The ratio of these values is similar to the ratio of compressive strengths at the two rates (45 MPa and 4 MPa).

The Poisson's ratio of PBS 9501 also depends on strain. However, it is important to distinguish between the Poisson's ratio of a specimen and that of the bulk material. In particular the value for a specimen depends on the amount of fracture

in the specimen. It is unlikely that such a material would not expand on deformation, since the crystals themselves begin at approximately the maximum packing density. Therefore, the boundaries on the value of Poisson's ratio are 0.5 and 1.5 (figure 6.41). This is a large range; however, if this is translated into bounds on the stress-strain curve it does not have a large effect until well after the peak stress (figure 6.42).

Finally, observation of the strain discontinuities in the quiver plots on PBS 9501 show that the discontinuities appear before the rapid drop in stress. This indicates that the discontinuities and fracture are the cause, rather than the result, of this drop. It is likely that the material breaks up into a number of fragments and then stops. This is supported by both the levelling off of the stress-strain curves (figures 6.34 and 6.42) and the unchanging value of the specimen Poisson's ratio (figure 6.41) at strains above 0.08.

6.7 SUGGESTIONS FOR FURTHER WORK

- Rigorous comparison of displacement data from speckle calculations and finite element modelling of Hopkinson bar experiments.
- Application of speckle measurements to inhomogeneously deforming materials, such as quasi-brittle materials like concrete or non-volume conserving materials like foams.
- Further experiments on polymer materials to investigate the behaviour of the dynamic and static Poisson's ratio after yield.
- Interrupted experiments on PBS 9501 to investigate the use of line laser measurements for damage quantification.

6.8 REFERENCES

Awaji, H. and Sato, S. (1979). "Diametral compressive testing method." *J. Engng Mater. Technol.* **101** 139- 147.

Bussac, M.-N., Collet, P., Gary, G. and Othman, R. (2002). "An optimisation method for separating and rebuilding one-dimensional dispersive waves from multi-point measurements: Application to elastic or viscoelastic bars." *J. Mech. Phys. Solids* **50** 321-249.

Gåsvik, K. J. (2002) "Optical Metrology", John Wiley and Sons.

Goldrein, H. T., Rae, P. J., Palmer, S. J. P. and Field, J. E. (2002). "Construction of a high-resolution moiré interferometer for investigating microstructural displacement fields in materials." *Phil. Trans. R. Soc. Lond. A* **360** 939-952.

Gorham, D. A. (1982). "A technique to improve frame-filling in the high speed photographic recording of symmetrical events." *J. Phys. E: Sci. Instrum.* **15** 562-564.

Grantham, S. G. and Field, J. E. (2003). "Speckle correlation methods applied to ballistics and explosives." *Proc. SPIE* **4933** 27-32.

Gray III, G. T., Blumenthal, W. R., Idar, D. J. and Cady, C. M. (1998) "Influence of temperature on the high strain-rate mechanical behavior of PBX 9501" in "Shock Compression of Condensed Matter - 1997", ed. S. C. Schmidt, D. P. Dandekar and J. W. Forbes, publ. Woodbury, New York, American Institute of Physics: pp. 583-586.

Gray III, G. T., Idar, D. J., Blumenthal, W. R., Cady, C. M. and Peterson, P. D. (2000) "High- and low-strain rate compression properties of several energetic material composites as a function of strain rate and temperature" in "Proc. 11th Int. Detonation Symposium", ed. J. M. Short and J. E. Kennedy, publ. Arlington, Virginia, Office of Naval Research: pp. 76-84.

Huntley, J. M. (1989). "Speckle photography fringe analysis: Assessment of current algorithms." *Appl. Opt.* **28** 4316-4322.

Kajberg, J. and Sjödahl, M. (2000) "Optical methods to study material behaviour at high strain rates" in "Proceedings of the IUTAM Symposium on Field Analysis for Determination of Material Parameters – Experimental and Numerical Aspects" publ. Kluwer Academic Publishers, Dordrecht, The Netherlands.

Kajberg, J. 2002 "High Strain-Rate Experiments using High-Speed Photography" *Licentiate Thesis, Luleå University of Technology, Luleå, Sweden*. ISSN: 1402 - 1757

Nowacki, W. K. (1994). "Dynamic compression of a brittle spherical specimen." *Engng. Trans.* **42**(3) 263- 279.

Palmer, S. J. P., Field, J. E. and Huntley, J. M. (1993). "Deformation, strengths and strains to failure of polymer bonded explosives." *Proc. R. Soc. Lond. A* **440** 399-419.

Peters, W. H. and Ranson, W. F. (1982). "Digital imaging techniques on experimental stress analysis." *Opt. Engng* **21** 427- 431.

Pope, P. H. and Field, J. E. (1984). "Determination of strain in a dynamic compression test." *J. Phys. E: Sci. Instrum.* **17** 817-820.

Quidot, M. (2003). "Numerical simulation of the dynamic Brazilian test on a high filled polymer." *J. Phys. IV France* **110** 371-376.

Rae, P. J. (2000). "Quasistatic studies on the deformation, strength and failure of polymer bonded explosives", Cambridge University PhD thesis.

Rae, P. J., Goldrein, H. T., Palmer, S. J. P., Field, J. E. and Lewis, A. L. (2002a). "Quasistatic studies of the deformation and failure of b-HMX based polymer bonded explosives." *Proc. R. Soc. Lond. A* **458** 743-762.

Rae, P. J., Palmer, S. J. P., Goldrein, H. T., Field, J. E. and Lewis, A. L. (2002b). "Quasi-static studies of the deformation and failure of PBX 9501." *Proc. R. Soc. Lond. A* **458** 2227-2242.

Rae, P. J., Palmer, S. J. P., Goldrein, H. T., Lewis, A. L. and Field, J. E. (2004). "White-light digital image cross-correlation (DICC) analysis of the deformation of composite materials with random microstructure." *Optics Lasers Engng* **41** 635-648.

Ramesh, K. T. and Narasimhan, S. (1996). "Finite deformations and the dynamic measurement of radial strain on compression Kolsky bar experiments." *Int. J. Solids Structures* **33** 3723-3738.

Sjödahl, M. (1994a). "Electronic speckle photography: Increased accuracy by non-integral pixel shifting." *Appl. Opt.* **33** 6667-6673.

Sjödahl, M. (1994b) Strain field measurements using electronic speckle photography: A comparison in "Recent Advances in Experimental Mechanics", ed. S. Gomes, publ. Rotterdam, Balkema: pp. 325-330.

Sjödahl, M. (2001) Digital Speckle Photography in "Digital Speckle Pattern Interferometry and Related Techniques", ed. P. K. Rastogi, publ. Chichester, John Wiley and Sons: pp. 337- 362.

Sjödahl, M. and Benckert, L. R. (1993). "Electronic speckle photography: Analysis of an algorithm giving the displacement with subpixel accuracy." *Appl. Opt.* **32** 2278-2284.

Sjödahl, M. and Benckert, L. R. (1994). "Systematic and random errors in electronic speckle photography." *Appl. Opt.* **33** 7461-7471.

Sutton, M. A., Wolters, W. J., Peters, W. H., Ranson, W. F. and McNeill, S. R. (1983). "Determination of displacements using an improved digital correlation method." *Image Vision Computing* **1** 133-139.

Swantek, S. D., Wicks, A. L. and Wilson, L. T. (2001). "An optical method of strain measurement in the split Hopkinson pressure bar." *Proc. SPIE* **4359** 1471-1477.

Verleysen, P. and Degrieck, J. (2004a). "Experimental investigation of the deformation of Hopkinson bar specimens." *Int. J. Impact Engng* **30** 239-253.

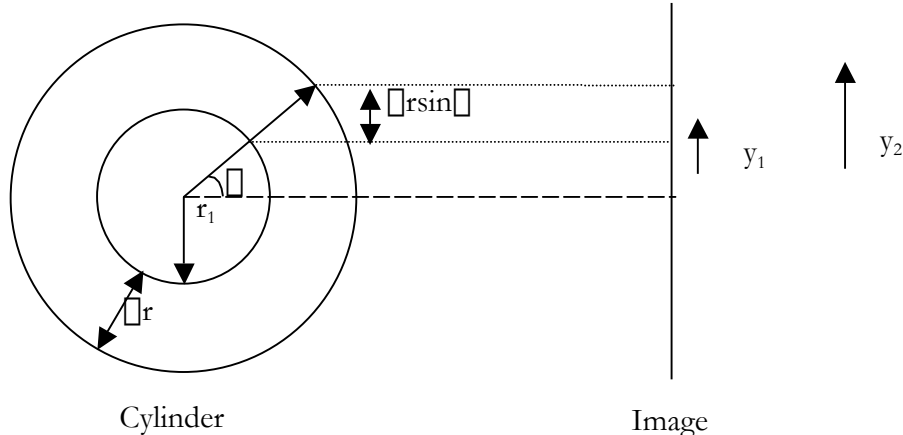
Verleysen, P. and Degrieck, J. (2004b). "Optical measurement of the specimen deformation at high strain rate." *Exper. Mech.* **44** 247-252.

Walley, S. M., Proud, W. G., Rae, P. J. and Field, J. E. (2000). "Comparison of two methods of measuring the rapid temperature rises in split Hopkinson bar specimens." *Rev. Sci. Instrum.* **71** 1766-1771.

Zehnder, A. T., Guduru, P. R., Rosakis, A. J. and Ravichandran, G. (2000).
"Million frames per second infrared imaging system." *Rev. Sci. Instrum.* **71**
3762-3768.

APPENDIX 1

Calculation of radial strain from photographs



Consider a cylinder, which is imaged on a plane normal to its radius. As the cylinder expands radially, a point that was imaged at $y_1 = r_1 \sin \Delta$ moves to $y_2 = r_2 \sin \Delta$, where $y_2 = y_1 + \Delta y$ and $r_2 = r_1 + \Delta r$. Thus:

$$\Delta y = \Delta r \sin \Delta \quad (A1.1)$$

or $\Delta y = \Delta r \frac{y}{r} \quad (A1.2)$

At the top of the cylinder the change in position on the film is equal to the change in radius (neglecting effects of magnification). A point on the cylinder axis does not move on the film.

The results of this is that the engineering radial strain of the specimen is the same as the strain calculated in the y -direction on the photograph;

$$\frac{\Delta y}{y} = \frac{\Delta r}{r} \quad (A1.3)$$

This is also the case for true strains, since the true strain ϵ is related to the engineering strain e by:

$$\epsilon = \ln(1 + e). \quad (A4.4)$$

A useful property of circles is that for some point on the line representing the image there is always a normal to the line that is radial to the circle, regardless of the orientation of the line. This means that as long as the camera can see the cylindrical specimen the strains calculated from the image will be correct, even

though the absolute displacements will appear to be asymmetric. This is not the case in the longitudinal direction where careful alignment is required.

APPENDIX 2

Papers on energetic materials and associated experimental techniques published during the period of this research contract by members of the PCS Fracture and Shock Physics Group, University of Cambridge, UK.

Those marked in red are available as paper copies only.

2003 J.E. Balzer, W.G. Proud, S.M. Walley, J.E. Field "High-speed photographic study of the drop-weight impact response of RDX/DOS mixtures" *Combust. Flame* **135** 547-555

2003 S.G. Grantham, C.R. Siviour, W.G. Proud, S.M. Walley, J.E. Field "Speckle measurements of sampled deformation in the split Hopkinson pressure bar" *J. Phys. IV France* **110** 405-410

2003 W.G. Proud, E.J.W. Crossland, J.E. Field "High-speed photography and spectroscopy on determining the nature, number and evolution of hot spots in energetic materials" *Proc. SPIE* **4948** 510-518

2003 C.R. Siviour, S.M. Walley, W.G. Proud, J.E. Field "Hopkinson bar studies on polymer bonded explosives", in "Proc. 6th Seminar on New Trends in Research of Energetic Materials", ed. J. Vágenknecht, pp. 338-349, publ. Pardubice, Czech Republic, University of Pardubice

2004 J.E. Balzer, C.R. Siviour, S.M. Walley, W.G. Proud, J.E. Field "Behaviour of ammonium perchlorate-based propellants and a polymer-bonded explosive under impact loading" *Proc. R. Soc. Lond. A* **460** 781-806

2004 A. Chakravarty, W.G. Proud, J.E. Field "Small scale gap testing of novel compositions" in "Shock Compression of Condensed Matter – 2003" ed. M.D. Furnish, Y.M. Gupta, J.W. Forbes, pp. 935-938, publ. American Institute of Physics, Melville NY

2004 H. Czerski, M.W. Greenaway, W.G. Proud, J.E. Field "Monitoring phase-change in HMX during dropweight impact" in "Shock Compression of Condensed Matter – 2003" ed. M.D. Furnish, Y.M. Gupta, J.W. Forbes, pp. 771-774, publ. American Institute of Physics, Melville NY

2004 H. Czerski, M.W. Greenaway, W.G. Proud, J.E. Field "b-d phase transition during dropweight impact of cyclotetramethylene-tetranitroamine" *J. Appl. Phys.* **96** 4131-4134

2004 H. Czerski, M.W. Greenaway, W.G. Proud, J.E. Field “Phase change in HMX during impact experiments”, in “Energetic Materials: Structure and Properties”, paper 179, publ. Karlsruhe, Institut für Chemische Technologie

2004 J.E. Field, S.M. Walley, W.G. Proud, J.E. Balzer, M.J. Gifford, S.G. Grantham “The shock initiation and high strain rate mechanical characterization of ultrafine energetic powders and compositions” *Mater. Res. Soc. Symp. Proc.* **800** 179-190

2004 J.E. Field, S.M. Walley, W.G. Proud, H.T. Goldrein, C.R. Siviour “Review of experimental techniques for high rate deformation and shock studies” *Int. J. Impact Engng* **30** 725-775

2004 S.G. Grantham, C.R. Siviour, W.G. Proud, J.E. Field “High-strain rate Brazilian testing of an explosive simulant using speckle metrology” *Meas. Sci. Technol.* **15** 1867-1870

2004 M.W. Greenaway, J.E. Field “The development of a laser-driven flyer system” in “Shock Compression of Condensed Matter – 2003” ed. M.D. Furnish, Y.M. Gupta, J.W. Forbes, pp. 1389-1392, publ. American Institute of Physics, Melville NY

2004 H.J. Prentice, W.G. Proud “Experimental investigation of ignition mechanisms in confined energetics”, in “Proc. 7th Seminar on New Trends in Research of Energetic Materials”, ed. J. Vágenknecht, pp. 235-243, publ. Pardubice, Czech Republic, University of Pardubice

2004 W.G. Proud, I.J. Kirby, J.E. Field “The nature, number, and evolution of hot-spots in ammonium nitrate” in “Shock Compression of Condensed Matter – 2003” ed. M.D. Furnish, Y.M. Gupta, J.W. Forbes, pp. 1017-1020, publ. American Institute of Physics, Melville NY

2004 C.R. Siviour, M.J. Gifford, S.M. Walley, W.G. Proud, J.E. Field “Particle size effects on the mechanical properties of a polymer bonded explosive” *J. Mater. Sci.* **39** 1255-1258

2004 C.R. Siviour, S.G. Grantham, D.M. Williamson, W.G. Proud, S.M. Walley, J.E. Field “High resolution optical analysis of dynamic experiments on PBXs”, in “Proc. 7th Seminar on New Trends in Research of Energetic Materials”, ed. J. Vágenknecht, pp. 277-284, publ. Pardubice, Czech Republic, University of Pardubice

2004 C.R. Siviour, D.M. Williamson, S.G. Grantham, S.J.P. Palmer, W.G. Proud, J.E. Field “Split Hopkinson bar measurements of PBXs” in “Shock Compression of Condensed Matter – 2003” ed. M.D. Furnish, Y.M. Gupta, J.W. Forbes, pp. 804-807, publ. American Institute of Physics, Melville NY

2004 D. Williamson, S. Palmer, J. Field, W. Proud “Deformation and fracture of energetic materials and their simulants”, in “Proc. 7^h Seminar on New Trends in Research of Energetic Materials”, ed. J. Vágenknecht, pp. 349-359, publ. Pardubice, Czech Republic, University of Pardubice

2004 D. Williamson, S. Palmer, S. Grantham, W. Proud, J. Field “Mechanical properties of PBS9501” in “Shock Compression of Condensed Matter – 2003” ed. M.D. Furnish, Y.M. Gupta, J.W. Forbes, pp. 816-819, publ. American Institute of Physics, Melville NY

2005 C.R. Siviour, J.L. Jordan “A miniaturized split Hopkinson pressure bar for very high strain rate testing”, Air Force Research Laboratory Report no. AFRL-MN-EG-TR-2005-7014, Eglin Air Force Base, Florida

2005 S.G. Grantham, W.G. Proud, J.E. Field “Digital speckle radiography of explosives”, to be published in Proc. 12th Int. Detonation Symposium

2005 P.J. Rae, H.T. Goldrein, S.J.P. Palmer, R.W.P. White, A.L. Lewis “The use of digital image cross-correlation (DICC) to study the mechanical properties of a PBX”, to be published in Proc. 12th Int. Detonation Symposium

2005 S.M. Walley, J.E. Field, M.W. Greenaway “Crystal sensitivities of energetic materials”, accepted for publication in *Materials Science & Technology*